SEPTEMBER 1957

A.I.Ch.E. JOURNAL

OCT 23 1957
EAST ENGINEERING LIBRARY

Published by the American Institute of Chemical Engineers

CONTENTS

Interaction Between a Turbulent Air Stream and a Moving Water Surface	Thomas J. Hanratty and James M. Engen
Discharge Coefficients Through Perforated Plates	P. A. Kolodzie, Jr., and Matthew Van Winkle
Nusselt Values for Estimating Turbulent Liquid Metal Heat Transfer in Noncircular Ducts	James P. Hartnett and Thomas F. Irvine, Jr.
Equilibrium Ratios of Hydrogen and the Critical Loci of Hydrogen-paraffin Mixtures	J. M. Lenoir and H. G. Hipkin
Two-phase Pressure Drops in Large-diameter Pipes	R. C. Reid, A. B. Reynolds, A. J. Diglio, I. Spiewak, and D. H. Klipstein
Surface Tension of Acetone-water Solutions Up to Their Normal Boiling Points	Katherine S. Howard and R. A. McAllister
Simple Theory of an Idealized Turbulent Mixer	Stanley Corrsin
Effect of Water Vapor on the Catalytic Oxidation of Nitric Oxide	Omer Kircher and O. A. Hougen
Measured Plate Efficiencies and Values Predicted from Single-phase Studies	F. E. Rush, Jr., and Clifford Stirba
Drying of Sand on a Hot Surface	R. W. Ludt
Heat Transfer Coefficients for Condensing Organic Vapors of Pure Components and Binary Mixtures	Bernard S. Pressburg and James B. Todd
Graphical Solution of Turbulent-flow Diffusion Equations	P. A. Longwell
Two-phase, Steam-water Critical Flow	H. S. Isbin, J. E. Moy, and A. J. R. Da Cruz
Catalyzed Gas-liquid Reactions in Trickling-bed Reactors	B. D. Babcock, Glor T. Mejdell, and O. A. Hougen
Studies on Effective Thermal Conductivities in Packed Beds	Sakae Yagi and Daizo Kunii
Behavior of Suspended Particles in a Turbulent Fluid	S. K. Friedlander
Determination of the Chemical Properties of an Oxide Catalyst in a Closed System	C. D. Holland and P. G. Murdoch
Evaluation of the Heat Requirements in Batch Distillation Operations	J. G. Stiehl and James H. Weber
Gas Mixing in a Square Duct	Eugene Miller, S. P. Foster, R. W. Ross, and Kurt Wohl
Thermal and Material Transfer in Turbulent Gas Streams: Local Transport from Spheres	N. T. Hsu and B. H. Sage
Effects of Bubbling and Stirring on Mass Transfer Coefficients in Liquids	D. L. Johnson, Hirotaro Saito, J. D. Polejes, and O. A. Hougen
Effect of Liquid Physical Properties and Flow Rates on the Surface Area of Sprays from a Pressure Atomizer	J. A. Consiglio and C. M. Sliepcevich
Critical Constants of the Aromatic Hydrocarbons	George Thodos

Practical, Efficient, and Economical

SOLVENT EXTRACTION

with

YORK-SCHEIBEL LIQUID-LIQUID EXTRACTORS

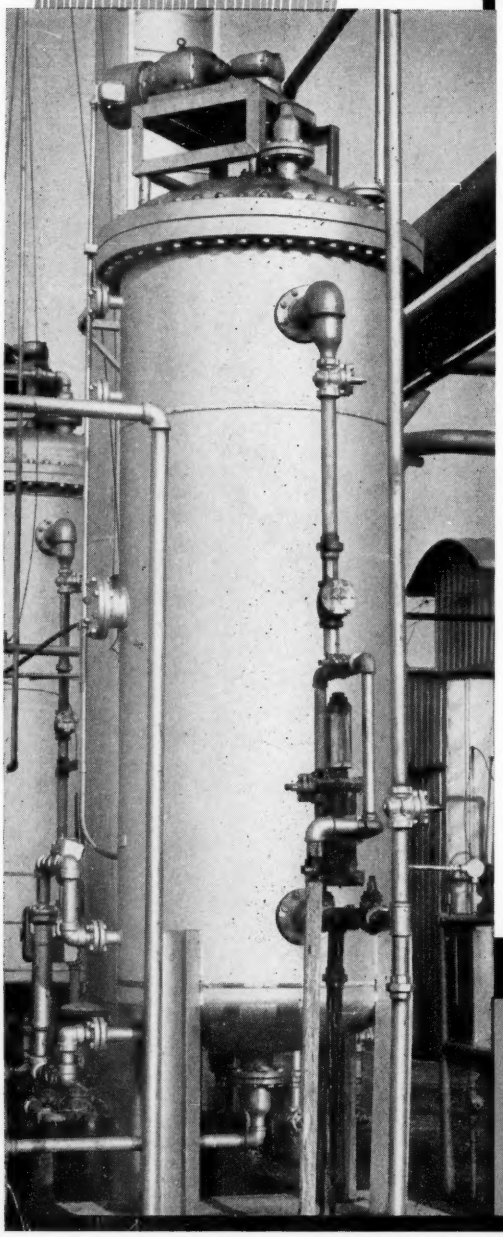

The YORK-SCHEIBEL patented multi-stage extraction column:

- Is ideal for the common multi-stage, countercurrent extractions in which the feed material is contacted with a single solvent.
- Is effective and efficient for fractional liquid extraction in which the feed material is contacted with two selective and immiscible solvents flowing countercurrent through the column.
- May be designed for liquid streams carrying solids in suspension.

The columns employ agitators in each stage to insure complete liquid-liquid contacting. The phase separating sections between the mixing zones consist of wire mesh packing, a new arrangement of baffles, or both baffles and packing.

High stage efficiencies are obtained even with difficult-to-separate materials. Here are a few of the extractions for which York-Scheibel columns have no equal:

- *close boiling mixtures*
- *non-volatile mixtures*
- *structural isomers*
- *materials from dilute solutions*
- *azeotropic mixtures*
- *impurities and color bodies*
- *heat sensitive materials*

Check these outstanding features:

- ✓ *Single, compact column*
- ✓ *High throughput capacity*
- ✓ *Efficient laboratory, pilot plant and large scale performance*
- ✓ *High efficiency*
- ✓ *Low cost per stage*
- ✓ *Low stage height*

SEND INFORMATION on your requirements and let York engineers recommend the best design for your conditions.

YORK

YORK PROCESS EQUIPMENT CORP.
4 Central Avenue, West Orange, N.J.
Send for latest literature giving complete details

A.I.Ch.E. JOURNAL

SEPTEMBER 1957 · VOL. 3, NO. 3

PUBLISHER
F. J. Van Antwerpen
EDITOR
Harding Bliss
ADVERTISING MANAGER
L. T. Dupree

ADVISORY BOARD

C. M. Cooper, O. E. Dwyer, W. C. Edmister, E. R. Gilliland, A. N. Hixson, H. F. Johnstone, W. R. Marshall, Jr., R. H. Newton, R. L. Pigford, E. L. Piret, J. M. Smith, Theodore Vermeulen, R. R. White, R. H. Wilhelm

The A. I. Ch. E. Journal, an official publication of the American Institute of Chemical Engineers, is devoted in the main to theoretical developments and research in chemical engineering and allied branches of engineering and science. Manuscripts should be submitted to the New York office.

Grimm and Andersen: Move Over 297

Interaction Between a Turbulent Air Stream and a Moving Water Surface
Thomas J. Hanratty and James M. Engen 299

Discharge Coefficients Through Perforated Plates . . . . . *P. A. Kolodzie, Jr., and Matthew Van Winkle* 305

Nusselt Values for Estimating Turbulent Liquid Metal Heat Transfer in Noncircular Ducts
James P. Hartnett and Thomas F. Irvine, Jr. 313

Equilibrium Ratios of Hydrogen and the Critical Loci of Hydrogen-paraffin Mixtures
J. M. Lenoir and H. G. Hipkin 318

Two-phase Pressure Drops in Large-diameter Pipes
R. C. Reid, A. B. Reynolds, A. J. Diglio, I. Spiewak, and D. H. Klipstein 321

Surface Tension of Acetone-water Solutions up to Their Normal Boiling Points
Katherine S. Howard and R. A. McAllister 325

Simple Theory of an Idealized Turbulent Mixer . . . . . *Stanley Corrsin* 329

Effect of Water Vapor on the Catalytic Oxidation of Nitric Oxide . . . . . *Omer Kircher and O. A. Hougen* 331

Measured Plate Efficiencies and Values Predicted from Single-phase Studies
F. E. Rush, Jr., and Clifford Stirba 336

Drying of Sand on a Hot Surface . . . . . *R. W. Ludt* 343

Heat Transfer Coefficients for Condensing Organic Vapors of Pure Components and Binary Mixtures
Bernard S. Pressburg and James B. Todd 348

Graphical Solution of Turbulent-flow Diffusion Equations . . . . . *P. A. Longwell* 353

Two-phase, Steam-water Critical Flow . . . . . *H. S. Isbin, J. E. Moy, and A. J. R. Da Cruz* 361

Catalyzed Gas-liquid Reactions in Trickling-bed Reactors *B. D. Babcock, Glor T. Mejdell, and O. A. Hougen* 366

Studies on Effective Thermal Conductivities in Packed Beds . . . . . *Sakae Yagi and Daizo Kunii* 373

Behavior of Suspended Particles in a Turbulent Fluid . . . . . *S. K. Friedlander* 381

Determination of the Chemical Properties of an Oxide Catalyst in a Closed System
C. D. Holland and P. G. Murdoch 386

Evaluation of the Heat Requirements in Batch Distillation Operations . *J. G. Stiehl and James H. Weber* 391

Gas Mixing in a Square Duct . . . . . *Eugene Miller, S. P. Foster, R. W. Ross, and Kurt Wohl* 395

Thermal and Material Transfer in Turbulent Gas Streams: Local Transport from Spheres
N. T. Hsu and B. H. Sage 405

Effects of Bubbling and Stirring on Mass Transfer Coefficients in Liquids
D. L. Johnson, Hirotaro Saito, J. D. Polejes, and O. A. Hougen 411

Effect of Liquid Physical Properties and Flow Rates on the Surface Area of Sprays from a Pressure Atomizer
J. A. Consiglio and C. M. Sliepcevich 418

Critical Constants of the Aromatic Hydrocarbons . . . . . *George Thodos* 428

Errata 7

Communications to the Editor 9

Books 12

Publication Office, Richmond, Virginia. Published quarterly in March, June, September, and December by the American Institute of Chemical Engineers, 25 West 45 Street, New York 36 New York. Manuscripts and other communications should be sent to the New York office. Correspondence with the editor may be addressed to him at Yale University, 225 Prospect Street, New Haven 11, Connecticut. Statements and opinions in the *A.I.Ch.E. Journal* are those of the contributors, and the American Institute of Chemical Engineers assumes no responsibility for them. Subscriptions: one year, member $4.50, nonmember $9.00; two years, member $7.50, nonmember $15.00; additional yearly postage, Canada 50 cents, Pan American Union $1.50, other foreign $2.00 (foreign subscriptions payable in advance). Single copies: $3.00. Second-class mail privileges authorized at Richmond, Virginia. Copyright 1957 by the American Institute of Chemical Engineers. National headquarters of A.I.Ch.E. is concerned about nondelivery of copies of the *A.I.Ch.E. Journal* and urgently requests subscribers to give prompt notification of any change of address. Sixty days must be allowed for changes to be made in the records.

PROBLEM!

How extensive must testing and research be to determine the most feasible filtration technique and filter station for your process problem? This is Eimco's first concern.

Preliminary investigation begins with a visit from one of our competent field engineers. We rely upon him to become thoroughly oriented with your problem and to recommend testing and research procedure.

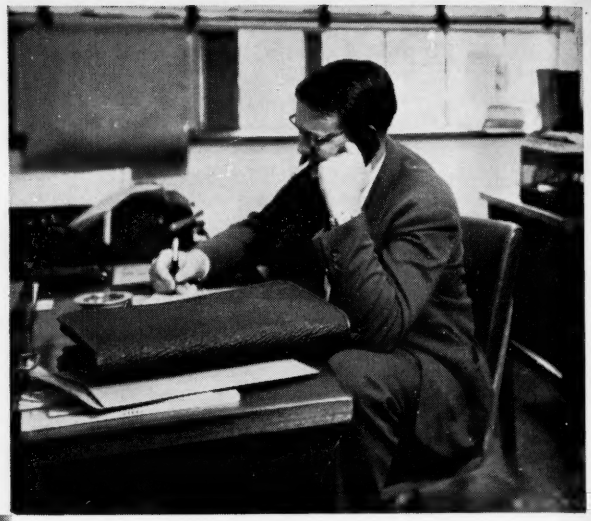

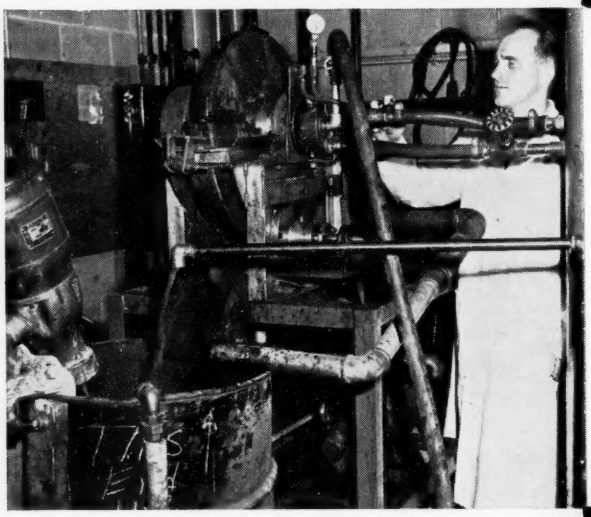

SOLUTION!

When field test work is not sufficient to accurately measure the effects of all variables and define all control factors . . or present a clear economic picture of the over-all operation . . it becomes economically sound to let the **Eimco Research and Development Center** provide the link between laboratory investigation and plant operation.

Our specialized manpower. . . . compiled research data and large scale testing facilities go to work for you at a very nominal fee.

RESULT!

Accurate conclusions fundamental to selection of a modern, cost saving filter station that gets you maximum production and profit from every $ invested in equipment and raw materials.

You may be pioneering a new process and don't have all the answers. . . or improper techniques and filter equipment may be robbing you of maximum production and profit. In either case, you can "start the ball rolling" toward a solution by contacting Eimco today.

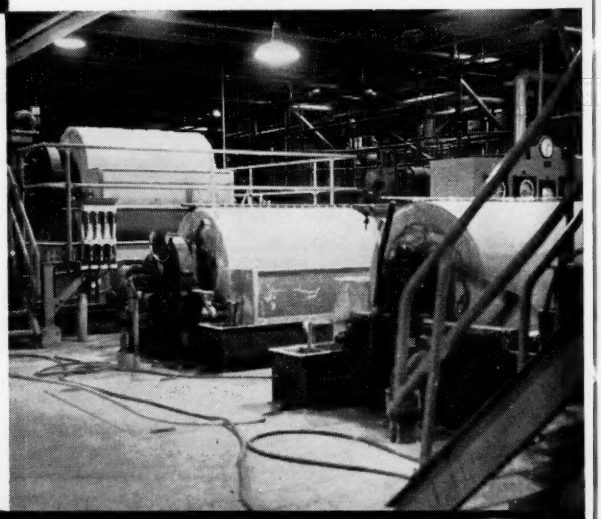

THE EIMCO CORPORATION

SALT LAKE CITY, UTAH

Research and Development Division, Palatine, Illinois • Process Engineers Inc. Division, San Mateo, California
Export Offices: Eimco Building, 51-52 South Street, New York 5, N. Y.
BRANCHES AND DEALERS IN PRINCIPAL CITIES THROUGHOUT THE WORLD

B-281

A.I.Ch.E. JOURNAL

Grimm and Andersen: Move Over

The book "The Demand and Supply of Scientific Personnel"* could be described as a modern fairy story if it were not such dull reading. In this book the authors attempt to prove that there has not been and there is not now a shortage of engineers. The same implication is made a little less clearly for chemical scientists. This conclusion seems little short of fantastic, at least to one in university teaching, where the corporate recruiters are so thick one can scarcely see the elms.

How can one explain the conclusions reached by these authors which are so obviously at variance with the common experience? Where did they go astray? It is our belief that they elected to define a shortage in an arbitrary way for which there is very little support and that they displayed a rather extensive ignorance of the engineering profession and how it is developing.

The authors express the opinion that "a shortage exists when the number of workers available (the supply) increases less rapidly than the number demanded at the salaries paid in the recent past." They then conclude that, since the salaries of engineers have declined in comparison with the wages of ordinary employees and the income of doctors and dentists, there is no shortage. This conclusion is so much open to criticism that one has difficulty in deciding just where to begin. First, this clearly assumes a free economy (and the authors admit this), but in this day of powerful labor unions and certain other associations it is naïveté in the highest degree to call this a free economy. The salaries paid any segment of the working population reflect many things, such as political pressure and geographical location, as well as demand. Second, the use of statistical data on one factor to establish a cause-and-effect relationship toward another factor is always dubious. The recent cigarette and cancer controversy is a case in point. Another example is the scholar who concluded that the great number of New Englanders in "Who's Who" was due to the stimulating effect of the New England climate. Those who live there are rather inclined to feel that such numbers were attained in spite of the climate. Third, the government data on salaries are themselves of doubtful value because they clearly include many people of subprofessional rank and because they seemingly exclude those very well-paid engineers who have become executives and managers. Fourth, probably the most acutely underpaid people at present are the school teachers and ministers; yet there is a considerable shortage of both.

It seems to this reviewer that shortages and salaries are two quite different things, particularly in the economy of our day, and that the relation between them is tenuous at best. One may take up engineering or teaching because of a love of the work without particular regard to the salary; man is different from a piece of copper, which will command a higher price when it is scarce. The emphasis on salaries leads the authors to make doubtful statements, dismissing contrary evidence. Thus, the fact that the demand for engineers in the help-wanted columns rose greatly from 1946 to 1950 is set aside because this "took place while relative earnings of engineers were not rising but falling."

The ignorance of the engineering profession exhibited by these authors stems largely from the government statistics. If one approaches statistics without imagination one will come up with some odd answers. The obvious flaw in these statistics and in the conclusions drawn from them is the inclusion of large numbers of subprofessionals. Thus, for example, the following percentages of workers in the various categories had *at most* 4 years of high school education (date 1950):

Chemical engineers	9.1%
Civil engineers	27.1%
Electrical engineers	26.5%
Mechanical engineers	31.8%
Chemists	21.6%

We chemical engineers may feel pleased at our position in this list, although it is interesting to note that there were seventy "chemical engineers" in the 14–19 age group according to this statistical source.

It is obvious that there has been included in these numbers a group of workers who could not possibly have been trained for engineering as it is now and as it will be in the future. This journal reports the most advanced work in chemical engineering, and the high school graduate who could digest it would be singular indeed. But the research work of today is the practice of tomorrow; the future will require of our engineers higher and higher degrees of intellectual training and competence. It is this ignorance of the highly skillful nature of engineering which leads the authors into such statements as: "But there is no warrant for the assertion that a rising demand for scientifically trained personnel is part and parcel of modern industries . . ." (page 64) and "There is no reason to believe that this component of supply [nongraduate engineers, including even nonhigh-school graduates] will diminish rapidly in the near future" (page 87). These are pure statements of opinion based on inadequate study. A brief examination of the current literature in any engineering field would have convinced the authors that engineering and industry are tending to require more and more technical skills. And there is a shortage of men with such skills.

We can take at least one lesson from this book. There is a great ignorance of the nature of the engineering profession even on the part of the nominally well-informed. We should be wise to present our profession more effectively to the public.

H. B.

*By David M. Blank and George J. Stigler, National Bureau of Economic Research, Princeton University Press, Princeton, N. J. (1957).

Spray Drying is the modern labor-saving process used to produce products with greater sales appeal, often at reduced production costs. Numerous processes in use today are subject to the same modernization as has been applied, with Bowen cooperation, in many leading industries:

Electronic industry benefits by a high quality finely blended homogenous Titania material which is easily extruded for special dielectric parts . . .

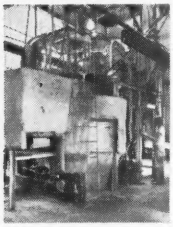

FIRST SPRAY DRIED BY
American Lava

Evaporation loss of crude oil can now be reduced by 80-90 per cent with nitrogen-filled microscopic phenolic spheres which form vapor seal on stored crude oil . . .

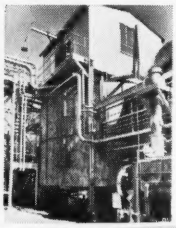

FIRST SPRAY DRIED BY
Bakelite

New sterile Plasma Volume Expander for intravenous injections has saved countless lives in both military and civilian use . . .

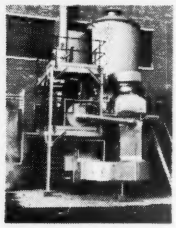

FIRST SPRAY DRIED BY
Commercial Solvents

Developing New Products on Bowen SPRAY DRYERS

Patented Bowen air cooling features made possible the large production of thermoplastic and thermosetting resin powders . . .

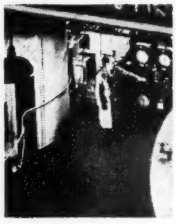

FIRST SPRAY DRIED BY
Plaskon

Controlled spherical shape, free-flowing characteristics and high density of spray dried Ferrites, makes possible superior performance of electrical cores . . .

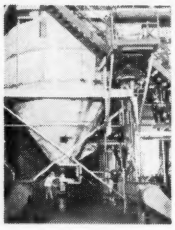

FIRST SPRAY DRIED BY
Stackpole Carbon

And, many other companies with whom Bowen has worked have pioneered with Bowen Equipment to produce a FIRST-of-its-kind product. Bowen engineers are available to work with you to incorporate Spray Drying in the production of your products. Whether you are producing a high cost quality product or a basic material in quantity where low cost is the determining factor, you should investigate Spray Drying.

Write for this Interesting Book

THE BOWEN LABORATORY SPRAY DRYER

We will be glad to send it — No obligation

BOWEN ENGINEERING, INC.
NORTH BRANCH 12, NEW JERSEY

BOWEN SPRAY DRYERS
Always Offer You More!

Recognized Leader in Spray Dryer Engineering Since 1926

Interaction Between a Turbulent Air Stream and a Moving Water Surface

THOMAS J. HANRATTY and JAMES M. ENGEN

University of Illinois, Urbana, Illinois

The interaction between a turbulent air stream and a water film flowing parallel to it was studied. The variables explored were the liquid flow rate, the gas flow rate, and the film height. The data were correlated in terms of a liquid and a gas Reynolds number. Thinner films or films having a lower Reynolds number were more stable. For the experiments reported in this research the transition from a smooth surface to a surface possessing two-dimensional waves occurs at $hU_\tau\rho_{liquid}/\mu_{liquid}$ of about 520. Transition from two-dimensional waves to a "pebbled" surface occurs at a value of this parameter of about 600. Theories presented in the literature for the initiation of waves on a liquid surface do not adequately describe the experimental results.

Problems involving the simultaneous flow of a gas stream and a liquid film are commonly met in engineering practice. Film coolers, falling-film-absorption towers, condensers, and the transportation of liquid-vapor mixtures are examples of processes involving such two-phase flow problems. A more thorough understanding of these processes could be derived from a better understanding of the nature of the interaction at the interface of the liquid and gas.

If a gas is blown parallel to a liquid surface, it will exert a drag on the surface and cause the liquid to flow. The drag will increase with gas flow. At high enough flows the surface will become unstable and waves will form. The drag of the gas on the liquid and the velocity profile in the gas then will be dependent upon the structure of the liquid surface. At extremely high flows liquid will be torn from the surface and dispersed in the gas stream.

The experiments described in this paper were undertaken to examine the interaction of an air stream and a water film flowing parallel to it. As they were carried out in a rectangular channel having an aspect ratio of 12:1, the gas flow could be considered as two dimensional. The test section was long enough for the height of the liquid film to have reached an equilibrium condition; there was no change in the momentum flow; and the pressure drop was a function of only the drag at the enclosing surfaces. The channel was made of transparent plastic so that the condition of the interface might be observed. Measurements of the pressure drop and of the velocity profile in the gas reflected the effect of changes of the liquid surface upon the flow in the gas phase.

James M. Engen is at present with Archer-Daniels-Midland Company, Minneapolis, Minnesota.

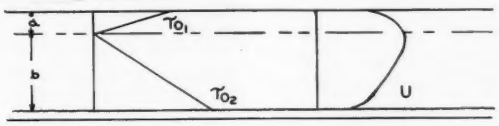

Fig. 1. Shear stress and velocity profile.

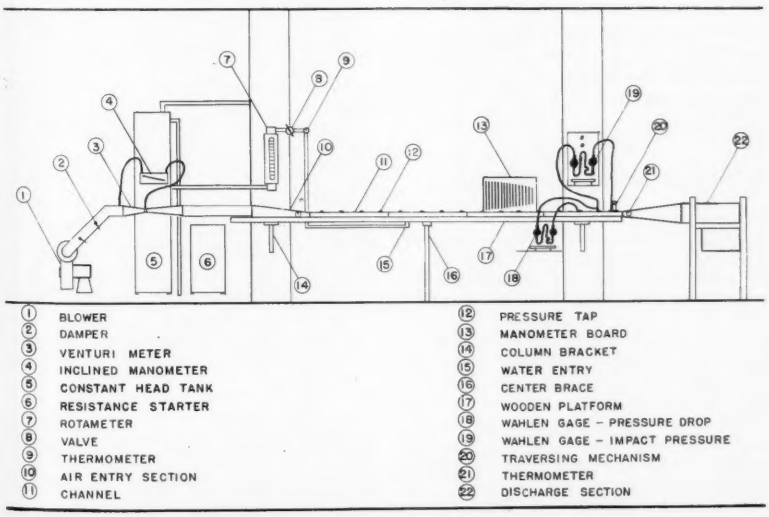

Fig. 2. Sketch of equipment.

THEORY

Flow in the Liquid Film

At low gas velocities where the surface of the liquid film is smooth, the liquid flow would be laminar. The Navier-Stokes equation for a two-dimensional flow may be used to relate the velocity distribution and the volumetric flow in the liquid to the drag of the gas at the surface.

$$u\frac{\partial u}{\partial x} + v\frac{\partial u}{\partial y} = -\frac{1}{\rho}\frac{\partial P}{\partial x} + \frac{\mu}{\rho}\frac{\partial^2 u}{\partial y^2} \qquad (1)$$

For a liquid film with a stable thickness

$$v = 0$$

$$\frac{\partial u}{\partial x} = 0$$

and the pressure drop in the liquid is equal to the pressure drop in the gas. Equation (1) becomes

$$\frac{1}{\rho}\frac{\partial P}{\partial x} = \frac{\mu}{\rho}\frac{\partial^2 u}{\partial y^2} \qquad (2)$$

If the boundary conditions

$$u = 0 \qquad \text{at } y = 0$$

$$g_c\tau_{0_2} = \mu\frac{\partial u}{\partial y} \qquad \text{at } y = h$$

are employed, Equation (2) may be integrated to give

$$u = \frac{g_c}{\mu}\frac{dP}{dx}\frac{y^2}{2} - \frac{g_c}{\mu}\frac{dP}{dx}hy + \frac{g_c}{\mu}\tau_{0_2}y \qquad (3)$$

The volumetric flow rate is

$$Q = \int_0^h u\,dy \qquad (4)$$

$$Q = \frac{g_c}{\mu}\frac{dP}{dx}\frac{h^3}{6} - \frac{g_c}{\mu}\frac{dP}{dx}\frac{h^3}{2} + \frac{g_c}{\mu}\tau_{0_2}\frac{h^2}{2}$$

When the liquid surface is wavy or when the flow is turbulent, no simple expressions such as Equations (3) and (4) can be obtained.

Practically all the theories (*1*) for surface waves have been developed for nonviscous fluids. Although these theories would not be useful in predicting the volumetric flow in the film, they do give a relation between the wave velocity and

Table 1

Comparison of Actual and Predicted Wave Lengths

Run No.	t Strob (sec.)	λ^* (cm.)	c^* (cm./sec.)	$t^* = \lambda^*/c^*$ (sec.)	c^{**}calc. (cm.)/(sec.)	Condition
66	0.046	1	30	0.033	25	Two-dimensional waves
67	0.050	1.25	23	0.044	24	Two-dimensional waves
68	0.040	1	30	0.033	25	Two-dimensional waves
69	0.040	0.50	30	0.017	31	Squalls
70	0.054	0.50	20	0.025	31	Squalls

*visual observations.
**using λ^* and Equation (6).

the wave length which approximates the properties of some liquid surfaces observed in this research. For a two-dimensional wave in an irrotational fluid of height h, Lamb (*1*) gives the following expression:

$$c^2 = \frac{g\lambda}{2\pi}\tanh\left(\frac{2\pi h}{\lambda}\right) + \frac{2\pi T}{\rho\lambda}\tanh\left(\frac{2\pi h}{\lambda}\right) \qquad (5)$$

When $h > \frac{1}{2}\lambda$, the equation reduces approximately to

$$c^2 = \frac{g\lambda}{2\pi} + \frac{2\pi T}{\rho\lambda} \qquad (6)$$

The wave length may also be described in terms of the time of oscillation t by using the relation

$$c = \lambda/t \qquad (7)$$

Substituting for c in Equation (6) one obtains

$$\lambda^2 - \frac{g\lambda t^2}{2\pi} - \frac{2\pi T t^2}{\rho\lambda} = 0 \qquad (8)$$

Flow in the Gas

For practically all the experiments reported in this paper the gas was turbulent. Except for the immediate vicinity of the wall a turbulent-flow field in a smooth channel may be described by an empirical equation of the form

$$u^* = A \log y^* + B \qquad (9)$$

For very small-sized roughnesses on the walls Equation (9) is still valid and the surface may be considered "hydraulically smooth." For sufficiently large roughnesses the shear stress at the surface τ_0 will increase as the size of the roughness increases. Likewise, for such a surface the constant B will be dependent upon the surface condition. As the roughness size is increased, a situation is eventually reached at which the flow profile is independent of the fluid viscosity. Such a condition is described as a "completely roughened" surface and the velocity profile data may be correlated in terms of the roughness size k_s.

$$u^* = A \log y/k_s + C \qquad (10)$$

The constant A describing the slope in Equations (9) and (10) would be the same. For a surface which has been completely roughened with sand Schlichting (*2*) gives the following equation:

$$u^* = 5.75\frac{y}{k_s} + 8.5 \qquad (11)$$

This equation may be used to calculate an "equivalent sand roughness" for non-smooth liquid surfaces.

In the experiments described in this paper the gas flowed through a channel with an upper surface that may be considered "hydraulically smooth" and a lower surface that consisted of a water film moving slowly relative to the gas flow. If the liquid surface is not smooth the shear stress possibly might be larger at the bottom than at the top of the enclosed gas space. The velocity profile in the gas will be distorted as indicated in Figure 1. The maximum in the velocity profile will be a condition of zero stress. Momentum balances may be written for a unit width of the channel to give expressions which relate the distortion of the velocity profile to the shear stresses at the upper and lower surfaces.

$$a \times 1 \times \Delta P = \tau_{0_a} \times 1 \times \Delta L \qquad (12)$$

$$b \times 1 \times \Delta P = \tau_{0_b} \times 1 \times \Delta L \qquad (13)$$

If the location of the maximum in the velocity profile, the location of the liquid surface, and the pressure drop are known, the shear stress at both surfaces can be calculated.

DESCRIPTION OF THE EXPERIMENTS

A sketch of the experimental equipment is shown in Figure 2. The rectangular channel, which was 1.016 in. high and 12 in. wide, was made of Plexiglas in four sections, each 4 ft. long. The first and second were air-stream calming sections. The second section had slots cut in the sides to hold a flat 20-gauge galvanized iron sheet. This sheet was held 1/16 in. from the bottom by brass spacers; the water entered under it and flowed out forming an even film. The third and fourth sections were calming sections for film entry effects. The fourth served also as a test section.

Pressure taps glued over 1/64-in. holes in the top wall were placed at 1-ft. intervals along the length. Velocity measurements were made with an impact tube at a position 6 in. from the exit of the channel. The impact tube, which was mounted to a traversing mechanism that allowed its position to be measured to 0.001 in., was made from a stainless steel hypodermic needle having a 0.032-in. I.D. and a 0.050-in. O.D. Its leading edge was rounded into a hemispherical shape and it was soldered into a ⅛-in. brass tube with a 1/16-in. I.D.

The impact pressure and the static pressure drop were measured with a Wahlen micromanometer (*3*) that had a precision of ±0.0005 in. methanol over a 1-in. range.

The height of the liquid film was measured in two ways; neither was completely satisfactory. The impact tube was brought to the level of the liquid surface and was positioned by being looked at from above and below the film in order to eliminate the illusion of the meniscus rising on the sides of the tube. This method works well for smooth films; however, it is difficult to employ when the surface is rough. A machinist's scale was placed on the outside wall, and with care one could measure the liquid height within 1/64 in. at the first transition and within 2/64 in. at the second transition.

The wave velocity was approximated by timing the travel of a wave over a 3- to 5-ft. length with a stop watch, although a Strobotac was used in some runs. The frequency chosen with the instrument was

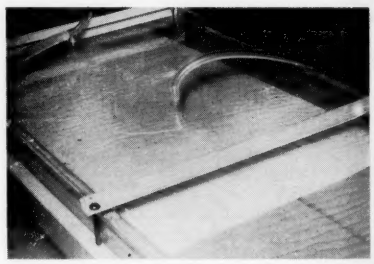

Fig. 3. Photograph of two-dimensional waves

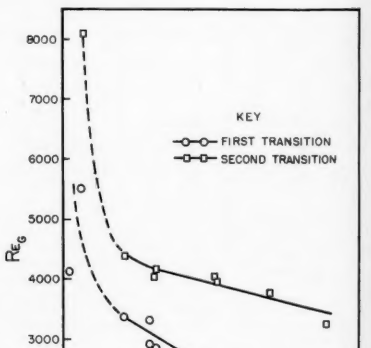

Fig. 4. Re_G vs. Re_L for first two transitions.

that frequency which caused a change in direction of the image.

RESULTS

The effect of water height, liquid flow rate, and gas flow rate was explored under conditions that prevented these quantities from being varied independently. Results were obtained over a range of mean air velocities of 3.8 to 178 ft./sec. and of Re_G based on the thickness of the gas phase H from 945 to 84,000. The liquid height varied from 0.16 to 0.21 in.; the mean liquid velocity ranged from 0.01 to 0.30 ft./sec.; and the Re_L, from 11.9 to 508.

The effect of the gas flow upon the liquid can be described in terms of five types of liquid surfaces: (1) smooth, (2) two-dimensional waves, (3) squalls, (4) roll waves, and (5) dispersed flow.

Two-dimensional Waves

The first disturbance that appeared on the liquid surface as the gas rate was increased was small ripples that quickly formed two-dimensional waves. For an average film thickness greater than 1/8 in., these two-dimensional waves were nearly 1 cm. apart and traveled at a velocity of from 0.75 to 1 ft./sec. They were low-amplitude waves with heights less than 0.005 in. in all cases. As shown in Figure 3, they were curved; however they extended the complete width of the channel. The relation between the wave velocity and wave length could be approximated by Equation (6). (See Table 1.)

A transition point to a disturbed surface was defined as the point where the first small ripples appeared. Except at very low liquid rates this was coincident with the point at which they disappeared. The gas velocity at which waves first appeared depended on the flow conditions in the liquid. Since the liquid height and liquid flow rate could not be varied independently, the exact role of these two variables in effecting the transition was not ascertained. Results on the effect of liquid flow conditions upon the transition gas velocity are tabulated in Table 2. For Re_L less than 100, U_{max} varied from 3.8 to 9.0 ft./sec. Figure 4 shows the relation between Re_G and Re_L at the first transition. Figure 5 shows the relation between Re_G and the liquid height. A Reynolds number expressed in terms of both the gas and liquid flow properties may be defined at the transition point as

$$Re^* = \frac{hU_\tau \rho_{liquid}}{\mu_{liquid}}$$

Since pressure-drop measurements were made only for runs at the first transition, the parameter τ_{0_2} could be calculated only for a fraction of the data obtained. As shown in Table 3, the transition point occurred at a value of Re^* of approximately 520.

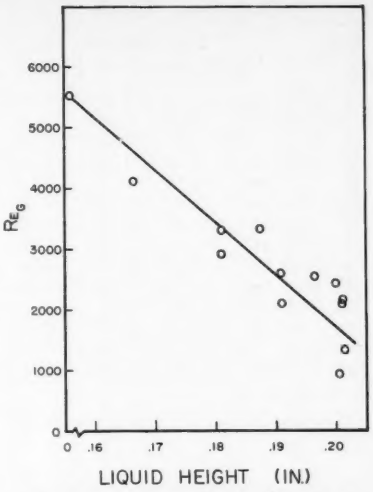

Fig. 5. Re_G vs. liquid height for first transition.

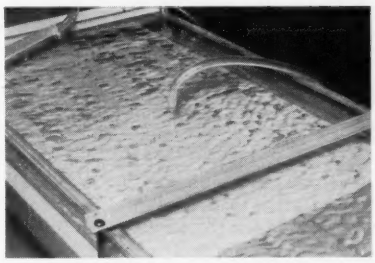

Fig. 6. Photograph of squall surface.

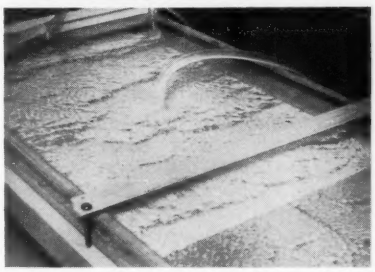

Fig. 7. Photograph of roll waves.

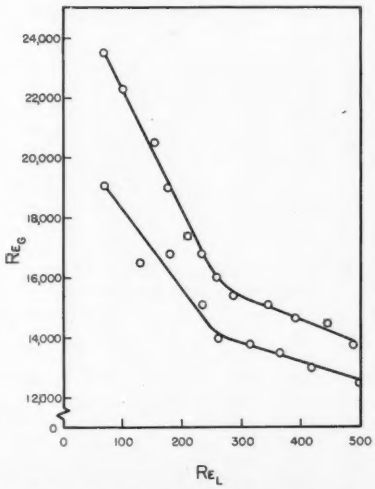

Fig. 8. Re_G vs. Re_L for third transition.

The Re_G range, 1,000 to 5,000, over which two-dimensional waves first formed, was in the same range as the transition to turbulence in the gas phase; however, the appearance of a disturbed liquid surface was not coincident with the transition to gas-phase turbulence. In some runs a smooth surface coexisted with a fully developed gas-phase turbulence. Likewise transition to a disturbed surface was possible without the existence of a fully developed turbulent gas flow.

Squalls

The two-dimensional wave structure existed only over a small portion of the range of variables investigated. If the air velocity is increased slightly above the first transition point, the two-dimensional waves break into a squall surface, which is shown in Figure 6. These are characterized by a "pebbled" appearance having a wave length of 0.5 to 1 cm. and a width nearly equal to the wave length. The breakdown first appeared as a streak "slicing" down through the two-dimensional waves about 4 to 5 ft. from the point of liquid entry. A slight increase in the air velocity then caused a complete breakup into squalls traveling at nearly the same velocity as the two-dimensional waves.

A second transition was defined at the point where the first streaks appeared. In all cases the transition point did not depend on whether it was approached from high or low gas velocities. The appearance of the squall surface depended on the liquid flow properties; this relation is summarized in Table 4. For Re_L greater than 100 the range of maximum gas velocities (U_{max}) at which this second transition occurred was from 10 to 12 ft./sec. Figure 4 shows a plot relating Re_G to Re_L at the transition. Values of Re^* have been calculated and are presented in Table 5. The second transition appears to be characterized by a value of Re^* of about 600.

The height of the liquid film calculated from Equation (4), a laminar flow being assumed, was much lower than the measured height.

Roll Waves

The squall surface was stable over a wide range of gas flows. Eventually, however, as the gas rate was increased roll waves appeared on the squall surface. This might be analogous to the slugging observed in two-phase flow in pipes. A slug of liquid was picked up and carried over the top of the liquid surface by the gas at a very rapid rate. Figure 7 shows these roll waves. They traversed the complete width of the channel for high Re_L but were only 3 to 4 in. long at low Re_L. They traveled about 2 ft./sec. while the squalls still present traveled approximately 1 ft./sec. The squalls formed a few inches from the liquid entry section,

but the roll waves required 3 to 4 ft. to form.

A third transition was defined as the point where the roll waves first appeared and it was found to be coincident with the point where they disappeared when Re_L was greater than 250. When Re_L was less than 250 the point of transition was dependent on whether the roll waves were appearing or disappearing. The transition was easily determined; however the data were not reproducible. Figure 8 reports the range of variables over which this transition occurred. The parameter Re^* could not be evaluated because of the difficulty of accurately measuring the thickness of the liquid film.

Dispersed Flow

At extremely high flow rates droplets are torn from the liquid surface and the liquid becomes dispersed in the gas phase. At $Re_L = 470$ and $Re_G = 39{,}300$ ($U_M =$ 83 ft./sec.), small droplets began to appear on the top wall of the channel; for $Re_L = 387$ the Re_G must equal 45,100 ($U_M = 95$ ft./sec.); at $Re_L = 69$ the Re_G must be 84,500 ($U_M = 178$ ft./sec.). As the liquid film becomes thinner, or as the Re_L becomes smaller, it becomes much more difficult to disperse the liquid phase.

Effect of the Liquid Surface upon the Gas Flow

The interaction of the roughened liquid surfaces upon the gas is reflected in the form of the velocity profiles and in the magnitude of the shear stress at liquid-gas interface.

Velocity profiles measured at the first and second transition points showed no distortion. (See Figure 9.) However, as the gas velocity was increased past the second transition point an increased interfacial shear stress and therefore a distorted velocity profile was obtained. As shown in Figure 10, the shift of the U_{max} from the center line was 0.075 in. The surface was quite rough during this run. It possessed a pebbled appearance, the height of each "pebble" being estimated at about 0.010 in. Run 54, shown in Figure 10, and run 14, shown in Figure 11, have nearly the same Re_L (127 and 170 respectively) and different Re_G; however the velocity profiles are very similar. Figure 12 shows the velocity profile for run 55 with Re_L equal to 508. This shift of U_{max} from the center is nearly 0.140 in. The same is true in run 56, which is shown in Figure 13. At higher values of Re_L thicker films resulted and the squall surfaces became rougher. The height of the "pebbles" in runs 55 and 56 was close to 0.030 in. The interfacial shear stress and therefore the distortion of the velocity profile appear to be related to the height of the roughnesses on the liquid surface.

The velocity-profile data for runs 14, 54, 55, and 56 have been plotted as u^* vs. log y^* in Figure 14. The solid line

Table 2—First Transition

Run No.	Re_G	Re_L	U_{max} (ft./sec.)	Liq. vel. (ft./sec.)	Liq. ht. (in.)
17	3320	146	9.00	0.109	0.18
18	2560	287	7.03	0.203	0.19
19	4140	11.9	11.0	0.0097	0.17
20	2920	147	7.80	0.110	0.18
21	2090	303	6.10	0.222	0.19
22	945	492	3.80	0.323	0.21
23	2490	257	7.04	0.173	0.20
25	2120	347	6.30	0.222	0.21
27	2090	255	6.40	0.164	0.21
29	2860	156	7.96	0.107	0.20
31	3380	102	8.80	0.074	0.19
33	1330	442	4.40	0.276	0.22
35	5510	37.5	15.1	0.0325	0.16
*37	2270	151	6.50	0.102	0.20

*Run taken at U_{max} only 80% of U_{max} for first transition.

Table 3—Values of $Re^* = hU\tau\rho_l/\mu_l$ for the First Transition

Run No.	Re_G	Re_L	h (in.)	$U\tau$ (ft./sec.)	Re^*
15	3100	490	0.191	0.39	520
16	8600	20	0.076	1	540
17	3300	150	0.181	0.33	420
19	4100	12	0.166	0.45	530

represents data obtained by Laufer (*4*) for smooth-walled channels; the hollow points represent the profiles from the top dry wall and are in approximate agreement with Laufer's data; the solid points represent the profiles from the rough liquid surface. These data are parallel to the dry-wall data but are displaced downward. They appear to be of the form observed for artificially sand-roughened surfaces. "Equivalent sand roughnesses" k_s have been calculated from Equation (11). Table 6 shows the values of k_s, for runs 14 and 54, about

Table 4—Second Transition

Run No.	Re_G	Re_L	U_{max} (ft./sec.)	Liq. vel. (ft./sec.)	Liq. ht. (in.)
24	3970	275	11.0	0.192	0.18
26	3790	347	10.1	0.245	0.19
28	4000	258	10.9	0.178	0.20
30	4170	156	11.3	0.116	0.18
32	4390	104	12.0	0.078	0.17
34	3240	442	9.0	0.283	0.21
36	8100	37.5	19.9	0.048	0.10
39	4020	151	11.1	0.107	0.20

Table 5—Values of $Re^* = hU\tau\rho_l/\mu_l$ for the Second Transition

Run No.	Re_G	Re_L	h (in.)	$U\tau$ (ft./sec.)	Re^*
24	4000	260	0.181	0.46	580
26	3800	350	0.191	0.44	590
28	4000	260	0.196	0.46	640
30	4200	160	0.181	0.48	610
32	4400	100	0.171	0.50	600
34	3200	440	0.211	0.38	560
36	8100	38	0.106	0.88	660

0.007 in., and for runs 55 and 56, about 0.03 in. These were the approximate sizes of the roughnesses on the pebbled liquid surface.

DISCUSSION OF RESULTS

The results of the experiments described in this paper on a flowing liquid film are in qualitative agreement with observations of the effect of wind velocity upon the surface of large bodies of water (*5*) and of experimental investigations of the effect of blowing air over a container of water (*6*). They should present further insight into the problem of understanding the role of an air stream in initiating wave formation on a liquid surface. The present experimentation shows that the transition from one type of surface to another depends upon the flow conditions of the liquid film. Thin water films or films of low Re_L are more stable. The characterization of the film stability in terms of the parameter $Re = (hU_\tau\rho_{liquid})/\mu_{liquid}$ is suggested from the results. Not enough data were obtained to support the universality of this parameter. The effect of the pebbled liquid surface upon the gas flow appears to be the same as that of a surface artificially roughened with sand of approximately the same size as the wavelets.

The quantitative results presented for the initiation of a surface instability are not adequately described in terms of theories in the literature. An excellent survey of these theories has been presented by Ursell (*5*). Neither the analysis of Kelvin based on frictionless fluid streams nor the "sheltering" theory of Jeffrey give the same dependence of the stability on the liquid flow properties as evidenced from the experiments reported in this paper; however there is an approximate quantitative agreement between the experimental velocity required to raise waves at first and that predicted by these theories.* Recently analyses of the problem based on the Orr-Sommerfeld equation have been presented in the literature (*7*, *8*). Yih (*7*), who analyzed the case of a film flowing down a vertical fall, predicted a critical $Re_L = 1.5$. This is very much smaller than the values

*This agreement has been pointed out by C. V. Sternling, who drew up the following comparison:

Formulas:

Jeffrey's analysis	Frictionless case
$U = 4.4(\mu_L g/\rho_G)^{1/3}$	$U = 1.41(g\rho_L g G/\rho_G^2)^{1/4}$
$c = \frac{1}{3}U$	$c = \sqrt{\rho_G/\rho_L}\,U$
$\lambda = 2\pi c^2/g$	$\lambda = \pi c^2/g$

Comparison with data:

	Jeffrey	Friction-less	Experi-mental
U, cm./sec.	107	608	130 to 460
c, cm./sec.	35.7	23.2	23 to 30
λ, cm.	8.1	1.73	1 to 1.25

VELOCITY (FT./SEC.)

VELOCITY (FT./SEC.)

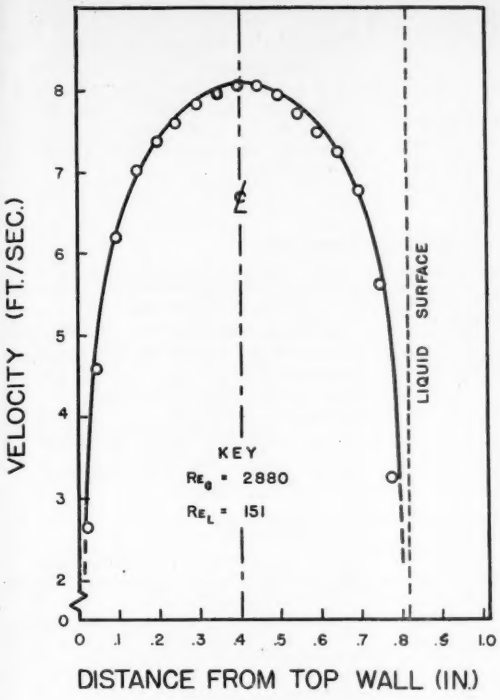

Fig. 9. First-transition velocity profile, run 38.

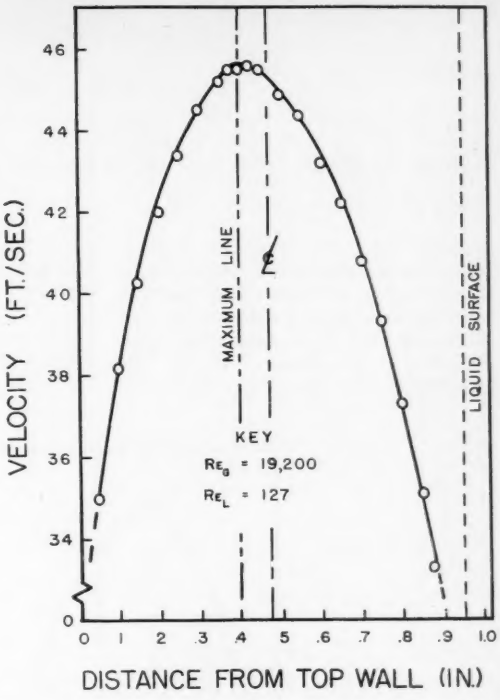

Fig. 10. Third-transition velocity profile, run 54.

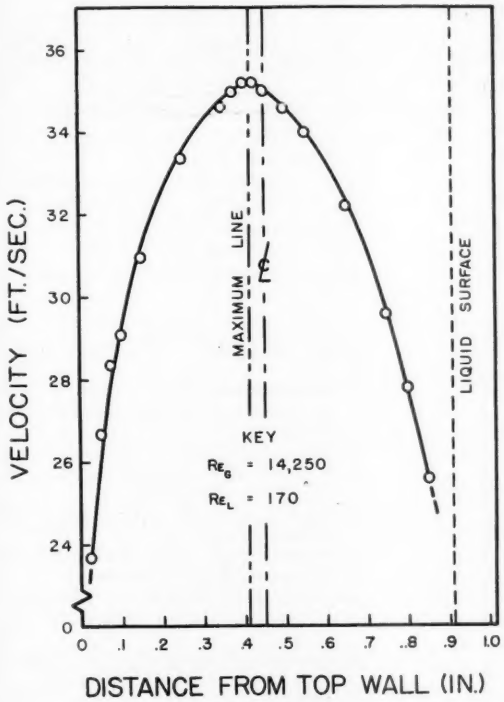

Fig. 11. Velocity profile, run 14.

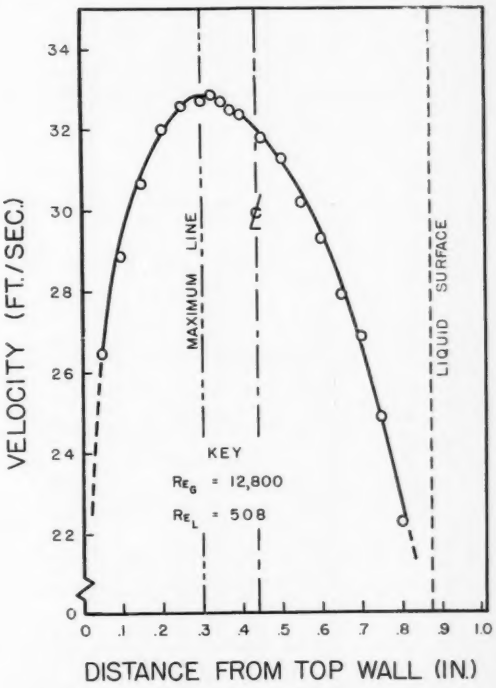

Fig. 12. Velocity profile, run 55.

TABLE 6

EQUIVALENT SAND ROUGHNESSES

Run No.	Re_G	Re_L	U_{max} (ft./sec.)	τ_{0_1} (lbs./ft.²)	τ_{0_2} (lbs./ft.²)	k_s (in.)
14	14,250	170	35.2	0.00661	0.00787	0.0077
54	19,200	127	45.6	0.00852	0.0117	0.0061
55	12,800	508	32.9	0.00562	0.0107	0.036
56	13,900	508	35.6	0.00623	0.0116	0.030

reported here. (See Table 2.) Experimental measurements of Keulegan (*6*) on the initiation of waves in a basin of water on the bottom of a channel through which air was blown gave critical gas velocities in the range of 200 to 900 cm./sec. The experiments reported in this paper involved a flowing liquid film; the basic flow field in the water was quite different from that in Keulegan's experiments. A direct comparison is therefore not possible; however, the critical gas velocity in the two investigations is of the same magnitude.

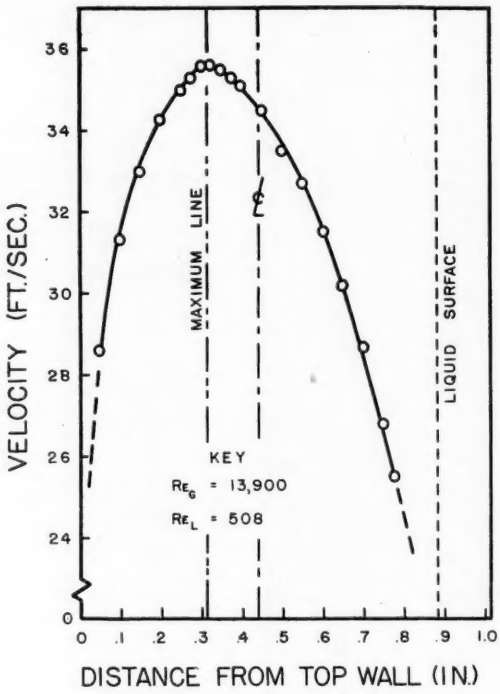

Fig. 13. Velocity profile, run 56.

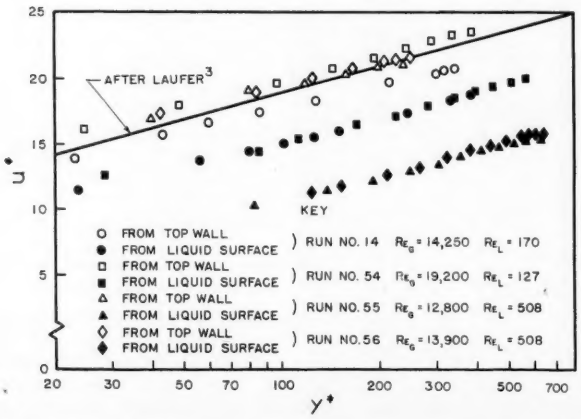
AFTER LAUFER[3]
KEY
FROM TOP WALL
FROM LIQUID SURFACE
RUN NO. 14 Re_G = 14,250 Re_L = 170
RUN NO. 54 Re_G = 19,200 Re_L = 127
RUN NO. 55 Re_G = 12,800 Re_L = 508
RUN NO. 56 Re_G = 13,900 Re_L = 508

Fig. 14. Comparison of data with Laufer's velocity measurements in dry channel.

ACKNOWLEDGMENT

The idea for this research program came from discussions with C. V. Sternling and R. R. Hughes of Shell Development Company, and the research was partially supported by the Office of Ordnance Research. The authors are grateful for their interest.

NOTATION

a = distance from maximum in velocity profile to top wall
b = distance from maximum in velocity profile to liquid surface
c = wave velocity
g = gravitational constant
h = liquid film thickness
H = thickness of the gas phase
k_s = equivalent sand roughness
λ = wave length
P = pressure
ρ = density
Q = volumetric liquid flow rate
Re_G = gas-phase Reynolds Number $(HU_m\rho/\mu)$
Re_L = liquid-phase Reynolds number $(hQ\rho/S\mu)$
Re^* = surface characterization parameter $hU_\tau\rho/\mu$
S = cross-sectional area of the channel
t = time of oscillation
T = surface tension
τ_{0_1} = shear stress at the top wall
τ_{0_2} = shear stress at the liquid surface
u = liquid velocity in x direction
U = point gas velocity in x direction
U_m = mean gas velocity $(1/H \int_0^H U\, dy)$
U_{max} = maximum gas velocity
u^* = velocity parameter U/U_τ
U_τ = friction velocity $(g_c\tau_0/\rho)^{1/2}$
μ = viscosity
v = liquid velocity in y direction
w = liquid velocity in z direction
W = liquid weight rate of flow
y = distance from a surface
y^* = distance parameter $yU_\tau\rho/\mu$

LITERATURE CITED

1. Lamb, Horace, "Hydrodynamics," 6 ed., pp. 363-475, Cambridge University Press (1953).
2. Schlichting, Hermann, "Boundary Layer Theory," McGraw Hill Book Company, Inc., New York (1955).
3. Engen, James M., M.S. thesis, Univ. Illinois, Urbana (1956).
4. Laufer, John, *Natl. Advisory Comm. Aeronaut. Rept.* 1053 (1951).
5. Ursell, F., "Surveys in Mechanics," p. 216, Cambridge University Press (1956).
6. Keulegan, Garbis, H., *J. Research, Natl. Bur. Standards*, **46**, no. 5, 358 (1951).
7. Yih, Chia-Chun, "Proceedings of Second U. S. National Congress of Applied Mechanics," p. 623 (1955).
8. Lock, R. C., *Proc. Cambridge Phil. Soc.*, **50**, 105–24 (1954).

Discharge Coefficients Through Perforated Plates

P. A. KOLODZIE, JR., and MATTHEW VAN WINKLE

University of Texas, Austin, Texas

The design variables that affect the pressure drop across dry perforated plates were determined and correlated. Average orifice coefficients were calculated for the perforated plates by using a modified form of the single-orifice flow equation.

The variables which affected the orifice coefficients were found to be the hole diameter, hole pitch, plate thickness, fraction of the plate covered by the perforated area, and a Reynolds number based on the hole diameter. The orifice coefficients have been correlated with these variables in dimensionless groupings.

The correlation presented covers a practicable range of variables for which the pressure drop may be predicted in design.

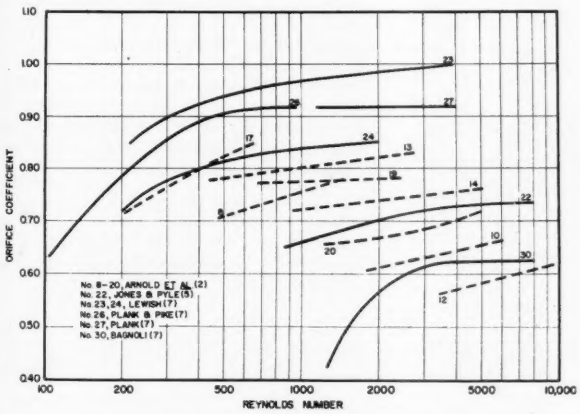

Fig. 1. Some results of previous investigators.

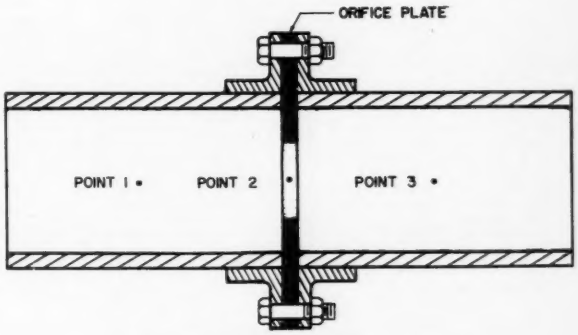

Fig. 2. Single-orifice plate in a circular conduit.

In the past few years there has been an increase in industrial use of perforated-plate distillation columns, as for many services the perforated-plate column has been found equivalent to, or better than, the generally used bubble-cap column. Since the perforated-plate column has come into general use only recently, however, there is still a lack of reliable design information.

One of the important design considerations in a distillation column is the pressure drop through the column. The major portion of the pressure drop is that through the plates. For design purposes the pressure drop across or through a plate has generally been considered to be a combination of two effects: (1) the pressure drop caused by the liquid head on the plate and (2) the pressure drop caused by the discharge of the vapor through the dry plate. This study was concerned with the second of these two effects. An investigation was undertaken to determine and correlate those variables which affected the pressure drop across dry perforated plates.

PREVIOUS INVESTIGATIONS

Some data on dry-perforated-plate pressure drop have already been reported by various authors (*2*, *4* to *8*) in connection with other distillation studies. The results obtained by some of the investigators are plotted in Figure 1. Table 1 is a compilation

TABLE 1
PLATE DATA OF PREVIOUS INVESTIGATORS

Plate	Investigator	Hole diam., in.	Free area, % column	T/d ratio	P/d ratio
1	*8*	0.125	0.7*	2.00	4.00†
2		0.1875	12.7*	1.33	2.67†
3		0.1875	3.2*	1.33	5.33†
4		0.1875	5.7*	1.33	4.00†
5		0.1875	5.7*	2.00	4.00†
6		0.1875	5.7*	0.67	4.00†
7		0.25	5.7*	1.00	4.00†
8	*2*	0.038	4.3	0.764	3.30‡
9		0.059	3.9	0.492	3.70†
10		0.139	4.5	0.209	3.47†
11		0.250	4.5	0.115	3.48†
12		0.312	4.1	0.093	3.48†
13		0.083	10.5	0.350	3.27†
14		0.177	12.0	0.164	2.12†
15		0.235	11.9	0.123	2.12†
16		0.376	11.5	0.077	2.16†
17		0.039	18.5	0.743	1.62‡
18		0.062	17.1	0.468	1.77†
19		0.144	17.8	0.201	1.74†
20		0.249	17.4	0.117	1.75†
21		0.309	16.2	0.094	1.82†
22	*5*	0.125	6.7	0.496	3.00†

P. A. Kolodzie, Jr., is at present with Humble Oil and Refining Company, Houston, Texas.

TABLE 1.—*Continued*
PLATE DATA OF PREVIOUS INVESTIGATORS

Plate	Investigator	Hole diam., in.	Free area, % column	T/d ratio	P/d ratio
23	7 (Lewish)	0.039	21.8	0.570	2.04†
24		0.125	23.2	0.147	1.98†
25		0.033	4.82	0.498	4.33†
26	7 (Plank and Pike)	0.059	20.0	0.361	2.13†
27	7 (Plank)	0.059	20.0	0.361	2.13†
28	7 (Bagnoli)	0.125	1.22	——	7.50†
29		0.125	1.22	——	9.00†
30		0.125	2.24	——	6.00†
31	6	0.197	1.04	0.060	8.00†
32		0.197	4.59	0.060	4.00†
33		0.118	1.01	0.133	8.00†
34		0.118	4.51	0.133	4.00†
35		0.0787	1.30	0.200	8.00†
36		0.0787	4.70	0.200	4.00†
37		0.0393	1.24	0.400	8.00†
38		0.0393	4.64	0.400	3.00†
39		0.197	9.05	3.16	3.20†
40		0.0787	1.45	7.90	8.00†
41	4	0.125	18.8	1.00	2.00†
42		0.125	4.9	1.00	4.00†
43		0.250	5.4	1.00	4.00†
44		0.250	19.0	1.00	2.00†
45		0.500	4.9	1.00	4.00†
46		0.500	21.5	1.00	2.00†
47		0.375	5.1	1.00	4.00†
48		0.250	9.5	1.00	3.00†

*Estimated.
†Triangular.
‡Square.

of the physical data for the perforated plates used by the various investigators. (Curves in Figure 1 correspond numerically to plate numbers in Table 1.)

Baines and Peterson (*3*) made a partial study of perforated barriers some years ago as part of an investigation on pressure drops across screens. They predicted that the discharge coefficients through the barriers were a function of a Reynolds number, solidity ratio, and perforation pattern.

Mayfield *et al.* (*8*) reported on one of the first investigations related to the design of perforated-plate columns. A study of dry-plate pressure drop was made on a 6-in.-diam. column using air. They concluded from their work that the discharge coefficients through the plates were independent of plate thickness, drilling pattern, and hole size. It was indicated that the coefficient did not vary with the Reynolds number over the ranges covered. Shortly after the appearance of the work of Mayfield *et al.* (*8*), Arnold *et al.* (*2*) reported a similar study using air in 6- and 15-in.-diam. columns. Arnold concluded that the discharge coefficients were a function of hole size, free area, and Reynolds number. These authors reported that an attempt at a correlation by use of a modified Reynolds number was unsuccessful and they proposed the following correlation:

$$P = kv^{1.8} \qquad (1)$$

where k, a dimensional constant, was assumed to be dependent only on hole diameter and free area.

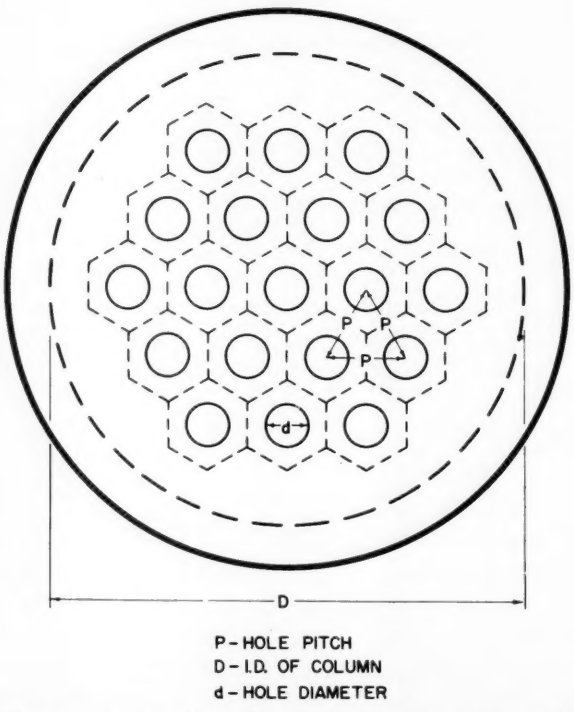

Fig. 3. A perforated plate with the holes on an equilateral-triangle pitch.

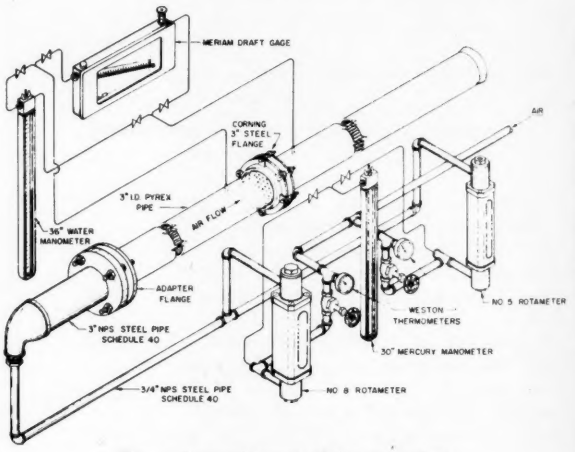

Fig. 4. General layout of the apparatus.

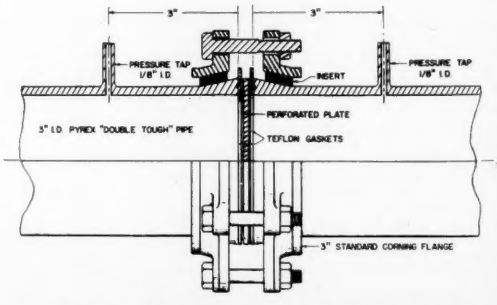

Fig. 5. Detail of pressure-tap and flange arrangement.

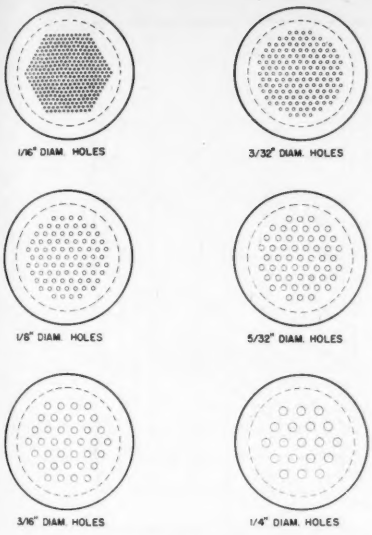

Fig. 6. Perforated-plate layouts for a pitch-to-hole-diameter ratio of 2.0.

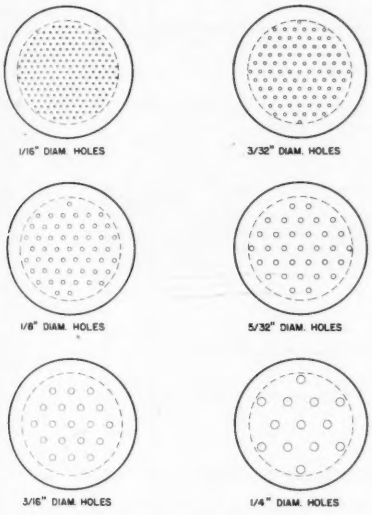

Fig. 7. Perforated-plate layouts for a pitch-to-hole-diameter ratio of 3.0.

Lewish (7), reported a study of the variables affecting pressure drop across perforated plates, using water in a 1.5-in.-diam. column. He also reported some work done by Bagnoli, Plank, and Plank and Pike. In general, Lewish verified the findings of Arnold and in addition concluded that a Reynolds number based on the perforation diameter was a definite correlating factor. The variable of plate thickness was not studied by Lewish. Kamei *et al.* (6) reported that discharge coefficients for dry perforated plates were a function of hole diameter and plate thickness only he tested a number of plates of different design using air in a 5.12-in.-diam. column.

Recently Hunt *et al.* (4) reported a study on a 6-in.-diam. column using air, Freon 12, carbon dioxide, argon, and methane. These authors proposed a dry-plate correlation based on the analogy between a plate perforation and a short tube with entrance and exit losses. Hunt *et al.* suggested that the discharge coefficients were probably affected by the plate-thickness-to-hole diameter ratio. In their study, however this ratio was limited to 1.0.

THEORETICAL CONSIDERATIONS

The number and nature of the variables involved in a study of pressure drop

Table 2
Physical Data for Perforated Plates

Hole diam., in.	T/d ratio	No. holes	Free area, % column	Hole diam., in.	T/d ratio	No. holes	Free area % column
Hole pitch to hole diameter = 2.0				Hole pitch to hole diameter = 3.0			
0.0625	1.30	331	14.50	0.0625	1.30	207	9.08
0.0938	0.86	151	14.75	0.0938	0.86	93	9.08
0.125	0.65	85	14.75	0.125	0.65	52	9.03
0.1563	0.52	55	14.93	0.1563	0.52	33	8.96
0.1875	0.43	37	14.45	0.1875	0.43	19	7.42
0.250	0.33	19	13.20	0.250	0.33	13	9.03
0.0625	2.00	331	14.50	0.0625	2.00	207	9.08
0.0938	1.33	151	14.75	0.0938	1.33	93	9.08
0.125	1.00	91	15.80	0.125	1.00	52	9.03
0.125	1.00	85	14.75	0.125	1.00	37	6.42
0.125	1.00	61	10.60	0.125	1.00	31	5.38
0.125	1.00	37	6.42	0.125	1.00	19	3.30
0.1563	0.80	55	14.93	0.1563	0.80	33	8.96
0.1875	0.67	37	14.45	0.1875	0.67	19	7.42
0.250	0.50	19	13.20	0.250	0.50	13	9.03
0.0625	3.00	331	14.50	0.0625	3.00	207	9.08
0.0938	2.00	151	14.75	0.0938	2.00	93	9.08
0.125	1.50	85	14.75	0.125	1.50	52	9.03
0.1563	1.20	55	14.93	0.1563	1.20	33	8.96
0.1875	1.00	37	14.45	0.1875	1.00	19	7.42
0.250	0.75	19	13.20	0.250	0.75	13	9.03
0.0625	4.00	331	14.50	0.0625	4.00	207	9.08
0.0938	2.67	151	14.75	0.0938	2.67	93	9.08
0.125	2.00	85	14.75	0.125	2.00	52	9.03
0.1563	1.60	55	14.93	0.1563	1.60	33	8.96
0.1875	1.33	37	14.45	0.1875	1.33	19	7.42
0.250	1.00	19	13.20	0.250	1.00	13	9.03
Hole pitch to hole diameter = 4.0				Hole pitch to hole diameter = 5.0			
0.0625	1.30	121	5.31	0.0625	1.30	77	3.37
0.0938	0.86	55	5.37	0.0938	0.86	37	3.61
0.125	0.65	31	5.38	0.125	0.65	19	3.30
0.1563	0.52	19	5.17	0.1563	0.52	13	3.35
0.1875	0.43	13	5.07	0.1875	0.43	7	2.73
0.250	0.33	7	4.87	0.250	0.33	7	4.87
0.0625	2.00	121	5.31	0.0625	2.00	77	3.37
0.0938	1.33	55	5.37	0.0938	1.33	37	3.61
0.125	1.00	31	5.38	0.125	1.00	19	3.30
0.1563	0.80	19	5.17	0.1563	0.80	13	3.53
0.1875	0.67	13	5.07	0.1875	0.67	7	2.73
0.250	0.50	7	4.87	0.250	0.50	7	4.87
0.0625	3.00	121	5.31	0.0625	3.00	77	3.37
0.0938	2.00	55	5.37	0.0938	2.00	37	3.61
0.125	1.50	31	5.38	0.125	1.50	19	3.30
0.1563	1.20	19	5.17	0.1563	1.20	13	3.53
0.1875	1.00	13	5.07	0.1875	1.00	7	2.73
0.250	0.75	7	4.87	0.250	0.75	7	4.87
0.0625	4.00	121	5.31	0.0625	4.00	77	3.37
0.0938	2.67	55	5.37	0.0938	2.67	37	3.61
0.125	2.00	31	5.38	0.125	2.00	19	3.30
0.1563	1.60	19	5.17	0.1563	1.60	13	3.53
0.1875	1.33	13	5.07	0.1875	1.33	7	2.73
0.250	1.00	7	4.87	0.250	1.00	7	4.73

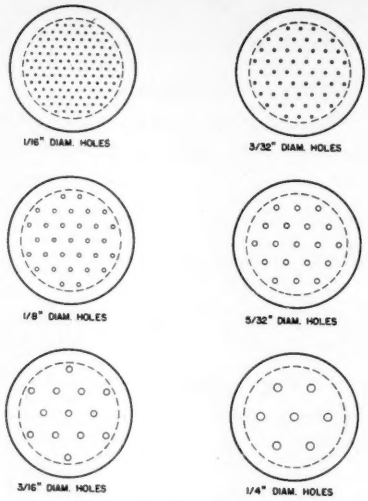

Fig. 8. Perforated-plate layouts for a pitch-to-hole–diameter ratio of 4.0.

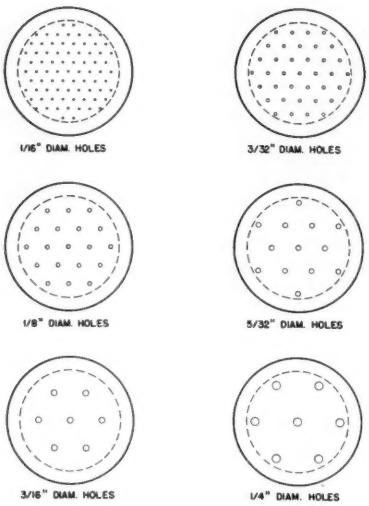

Fig. 9. Perforated-plate layouts for a pitch-to-hole–diameter ratio of 5.0.

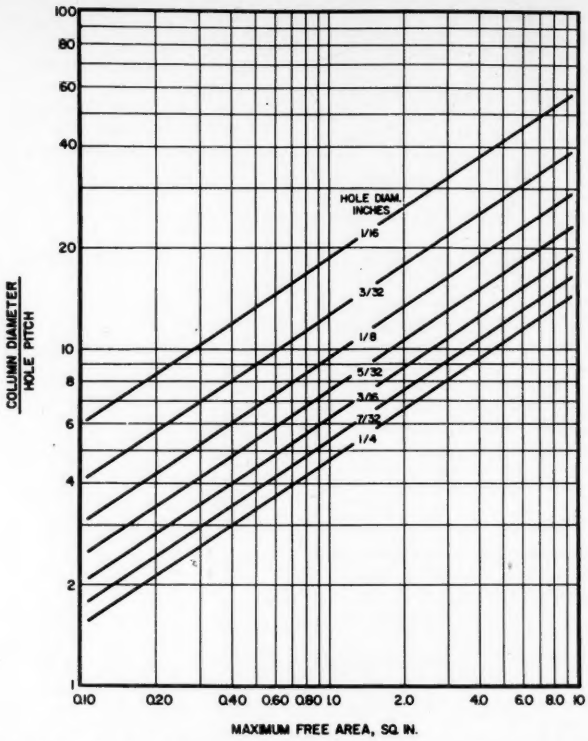

Fig. 10. Correlation for obtaining maximum free area for circular plates with holes on equilateral-triangular pitch.

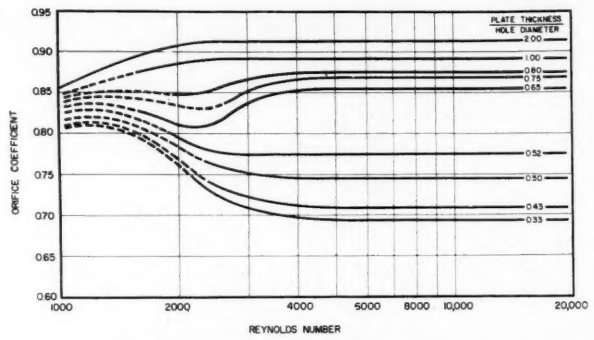

Fig. 11. Plot of orifice coefficient and Reynolds number for a pitch-to-hole–diameter ratio of 2.0.

across perforated plates make a rigorous theoretical analysis almost impossible. In this study a semiempirical approach was used. Discharge coefficients were calculated for the perforated plates and correlated against the physical characteristics of the fluid, column, and plate.

A typical perforated plate is shown in Figure 3. It was assumed to be composed of a number of individual orifices acting independently and in parallel. Although there is no theoretical basis for this assumption, it appears logical and allows the application, in part, of single-orifice relations. For a horizontal circular conduit containing a single circular orifice (Figure 2), a generally accepted flow equation for a compressible fluid is

$$v_2 = \frac{C}{Y}\sqrt{\frac{2g(-\Delta P_{1,3})}{\rho_1\left[1-\left(\frac{A_2}{A_1}\right)^2\right]}} \qquad (2)$$

For the perforated plate, it was assumed that the fluid flowing distributed equally among all holes. For this case the continuity equation can be written as

$$A_D v_D = (\text{No. holes})\,(A_d)(v) = A_f v \qquad (3)$$

where v_D = fluid velocity at A_D
v = fluid velocity at A_d

Incorporating Equation (3) in the derivation of Equation (2) and altering the notation will give

$$v = \frac{C}{Y}\sqrt{\frac{2g(-\Delta P)}{\rho_D\left[1-\left(\frac{A_f}{A_D}\right)^2\right]}} \qquad (4)$$

Equation (4) is the flow equation for perforated plates analogous to Equation (2) for single orifices.

A special A.S.M.E. report (*1*) has shown that the single-orifice coefficient can be correlated with the physical prop-

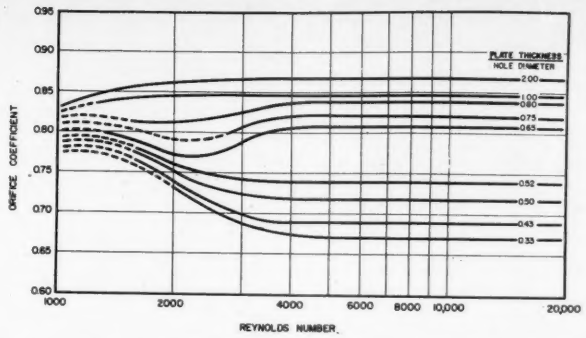

Fig. 12. Plot of orifice coefficient and Reynolds number for a pitch-to-hole–diameter ratio of 3.0.

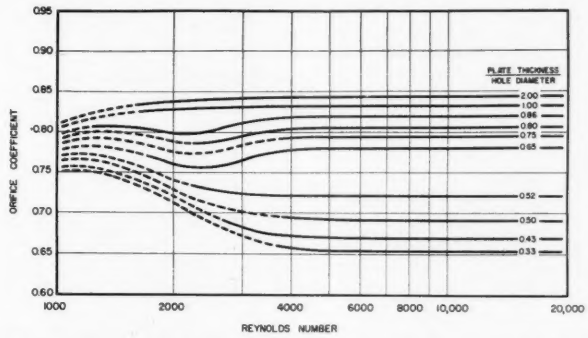

Fig. 13. Plot of orifice coefficient and Reynolds number for a pitch-to-hole–diameter ratio of 4.0.

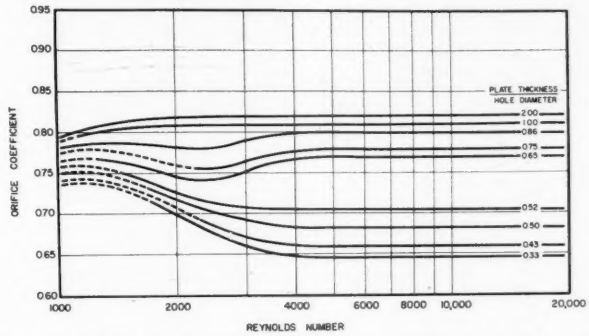

Fig. 14. Plot of orifice coefficient and Reynolds number for a pitch-to-hole–diameter ratio of 5.0.

erties of the conduit, fluid, and orifice plate through use of certain dimensionless groups. By dimensional analysis,

$$C = \mathfrak{F}\left[\left(\frac{dv\rho}{\mu}\right), \left(\frac{d}{D}\right), \left(\frac{T}{d}\right)\right] \qquad (5)$$

Though not included in the dimensional analysis, the coefficient has also been shown to be a function of pressure-tap location and shape of the upstream orifice edge.

Based on experimental work and the A.S.M.E. report (*1*), the variables that were considered to affect the orifice coefficient for perforated plates were

1. Fluid velocity through the orifice v
2. Fluid density ρ
3. Fluid viscosity μ
4. Hole diameter d
5. Hole pitch P
6. Free area of plate A_f
7. Maximum free area possible if total area of the plate were perforated A_t
8. Thickness of the plate T

Consideration of these variables in a dimensional analysis gave

$$C = \mathfrak{F}\left[\left(\frac{dv\rho}{\mu}\right), \left(\frac{d}{P}\right), \left(\frac{T}{d}\right), \left(\frac{A_f}{A_t}\right)\right] \qquad (6)$$

Pressure-tap location and shape of the upstream orifice edge were held constant in this investigation. The dimensionless groups in Equation (6) were used as the basis for correlating the experimental data.

EXPERIMENTAL WORK

The experimental equipment (Figure 4) was designed specifically to measure pressure drop across perforated plates at known flow rates. Air, the only fluid used, was obtained from a 100 lb./sq. in. gauge system available in the laboratory. Two Fisher and Porter Flowrators (tube sizes 5 and 8) connected in parallel were used to measure the air flow rate. Depending on the flow range required one or the other flowrator was used. The temperature (Weston dial-type thermometer) and pressure (Meriam standard 30-in. mercury manometer) were measured at the entrance of each flowrator. The perforated plates were flanged between two sections of 3-in. I.D. Pyrex pipe. A 48-in. length of straight pipe was used as the upstream approach to the plate to avoid interference from upstream fittings (*9*). Pressure taps were located 3 in. upstream and 3 in. downstream from the plate. Details of the flange arrangement are shown in Figure 5. Pressure drops across the plates of less than 2 in. of water were measured with a Meriam draft gauge calibrated in 0.01-in. divisions. A Meriam standard 36-in. water manometer was used to measure pressure drops exceeding 2 in. of water.

A systematic method was used in making the plates so that a practical range of variables might be tested. Pitch-to-hole diameter ratios of 2.0, 3.0, 4.0 and 5.0 were selected with all plates being laid out on an equilateral-triangle pattern. Hole sizes of 1/16-, 3/32-, 1/8-, 5/32-, 3/16-, and 1/4-diam. were used. All holes were drilled on a vertical drill press with the plates backed by wooden blocks to prevent excess burring. After drilling, the plates were drawn across No. 0 emery paper on a flat surface to knock off the burrs. Thicknesses of the plates were 0.081, 0.125, 0.1875, and 0.25 in. Plates with 0.125-, 0.1875-, 0.25-in. thicknesses were made of red brass and the 0.081-in.-thick plates were made of yellow brass. All plates were 3.78 in. in diameter.

Combinations of all variables were used so that for each P/d ratio there were twenty-four different plates. Six additional plates were also used in a study of free-area effects. The physical data on the plates are listed in Table 2. Actual layout patterns for the plates are shown in Figures 6 to 9 and 20. In laying out the hole patterns on the plates, it was realized that the spread of holes over the plate would probably affect the orifice coefficient (shown later); therefore, the plates were laid out so that the holes covered a major portion of the plate. In this manner the effect of P/d, plate thickness, and hole diameter could be studied on the same basis.

The maximum number of holes that can be fully exposed on a circular plate depends upon the plate diameter and the hole pitch.

The free area will depend on the number and size of the holes used. A correlation relating plate diameter, hole pitch, and hole size to maximum free area is presented in Figure 10. The correlation was arrived at by simple geometric relations and will hold only for an equilateral-triangular hole pattern.

Several checks were made at the outset of the investigation to determine the degree of reproducibility which could be expected from the equipment and procedures used. Several runs were made independently on the same plate to check the consistency of the data. A comparison of the pressure drops yielded a maximum difference of only 3%. A check was also made to determine how closely the plates themselves could be reproduced. Identical plates were tested and a comparison of the pressure drops yielded a maximum difference of only 2%. It was concluded, therefore, that the methods used would produce plates which would give comparable results. Since the patterns on some of the plates were not symmetrical, it was necessary to determine the effect of the relative rotational position of the plates with respect to the pressure taps. No effect on pressure drop was found.

EXPERIMENTAL RESULTS

In the calculations involving the air flow, the ideal-gas law was used. The air was considered to be dry and to have a molecular weight of 29.0. Orifice coefficients were calculated from Equation (4) after certain simplifications had been introduced. Since the pressure drop did not exceed 15 in of water, an average air density of 0.0731 lb./cu. ft. (temperature = 95°F., pressure = 775 mm. Hg) was used. For the small pressure drops that were encountered, the expansion factor was found to be nearly unity (*11*). Incompressible flow was assumed. The average possible error was estimated to be about 2% for the calculated coefficients.

In following through with the dimensional analysis, a Reynolds number based on the hole diameter was calculated, an average viscosity for air (temperature = 95°F.) being obtained from Perry (*10*). For each P/d ratio, the orifice coefficient was plotted vs. the Reynolds number (Figures 11 to 14) for various parameters of T/d ratio. When all data points had been plotted, the curves became obliterated by the large number of overlapping points. To enhance the clarity of presentation the points were omitted from the figures. The curves presented represent the best average of the points (within 3% maximum deviation). In general, the Reynolds number covered a range from 2,000 to 20,000. The dashed lines in the figures represent extrapolation beyond the experimental data. These extrapolations were based on interpolation of the existing curves and the symmetry which existed for the various P/d groupings. Beyond a Reynolds number of 4,000 the coefficients became constant.

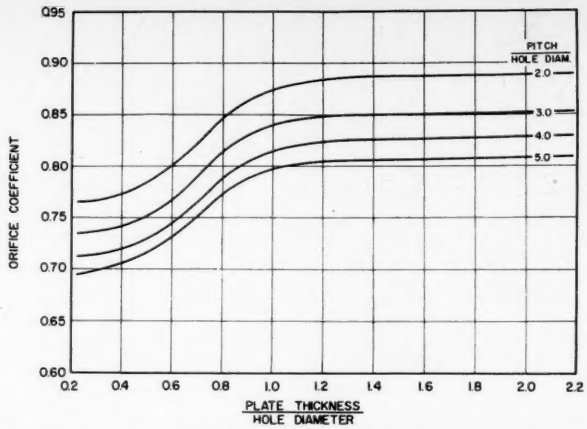

Fig. 15. Cross plot of Figures 11, 12, 13, and 14 at a Reynolds number of 2,000.

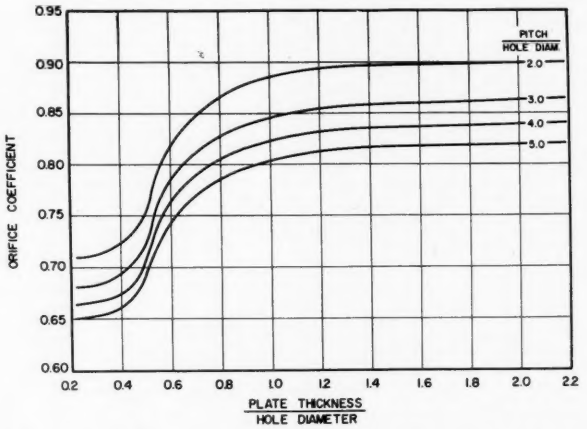

Fig. 16. Cross plot of Figures 11, 12, 13, and 14 at a Reynolds number of 3,000.

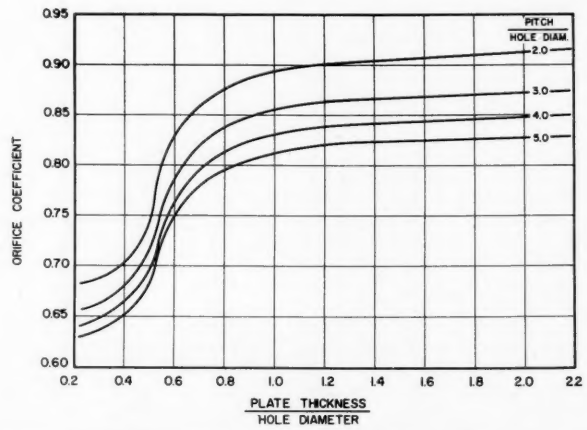

Fig. 17. Cross plot of Figures 11, 12, 13, and 14 at a Reynolds number of 10,000.

The general shape of the curves representing the smaller T/d ratios is similar to that of curves of the same type for the thin-plate ($T/d < 0.125$) single orifice.

Cross plots were made from Figures 11, 12, 13, and 14 to determine the effect of the P/d ratio. The resulting plots were of coefficient vs. T/d ratio with the P/d ratio as parameter. Cross plots were

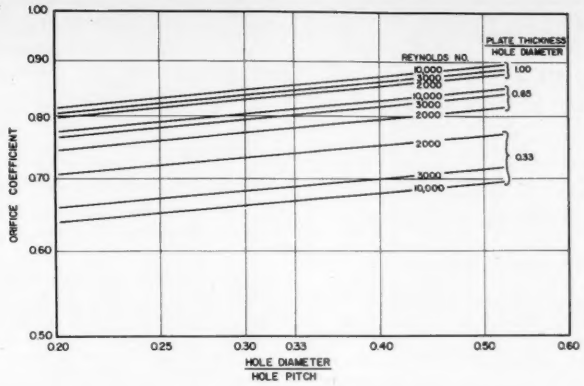

Fig. 18. Cross plots of Figures 15, 16, and 17 at various plate-thickness–to–hole-diameter ratios.

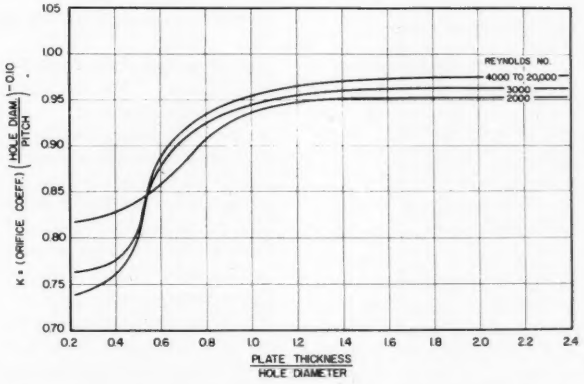

Fig. 19. A correlation relating orifice coefficient for perforated plates with the physical characteristics of the plate and gas.

taken at Reynolds numbers of 2,000, 3,000, and 10,000 (Figures 15 to 17). Since the coefficients are constant above Reynolds numbers of 4,000, Figure 17 will apply for a Reynolds number range from 4,000 to 20,000 and probably beyond.

Upon inspection of Figures 15, 16, and 17, a definite trend was noted between the curves of the different P/d ratios. A plot of coefficient vs. of d/P ratio on log-log paper revealed a series of straight parallel lines at the various T/d ratios (Figure 18). These curves can be expressed by the relation

$$\log C = \log K + \alpha \log \left(\frac{d}{P}\right) \qquad (7)$$

where K = constant (function of T/d)

The family of curves can be represented by

$$C = K\left(\frac{d}{P}\right)^{0.10} \qquad (8)$$

Equation (8) can be rearranged to

$$K = C\left(\frac{d}{P}\right)^{-0.10} \qquad (9)$$

Since the value of K is constant for any T/d ratio, the curves in Figures 15, 16, and 17 may be represented as one curve by plotting K vs. T/d ratio. Figure 19 is a plot of K vs. T/d at Reynolds numbers of 2,000, 3,000, and 4,000 to 20,000.

The correlation presented in Figure 19 was derived by using perforated plates with holes covering a majority of the cross-sectional areas available. In distillation practice, however, chord weirs and downcomers limit the perforated area available. Perforated area is the area effectively covered with holes. In order to determine what effect the perforated area would have, several plates with different free-area patterns were tested. The layouts were chosen to simulate distillation-column plates (Figure 20). The physical characteristics of these plates are given in Table 2. The pressure drops for these plates were found to be independent of the rotational position of the pattern in relation to the pressure taps. Orifice coefficients for these plates were plotted against the Reynolds number with the free area as the resulting parameter (Figure 21).

The fraction of perforated area on the plates was expressed as a ratio of the

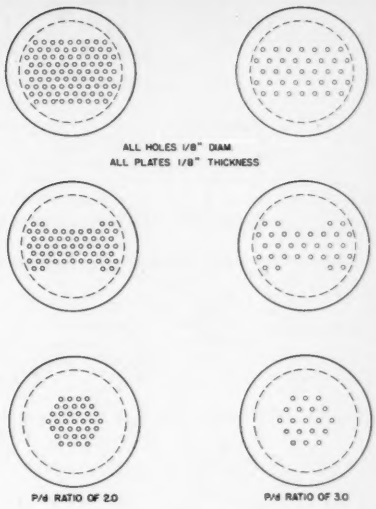

Fig. 20. Perforated-plate layouts for the free-area study.

actual free area (A_f) to the maximum free area (A_t) possible if the total area of the plate were perforated at the same P/d ratio and pattern. The maximum free area was determined from the correlation presented in Figure 10. At any given A_f/A_t ratio the A_f/A_D ratio is a function only of the P/d ratio. Figure 22 is a cross plot of Figure 21 at a Reynolds number 5,000. The coefficients were plotted vs. A_f/A_t ratio with the P/d ratio as the parameter. The dashed lines represent approximations based on a single data point. The curves shown are for a T/d ratio of 1.0, but they show the trends that can probably be expected at all T/d ratios. From Figure 22 it was concluded that the orifice coefficient is not affected by the distribution of the holes on a plate as long as the A_f/A_t ratio is greater than 0.60. Since the correlation in Figure 19 is based on A_f/A_t ratios of greater than 0.60, the correlation will apply between A_f/A_t ratios of 0.60 and 1.00. In actual practice the A_f/A_t ratio usually falls between 0.60 and 0.70.

APPLICATION OF CORRELATION

A generalized correlation is presented in Figure 19 which can be used for the design of perforated plates insofar as the dry-plate pressure drop is concerned. The correlation covers a wide range of practicable variables which are sufficient to cover most design needs. Although the correlation particularly applies to equilateral-triangular hole pattern, it may prove to be applicable to other arrangements.

The correlation presented was based only on air, the original supposition being that the Reynolds number is the criterion for dynamic similarity and

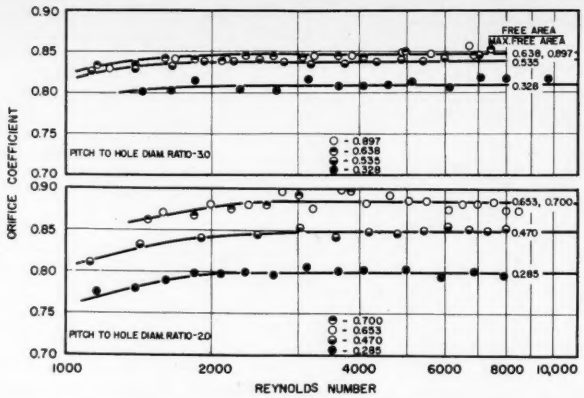

Fig. 21. Effect of free area on the orifice coefficient at a plate-thickness–to–hole-diameter ratio of 1.0.

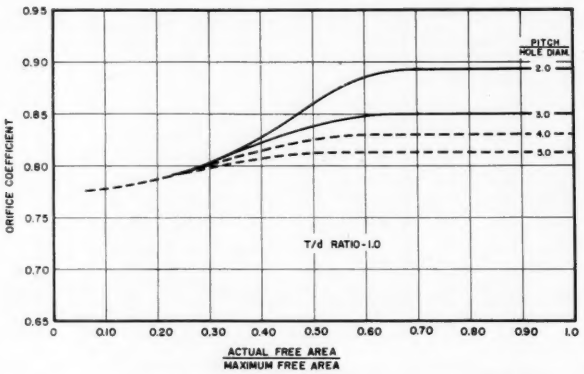

Fig. 22. Cross plot of Figure 21 at a Reynolds number of 5,000.

would generalize the correlation for other gases. Data presented by Hunt *et al.* (*4*) for air, carbon dioxide, methane, Freon 12, and argon were compared with values predicted from this correlation and found to have an average deviation of less than 5%. This seems to indicate that the correlation is applicable, in general, to other gases.

Although the correlation is based on data obtained from small-scale equipment, the dimensionless groups used in the correlation should allow application to larger columns. Scaling up of this type has been indicated by Mayfield *et al.* (*8*). Arnold *et al.* (*2*) also claim good agreement between 6 and 15-in.-diam. columns. A comparison was made between this correlation and the data presented by other investigators using larger columns. Data reported by Arnold *et al.* had an average deviation of less than 3%. Deviation from the data reported by Mayfield *et al.* was as high as 33% in one case, but generally the average was about 10%. Both Hunt and Mayfield used 6-in. columns and Arnold used 6- and 15-in. columns. With some reservations, it seems reasonable that the correlation presented can be applied to larger diameter columns.

Certain generalizations can be made from the correlation about perforated-plate design. As a rule it is desirable to maintain a low dry-plate pressure drop across the plate. The following conditions were found to give the maximum coefficients: (1) T/d ratio of 1.0 or greater, (2) P/d ratio of 2.0 or less, and (3) A_f/A_t ratio from 0.60 to 1.00. For these conditions the optimum Reynolds-number range was found to be 4,000 to 20,000.

APPLICATION TO DESIGN OF COLUMNS

Although a Reynolds-number range from 2,000 to 20,000 has been covered in this work, the majority of commercial designs operate in a Reynolds-number range from 3,500 to 15,000. In this range the orifice coefficient becomes independent of Reynolds number and so the design engineer's use of these data is simplified.

It should be emphasized clearly that the data and correlations presented here were obtained from carefully finished plates and that commercially available plates may not have the same characteristics. Comparisons of these data and those obtained from commercial types of perforations (*2*, *8*) have been shown to be in good agreement.

NOTATION

A = cross-sectional area
A_f = free area of holes on a plate
A_t = maximum free area possible on a plate
C = average orifice coefficient
d = hole or orifice diameter
D = inside diameter of column or conduit
g = gravity constant
K = constant
P = hole pitch
ΔP = pressure drop across a perforated plate
T = plate thickness
v = average fluid velocity in the orifice
Y = average expansion factor for the fluid
α = slope of curves
ρ = fluid density in the orifice
ρ_D = fluid density at upstream pressure tap
μ = fluid viscosity in the orifice

Subscripts

d = orifice or hole
D = column or conduit
1 = condition upstream from orifice
2 = condition in the orifice
3 = condition downstream from orifice

LITERATURE CITED

1. Am. Soc. Mech. Engrs. Special Committee on Fluid Meters, "Fluid Meters," Part I, New York (1937).
2. Arnold, D. S., C. A. Plank, and E. M. Schoenborn, *Chem. Eng. Progr.*, **48**, 633 (1952).
3. Baines, W. D., and E. G. Peterson, *Trans. Am. Soc. Mech. Engrs.*, **73**, 467 (1951).
4. Hunt, C. d'A., D. N. Hanson, and C. R. Wilke, *A.I.Ch.E. Journal*, **1**, 441 (1955).
5. Jones, J. B., and C. Pyle, *Chem. Eng. Progr.*, **51**, 424 (1955).
6. Kamei, S., T. Takamatau, S. Mizuno, and Y. Tomizawa, *Chem. Eng.* (*Japan*), **18**, No. 3, 108 (1954).
7. Lewish, W. T., *Prog. Report No. 7, Atomic Energy Comm.*, Microcard ORO 142 (1954).
8. Mayfield, F. D., W. L. Church, A. C. Green, D. C. Lee, and R. W. Rassmussen, *Ind. Eng. Chem.*, **44**, 2238 (1952).
9. Perry, J. H., ed., "Chemical Engineers' Handbook," 3 ed., p. 407, McGraw-Hill Book Company, Inc., New York (1950).
10. *Ibid.*, p. 371.
11. Stearns, R. F., R. J. Russell, R. M. Jackson, and C. A. Larson, "Flow Measurements with Orifice Meters," D. Van Nostrand Company, New York (1951).

Nusselt Values for Estimating Turbulent Liquid Metal Heat Transfer in Noncircular Ducts

JAMES P. HARTNETT and THOMAS F. IRVINE, JR.

University of Minnesota, Minneapolis, Minnesota

A simple expression for estimating the turbulent forced-convection heat transfer performance of liquid metals flowing through noncircular ducts is presented. This equation requires the knowledge of the slug Nusselt number evaluated for the specific geometry and for the pertinent boundary conditions. Such Nusselt values are presented herein for a number of technically important geometries. One check on the heat transfer prediction given by Equation (4) is in the case of an annular duct with constant heat flow through the outer wall with the inner wall insulated, for which experimental data exist. The prediction agrees within 20% with the experimental data.

Several possible boundary conditions that may exist in noncircular cross sections are thoroughly discussed, and it is hoped that as a result this paper may serve to clarify some of the confusion existing in the literature.

Liquid metals continue to be of considerable interest as primary coolants in nuclear power plants. Examples may be found in the sodium reactor experiment of Atomics International and in the fast breeder reactor being planned by Power Reactor Development Company, both of which use sodium as the coolant. In such applications the geometry of the cooling passages through which the liquid metal flows is determined by engineering and nuclear considerations which frequently dictate noncircular shapes. The purpose of the present paper is to provide a method of estimating the convective heat transfer and wall-temperature distribution for turbulent flow of liquid metals through passages having such noncircular cross sections.

NUSSELT NUMBER EQUATION FOR TURBULENT LIQUID METAL FLOW

It has been pointed out by Lyon (*1*), Claiborne (*2*), and others that turbulent forced-convection heat transfer performance of liquid metals may be estimated by an appropriate combination of the separate contributions due to molecular conduction and turbulent exchange. Since the velocity profile in turbulent flow approximates a slug flow profile (constant velocity across the passage cross section), it is reasoned that the convective contribution due to molecular conduction should be obtainable from the energy-equation solution by utilizing the actual temperature or heat-flow boundary conditions but assuming the slug velocity distribution. The resulting slug Nusselt number is then decreased somewhat to account for the fact that the actual velocity profile is not uniform but falls off in the region of the walls. The turbulent contribution must then be added to the modified slug Nusselt number to give an expression of the following form for the actual Nusselt number:

$$Nu = C(Nu_s) + \text{turbulent contribution} \quad (1)$$

where Nu = Estimated Nusselt number for turbulent liquid metal flow
Nu_s = slug Nusselt number
C = correction factor for actual velocity profile

Specifically, if the circular tube is considered, the Lyon equation (*1*) which is based on the results of extensive calculations using the momentum analogy approach is expressed as

$$Nu = 7.0 + 0.025\,(Pe)^{0.8} \quad (2)$$

Since the Nusselt number for slug flow under the same boundary conditions is 8.0, comparison of the Lyon equation with Equation (1) yields a value of C of $\frac{7}{8}$ and a turbulent contribution of $0.025\,(Pe)^{0.8}$.

On this basis Seban and Shimazaki (*3*) proposed the following expression for the case of constant wall temperature for the circular tube where the slug Nusselt number is 5.8:

$$Nu = \tfrac{7}{8}(5.8) + 0.025\,(Pe)^{0.8}$$

or

$$Nu = 5.0 + 0.025\,(Pe)^{0.8} \quad (3)$$

This expression agrees with the results obtained by the momentum analogy (*3*).

A recent survey by Lubarsky and Kaufman (*4*) of all available liquid metal pipe-flow data indicates that Equations (2) and (3) yield results which are somewhat higher than experimental data; however, by use of the survey detailed in reference *4*, the constants appearing in Equations (2) and (3) were revised downward to agree with the pipe-flow data. This was done and the following equation is recommended by the present authors for an estimate of the convective heat transfer for a liquid metal (Prandtl number less than 0.1) flowing turbulently through a duct circular or noncircular in cross section:

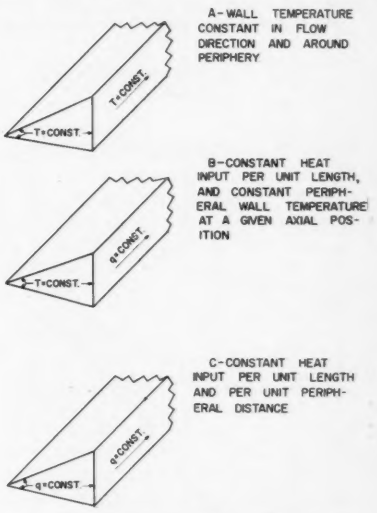
A- WALL TEMPERATURE CONSTANT IN FLOW DIRECTION AND AROUND PERIPHERY
T=CONST.
T=CONST.
B- CONSTANT HEAT INPUT PER UNIT LENGTH, AND CONSTANT PERIPHERAL WALL TEMPERATURE AT A GIVEN AXIAL POSITION
q'=CONST.
T=CONST.
C- CONSTANT HEAT INPUT PER UNIT LENGTH AND PER UNIT PERIPHERAL DISTANCE
q"=CONST.
q"=CONST.

Fig. 1. Boundary conditions of importance for noncircular ducts.

$$Nu = \tfrac{2}{3}Nu_s + 0.015\,(Pe)^{0.8} \quad (4)^*$$

The main purpose of this paper is to present all available slug Nusselt values for ducts with noncircular cross sections. In the interest of completeness, previously reported values are included, and, in addition, a number of new solutions are given. It should be emphasized that Equation (4) is not valid for ordinary fluids such as air or water but is restricted to liquid metals.

In those cases where the wall boundary condition is one of constant heat flux everywhere, the knowledge of the resulting wall-temperature distribution is of more importance than the Nusselt numbers. For several geometries of importance such wall-temperature distributions are given for the limiting case of low turbulent Reynolds numbers. All results are presented in a form convenient for engineering calculations.

BOUNDARY CONDITIONS IN NONCIRCULAR DUCTS

Considerable confusion is apparent in the literature concerning the possible boundary conditions and their implica-

*In the original manuscript the constant 0.019 appeared rather than 0.015. The revision downward was suggested by H. C. Claiborne and brings the equation into better agreement with the experimental data.

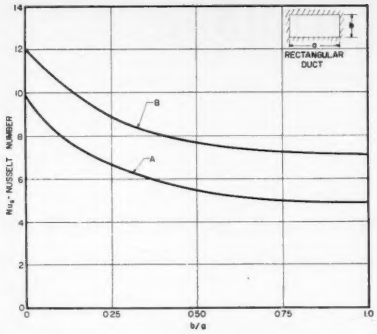

Fig. 2. Slug Nusselt numbers for rectangular duct.

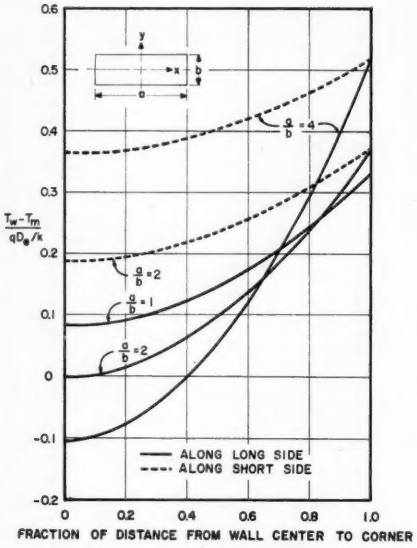

Fig. 3. Limiting wall-temperature distribution for rectangular duct with constant heat flux everywhere.

tions in noncircular ducts. This has been previously pointed out by Eckert, Irvine, and Yen (5). For a circular pipe no ambiguity is encountered, and two boundary conditions of major importance are usually considered: constant wall temperature and constant heat input per unit length. If attention is restricted to conditions of established hydrodynamic and thermal fields, the constant-wall-temperature case requires the fluid temperature gradually to approach the wall value in the flow direction. In the second case of constant heat input each increment of surface area transfers the same heat flow to the fluid and consequently the wall and fluid temperatures increase linearly with length at the same rate. Owing to the symmetry of the circular tube, the wall temperature is constant around the circumference at any cross section and the thermal properties of the wall material do not enter into any circumferential considerations.

On the other hand, if a geometry is considered which lacks circular symmetry, such as the triangle, rectangle, or ellipse, the situation becomes more complex. In these cases with constant heat generation a peripheral temperature gradient can exist at a given cross section and the thermal properties of the wall can enter into the problem. In addition, the source of the heat generation must be specified, i.e., on the outer or inner surface of the wall or within the wall itself. Three tractable boundary conditions of technical interest may therefore be distinguished for ducts with noncircular cross sections, as shown on Figure 1:

1. The wall temperature remains constant everywhere (designated throughout the paper as case A).
2. The heat input per unit length is constant and the wall temperature is constant around the periphery at a given axial position. This condition requires the local heat input to the fluid to vary around the periphery. In practice this will occur if the heat is uniformly generated at the outer duct wall and if the wall conduction is very large in the peripheral direction. In contradistinction to case 3 below, this may be called the thick-walled duct with uniform heat generation (case B).
3. The heat input per unit area is constant in both the peripheral and flow direction. This condition requires the wall temperature to vary around the periphery at a given axial position and can be realized in practice in a very thin-walled duct (zero peripheral wall conductivity) where the heat is uniformly generated at the outer duct wall (case C).

It may be noted that cases B and C are identical for circular tubes and infinite slots.

In addition to these cases, if the geometry of interest has independent boundary surfaces such as an annulus, other boundary conditions may be considered:

1. Constant heat input on one wall with the other wall insulated.
2. Constant heat input on both walls. This condition requires the temperature of the inner and outer walls to be different at the same cross section.
3. Constant heat input per unit length with equal peripheral wall temperatures at every cross section. This condition requires a different heat rate from the inner and outer surfaces to the fluid.
4. Constant wall temperature everywhere.
5. Constant wall temperature on one wall with the other wall insulated.

Although other combinations are possible, these will serve to demonstrate the many different boundary conditions which may be encountered. In particular it should be pointed out that care must be taken to utilize the correct slug-flow solution (i.e., the one corresponding to the correct boundary conditions) in evaluating Equation (4).

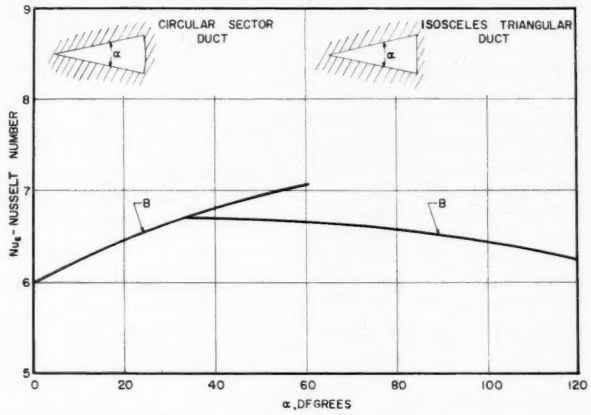

Fig. 4. Slug Nusselt numbers for circular-sector duct and isosceles-triangular duct.

DISCUSSION OF THE SLUG-FLOW DIFFERENTIAL EQUATION

For a fluid in steady duct flow with constant property values under the conditions of fully developed velocity and temperature fields, the energy equation assumes the following form:

$$\frac{\partial^2 T}{\partial x^2} + \frac{\partial^2 T}{\partial y^2} = \frac{w}{\kappa}\frac{\partial T}{\partial z} \qquad (5)$$

The velocities in the x and y directions perpendicular to the flow are zero.

The axial conduction term $\partial^2 T/\partial z^2$ has been omitted in Equation (5) as its contribution is negligible in case A. For cases B and C the axial conduction term is identically zero under the fully developed thermal conditions assumed in the analysis.

In the following solutions the velocity w is taken as constant at any cross section or longitudinal position. The previously defined cases A, B, and C will be discussed in more detail.

Case A: Wall Temperature Everywhere Constant

Under these conditions the fluid longitudinal temperature gradient $\partial T/\partial z$

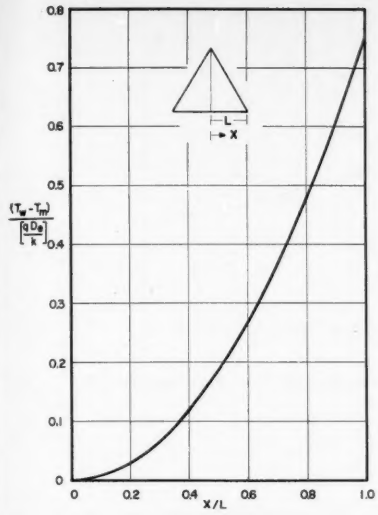

Fig. 5. Limiting wall-temperature distribution for equilateral-triangular duct with constant heat flux everywhere.

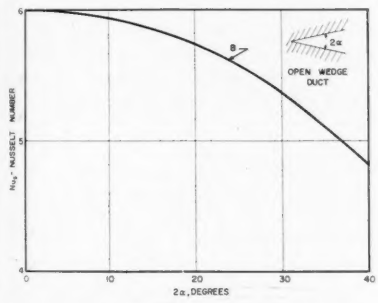

Fig. 6. Slug Nusselt numbers for infinite open-wedge duct for boundary condition *B*.

changes in the downstream direction as the mean fluid temperature approaches the wall value. One of the earliest reported solutions for this case was by Graetz (*6*) for slug flow through a circular pipe. Fortunately, the differential equation (5) also describes the temperature field as it changes with time in a solid of the same shape and as a result some useful slug-flow-convection solutions have appeared in the heat-conduction literature for the constant-wall-temperature boundary condition. For example, Carslaw and Jaeger (*7*) present the temperature distributions for the rectangle and annulus, and Jaeger (*8*) treats the circular sector and open wedge. A number of these solutions are translated into a form usable for engineering calculations and are presented in a later section.

Case B: Constant Heat Input Per Unit Length, Constant Peripheral Wall Temperature

Under these conditions a simple heat balance will show the longitudinal temperature gradient to be constant. The differential equation (5) reduces to Poisson's equation in two dimensions; i.e.,

$$\frac{\partial^2 T}{\partial x^2} + \frac{\partial^2 T}{\partial y^2} = \text{constant} \qquad (6)$$

This equation has been extensively studied in mathematical physics as it describes a great number of physical phenomena. In particular, Equation (6) describes the velocity field in the laminar flow of a fluid under the conditions of a fully developed velocity field. Eckert and Irvine (*9*) recently collected available velocity-distribution solutions for noncircular cross sections and in addition have obtained solutions for new shapes. Their results are essentially reported as the product of the friction factor f and the Reynolds number where the friction factor is defined as

$$f = \frac{\dfrac{\partial P}{\partial z}}{\rho \bar{w}^2 / 2D_e} \qquad (7)$$

Inspection of the governing differential equations, the friction-factor definition, and the definition of the slug Nusselt number yields the following interesting relation between the friction factor and the slug Nusselt number:

$$Nu_s = \frac{f \cdot Re}{8} \qquad (8)$$

The obvious result is that all calculations by Eckert and Irvine (*9*) may be directly converted to slug Nusselt numbers.

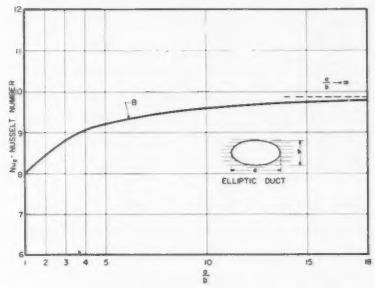

Fig. 7. Slug Nusselt numbers for elliptic duct for boundary condition *B*.

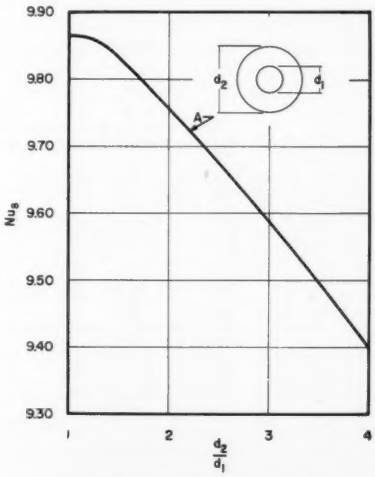

Fig. 8. Slug Nusselt numbers for annular duct with constant wall temperature, boundary condition *A*.

Case C: Constant Heat Input Per Unit Surface Area Everywhere on Boundary Walls

This boundary condition requires the temperature gradient normal to the inner wall surface to be constant at all wall locations. Because of constant longitudinal heat addition, the differential equation is once again in the form of Poisson's equation, Equation (6). While case *C* is considerably easier to approach in practice than case *B* (case *C* being a thin-walled duct with constant heat addition at the exterior of the duct), the solution of the differential equation is more difficult.

In both previous cases the slug Nusselt number was the heat transfer parameter of primary interest. In this case where the heat flux is already specified, the peripheral-wall-temperature distribution is generally of greater concern, as structural considerations normally dictate a maximum possible operating temperature. Limiting wall temperature distributions therefore will be given for case *C*; it should be emphasized, however, that such results are strictly valid only for the slug-flow velocity distribution with heat transfer only by molecular conduction. Thus these limited temperature distributions approximate conditions to be expected for turbulent flow at Reynolds numbers slightly above the critical value. As the Reynolds number is increased, turbulent exchange will have a mitigating effect on the wall temperature gradients. However, the solutions point out the locations of maximum temperature.

PRESENTATION OF SLUG NUSSELT NUMBERS AND WALL-TEMPERATURE DISTRIBUTIONS

The values of slug Nusselt numbers and wall-temperature distributions will be given in this section for all three boundary conditions under the heading of the particular geometry.

Rectangular Duct

For this geometry the solutions for boundary conditions *A* and *B* are shown in Figure 2. The constant-wall-temperature boundary condition, case *A*, is treated by Carslaw and Jaeger (*7*) and case *B* is treated by Timoshenko (*10*) and by Claiborne (*2*) although some confusion with respect to boundary conditions *A* and *B* is evident in this last reference.

The wall-temperature distribution for case C from this reference (*2*) is given below and plotted in Figure 3.

$$\left[\frac{T_w - T_m}{qD_e/k}\right]_{y=b/2} = \frac{x^2}{aD_e} + \frac{b}{4D_e} - \frac{a+b}{12D_e} \quad (9)$$

$$\left[\frac{T_w - T_m}{qD_e/k}\right]_{x=a/2} = \frac{a}{4D_e} + \frac{y^2}{bD_e} - \frac{a+b}{12D_e} \quad (10)$$

The center of the coordinate axis is taken as the geometric center of the rectangle and x and y are measured from this point.

This dimensionless presentation for case C was chosen since the hydraulic diameter D_e, the fluid thermal conductivity k, and the heat flux q will necessarily be specified, and the local fluid bulk temperature T_m is readily calculated (since q is known and the fluid temperature at the duct entrance will be known), and therefore the only unknown is T_w. It is apparent from Figure 3 that the maximum wall temperature will occur in the corners.

It is of interest to note that the rectangle includes as special cases (1) the square duct when the two sides are of equal magnitude and (2) the infinite slot when the ratio of the sides goes to zero.

Isosceles-triangular Duct and Circular-sector Duct

The triangular-shaped duct is frequently encountered in practice, and so these solutions are particularly useful. The circular-sector duct is included in this section as it should closely approximate the isosceles triangle in those cases where the apex angle α is small. The constant-wall-temperature case (case A) has been treated (*8*) for the circular-sector duct, but no comparable solution was found for the isosceles-triangular duct. For boundary condition B the results are shown in Figure 4, which presents both the circular-sector and the isosceles-triangle values. The isosceles-triangular-duct values were obtained by converting an approximate velocity-distribution solution previously given by Nuttall (*11*), and these results become somewhat questionable at small angles. It is therefore recommended that the approximate isosceles-triangular-duct results be used only above 30 deg. and the circular sector utilized at smaller angles. It is of interest that the slug Nusselt value exhibits only small change over a wide range of apex angles.

The constant heat-flux boundary condition, case C, has been discussed for the circular-sector duct (*2*) but considerable work would be required to convert the results into an engineering form. No comparable solution for the general isosceles-triangular duct is known, although the special case of the equilateral triangle is tractable (*2*). The resulting wall-temperature distribution for the equilateral triangle is shown in Figure 5. As expected, the maximum wall temperature occurs in the corners. It is of additional interest that at the midpoint of the walls the wall temperature is exactly equal to the bulk fluid temperature.

It has been pointed out in (*12*) that in ducts with triangular cross sections, it is possible to have laminar flow in the corners when it might normally be expected that turbulent flow exists. Some caution must therefore be exercised in applying turbulent relations to ducts having narrow corner regions.

Open Wedge or Infinite Wedge

This particular geometry is of interest even though it will seldom be found in practice, as it has been shown in reference *12* that for small angles the effect of the base wall on the fluid near the apex becomes negligible. It is therefore possible to investigate the heat transfer conditions in the critical apex regions with expressions which are considerably simpler than those for the circular sector.

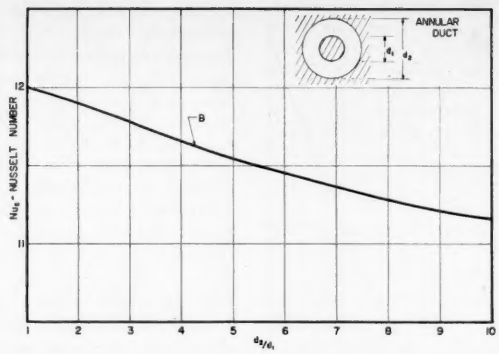

Fig. 9. Slug Nusselt numbers for annular duct for boundary condition *B*.

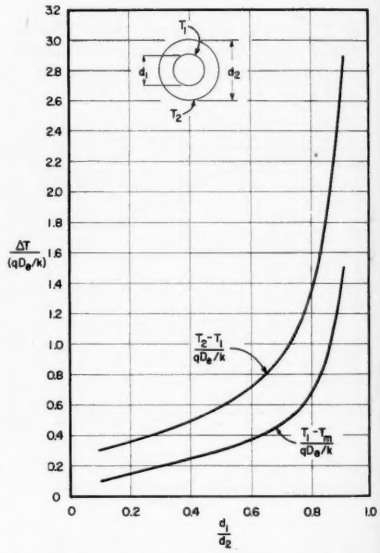

Fig. 10. Limiting wall-temperature distribution for annular duct with constant heat flux everywhere, boundary condition *C*.

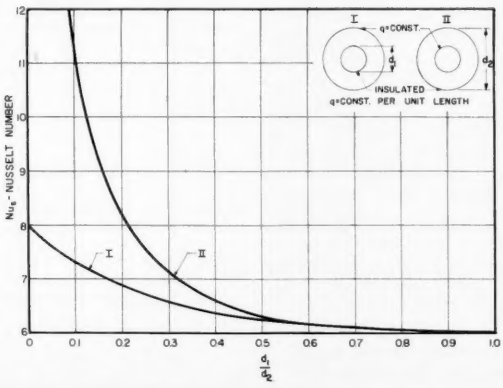

Fig. 11. Slug Nusselt numbers for annular duct with constant heat input on one wall with the other wall insulated.

Table 1. Summary of Slug-flow Solutions for Various Geometries

Geometry	Boundary condition (See Fig. 1)	Slug Nusselt numbers	Slug-flow Wall-temperature distribution
Rectangle	*A*	Fig. 2	
	B	Fig. 2	
	C		Eq. (10), Fig. 3
Circular Sector	*A*	Available in Ref. (8)	
	B	Fig. 4	
	C		Available in ref. (2)
Isosceles triangle	*A*	No Solution Obtained	
	B	Fig. 4	
	C		No general solution obtained
Equilateral triangle	*A*	No Solution Obtained	
	B	Table II and Fig. 4	
	C		Fig. 5
Open wedge	*A*	Available in Ref. (8)	
	B	Fig. 6	
	C		No solution obtained
Ellipse	*A*	No Solution Obtained	
	B	Fig. 7	
	C		Available in ref. (2)
Annulus	*A*	Fig. 8	
	B	Fig. 9	
	C		Fig. 10
	Constant heat input on one wall with the other wall insulated	Fig. 11	

The solution to case *A* is given in reference *9*, while the slug Nusselt numbers for case *B* are given in Figure 6. No solution was obtained for case *C*.

Ellipse

For the ellipse the slug Nusselt number for case *B* is shown in Figure 7. No solution for cases *A* and *C* has been found although reference *2* has an expression for the solution to case *C* in the form of unevaluated Fourier coefficients.

Annular Duct

As discussed in an earlier section, a large number of boundary conditions are possible for this geometry. Figure 8 presents the slug Nusselt values for the case where both walls are at constant temperature. The Nusselt value for the case of constant heat input per unit length with both inner and outer walls at the same temperature at a given axial position is presented in Figure 9; for this case the heat input per unit area is not the same at both wall surfaces. Figure 10 presents the wall-temperature variation for the case where there is uniform heat input per unit area from every element of both wall surfaces. Finally, the case of constant heat input on one wall with the other wall insulated is shown in Figure 11.

SUMMARY AND RESULTS

The summary of the available slug-flow solutions as previously discussed is presented in Table 1, which provides a ready reference as to the availability and location of essentially all technically important noncircular geometries. For additional convenience a second table, Table 2, summarizes slug Nusselt values for simple geometries of technical importance. All values appearing in Table 2 are special cases of the more general geometries covered in Table 1.

Table 2. Slug Nusselt Numbers for Simple Geometries

Geometry	Boundary condition (See Fig. 1)	Slug Nusselt number
Circle	*A*	5.80
	B	8.0
Square	*A*	$\pi^2/2 = 4.93$
	B	7.03
Equilateral triangle	*A*	
	B	6.67
Infinite slot	*A*	$\pi^2 = 9.87$
	B	12
Infinite slot with one wall insulated	*A*	$\pi^2/2 = 4.93$
	B	6
90-deg. isosceles triangle	*A*	
	B	6.55

ACKNOWLEDGMENT

The authors acknowledge their debt to James Yen and William Welsh for carrying out many of the lengthy calculations reported herein.

NOTATION

English Letter Symbols

a = length of long side of rectangle
b = length of short side of rectangle
C = constant
c_p = specific heat at constant pressure
D_e = equivalent or hydraulic diameter $\left(\frac{4 \text{ cross section area}}{\text{perimeter}}\right)$
d = diameter of annulus
f = friction factor, defined in Eq. (7)
h = heat transfer coefficient, defined as $q/T_w - T_m$
k = thermal conductivity
p = pressure
q = heat rate per unit area
T = temperature
w = velocity in z direction
$\bar{w}$ = mean velocity for actual laminar flow profile as utilized in Eq. (7)
x, y, z = coordinate directions

Subscripts

s = slug
m = mean or bulk conditions
e = hydraulic or equivalent
w = wall conditions

Dimensionless Ratios

Nu = Nusselt number, hD_e/k
Pr = Prandtl number, $\mu c_p/k$
Pe = Peclet number, $\rho c_p \bar{w} D_e/\kappa$
Re = Reynolds number $\rho \bar{w} D_e/\mu$

Greek Symbols

α = angle
κ = thermal diffusivity
ρ = density
μ = dynamic viscosity

LITERATURE CITED

1. Lyon, R. N., *Oak Ridge Nat. Lab. Rept.* 361 (August, 1949).
2. Claiborne, H. C., *Oak Ridge Natl. Lab. Rept.* 985 (May, 1951).
3. Seban, R. A., and T. T. Shimazaki, *Trans. Am. Soc. Mech. Engrs.*, **73**, 803 (1951).
4. Lubarsky, B., and S. J. Kaufman, *Natl. Advisory Comm. Aeronaut. Tech. Note* 3336 (March, 1955).
5. Eckert, E. R. G., T. F. Irvine, Jr., and J. T. Yen, *Wright Air Development Center Tech. Rept.* 56-98, Wright-Patterson Air Force Base, Ohio (April, 1956).
6. Graetz, L., *Ann. Phys. Chem.*, **25**, No. 7, p. 337 (1885).
7. Carslaw, H. S., and J. C. Jaeger, "Conduction of Heat in Solids," Oxford at the Clarendon Press (1947).
8. Jaeger, J. C., *Phil. Magazine*, **7**, 33 (1942).
9. Eckert, E. R. G., and T. F. Irvine, Jr., *Proc. Fifth Midwestern Conference on Fluid Mechanics*, Univ. of Michigan (1957).
10. Timoshenko, S., "Theory of Elasticity," McGraw-Hill Book Company, Inc., London (1934).
11. Nuttall, H., "Flow of a Viscous Incompressible Fluid, Expression for a Uniform Triangular Duct," *Engineering*, Vol. 178, p. 299, 1954.
12. Eckert, E. R. G., and Irvine, T. F., Jr., "Flow in Corners of Passages with Non-Circular Cross Sections," *Transactions, ASME*, Vol. 78, p. 789, May 1956.
13. Seban, R. A., and Casey, D. F., "Heat Transfer to Lead Bismuth in Turbulent Flow in an Annulus," ASME Paper No. 56-A-62, 1956.

Equilibrium Ratios of Hydrogen and the Critical Loci of Hydrogen-paraffin Mixtures

J. M. LENOIR and H. G. HIPKIN

C. F. Braun and Company, Alhambra, California

This paper presents a correlation to predict the equilibrium ratios of hydrogen in hydrocarbon mixtures by use of the parameters of pressure and convergence pressure. Also a procedure to predict convergence pressures of hydrogen-containing mixtures was developed from a correlation of critical loci. With the predicted convergence pressure the measured values of hydrogen equilibrium ratios in binary hydrogen-paraffin mixtures were predicted with a statistical deviation of 8.1% for 237 measurements. Including hydrogen-olefin and multicomponent mixtures of hydrogen, paraffins, and olefins, the statistical deviation was found to be 11.3% for a total of 375 comparisons with measured values of hydrogen equilibrium ratios.

With the increased use of catalytic cracking and catalytic reforming, mixtures of hydrogen and hydrocarbons are more and more commonly encountered. Often the phase behavior of such mixtures must be predicted under fairly high pressures. The prediction of the equilibrium ratios of hydrogen itself is important. In addition, the presence of hydrogen has a large effect on the critical locus of the system and appreciably influences the equilibrium ratios of the hydrocarbons. For liquid phases that are primarily paraffin hydrocarbons this paper presents a correlation to predict equilibrium ratios and convergence pressures for hydrogen containing mixtures. The development is based on published experimental measurements of equilibrium ratios and critical loci (*1, 2, 3, 4, 9, 11, 14, 17*).

METHOD OF CORRELATION

For hydrocarbons equilibrium ratios have been correlated by the use of convergence pressure Pg (*6, 10, 13, 15, 16, 18*), which is the isothermal projection to the critical locus of the binary mixture and is defined by the identity of the two binary components and the temperature. For a multicomponent mixture the convergence pressure may be determined by the isothermal projection to an equivalent binary critical locus (*6*) identified in general by hypothetical components (*10*). Mathematically, the equilibrium ratio $K = y/x$ is dependent upon four parameters,

$$K = f(i, T, Pg, P) \qquad (1)$$

A study of the equilibrium ratios of light hydrocarbons shows that at high temperatures and constant convergence pressure the equilibrium ratios become independent of temperature (*10, 12*). This independence of temperature as a variable begins at about 2.3 times the critical temperature of the component. Figure 1 illustrates this for methane, ethylene, and ethane. On the basis that this is a general relation, at constant convergence pressure the equilibrium ratios of hydrogen are essentially independent of temperature at temperatures above −300°F. The equilibrium-ratio relation for hydrogen reduces to

$$K = f(P, Pg) \qquad (2)$$

This equation has been used to prepare a chart for the prediction of hydrogen equilibrium ratios.

With the experimental data a series of plots was prepared of the equilibrium ratios of hydrogen as a function of pressure. Figure 2 illustrates the results for hydrogen in propane (*3, 17*). Other plots were made for hydrogen in methane (*2, 11*), ethane (*17*), *i*-butane (*4*), butane (*1*), trimethylpentane (*4*), and dodecane (*4*). On Figure 2, where the four lowest curves intersect the $K = 1$ line, the convergence pressures are directly established as 1,580, 3,430, 7,880, and 10,000 lb./sq. in. abs. Two methods can be used to establish the convergence pressure for the curves that do not cross $K = 1$ at pressures below 10,000 lb./sq. in. abs. Convergence pressures can be approximated by extrapolation to the $K = 1$ line if similitude to the shapes of the identified curves is used. By this method, for example, the curve labeled −150°F. gas a convergence pressure of 50,000 ± 20,000 lb./sq. in. abs. A better procedure is to plot identified convergence pressures against the equilibrium ratio at constant pressure on logarithmic graph paper, as illustrated on Figure 3. Such plots are straight lines if none of the curved portions of Figure 2 are included. By extrapolation of the straight lines of Figure 3, convergence-pressure identities above 10,000 lb./sq. in. abs. were estimated. With convergence-pressure identities for all experimental log K vs. log P plots, Figure 4 was developed by customary cross-plotting techniques. The chart shows hydrogen equilibrium ratios in paraffinic mixtures as a function of pressure and convergence pressure and is based upon measurements at temperatures from −200° to 303°F.

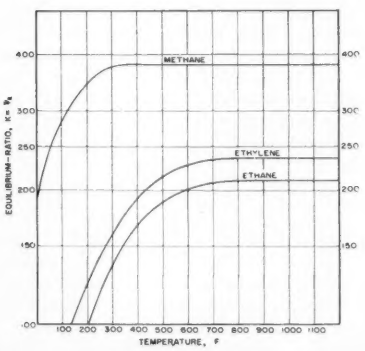

Fig. 1. Equilibrium ratios at 10 lb./sq. in. abs., constant convergence pressure of 5,000 lb./sq. in. abs.

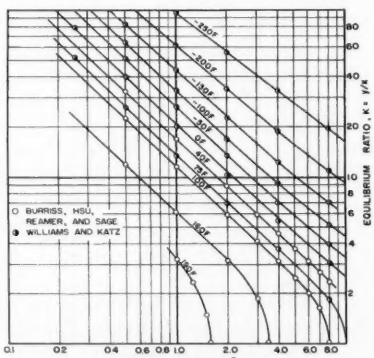

Fig. 2. Hydrogen equilibrium ratios in propane.

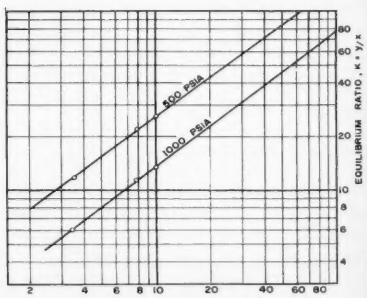

Fig. 3. Equilibrium ratios vs. convergence pressure.

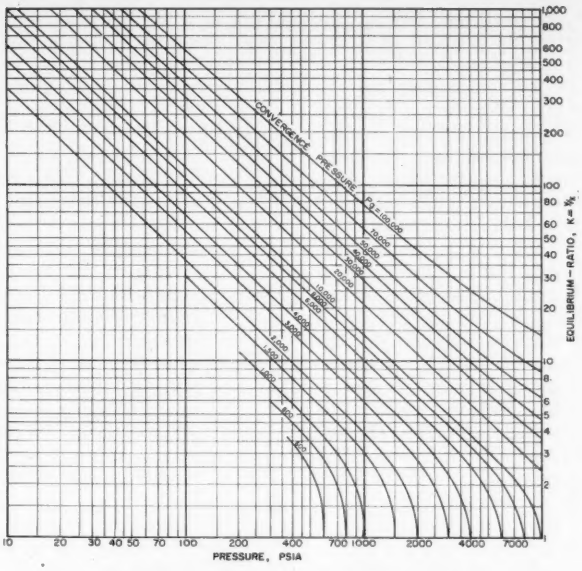

Fig. 4. Equilibrium ratios of hydrogen.

TABLE 1. COMPARISON OF EXPERIMENTAL AND PREDICTED HYDROGEN EQUILIBRIUM RATIOS
Binary Mixtures

Heavy component	Reference	Temp. °F.	Pressure, lb./sq. in. abs.	Predicted K	Measured K	Deviation, %
Methane	11	−175	630	11.7	11.5	1.7
Ethane	17	50	2,500	2.10	2.14	−1.6
Propane	3	40	2,500	6.6	7.09	−7.0
Butane	1	75	1,130	16.1	15.4	4.5
i-Butane	4	250	1,500	2.5	2.61	−4.2
Heptane	9	77	735	27	28.8	−6.2
Octane	9	122	735	24	25.3	−5.1
Trimethylpentane	4	100	175	103	110	−6.4
Dodecane	4	300	1,021	13.0	12.6	3.2

TABLE 2. COMPARISON OF EXPERIMENTAL AND PREDICTED HYDROGEN EQUILIBRIUM RATIOS
Ternary and Multicomponent Systems (*2, 17*)

Temp., °F.	Pressure, lb./sq. in. abs.	x_{H_2}	EBP_L	EBP_H	Pg predicted	K predicted	K measured	Deviation, %
Hydrogen-ethylene-ethane								
−100	1,000	4.1	−393	−139	22,000	23.1	22.4	3.1
−100	8,000	30.7	−393	−140	22,000	3.1	3.03	2.3
Hydrogen-ethylene-propane								
−100	1,000	3.1	−393	−83	32,000	28.2	30.1	−6.3
−100	8,000	21.7	−393	−80	32,000	4.45	4.38	1.6
Hydrogen-propylene-propane								
−100	1,000	2.8	−393	−50	37,000	34.0	35.4	−4.0
−100	8,000	18.1	−393	−50	37,000	5.2	5.47	−4.9
Hydrogen-methane-propylene								
−100	500	0.728	−376	−98	12,200	26	20.6	26.2
−100	500	1.36	−393	−54	35,500	62	72.5	−14.5
Hydrogen-methane-propane								
0	500	0.329	−375	−59	7,500	23	23.1	−0.4
−200	1,000	1.79	−393	−53	74,000	60	55.3	8.5
Hydrogen, methane, ethylene, ethane, propylene, propane								
0	500	1.04	−391	−59	15,500	36	36.8	−2.2
−100	500	1.34	−389	−64	27,700	50	49.1	1.8

CRITICAL LOCI

With the curves of Figure 4, and experimental values of equilibrium ratios, the convergence pressures for the hydrogen-paraffin mixtures were determined for various temperatures. Figure 5 shows convergence pressures for various systems of hydrogen in paraffins ranging from methane to dodecane. Figure 5 is also a plot of critical-pressure loci, since the convergence- and critical-pressure loci are identical for binary systems. Figure 6, which shows the results of cross plotting Figure 5 with the boiling point of the paraffin hydrocarbon as a correlating parameter, is the correlation prepared for predicting convergence pressure of hydrocarbon mixtures containing hydrogen.

EXAMPLE

A liquid mixture of 0.062 mole fraction hydrogen and 0.938 mole fraction propane is at the bubble point at 100°F. and 1,000 lb./sq. in. abs. The boiling point of propane is −44°F. From Figure 6 the predicted convergence pressure is 7,800 lb./sq. in. abs. From Figure 4 the equilibrium ratio for hydrogen is 11.9. Burriss, Hsu, Reamer, and Sage (*3*) measured a convergence pressure of 7,880 lb./sq. in. abs. and an equilibrium ratio of 11.57.

PREDICTION ACCURACY

Table 1* illustrates the accuracy of prediction compared with experimentally measured values of equilibrium ratios in binary hydrogen-paraffin mixtures. Figures 4 and 6 predict the measured equilibrium ratios with an average arithmetic deviation of 5.9%, a trend of 0.7%, and a statistical deviation (root mean square) of 8.1%, by means of 237 measured values of equilibrium ratios. If the accuracy study is confined to convergence-pressure values over 40,000 lb./sq. in. abs., for twenty-four data points of binary hydrogen-paraffin mixtures the arithmetic-prediction deviation from the experimental values is 6.1% with an 8.1% statistical deviation, an indication that the extrapolation procedure used to identify the high convergence-pressure lines is reasonably satisfactory.

Williams and Katz (*17*) and Likhter and Tikhonovich (*11*) have measured hydrogen equilibrium ratios in binary mixtures of hydrogen with olefins. Figures 4 and 6 predict the experimental results of Williams and Katz for propylene, with an average deviation 12.7% low. For ethylene the predicted results average 14.7% higher than the measurements of Likhter and Tikhonovich, and 2.2% lower than the values of Williams and Katz. Although Figures 4 and 6 were developed for use with paraffins,

*Tabular material has been deposited as document 5302 with the American Documentation Institute, Photoduplication Service, Library of Congress, Washington 25, D. C., and may be obtained for $1.25 for photoprints or 35-mm. microfilm.

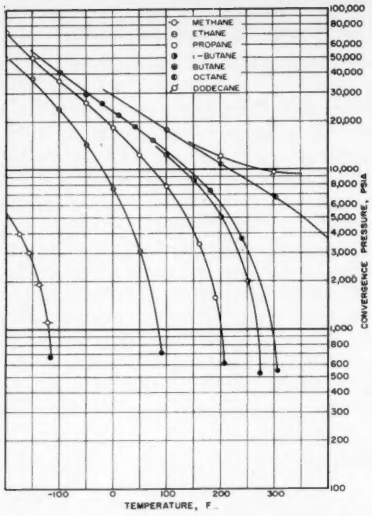

Fig. 5. Critical loci, hydrogen-paraffin mixtures.

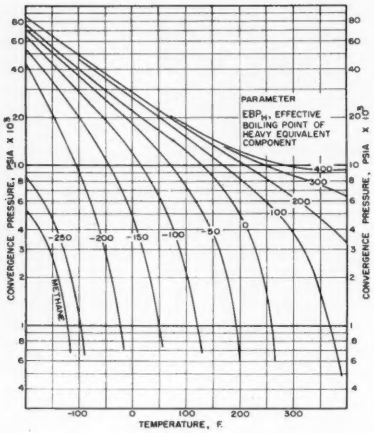

Fig. 6. Critical loci, hydrogen-paraffin mixtures.

they can be used with olefins with possibly somewhat poorer accuracy. The statistical deviation with olefin compounds is 14.2%.

Krichevskii and Efremova (*8*), who measured solubilities of hydrogen in benzene, derived hydrogen equilibrium ratios from these data that are 2.9 times larger than those predicted by Figures 4 and 6. The situation is similar with the hydrogen-benzene data of Gonikberg (*5*) and Inamvez and associates (*7*). Without correction it is unsafe to use this method for mixtures containing large amounts of aromatics.

MULTICOMPONENT SYSTEMS

Figures 4 and 6 are also useful in the prediction of hydrogen equilibrium ratios in multicomponent systems. The primary problem is to ascertain the mixture convergence pressure. This can be done by the use of the equivalent binary concept (*6, 10*). The identity of the two equivalent binary components may be described by their effective boiling points EBP_L and EBP_H and may be computed by a technique of averaging the component composition of the liquid phase (*10*). For ternary and multicomponent mixtures, Table 2 shows computed effective boiling points that identify the equivalent binary. For the systems listed in Table 2 it is safe to assume that the effective boiling point of the equivalent lighter component is the same as the *EBP* value, namely −393°F., of hydrogen itself when the hydrogen content of the liquid phase exceeds 1½%. The values of convergence pressure for systems where the value of EBP_L is greater than −393° are obtained by logarithmically averaging the convergence pressure obtained from Figure 6 and the convergence pressure with methane as the lighter component, obtained from the literature (*6, 10, 13, 16*). When these procedures are used to compute the equilibrium ratios in multicomponent systems, the predicted values deviate from the measured values by an arithmetic average of 11.3% and a statistical deviation of 17.7%. Over all, including binary, ternarys, and multicomponent mixtures, the average arithmetic prediction accuracy is 7.8%, with a statistical deviation of 11.3%, based on 375 measured values.

EFFECT OF HYDROGEN ON HYDROCARBON EQUILIBRIUM RATIOS

The addition of hydrogen to a hydrocarbon liquid phase results in a marked increase in the convergence pressure, with resulting modification of the equilibrium ratios. A small fraction of a mole per cent of hydrogen is often significant. The change in equilibrium ratios of the hydrocarbons can be corrected by the change in convergence pressure. With the correct convergence pressure established, the conventional prediction methods (*12, 13, 15, 16, 18*) may be used to predict the hydrocarbon equilibrium ratios, provided that the liquid phase is predominantly composed of hydrocarbons. Equilibrium ratios for systems where the liquid phase contains more than 10 mole % hydrogen cannot be safely predicted by these methods.

NORMAL BEHAVIOR

The equilibrium ratios of hydrogen have often been thought anomalous in their behavior because the equilibrium ratios decrease with increasing temperature. The reason for this is shown in Figure 6, which illustrates that as the temperature increases the convergence pressure decreases, with resulting decrease in equilibrium ratio. On the basis of the convergence-pressure concept, the behavior of the equilibrium ratios of hydrogen is conventional and fits in with the procedures for correlating hydrocarbon equilibrium ratios in a normal manner.

NOTATION

i = identity of a component
EBP_H = atmospheric-pressure boiling point of the hypothetical heavier component of the binary system having the same convergence pressure as the actual ternary or multicomponent system, *F*
EBP_L = The atmospheric-pressure boiling point of the hypothetical lighter component of the binary system having the same convergence pressure as the actual ternary or multicomponent system, *F*
K = equilibrium ratio, y/x
P = pressure, lb./sq. in. abs.
Pg = convergence pressure
T = temperature, °F.
y = mole fraction, vapor phase
x = mole fraction, liquid phase

LITERATURE CITED

1. Aroyan, H. J., and D. L. Katz, *Ind. Eng. Chem.*, **43**, 185 (1951).
2. Benham, A. L., and D. L. Katz, *A.I.Ch.E. Journal*, **3**, 33 (1957).
3. Burriss, W. L., N. T. Hsu, H. H. Reamer, and B. H. Sage, *Ind. Eng. Chem.*, **45**, 210 (1953).
4. Dean, M. R., and J. W. Tooke, *ibid.*, **38**, 389 (1946).
5. Gonikberg, M. G., *J. Phys. Chem.*, **21**, 745 (1947).
6. Hadden, S. T., *Chem. Eng. Progr. Symposium Ser.* No. 7, **49**, 53 (1953).
7. Inamvez, V. V., V. P. Teodorovich, A. P. Resmovich, and V. C. Armenovich, *J. Phys. Chem. U.S.S.R.*, **22**, 833 (1948).
8. Krichevskii, I. R., and G. D. Efremova, *Zhur. Fiz. Khim. U.S.S.R.*, **22**, 1116 (1948).
9. Lachowicz, S. K., D. M. Newitt, and K. E. Weale, *Trans. Faraday Soc.*, **51**, 1198 (1955).
10. Lenoir, J. M., and G. A. White, *Petroleum Refiner*, **32**, No. 10, 121; No. 12, 115 (1953).
11. Likhter, A. I., and N. P. Tikhonovich, *J. Tech. Phys. U.S.S.R.*, **9**, 1916 (1939); **10**, 1201 (1940).
12. Myers, H. S., and J. M. Lenoir, *Petroleum Refiner*, **36**, No. 2, 157 (1957).
13. Natural Gasoline Association of America, "Equilibrium Ratio Data Book," Tulsa (1955).
14. Nelson, E. E., and W. S. Bonnell, *Ind. Eng. Chem.*, **35**, 204 (1943).
15. Organick, E. I., and G. G. Brown, *Chem. Eng. Progr. Symposium Ser.* No. 2, **48**, 28 (1952).
16. Rzasa, M. J., E. D. Glass, and J. B. Opfell, *Chem. Eng. Progr. Symposium Ser.* No. 2, **48**, 28 (1952).
17. Williams, R. B., and D. L. Katz, *Ind. Eng. Chem.*, **46**, 2512 (1954).
18. Winn, F. W., *Chem. Eng. Progr. Symposium Ser.* No. 2, **48**, 121 (1952).

Two-phase Pressure Drops in Large-diameter Pipes

R. C. REID, A. B. REYNOLDS, A. J. DIGLIO, I. SPIEWAK, and D. H. KLIPSTEIN

Massachusetts Institute of Technology, Oak Ridge, Tennessee

In gas-liquid two-phase flow one may imagine four possible *flow types*: viscous-turbulent, turbulent-viscous, viscous-viscous, and turbulent-turbulent, each being defined by the type of flow in liquid and gas phases respectively. Flow in either phase with Reynolds numbers greater than 2,000 is arbitrarily considered turbulent.

In addition to characterizing flow by the type, it is common to identity it also by some graphic description which defines a *flow pattern*. Flow patterns appear to vary both with mass velocity and with the mass velocity ratios of gas-to-liquid (*1, 2*). Approximately in the order of occurrence, as the ratio of gas-to-liquid flow increases, seven specific flow patterns are observed (*1*):

1. *Bubble flow*: Flow in which bubbles of gas move along the upper part of the pipe at approximately the same velocity as the liquid.
2. *Plug flow*: Flow in which alternate plugs of liquid and gas move along the upper part of the pipe.
3. *Stratified flow*: Flow in which the liquid flows along the bottom of the pipe and the gas flows above, over a smooth liquid-gas interface.
4. *Wavy flow*: Flow which is similar to stratified flow except that the gas moves at a higher velocity and the interface is disturbed by waves traveling in the direction of flow.
5. *Slug flow*: Flow in which a wave is picked up periodically by the more rapidly moving gas to form a frothy slug which passes through a pipe at a much greater velocity than the average liquid velocity.
6. *Annular flow*: Flow in which the liquid forms in a film around the inside wall of the pipe and the gas flows at a high velocity in a central core.
7. *Spray flow*: Flow in which most or nearly all the liquid is entrained as spray by the gas.

Isben, Moen, and Mosher (*4*) have discussed the complex problems of predicting or correlating two-phase pressure drops in pipes. Engineering estimates using correlating methods such as those proposed by Chenoweth and Martin (*3*) and by Lockhart and Martinelli (*6*) are usually satisfactory, but may be improved if additional experimental parameters are included (*2, 4, 5*).

CHENOWETH AND MARTIN CORRELATION

The general correlation proposed by Chenoweth and Martin, shown in Figure 1, is limited to the turbulent-turbulent type of flow and does not specifically include the concept of flow pattern.

The abscissa denotes the superficial liquid-volume fraction and the ordinate represents the ratio of the two-phase pressure drop to a fictitious all-liquid pressure drop, $\Delta P_{TP}/\Delta P_L{}^*$. The calculation of $\Delta P_L{}^*$ is described below. The family of lines on the plot refers to different values of the ratio of the fictitious all-gas to all-liquid pressure drops, $\Delta P_G{}^*/\Delta P_L{}^*$. Each fictitious single-phase pressure drop is calculated from single-phase friction-factor correlations and is based on the *total mass* flow rate of both liquid and gas. Calculating $\Delta P_L{}^*$ requires use of the physical properties of the liquid phase and $\Delta P_G{}^*$, the physical properties of the gas phase.

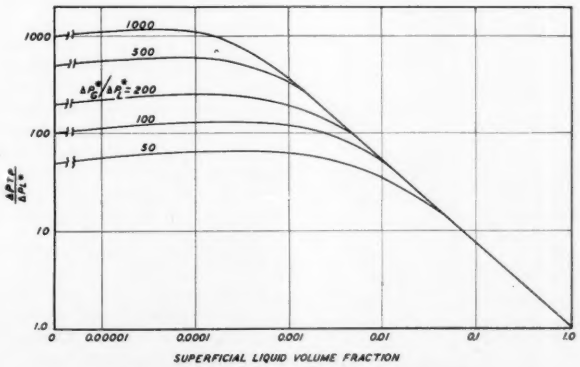

Fig. 1. Chenoweth and Martin correlation.

LOCKHART AND MARTINELLI CORRELATION

In the method proposed by Lockhart and Martinelli (*6*), two-phase pressure-drop data are correlated by plotting log ϕ_G as a function of the parameter, log X. Four different plots are given by Lockhart and Martinelli to cover the four possible flow types. Flow patterns are not specifically considered.

DISCUSSION OF CORRELATIONS

The correlations developed by Lockhart and Martinelli were based on experimental two-phase pressure-drop data taken in small-diameter pipes at pressures up to 50 lb./sq. in. abs. Chenoweth and Martin correlated these data as well as data of their own taken in pipes to 3 in. and at pressures up to 100 lb./sq. in. abs. The low-pressure Chenoweth and Martin data, even in the 3-in. pipe, agreed reasonably well with the Lockhart-Martinelli correlation, but the high-pressure data showed definite deviations, in some cases by as much as 250%. The Chenoweth and Martin correlation, while empirical and applicable only when the flow type is turbulent-turbulent, is reported to apply to most of the applicable experimental two-phase pressure-drop data within ±20 to 30%; the data tested resulted from experiments in pipes from 0.5- to 3.5-in. diam., with pressures varying from atmospheric to 100 lb./sq. in abs., and with fluid-gas systems involving air and water, kerosene, benzene, and diesel oil.

Pressure-drop data for pipe sizes above 3.5 in. are very scarce. Baker (*2*) has presented a few results for gas-oil flow in 4- to 10-in. pipes at pressures around 1,000 lb./sq. in. abs. To extend Baker's results and to determine the validity of the Chenoweth and Martin and Lockhart-Martinelli correlations for low-pressure air-water flow in large-diameter pipes were the purposes of this investigation.

Table 1. Summary of Data and Calculations

Flow rates: Air, std. cu. ft./min.	Flow rates: Water, gal./min.	Pressure drops: ΔP_{TP}, in. H_2O	Pressure drops: ΔP_L, in. H_2O	Pressure drops: ΔP_G†, in. H_2O	P_{system}, lb./sq. in. abs. (avg.)
4-in. pipe					
100	98	21.26	4.68	0.230	21.3
200	100	37.25	4.86	0.780	22.0
300	106	57.14	5.42	1.60	22.2
400	106	71.57	5.42	2.76	21.4
300	103	51.68	5.17	1.63	21.8
100	155	28.86	10.53	0.165	30.2
200	155	45.24	10.53	0.575	29.9
300	155	61.43	10.53	1.20	29.6
400	155	79.95	10.53	2.00	29.8
300	155	67.28	10.53	1.21	29.5
100	198	42.51	15.11	0.200	24.9
150	189	52.26	16.38	0.344	29.8
200	198	87.75	16.38	0.714	24.1
300	198	105.7	16.38	1.47	24.3
400	185	117	14.43	1.94	30.6
6-in. pipe					
100	192	5.85	1.86	0.043	27.1
200	192	8.40	1.86	0.17	27.6
300	192	10.08	1.86	0.36	27.0
400	192	14.62	1.86	0.645	26.9
485	192	15.25	1.86	0.900	27.4
400	192	14.43	1.86	0.630	27.4
100	415	17.48	8.50	0.042	27.9
200	415	23.90	8.50	0.17	27.8
300	432	29.80	8.98	0.35	27.7
400	415	27.90	8.50	0.628	27.7
485	415	33.20	8.50	0.894	27.6
100	398	16.20	8.80	0.046	28.9
200	399	19.80	8.80	0.16	28.8
300	399	24.90	8.80	0.34	28.3
400	398	30.90	8.80	0.595	29.1
455	397	31.60	8.80	0.744	29.1
200	396	22.50	8.80	0.17	28.3
400	396	31.20	8.80	0.627	28.1
100	498	24.0	12.4	0.041	28.8
100	500	23.4	12.4	0.042	28.3
150	500	24.5	12.4	0.094	28.3
200	500	33.2	12.4	0.17	28.2
300	502	41.7	12.4	0.37	26.5
300	500	34.4	12.4	0.33	29.1
400	502	47.2	12.4	0.66	26.4
400	500	47.4	12.4	0.66	26.3
200	495	29.6	12.3	0.17	28.1
400	500	37.4	12.4	0.59	29.6

†Corrected to system pressure by Fanning equation.

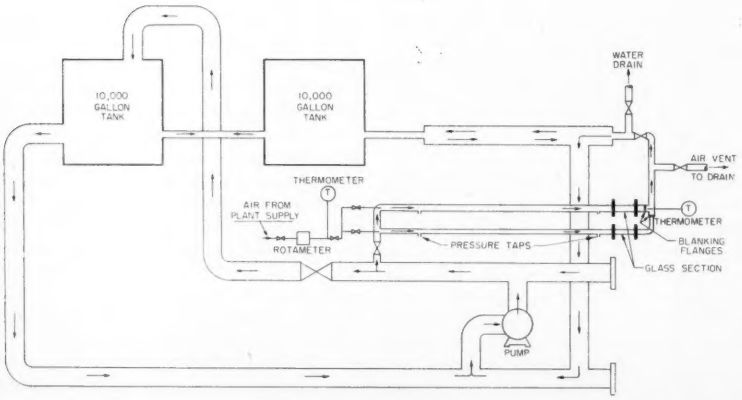

Fig. 2. Flow sheet of system.

EXPERIMENT

To investigate two-phase flow in large pipes, both 4- and 6-in. commercial steel pipes were installed in parallel on a straight horizontal run of 76 ft. A flow sheet of the system is shown in Figure 2. The pipes were interconnected at both ends but provision was made for the insertion of blank flanges at the downstream end to permit the full flow to be directed through each pipe separately. A water supply was connected to the upstream end, and an orifice meter and gate valve were installed in the supply line to measure and control the water-flow rate. Water was circulated through the system and back to surge tanks by a pump. Air, taken from a plant air header, was throttled by a gate valve and measured by a rotameter.

To measure the pressure differential down the length of a pipe, taps were placed along the bottom of each pipe 56 ft. apart, with calming sections of 10 ft. at each end to minimize the effects which bends leading into and away from the pipes might have had on flow within the test section. The pressure differential between the bottom taps was transmitted by water through ⅛-in. copper tubing to a vertical 50-in. manometer containing 2.95 specific gravity Meriam oil. The vertical manometer could be read to the nearest 0.05 in. Snubbers at the manometer terminals dampened the fluctuating pressure of the system, allowing measurement of the average pressure differential; however the snubbers could be by-passed to permit readings with partial or no snubbing. The absolute system pressure was measured by Bourdon-tube (1 to 100 lb./sq. in. gauge) pressure gauges at the first tap of each test section.

Glass sections 12 in. long were installed in the downstream end of each pipe, so that the flow pattern might be observed. Bimetallic thermometers indicated the temperature of the air before it passed to the pipe test sections and the temperature of the two phases as the fluid left the test section. In almost all the experimental runs the temperature of the air and water remained between 20° and 25°C.

In each series of runs the water-flow rate was kept constant and the air-flow rate was increased from 100 to about 500 std. cu. ft./min. Pressure differentials were measured with snubbers in the transmitting lines to damp out any oscillations caused by the slugging flow of the air and water. To ensure that equilibrium was attained with the snubbers in the line, measurements were made only after the manometer level became constant. For each run two pressure differentials were measured and averaged. To indicate the reproducibility of the data, at the end of each series of runs every fourth run of the series was repeated.

Pressure drops resulting from the slight increase in gas volume due to water vaporization or to the increase in momentum of the exit gas stream were estimated and found to be negligible compared to the measured pressure drop.

Single-phase pressure drops were experimentally determined and were compared with values calculated by use of roughness factors of 0.00015 and 0.0015 ft., corresponding to new and old steel pipe. The experimental pressure drops were found to be between the calculated values, an indi-

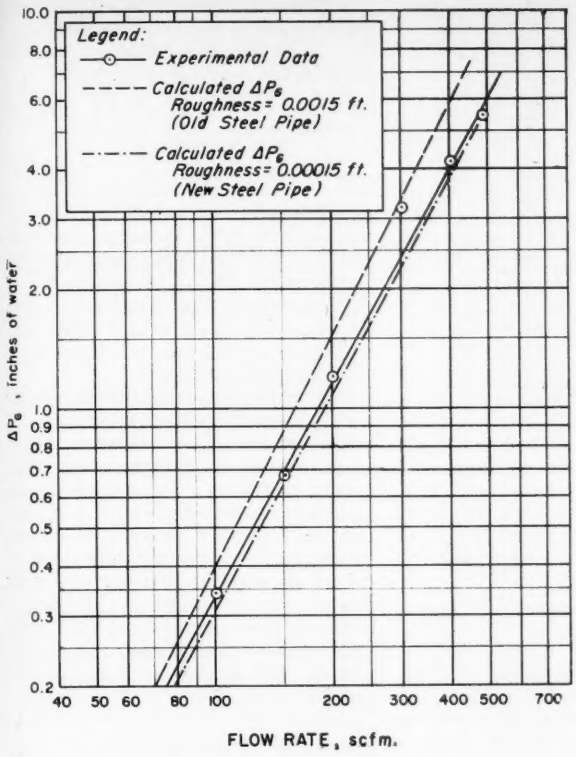
Legend:
Experimental Data
Calculated ΔP_G Roughness = 0.0015 ft. (Old Steel Pipe)
Calculated ΔP_G Roughness = 0.00015 ft. (New Steel Pipe)
ΔP_G, inches of water
FLOW RATE, scfm.

Fig. 3. ΔP_G vs. flow rate, gas phase, 4-in. pipe.
NOTE: Air flow at atmospheric pressure.

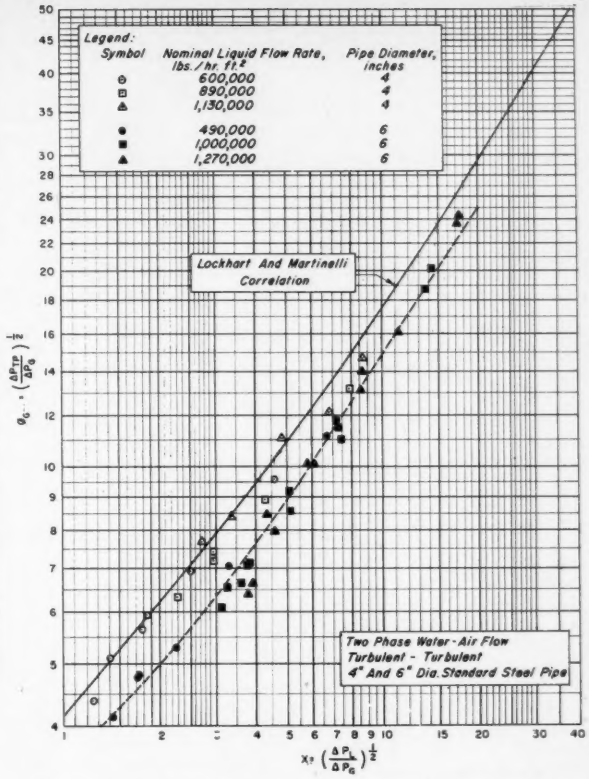

Fig. 4. ϕ_G vs. X for 4- and 6-in.-diam. standard steel pipes.

cation that the roughness of the wall was typical of steel pipe in service. Figure 3 shows the results of one such comparison.

RESULTS AND DISCUSSION OF RESULTS

The experimental data and calculated results are summarized in Table 1. The range of water- and air-flow rates investigated was 100 to 198 gal./min. with 100 to 400 std. cu. ft./min. for the 4-in. pipe and 192 to 500 gal./min. with 100 to 485 std. cu. ft./min. for the 6-in. pipe. With these high flow rates the flow type investigated here was turbulent-turbulent throughout.

A plot of the Lockhart-Martinelli correlation for turbulent-turbulent flow is shown in Figure 4, along with the experimental data taken in the present investigation. The 4-in. data are well represented by the correlation. The 6-in. data fell about 20% below the correlation but on a smooth parallel curve.

Comparison of the experimental data with the Chenoweth and Martin correlation in Figure 5 showed excellent agreement and no noticeable effects of pipe diameter. The family of curves shown in Figure 1 for different values of $\Delta P_G^*/\Delta P_L^*$ are not shown in Figure 5 since at high values of the superficial

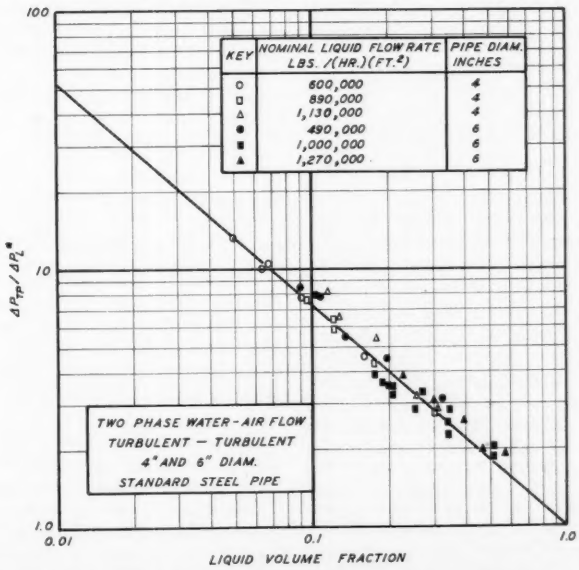

Fig. 5. Turbulent-turbulent two-phase water-air flow in 4- and 6-in.-diam. standard steel pipes.

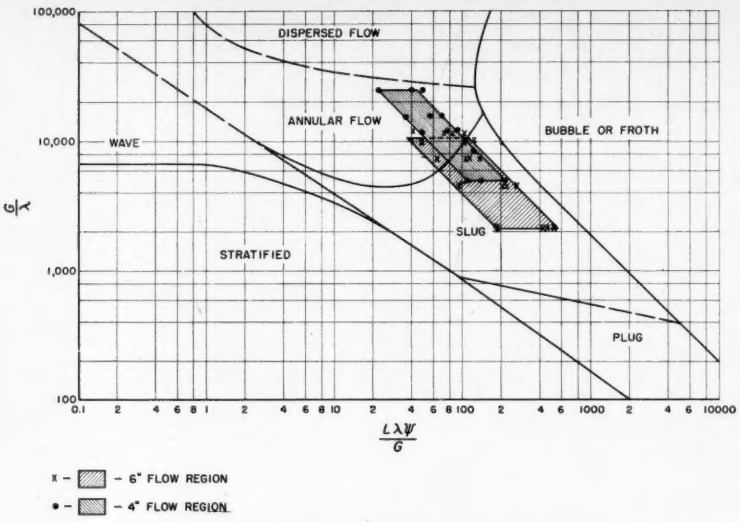

Fig. 6. Baker's correlation for flow-pattern regions.

liquid-volume fraction, all curves converge to a single line. In fact, above a superficial liquid volume fraction of 0.1, i.e., from 10 to 100% liquid, two-phase pressure drops may be estimated as follows:

$$\Delta P_{TP} = \Delta P_L^* \, (LVF)^{-0.86}$$

This relationship becomes especially interesting when it is observed that if one assumes the single-phase friction factor correlating charts to be applicable to two-phase flow problems, and superficial average densities and velocities are employed, one then obtains a similar relation, i.e.,

$$\Delta P_{TP} = \Delta P_L (LVF)^{-1}$$

COMPARISON WITH BAKER'S RESULTS

A comparison of the experimental results reported here with the data reported by Baker (*2*) on large-diameter pipes involves the concept of flow patterns. As noted previously, the flow pattern is believed to be a function of both the mass velocity and the ratio of the mass velocities of the liquid and gas flow. Baker correlates the mass velocity of the gas and the ratio of the mass velocities of the gas and liquid with the various flow-pattern regions. On Figure 6†, which shows Baker's correlation, experimental data points taken during the present investigation are plotted. If Figure 6 correctly defines the flow-pattern regions, the data taken here should be in both the slug and annular regions, although only slug flow was observed visually. The boundaries between patterns in Figure 6 are not definite and represent the average of the transition region between different patterns. Thus the data reported here may be interpreted as being between slug and annular flow.

Baker found that for turbulent-turbulent, two-phase flow in large-diameter pipes the Lockhart-Martinelli correlation requires modification depending upon what flow pattern is present. For the slug-flow region Baker suggested

$$\phi_G = \frac{1190 X^{0.815}}{L^{0.5}}$$

and for the annular flow region

$$\phi_G = (4.8 - 0.3125D) X^{(0.343 - 0.021D)}$$

The largest value of L in the slug-flow region investigated by Baker was 228,000; the minimum used here was 490,000. The data shown on Figure 4 cover a range in L of 490,000 to 1,270,000 and show no noticeable trends due to changes in L.

Baker's annular-flow-pattern correlation predicts that at a constant value of X, ϕ_G decreases as the diameter increases. This prediction agrees with the results reported here, although the use of Baker's equation for values of X much greater than unity yields curves well below the experimental values reported in Table 1. The largest value of X used by Baker for the annular region was 0.694 (8-in. pipe) and the minimum used in the present investigation was 1.2 (4-in. pipe).

CONCLUSIONS

Comparative application of the Lockhart-Martinelli and Chenoweth-Martin correlations indicates that the latter is more reliable in the range of pipe sizes and mass flow rates studied here. Extrapolation of this finding beyond the limits of this investigation, however, cannot be advised in view of the still very incomplete development of flow theory as applied to large pipes.

The comparison of the results of the present investigation with Baker's results may be summarized as follows: the effect of diameter on the pressure drop in the annular-flow-pattern region agrees qualitatively with that predicted by Baker; however, contrary to Baker's conclusions, no effect of liquid-flow rate was noted in the slug-flow region. Baker's data were taken for oil and gas at high pressure and at much lower liquid mass velocities than were the present data and should, perhaps, not be used for a valid comparison.

NOTATION

D = pipe diameter, in.
G = gas flow rate, lb./(hr.)(sq. ft.)
L = liquid flow rate, lb./(hr.)(sq. ft.)
LVF = superficial liquid volume fraction
ΔP_G or ΔP_L = pressure drop, as calculated from single-phase correlations if gas or liquid is flowing alone in pipe at same rate as in two-phase flow
ΔP_G^*, ΔP_L^* = fictitious single-phase pressure drop, as calculated from single-phase correlation if gas or liquid is flowing alone in pipe at the total mass flow rate of both streams. For ΔP_G^* the average physical properties of gas are used; for ΔP_L^* the average physical properties of liquid are used
ΔP_{TP} = two-phase pressure drop
ϕ_G = correlating factor, $(\Delta P_{TP}/\Delta P_G)^{1/2}$
X = correlating factor, $(\Delta P_L/\Delta P_G)^{1/2}$

LITERATURE CITED

1. Alves, G. E., *Chem. Eng. Progr.*, **50**, 449 (1954).
2. Baker, Ovid, *Oil & Gas J. 53*, 185 (1954).
3. Chenoweth, J. M., and M. W. Martin, *Petroleum Refiner*, **34**, 151 (1955).
4. Isben, H. S., R. H. Moen, and D. R. Mosher, *A.E.C.U.*-2994, Dept. of Chem. Eng., Univ. Minn. (November, 1954).
5. Johnson, H. A., and A. H. Abou-Sabe, *Trans. A.S.M.E.*, **74**, 977 (1952).
6. Lockhart, R. W., and R. C. Martinelli, *Chem. Eng. Progr.*, **45**, 39 (1949).

†The Ψ and λ terms are introduced in the correlation to allow for variation in the physical properties of different fluids.
$\Psi = (73/\gamma)/[\mu_L(62.3/\rho_L)^2]^{1/3}$
where ρ_L = density of liquid, lb./cu. ft.
γ = surface tension of liquid, dynes/cm.
μ_L viscosity of liquid, centipoises
$\lambda = [(\rho_G/0.075)(\rho_L/62.3)]^{1/2}$
where ρ_G = density of the gas, lb./cu. ft.

Surface Tension of Acetone-water Solutions Up to Their Normal Boiling Points

KATHERINE S. HOWARD and R. A. McALLISTER

North Carolina State College, Raleigh, North Carolina

The surface tensions against air of acetone-water solutions have been measured over the entire composition range from 20°C. to generally within 1° to 10°C. of the normal boiling points. The capillary-height method was employed and the results are thought to be accurate to better than ±0.5%.

Physical-property data for binary liquid systems up to the boiling points of the solutions are scarce, and the present status of the kinetic theory of liquids is not sufficiently developed to enable accurate predictions to be made over the entire composition and temperature range. One of the aims of Research Project 1, Tray Efficiencies in Distillation Columns, sponsored by the American Institute of Chemical Engineers, has been to determine the effect of the physical properties of the system on the distillation efficiency. The role of the boiling-point surface tension in relation to distillation efficiency, for example, is not well defined. As this lack of understanding can be attributed in part to the scarcity of surface-tension data at the boiling temperatures, one of the purposes of this investigation was to provide accurate surface-tension data up to the boiling point for use in distillation-efficiency correlations.

Morgan and Scarlett (*8*) have measured the surface tension of acetone-water solutions at 0°, 25°, and 45°C. using the drop-weight method. Traube (*13*) reported surface-tension measurements for acetone-water solutions (up to 2.0 mole %) at 15°C. as measured by the capillary-height method. All these data have been tabulated* and will be compared with the present work in the discussion of results below. Using only the data in the literature up to 45°C. would necessitate extrapolations from 11° to 55° to get the boiling-point surface tensions over the entire composition range. The accuracy of such an extrapolation would be doubtful, especially since the accuracy of the data themselves has not been confirmed.

*Tabular material has been deposited as document 5309 with the American Documentation Institute, Photoduplication Service, Library of Congress, Washington 25, D. C., and may be obtained for $1.25 for photoprints or 35-mm. microfilm.

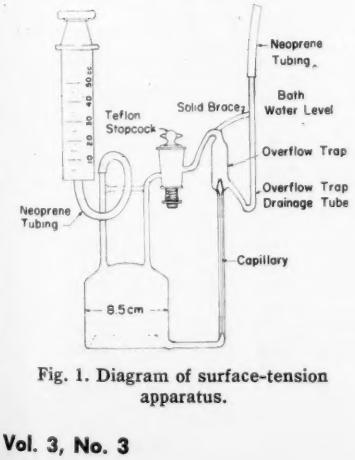

Fig. 1. Diagram of surface-tension apparatus.

EQUIPMENT AND PROCEDURE

Apparatus

Surface-tension Apparatus. The apparatus used for the capillary-height measurement was a modification of the design suggested by Richards and Carver (*10*), incorporating the overflow trap used by Young, Gross, and Harkins (*2*). The apparatus, shown in Figure 1, was constructed of Pyrex and was equipped with a Teflon stopcock. The capillary tube was selected from precision-bore Pyrex capillary tubing, rated as 0.25 ± 0.01 mm. I.D. In the selection of the capillary tube, its diameter was checked by the method described by Harkins (*3*), which involved filling the entire tube with a weighed volume of pure mercury and measuring its length to determine the average radius. The length of a short, weighed bead of mercury, placed at overlapping positions along the capillary, was repeatedly measured to determine any variation in radius caused by nonuniformity of the capillary bore. With this method, a 17-cm. capillary tube was selected having an average radius of 0.01338 cm., a maximum deviation of ±0.4%, and an average deviation of ±0.2%. An 8-cm. section near the center of this capillary had an average radius of 0.01340 cm. with a maximum deviation of ±0.15% and an average deviation of ±0.02%. The capillary was oriented in the apparatus so that this extremely uniform section might be used for all experimental work. After the construction of the apparatus the capillary was recalibrated, as described below, and the radius was found to have changed, probably in the annealing process.

The diameter of the large tube was of sufficient size (8.5 cm.) to avoid any curvature of the large meniscus.

To the large tube-side arm was attached a 50-ml. hypodermic syringe (Becton, Dickinson and Co.) in order to apply slight pressure for rinsing the capillary tube. The syringe connection was made with neoprene tubing which had been washed well with water and acetone. The capillary-tube-side arm was closed with a similar neoprene tube, equipped with a screw clamp.

Support and Lighting. For suspension in the water bath, the glass apparatus was mounted with thermometer clamps on a support constructed of ¼-in. iron. This support had an adjustable slit (13 cm. long; 0–1.5 cm. wide) located just behind the large tube of the surface-tension apparatus. For effective illumination of the large meniscus, a box containing a fluorescent lamp (GE 2A) and equipped with an adjustable slit identical to that of the support was placed behind the apparatus. The light source was mounted with a rack and pinion used for leveling the light slit with the support slit. This lighting method greatly facilitated accurate determination of the position of the large meniscus.

The capillary meniscus was illuminated by a standard adjustable-height microscope lamp (American Optical Co.).

Temperature Control. Accurate temperature control (±0.02°C.) in a 12-gal. water bath was provided by a tungsten-mercury thermoregulator (Fisher Scientific Co. 15-180-5) attached to a combination heater and circulating pump (E. H. Sargent and Co.). Cooling was provided by a seven-coil copper tube attached to a refrigerated water-methanol line. The temperature was measured by a thermometer which was graduated to 0.1°C. and which had been calibrated by the National Bureau of Standards.

Height Measurements. The large meniscus and the capillary meniscus heights were measured with cathetometers. During the early portion of the work a 40-cm. cathetometer, calibrated to 0.01 cm. (Eberbach and Son Co., Inc.) was used; later a 100-cm. cathetometer calibrated to 0.005 mm. (Fisher Scientific Co.) became available.

Solvents

Water. The water used both for calibration purposes and for preparation of acetone-water solutions was daily prepared from once-distilled water (Barnstead still) by redistillation in an all-quartz still, the middle cut (one-third the starting volume) being retained. Such water had a specific conductance of 1×10^{-6} reciprocal ohms and a refractive index, n_D^{25}, of 1.33250, and will be referred to as *conductivity water*.

Acetone. The acetone (Baker analyzed, 99.6% acetone) was analyzed by refractive index and its density was determined (*11*). From these data it was possible to prepare a refractive index vs. concentration curve for 98.0 to 100.0 mole % acetone for accurate determination of the water content (*11*). This analysis indicated that the actual composition of the starting material was 99.54 mole % acetone, 0.45 mole % water. Distillation of the material in a fractional distillation column packed with ⅛-in. I.D.

TABLE 1

SURFACE TENSION OF WATER USED IN THE CALIBRATION

Temperature, °C.	Surface tension,* dynes/cm.
15.00	73.531
20.00	72.800†
25.00	72.018
30.00	71.231
37.78	69.980
45.00	68.790
50.05	67.939
60.11	66.207
70.20	64.401

*With the exception of 20°C., the surface-tension values were calculated by use of the formulas (5)

$\sigma = 75.796 - 0.145t - 0.00024t^2$ (10° to 60°C.) (2)

$\sigma = 75.680 - 0.138t - 0.000356t^2 + 0.00000047t^3$ (3)

where t is in degrees centigrade.
The values calculated by the two formulas agree very closely, and the average of the two values is given in the table.

†Reported by Harkins and Brown (6).

TABLE 2

SURFACE TENSION AND DENSITY OF BENZENE USED IN THE CALIBRATION

Temperature, °C.	Surface tension,* dynes/cm.	Density,† g./cc.
20.00	28.858‡	0.87896
30.00	27.560‡	0.86840
50.05	24.950	0.8467
60.11	23.658	0.8358

*Calculated from the formula (5a)

$\sigma = 31.556 - 0.135t + 0.00006t^2$

†Averages of values compiled by Timmermans (12, p. 145).

‡At 20°C. the accepted value (5), (8), [Richards, T. W., and L. B. Coombs, *J. Am. Chem. Soc.*, **37**, 1656 (1915)] is 28.88 dynes/cm. and 27.61 dynes/cm. at 30°C. [Harkins, W. D., and Y. C. Cheng, *ibid.*, **43**, 35 (1921)]. If these values are used, the calculated radius from the benzene calibration is 0.01332 cm. ±0.2%.

Pyrex helices (packing 1 × 90 cm.) showed a boiling range of 56.1 to 56.2°C. (749 to 750 mm.).

Benzene. The benzene used for calibration purposes was prepared from starting material containing less than 0.02% water (Baker analyzed) having a refractive index (n_D^{25}) of 1.49762. Fractional crystallization was carried out three times, each time one-half the volume being allowed to freeze and this frozen portion retained. The refractive index increased to the value $n_D^{25} = 1.49798$ after the second crystallization and was unchanged by further crystallizations. The average of nine determinations reported by Timmermans (12) for 100% benzene is $n_D^{25} = 1.49800$. Analysis of this purified material for water by Karl-Fischer titration indicated a water content of 0.0146% by weight. This amount of water is probably introduced through handling and transferring of the sample for titration.

Calibration

Water. The apparatus was calibrated with water at 15°, 20°, 25°, 30°, 37.78° (100°F.), 50°, 60°, and 70°C. Conductivity water was distilled directly into the apparatus and its capillary rise was measured after a 45- to 60-min. temperature-equilibration period. (Details of the procedure involved

TABLE 3

SURFACE TENSION AND LIQUID AND VAPOR DENSITIES OF THE ACETONE-WATER SYSTEM

Mole % acetone	Liquid density,* g./cc.	Vapor density,† g./cc. × 10^3	Surface tension, dynes/cm.
15.00°C.			
0	0.9990995	1.203	73.39
0.125	0.99865	1.205	70.00
0.29	0.99805	1.21	67.00
0.60	0.9969	1.2	62.99
1.44	0.9938	1.2	57.33
2.03	0.99155	1.24	54.62
20.00°C.			
0	0.9982053‡	1.19	72.74
2.96	0.9868	1.26	50.80
5.63	0.9775	1.30	41.14
8.86	0.9665	1.34	39.40
14.59	0.9479	1.37	34.62
19.02	0.9338	1.38	32.52
24.95	0.9166	1.39	30.49
30.1	0.9034	1.40	29.40
46.1	0.8654	1.41	27.43
53.4	0.8515	1.41	26.77
60.8	0.8388	1.41	26.20
69.8	0.8252	1.42	25.59
77.5	0.8150	1.43	25.09
89.5	0.8007	1.46	24.17
98.6	0.7912	1.49	23.47
(100)			(23.24)**
25.00°C.			
0	0.9970470‡	1.17	71.94
5.80	0.9745	1.30	42.64
14.59	0.9441	1.39	33.56
24.95	0.9118	1.39	29.70
47.0	0.8587	1.41	26.57
67.7	0.8232	1.45	24.96
89.2	0.7955	1.49	23.42
98.6	0.7857	1.53	22.69
(100)			(22.57)**
37.78°C.			
0	0.9930473‡	1.11	69.91
0.11	0.99255	1.11	66.69
0.34	0.9914	1.1	62.90
0.71	0.9897	1.14	58.80
1.225	0.9874	1.2	55.04
1.54	0.98595	1.18	53.14
2.08	0.98355	1.20	50.54
2.99	0.9797	1.23	47.50
5.86	0.9676	1.32	40.29
14.63	0.9344	1.47	31.78
25.13	0.8997	1.50	27.96
47.3	0.8449	1.52	24.99
68.3	0.8084	1.53	23.25
87.9	0.7819	1.60	21.79
98.3	0.7713	1.68	21.07
(100)			(20.88)**
50.05°C.			
0	0.98802‡	1.02	68.05
0.11	0.9875	1.04	64.98
0.31	0.9864	1.1	61.73
0.635	0.98475	1.08	57.81
1.13	0.9823	1.1	53.58
1.43	0.9808	1.2	51.81
2.00	0.9780	1.2	48.96
2.89	0.9738	1.23	45.81
7.48	0.9532	1.41	36.13
14.20	0.9260	1.56	30.24
24.83	0.8890	1.63	26.64
35.0	0.8600	1.66	25.01
46.2	0.83345	1.68	23.93
60.9	0.8068	1.71	22.71
77.7	0.7805	1.77	21.36
90.2	0.7645	1.85	20.41
99.5	0.7555	1.96	19.60
(100)			(19.57)**

TABLE 3—(Continued)

SURFACE TENSION AND LIQUID AND VAPOR DENSITIES OF THE ACETONE-WATER SYSTEM

Mole % acetone	Liquid density,* g./cc.	Vapor density,† g./cc. × 10^3	Surface tension, dynes/cm.
60.11°C.			
0	0.98315‡	0.98	66.23
2.90	0.9677	1.26	44.44
2.90	0.9677	1.26	44.63
5.69	0.9540	1.44	37.45
11.07	0.9310	1.65	30.93
18.35	0.9022	1.78	27.41
29.4	0.86515	1.84	24.83
30.4	0.86245	1.84	24.63
70.20°C.			
0	0.97766‡	0.91	64.20
0.11	0.9771	0.9	61.83
0.325	0.9757	0.95	58.59
0.60	0.97395	0.99	55.39
1.08	0.9709	1.05	51.21
1.11	0.97075	1.05	51.19
1.45	0.96865	1.09	48.81
1.63	0.96755	1.11	47.77
1.87	0.9661	1.1	46.43
1.94	0.9657	1.1	46.42
2.77	0.9615	1.23	43.51
5.42	0.9486	1.46	36.77

*Thomas (*11*).
†Calculated from the activity coefficients of Brunjes and Bogart (*1*) and the vapor pressures of water (*9*, p. 149) and acetone (*9*, p. 153), on the assumption that the activity coefficients are independent of temperature, that no association occurs in the vapor phase, and that the perfect-gas law holds.
‡Perry (*9*).
**Extrapolated.

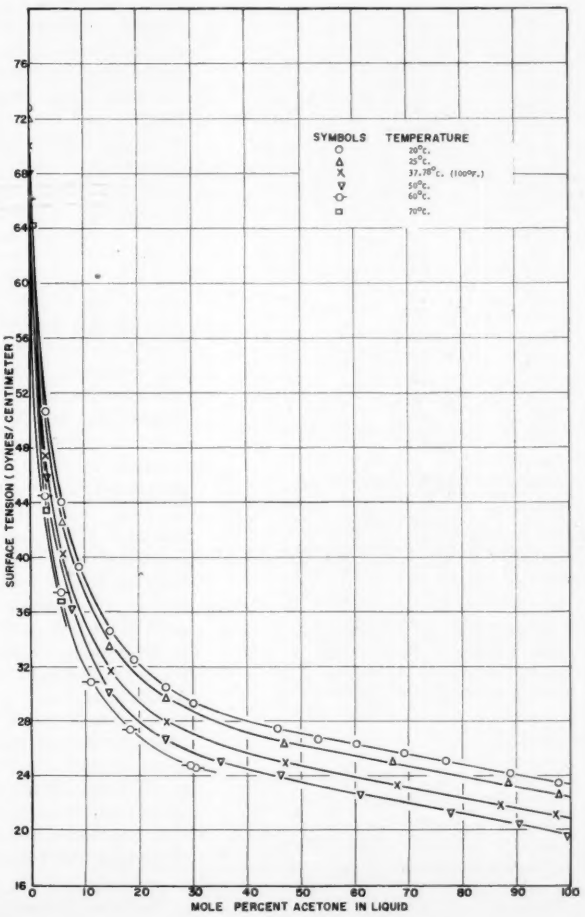

Fig. 2. Surface tension of acetone-water mixtures.

in this measurement are given below.) A minimum of three and a maximum of six determinations were carried out at each temperature. From these capillary-height measurements, the radius of the capillary was calculated by use of the formula

$$\sigma = \tfrac{1}{2} r g h (\rho_L - \rho_v) \qquad (1)$$

where

σ = surface tension, dynes/cm.
r = capillary radius, cm.
h = capillary height, cm.
g = acceleration due to gravity (979.771 cm./sec.^{2} here)
ρ_L = density of the liquid, g./cc.
ρ_v = density of the vapor, g./cc.

The density of water at each temperature required is that reported by Perry (*9*); the vapor densities were calculated from the vapor pressures listed by the same author; and the values used for the surface tension of water are given in Table 1. The average radius from this calibration was found to be 0.01332 cm. ± 0.10%, which is equivalent to a reproducibility of ±0.01 cm. in the capillary-height measurement. This radius was used in all surface-tension calculations.

Benzene. A calibration similar to the one reported with conductivity water was carried out with purified benzene at 20°, 30°, 50°, and 60°C. The values used for the surface tension and density of benzene are given in Table 2. The average radius from this calibration was found to be 0.01331 cm. ± 0.2% and, within experimental error, checked the value obtained from the calibration with water, although the precision was not so good.

Mercury. The average radius was checked by filling the capillary with a weighed sample of pure mercury and measuring its length. The average radius found by this method was 0.01330 cm., and, within experimental error, checked the value found when water and benzene were used for calibration.

Experimental Procedure

Acetone-water solutions were prepared daily from measured volumes of acetone and conductivity water. Their exact concentrations were determined by refractive index.

The procedure for determination of the capillary height was as follows: the sample (about 80 ml.) was introduced through the side arm of the large tube, with the apparatus in place on its support. The 50-ml. syringe was attached, with the plunger about halfway up and the apparatus was submerged in the constant-temperature bath, with the capillary exactly vertical. The Teflon stopcock, which had been lubricated with a *minimum* amount of silicone stopcock grease (Dow Corning), was closed and slight syringe pressure was applied to flush the capillary and to allow a solvent lock to form in the overflow-trap drainage tube. The stopcock was then opened to release pressure, the capillary side arm was closed, and the apparatus was allowed to stand 45 to 60 min. for temperature equilibration. At the end of this period the capillary side arm was opened for the remainder of the run, but a liquid lock was maintained in the overflow drainage tube. (Investigation showed that

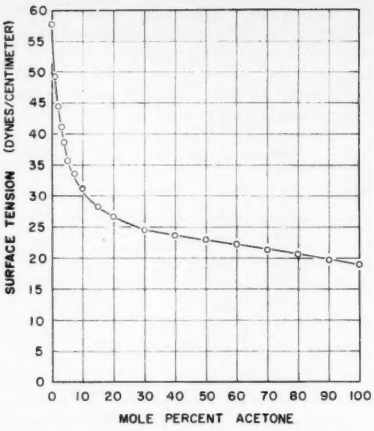

Fig. 3. Surface tension of acetone-water solutions at their normal boiling points.

no measurable difference in capillary height existed between runs, whether the side arm was open or closed, so long as there was no pressure differential between the large meniscus and the capillary meniscus.) The capillary was flushed in the same manner as before to ensure a fresh capillary surface, a minimum of 15 to 20 min. being allowed for the capillary meniscus to fall to rest. The time required for this stabilization was extensively investigated, water, benzene, and acetone-water solutions being used. The meniscus height was found to remain stationary, after a 10-min. stabilization period, for at least 24 hr.

After the stabilization period the positions of the large meniscus and the capillary meniscus were recorded at 10-min. intervals until triplicate identical readings had been obtained. The capillary was then reflushed to obtain a fresh surface and the whole reading procedure was repeated, usually twice. The agreement in capillary height found by three such successive observations (flushing the capillary between each run) was always within ± 0.01 cm. and the differences were rarely greater than ± 0.005 cm. At the completion of the set of runs samples were withdrawn from the large tube for analysis by refractive index. Comparison of the solution analysis before and after such a set of runs showed very little ($< 0.1\%$), if any, change in concentration.

With acetone-water solutions at 60° and 70°C., it was important to flush the capillary with at least 2 cc. of solution in order to obtain reproducible and constant results. Incomplete rinsing resulted in a steadily increasing capillary height at these higher temperatures.

Cleaning. Great care was exercised to provide a scrupulously clean glass surface within the apparatus. The standard cleaning procedure used here involved soaking overnight in chromic acid (concentrated sulfuric acid saturated with potassium dichromate), rinsing eight times with conductivity water, soaking overnight in conductivity water to remove adsorbed chromic acid, and drying in an air oven at 105°C. Prior to the acid treatment the area exposed to stopcock grease was scrubbed with an alkaline detergent solution. This cleaning procedure was carried out at least once a week; between these cleanings the apparatus was rinsed well with conductivity water and dried at 105°C.

Analytical Procedure

All analyses were made by determining the refractive index of the solution and reading the acetone concentration from a standard curve of refractive index vs. mole percentage of acetone. The standard curve was prepared by determining the refractive indexes of solutions which had been prepared by mixing weighed samples of acetone and conductivity water. All weights used in calculating the compositions of the solutions were the corrected vacuum weights. The chain, the rider, and the brass weights used in the analytical balance were checked against National Bureau of Standards calibrated weights, and corrections were noted.

The curve* for refractive index vs. acetone concentration has a maximum at 40 to 42 mole % acetone, and for this reason refractive index alone is not a suitable analysis in the region of 35 to 45 mole % acetone.

Table 4
Surface Tensions of Acetone-Water Solutions at Their Normal Boiling Points

Mole % acetone	Boiling point, °C.*	Surface tension, dynes/cm.
0	100.00	57.85
0.2	98.53	56.02
0.4	97.10	53.77
0.6	95.70	51.84
0.8	94.33	50.08
1.0	92.99	48.83
1.2	91.64	47.71
1.4	90.30	46.39
1.6	89.00	45.58
1.8	87.74	44.74
2.0	86.50	43.97
3.0	81.32	41.37
4.0	77.60	39.28
5.0	75.00	37.13
7.5	70.20	33.60
10.0	66.72	30.03
15.0	63.4	28.39
20.0	62.2	26.61
30.0	61.0	24.62
40.0	60.4	23.62
50.0	59.8	22.98
60.0	59.3	22.23
70.0	58.8	21.46
80.0	58.2	20.67
90.0	57.4	19.89
100.0	56.2	18.98

*These temperatures were obtained from the data of Brunjes and Bogart (*1*), D. F. Othmer and R. F. Benenati [*Ind. Eng. Chem.*, **37**, 299 (1945)] and J. C. Chu ["Distillation Equilibrium Data," Reinhold Publishing Corporation, New York (1950), p. 24]. More weight was given to the data of Brunjes and Bogart, since they showed more internal consistency.

RESULTS

The measured surface tension of the acetone-water system at various temperatures is shown in Table 3. These values were calculated from the capillary-height measurements by use of formula 1. The vapor and liquid densities of each solution are also given. The surface-tension results are shown graphically in Figure 2.

From the data of Table 3 the surface-tension-vs.-temperature curve was prepared and extrapolated to the normal boiling point. In no case was the extrapolation range greater than 23°C.; it averaged 8°C. Table 4 gives the surface-tension values at the normal boiling point, together with the boiling temperatures. The boiling-point surface tensions are shown in Figure 3.

DISCUSSION

The surface tensions of acetone-water solutions reported here have been compared* with those determined by Morgan and Scarlett (*8*). The comparison indicates that Morgan and Scarlett's data average 1.5% higher than those of the authors. The "100%" acetone which they used was characterized as $d_4^{20} = 0.79170$. By the method described by Thomas (*11*), this density corresponds to 98.16 mole % acetone, on the assumption that the only contaminant in the sample was water. On this basis Morgan and Scarlett's weight percentage figures were converted to mole percentage and a correction was made for the water content of the acetone used. In addition, erroneous assumptions regarding the relationship between the observed and the ideal drop weights were made by Morgan and Scarlett in the calculation of surface tension from the experimental data. Young and Harkins (*14*) attempted to correct these errors in 1928, but since no accurate measurements of the densities of acetone-water mixtures were available, these recalculations are not currently valid. With regard for all these factors, the data of Morgan and Scarlett were recalculated by use of the drop-weight corrections of Young and Harkins and recent accurate determinations by Thomas (*11*) of the densities of acetone-water solutions.

As an example of other errors which might be involved, Morgan and Scarlett suspended the drops for 5 min. before allowing them to fall. Harkins later indicated (*7*), however, that it is often necessary to lengthen the time of suspension of drops of volatile liquids where one component adsorbs preferentially in the surface. In the case of acetone-water, if the drop falls before surface adsorption of acetone is at its equilibrium value, there will be excess water in the surface layer and the resulting surface tension will be artificially high. Since Morgan and Scarlett's data appear to be high, the foregoing discussion is offered as a possible explanation.

A comparison* of the surface tensions of acetone-water solutions at 15°C. with

*See footnote on page 325.

*See footnote on page 325.

those reported by Traube (*13*) shows that the latter's data are an average of 0.6% higher than those reported here. Two factors may contribute to this difference. Probably the concentrations Traube reports are slightly in error, because of his failure to use anhydrous acetone. The density of the material he started with is not reported and thus the water content cannot be estimated by the method described previously (*11*). The presence of only a trace quantity of water in the starting acetone would make his reported compositions high. Correction of this effect would bring his data into better agreement with those reported here. Considering the refinements in technique which have occurred since 1891, the agreement of the Traube data is excellent.

ACKNOWLEDGMENT

This work was carried out in connection with Research Project 1, Tray Efficiencies in Distillation Columns, sponsored by the American Institute of Chemical Engineers. The authors gratefully acknowledge the support and encouragement of the A.I.Ch.E. Research Committee during the course of this investigation.

They are also indebted to D. E. Sampson of the University of North Carolina for the construction of the apparatus and to D. G. Bethune, Department of Chemical Engineering, North Caroline State College, for the benzene analyses.

LITERATURE CITED

1. Brunjes, A. S., and M. J. P. Bogart, *Ind. Eng. Chem.*, **35**, 258 (1948).
2. Harkins, W. D., "Technique of Organic Chemistry," (A. Weissberger, ed.), vol. I, Part 1, 2 ed., p. 366, Interscience Publishers, Inc., New York (1949).
3. *Ibid.*, p. 368.
4. *Ibid.*, p. 374.
5. (a) Harkins, W. D., "Physical Chemistry of Surface Films," p. 79, Reinhold Publishing Corporation, New York (1949).
   (b) Reference *2*, p. 369.
6. ———, and F. E. Brown, *J. Am. Chem. Soc.*, **41**, 499 (1919).
7. Harkins, H. N., and W. D. Harkins, *J. Clin. Investigations*, **7**, 263 (1929).
8. Morgan, J. L. R., and A. J. Scarlett, Jr., *J. Am. Chem. Soc.*, **39**, 2275 (1917).
9. Perry, J. H., "Chemical Engineers' Handbook," 3 ed., p. 175, McGraw-Hill Book Company, Inc., New York (1950).
10. Richards, T. W., and E. K. Carver, *J. Am. Chem. Soc.*, **43**, 827 (1921).
11. Thomas, K. T., and R. A. McAllister, *A.I.Ch.E. Journal*, **3**, 161 (1947).
12. Timmermans, J., "Physico-Chemical Constants of Pure Organic Compounds," p. 147, Elsevier Publishing Company, New York (1950).
13. Traube, J., *Ann. Chem. Justus Liebigs*, **265**, 27 (1891).
14. Young, T. F., and W. D. Harkins, in "International Critical Tables," vol. IV, p. 467, McGraw-Hill Book Company, Inc., New York (1928).

Simple Theory of an Idealized Turbulent Mixer

STANLEY CORRSIN

The Johns Hopkins University, Baltimore, Maryland

With stationary isotropic turbulence postulated, the rate of decrease in concentration fluctuations of a scalar contaminant is estimated in terms of the turbulence scale and the power input to the system.

One of the simplest statistical measures of nonuniformity in a fluid mixer is the mean-square fluctuation in concentration.

A differential equation for $\overline{\gamma^2}(t)$ of a homogeneous field (i.e., all statistical functions invariant to translation) is obtained by multiplying the material conservation equation

$$\frac{\partial \gamma}{\partial t} + u_k \frac{\partial \gamma}{\partial x_k} = D\nabla^2\gamma \qquad (1)$$

(where u_k is turbulent velocity, and D is diffusivity by γ) and averaging. With homogeneity, this yields (*1*)

$$\frac{d\overline{\gamma^2}}{dt} = -2D\overline{\left(\frac{\partial \gamma}{\partial x_i}\right)\left(\frac{\partial \gamma}{\partial x_i}\right)} \qquad (2)$$

If restricted further to isotropic fields (i.e., all statistical functions invariant to rotation), the three mean-square derivatives can be characterized by a single length, analogous to G. I. Taylor's "microscale" of turbulence:

$$\overline{\left(\frac{\partial \gamma}{\partial x_i}\right)\left(\frac{\partial \gamma}{\partial x_i}\right)} = 6\frac{\overline{\gamma^2}}{l^2} \qquad (3)$$

which is the definition of $l(t)$.
Now

$$\frac{d\overline{\gamma^2}}{dt} = -12D\frac{\overline{\gamma^2}}{l^2} \qquad (4)$$

still an indeterminate equation since it has two unknown functions.

The time history of $\overline{\gamma^2}$, and indeed of considerably more detailed functions, has been studied both theoretically and experimentally in the case of turbulence which is "decaying," i.e., dying out by viscous dissipation at the same time as it mixes the scalar contaminant. From a practical viewpoint it seems of interest to carry out a simple analysis under the postulate that the turbulent motion is statistically stationary in time.

In fact it is well known that isotropy and stationariness are contradictory specifications for a turbulent motion; an isotropic turbulence has a continuous viscous loss of kinetic energy to internal energy, with no balancing supply of energy from mean motion. A turbulence which receives energy from a mean flow field cannot be isotropic. Nevertheless, the postulate is used here primarily for the *small* structure of the fluctuation fields [for the derivatives, as in Equation (3)], and the requisite condition of "local isotropy" has been reasonably well confirmed by experiment (*2, 3*) since its original proposal by Kolmogoroff (*4*).

Before introduction of any postulate other than local isotropy, (4) may be schematically integrated:

$$\overline{\gamma^2}(t) = \overline{\gamma_0{}^2}\exp\left\{-12D\int_0^t \frac{dt_1}{l^2(t_1)}\right\} \qquad (5)$$

RESTRICTION TO STATIONARY TURBULENCE

Characteristic Reynolds and Péclet numbers of the fields are

$$R_\lambda \equiv \frac{1}{\sqrt{3}}\frac{q'\lambda}{\nu}\,; \quad P_l \equiv \frac{1}{\sqrt{3}}\frac{q'l}{D} \qquad (6)^*$$

where q' is the root-mean-square resultant velocity fluctuation and λ is the dissipation scale of the turbulence, the Taylor microscale (*5*).

With sufficiently high R_λ and P_l and approximately equal large structures for the two fields, two different rough theoretical analyses (*1, 6, 7*) have predicted

$$\frac{l^2}{\lambda^2} \approx 2\frac{D}{\nu} \qquad (7)$$

*The $\sqrt{3}$ factor is included to be consistent with the isotropic form $R_\lambda = u'\lambda/\nu$.

An implied restriction in both theories is that the fluctuation decay rates are not sufficiently rapid to have influenced the form of power spectra (or correlation functions). In the present analysis, if it is now restricted to stationary turbulence, this suggests that (7) may not be valid for very large D/ν. In any case Equation (7) has received approximate experimental confirmation in the mixing of warm air behind a grid spanning a uniform wind-tunnel flow (7). It is hoped that these measurements will be done in water too.

With stationary turbulence, λ = constant, and so (7) gives l = constant and (5) reduces to

$$\overline{\gamma^2}(t) = \overline{\gamma_0^2} e^{-12(Dt/l^2)} \tag{8}$$

The time constant of this exponential approach to uniformity is

$$\tau = \frac{l^2}{12D} \tag{9}$$

When (7) applies, τ is expressible entirely in terms of the turbulence:

$$\tau = \frac{\lambda^2}{6\nu} \tag{10}$$

APPLICATION TO A MIXER

In isotropic turbulence Taylor showed that the rate of dissipation of turbulent kinetic energy per unit mass is (5)

$$\Phi = 10\nu \frac{\overline{u^2}}{\lambda^2} \tag{11}$$

For turbulence that is locally isotropic but not fully isotropic, it is prudent to replace (11) with

$$\Phi \approx \frac{10}{3} \nu \frac{\overline{q^2}}{\lambda^2} \tag{12}$$

To maintain a steady state, the mixing device must supply energy to the fluid at this rate. If η is the efficiency of the mixing device (e.g., a paddle propeller), the total power input is

$$P = \frac{10}{3} \eta M \nu \frac{\overline{q^2}}{\lambda^2} \tag{13}$$

where M is the mass of fluid.

In isotropic turbulence at large Reynolds number von Kármán and Howarth (8) deduced the approximate relation between dissipative scale λ and integral scale L

$$\frac{\lambda}{L} \sim \frac{1}{R_\lambda} \tag{14}$$

In locally isotropic, stationary, shear turbulence this form can be inferred by equating the turbulent production and dissipation rates.

Introducing an empirical constant of proportionality gives

$$\frac{\lambda}{L} \approx \frac{A}{R_\lambda} \tag{15}$$

or

$$q' \approx \frac{\sqrt{3} A L \nu}{\lambda^2} \tag{15a}$$

With (13) and (15a), τ can be expressed in terms of quantities more directly related to the mixer L and P:

$$\tau \approx \left\{ \frac{\eta A^2}{21.6} \frac{ML^2}{P} \right\}^{1/3} \tag{16}$$

$$\overline{\gamma^2}(t) \approx \overline{\gamma_0^2} e^{-t/\tau} \tag{17}$$

From turbulence measurements in the approximately isotropic turbulence behind grids, (10)

$$A \approx 20$$

The mixer efficiency η will doubtless vary considerably with geometry and does not appear to have been measured in practical installations. Appropriate measurements for grid-generated turbulence in a wind tunnel would be the static pressure drop across the grid and the turbulent-energy–dissipation rate close behind. These also seem to be unavailable. But the efficiency of a fully developed pipe flow as turbulence generator is given by the data of Laufer (9). He finds that the mean-flow kinetic energy (generated by static pressure-gradient work) is "dissipated" about half to internal energy directly and half to turbulent kinetic energy (which also eventually becomes internal energy). Laufer's results appear to be a very insensitive function of Reynolds number, especially at large Reynolds number, and so this dependence is neglected in the present crude estimate. Thus, for want of more applicable empirical information, one takes

$$\eta \approx 0.5$$

so that

$$\overline{\gamma^2}(t) \approx \overline{\gamma_0^2} \cdot \exp\left\{ -3.3 \left(\frac{ML^2}{P} \right)^{1/3} \cdot t \right\} \tag{18}$$

SCALING

Equation (16) provides simple scaling information for geometrically similar mixers at large Reynolds numbers.

An illustration is the determination of how much power is required to keep the same mixing time when the size is increased or decreased by a length factor K. The density is taken as constant. It has been found that the integral scale of turbulence is closely proportional to flow-system dimensions and independent of Reynolds number (10); hence

$$L' = KL \quad \text{and} \quad M' = K^3 M \tag{19}$$

Therefore, according to Equation (16), $\tau' = \tau$ is achieved with

$$P' = K^5 P \tag{20}$$

For $K > 1$ this considerable power requirement stems physically not only from the mass increase, but also from the need to increase q'. Equation (20) requires that both η and A be constant but is, of course, independent of the actual numerical values suggested in the previous section.

Equation (20) is not completely comparable with the results of direct dimensional reasoning on gross mixer properties by Kramers, Baars, and Knoll (11), because the angular speed of the stirrer appears explicitly. If, however, this is kept constant during scaling, the expression developed by them coincides with (20).

The combined dimensional reasoning and empirical approach of van de Vusse (12) apparently leads to $P' = K^{4.17} P$.

NOTATION

$\Gamma(x, y, z, t)$ = concentration

$\overline{\Gamma}$ = mean concentration, a constant when the field is statistically homogeneous in space

$\gamma(x, y, z, t) \equiv \Gamma - \overline{\Gamma}$ = concentration fluctuation

$\overline{\gamma^2}(t)$ = mean-square concentration fluctuation

ACKNOWLEDGMENT

This work was supported by Mechanics Branch, U. S. Office of Naval Research.

LITERATURE CITED

1. Corrsin, Stanley, *J. Aeronaut. Sci.*, **18**, No. 6 (June, 1951).
2. Townsend, A. A., *Proc. Cambridge Phil. Soc.*, **44**, 560 (1948).
3. Corrsin, Stanley, *J. Aeronaut. Sci.*, **16**, (December, 1949).
4. Kolmogoroff, A. N., *Comp. rend. acad. sci. U. R. S. S.* (*Doklady*), **30**, 4 (1941).
5. Batchelor, G. K., "The Theory of Homogeneous Turbulence," Cambridge Univ. Press (1953).
6. Corrsin, Stanley, *J. Appl. Phys.*, **22**, 4 (1951).
7. Kistler, A. L., Vivian O'Brien, and Stanley Corrsin, *Natl. Advisory Comm., Aeronaut. Research. Memo* 54D19 (June, 1954).
8. von Kármán, Theodore, and Leslie Howarth, *Proc. Roy. Soc.* (*London*), **A164**, 917 (January, 1938).
9. Laufer, John, *Natl. Advisory Comm. Aeronaut., Rep.* 1174 (1955).
10. Corrsin, Stanley, A.E. thesis, Calif. Inst. Technol. (1942).
11. Kramers, H., G. M. Baars, and W. H. Knoll, *Chem. Eng. Sci.*, **2**, 1 (1953).
12. van de Vusse, J. G., *ibid.*, **4**, Chap. 4 and 5, especially section 4.2 (1955).

Effect of Water Vapor on the Catalytic Oxidation of Nitric Oxide

OMER KIRCHER and O. A. HOUGEN

University of Wisconsin, Madison, Wisconsin

Extension of the kinetics of the catalytic oxidation of nitric oxide on activated carbon and silica gel confirms the rate-controlling step postulated by previous workers. The effect of variables including water vapor on the reaction rate is expressed by an equation containing the constants *a*, *b*, *c*, and *w*, which have been evaluated for both catalysts at 30°, 45°, and 60°C. The effect of water vapor is to reduce the reaction by reversible adsorption on the active sites of the catalyst. The value of *w* is dependent on temperature but independent of water-vapor concentration up to a relative humidity of 20%. Above 20% the value of *w* for activated carbon increases greatly with relative humidity, in agreement with the effect of capillary adsorption at high water contents.

In the Wisconsin process for nitrogen fixation, ambient air is heated to about 2,500°K. in a reversing pebble-bed furnace (*4*). At this temperature nitrogen and oxygen combine to form nitric oxide. The heat of reaction and heat losses are supplied by the combustion of an admixed fuel gas, and the resultant gaseous product contains about 2% nitric oxide along with the combustion products, including water vapor.

The nitric oxide is further oxidized to nitrogen dioxide by passing the gases through a fixed bed of silica gel or activated carbon. Water vapor, however, retards the catalytic rate of this secondary oxidation and thus reduces the capacity of the reactor. A rate equation for the catalytic oxidation of nitric oxide in a flow system having been previously established (*1*, *7*) in terms of pressure, temperature, and gas composition by use of silica gel and activated-carbon catalysts in a fixed bed, the purpose of the present investigation was to determine quantitatively the effect of water vapor on the kinetics of this same catalyzed reaction in order to decide how much water vapor it is economical to remove before the gas passes into the secondary reactor.

PREVIOUS WORK

Previous work on the catalytic oxidation of nitric oxide was carried out by Baker, Wong, and Hougen (*1*) and Rao and Hougen (*7*), who found that the apparent rate-controlling chemical step in the catalytic oxidation was a surface reaction between molecular oxygen in the gas phase and an adsorbed complex of nitric oxide. The catalytic reaction was postulated to occur through the following sequence of steps:

1. equilibrium formation of a nitric oxide dimer in the gas phase

$$2NO \rightleftarrows (NO)_2$$

2. equilibrium activated adsorption of the nitric oxide dimer

$$(NO)_{2(gas)} + (\text{active site}) \rightleftarrows (NO)_{2(ads)}$$

3. surface reaction between the adsorbed dimer and oxygen in the gas phase (This is the rate-controlling step.)

$$(NO)_{2(ads)} + O_{2(gas)} \rightleftarrows NO_{2(ads)} + NO_{2(gas)}$$

4. equilibrium desorption of nitrogen dioxide

$$NO_{2(ads)} \rightleftarrows NO_{2(gas)} + (\text{active site})$$

According to this postulation, the rate equation is expressed as follows:

$$r = \frac{p_{NO}^2 p_{O_2}}{a + b p_{NO}^2 + c p_{NO_2}} \qquad (1)$$

The kinetics of the homogeneous reaction has been investigated by Bodenstein (*3*), Hasche and Patrick (*5*), Trautz (*8*), and Treacy and Daniels (*9*). The last investigators postulated that the rate-controlling step was the reaction $NO_3 + NO \rightleftarrows 2NO_2$, where NO_3 was an intermediate complex resulting from the equilibrium oxidation of nitric oxide. Trautz first proposed that $(NO)_2$ was the intermediate complex. Either postulation accounts for the negative temperature coefficient of the over-all homogeneous reaction velocity constant based on a third order reaction rate equation.

$$2NO_{(gas)} + O_{2(gas)} \rightleftarrows 2NO_{2(gas)} \qquad (2)$$

$$r_H = k_H p_{NO}^2 p_{O_2}$$

Since the rate of homogeneous reaction at all degrees of conversion is small relative to the reaction rate catalyzed by silica gel and negligible with activated carbon, the exact form of the homogeneous rate equation is not essential when it is used in correcting the total reaction rate to obtain the catalytic reaction rate; hence, the simple third-order equation was used for the homogeneous reaction. The constant k_H in the third-order equation (2) was determined by Hasche and Patrick (*5*) and by Rao (*7*).

	30°C.	45°C.	60°C.
(*5*)	3,733	3,420	3,140
(*7*)	4,413	4,068	3,408

In this study the values obtained by Rao were used, as they were obtained on the same experimental equipment as was used in this investigation.

EXPERIMENTAL EQUIPMENT AND PROCEDURES

The experimental equipment was adapted from that used by Rao in his study of the catalytic oxidation of nitric oxide under essentially dry conditions (*7*). The principal modifications were the addition of equipment for introducing, controlling, and measuring the amount of water vapor in the feed. A photograph of the equipment is shown in Figure 1 and a flow chart in Figure 2.

The experimental reactor was of the series-integral type. This type is particularly advantageous in kinetic studies where available methods of analysis are not sufficiently accurate to permit the use of a differential-type reactor, and it has the additional advantage of permitting several simultaneous analyses to be made at several points in the reactor under the same constant conditions of entering feed. Constants in the rate equation were thus obtained from an integrated equation rather than by graphical differentiation.

The reactor consisted of four sections of ¾-in. stainless steel pipe each 6 in. long. Valves permitted by-passing the gas stream from any section directly to the outlet manifold. Control of the reactor pressure was maintained by a needle valve on the outlet manifold. The reactor assembly was immersed in a controlled-temperature bath to maintain nearly isothermal reaction conditions. The inlet air was measured by a calibrated orifice meter and the nitric oxide feed by a calibrated Fischer-Porter Flowrator.

The content of water vapor in the feed was controlled by bubbling a portion of the feed air through a column of water. The air streams were then recombined and the dew point was determined by use of a continuously recording dew-point hygrometer. The hygrometer used in the present work was constructed by Bickling (*2*).

The photometric analyzer used for the analysis of gases containing nitrogen dioxide was similar to that used in many other studies. It consisted of a Pyrex tube

Omer Kircher is at present with Continental Oil Company, Ponca City, Oklahoma

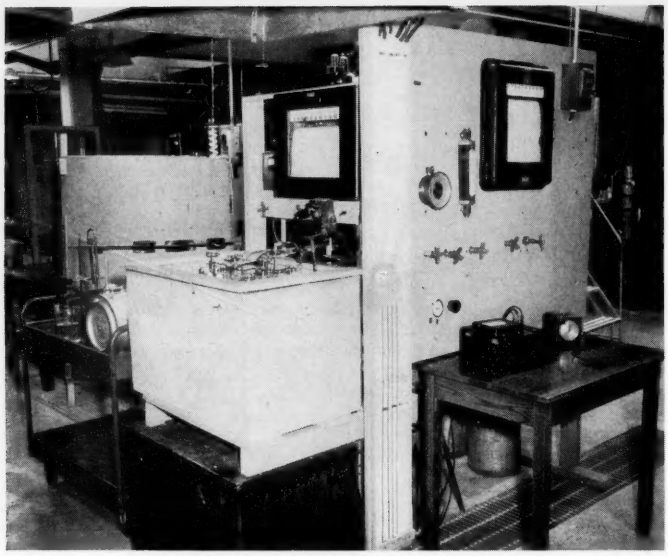

Fig. 1. Experimental equipment.

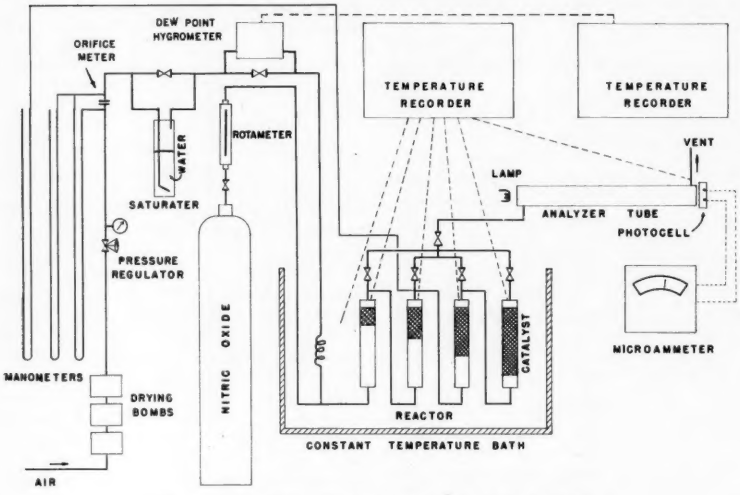

Fig. 2. Flow sheet, catalytic oxidation of nitric oxide.

1½ in. in diameter and 18 in. in length with flat ends. Outlets were located in the wall of the tube approximately ½ in. from each end.

The light source was an ordinary flashlight reflector powered by a 5-cell Edison battery. An ammeter and variable resistance in the lamp circuit permitted regulation of the light intensity. The light was filtered through a mixed solution of 2.5N calcium chloride and 0.4N copper chloride. This solution transmits light in the range of wave lengths from 460 to 600 mμ. Light of this frequency is absorbed by nitrogen dioxide but not by nitric oxide or nitrogen tetroxide. A barrier-layer type of photocell mounted opposite the light source permitted measurement of the intensity of the light passing through the tube.

The analyzer was calibrated by passing a carefully measured flow of air and nitric oxide over sufficient activated-carbon catalyst to give complete conversion (above 99%). From the established composition of the gas in the analyzer a series of points was obtained by varying the total pressure in the photometric cell. Several duplicate calibrations gave excellent agreement with points falling on the same line. During the experimental runs the entire flow from the reactor was passed continuously through the analyzer as a rapid, convenient, and continuous means of monitoring the product composition.

The nitric oxide used in these experiments was obtained from the Matheson Company in steel cylinders initially at 480 lb./sq. in. Compressed air was the source of oxygen.

The activated-carbon catalyst was Columbia activated carbon, grade CXA, obtained from the Carbide and Carbon Chemicals Company. The carbon was crushed and screened to 11 to 20 mesh before use and had a bulk density of 0.48 g./cc. The silica-gel catalyst, consisting of a 16- to 20-mesh granular gel with a bulk density of 0.69 g./cc., was obtained from the Davison Chemical Company. Both catalysts were dried for 1 hr. at 120°C. before being weighed and loaded into the reactor.

During the experimental work flow rates, pressure, temperature, and dew point of the feed were adjusted according to a predetermined experimental schedule and the system was allowed to reach steady state conditions before data were recorded.

Steady state conditions were assumed when no changes occurred in operating conditions and in fraction conversion after several hours of operation. Several identical pairs of runs preceded alternately by a run made at a higher partial pressure of water vapor and one at a lower partial pressure eliminated the uncertainty of nonequilibrium adsorption or of moving-band adsorption; furthermore the fact that there was no change in catalyst activity with either silica gel or activated carbon was established by periodically repeating a standard run. Flow rates of reactants, reaction temperature, reaction pressure, and dew point of the feed air were recorded. Analyses of the reacting gases were made at four points in the reactor by successively by-passing each section of the reactor, starting with the last section.

In the calculation of conversion it was necessary to take into account the equilibrium between nitrogen dioxide and nitrogen tetroxide and also to correct for the extent of the homogeneous reaction which occurred in the sampling lines and in the photometric analyzer cell. The extent of conversion in the free space of the reactor itself and in the prereactor space was found to be negligible. The homogeneous rate equation may be integrated to give the following equation if total moles and mole fraction of oxygen are assumed to be constant. This assumption is good for the low concentrations of nitric oxide used in this study. The complete data are presented in the thesis of Kircher (*6*).

$$F_t\, dy_{NO} = -r_H\, dV$$

$$\frac{V}{F_t} = \frac{1}{k_H \pi^3 y_{O_2(avg)}} \left[\frac{1}{y_{NO}''} - \frac{1}{y_{NO}'} \right] \quad (3)$$

REEVALUATION OF THE RATE CONTROLLING CHEMICAL STEP

The rate-controlling chemical step of the catalytic oxidation of nitric oxide has been reported by previous investigators as mentioned above. In order to confirm these decisions, a series of experiments was made with the dew point of the feed-gas stream below −25°C. Rates of reaction were determined by graphical differentiation of plots of conversion vs. catalyst-to-feed ratio.

As an academic exercise the rate-controlling chemical step was selected from sixty-seven postulated rate equations. A few of these equations were formally identical, and others could be eliminated by inspection of the experimental data. The remaining equations, of

which there were thirty-three, were tested by a least squares fit of the data. In most cases this calculation produced one or more negative coefficients. Since

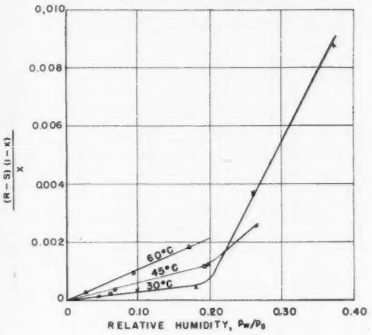

Fig. 3. Water-vapor adsorption term; catalyst, activated carbon; × 30°C., ○ 45°C., △ 60°C.

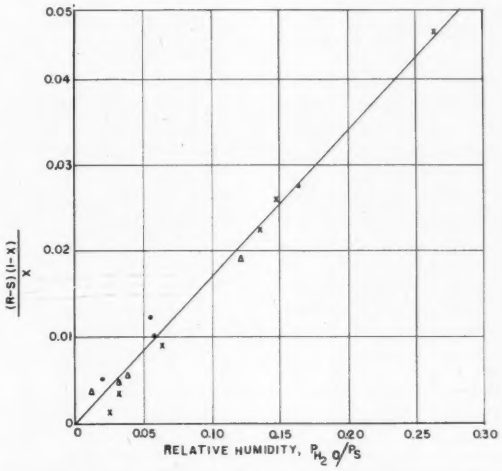

Fig. 4. Water-vapor adsorption term, effect of relative humidity; catalyst, silica gel; × 30°C., ○ 45°C., △ 60°C.

negative constants are not permissible under the assumptions of the derivation, such a result was taken as an indication that the particular rate equation was not consistent with the data, and was hence eliminated from further consideration. Several equations involving only two constants, both of which were assigned positive values by the least squares calculation, gave poor fits to the data and were also eliminated. Equations postulating the adsorption of nitrogen tetroxide gave poorer agreement than those assuming adsorption of nitrogen dioxide and were likewise eliminated. Six equations remained, all of which were based on surface-reaction–controlling processes. The equation which best agreed with the experimental data was the one previously selected by Rao and by Baker and Wong. Two other equations, which were based on the assumption of NO—O_2 complex, were about equally satisfactory in the range of conditions studied.

EFFECT OF WATER VAPOR

The effect of water vapor in reducing the rate of catalytic oxidation of nitric oxide may be accounted for in either of two ways: by assuming that the water vapor reduces the activity of the catalyst or that, by reversible adsorption, water molecules occupy active sites on the surface of the catalyst. The experimental data confirm the second theory. The effect of water vapor can be accounted for by the inclusion of the additional adsorption term wp_{H_2O} in the denominator of the rate equation.

$$r = \frac{p_{NO}^2 p_{O_2}}{a + bp_{NO}^2 + cp_{NO_2} + wp_{H_2O}} \quad (4)$$

In evaluating the effect of water vapor and determining the constant w, the use of direct experimental data relating conversion to catalyst-to-feed ratio was considered more reliable than obtaining rates by methods of graphical differentiation. This direct method involves integration of the rate equation.

$$Fdx = rdW$$

$$\frac{w}{F} = \int_0^x \frac{[a + bp_{NO}^2 + cp_{NO_2} + wp_{H_2O}]}{p_{NO}^2 p_{O_2}}\, dx \quad (5)$$

Partial pressures of the reactants may be expressed in terms of conversion x as follows:

$$p_{NO} = \frac{N_{NO}(1 - x)\pi}{(1 - 1/2xN_{NO})}$$

$$p_{O_2} = \frac{(N_{O_2} - 1/2xN_{NO})\pi}{(1 - 1/2xN_{NO})} \quad (6)$$

$$p_{NO_2} = \frac{xN_{NO}\pi}{(1 - 1/2xN_{NO})}$$

where N_{O_2}, N_{NO} = initial mole fraction of O_2 and NO in the feed. However, the integration of this equation can be greatly simplified for low concentrations of NO and high concentrations of O_2 by neglecting the small change in the total number of moles and assuming a constant average value for the mole fraction of oxygen. Under these assumptions, Equation (5) may be integrated to give

$$\frac{W}{F} = \frac{1}{m^2 n}\left\{(a + wp_{H_2O})\frac{x}{1 - x} + bm^2 x + cm\left[\frac{x}{1 - x} + \frac{\ln(1 - x)}{x}\right]\right\} \quad (7)$$

When the reaction takes place in the presence of water vapor, the partial pressure of water vapor remains constant and the integrated equation may be written

$$\left(\frac{W}{F}\right)_w = \left(\frac{W}{F}\right)_0 + \frac{1}{m^2 n}\left(\frac{x}{1 - x}\right)wp_{H_2O}$$

or

$$wp_{H_2O} = m^2 n\left[\left(\frac{W}{F}\right)_w - \left(\frac{W}{F}\right)_0\right]\frac{1 - x}{x}$$

$$= (R - S)\frac{1 - x}{x} \quad (8)$$

where

$(W/F)_w$ = experimental value in the presence of water vapor

$(W/F)_0$ = calculated value, absence of water vapor assumed

The values of $(R - S)[(1 - x)/x]$ for both catalysts are plotted in Figures 3 and 4 against relative humidity p_{H_2O}/p_s. If w is independent of partial pressure, straight lines should result for equitemperature conditions. For silica gel it will be observed (Figure 4) that a straight line results for conditions up to 25% relative humidity and that the results are independent of temperature. This is characteristic of the equilibrium-adsorption isotherm for water vapor on silica gel.

With activated carbon the isothermal lines are not coincident (Figure 3) and a sudden break occurs at a relative humidity of about 20%, an indication that below 20% relative humidity the adsorption-equilibrium constant is independent of partial pressure but that as the relative humidity increases above 20%, the value of w increases rapidly. This behavior is consistent with the capillary-adsorption curves characteristic of activated carbon. For clarity, the results on activated carbon below relative humidities of 20% have been replotted in Figure 5.

SUMMARY OF RATE-EQUATION CONSTANTS

Catalyst: Activated Carbon

Temperature, °C.	a	b	c	w
30	0.000283	0.521	0.00646	0.0812
45	0.000187	0.824	0.00658	0.0634
60	0.000181	0.942	0.01363	0.0544

Catalyst: Silica Gel

30	0.00398	3.109	0.242	4.06
45	0.00876	3.435	0.174	1.80
60	0.01597	3.382	0.176	0.865

The same rate-controlling step was obtained for both silica gel and activated carbon by all three sets of investigators (*1, 6, 7*); however, in this investigation higher initial reaction rates were obtained with both silica gel and activated carbon than in previous studies (*1, 7*), with corresponding different numerical values for the constants a, b, and c. With any batch of catalyst, however, the activity remained constant during the period of investigation. For precision these numerical constants require evaluation for each specific catalyst. It should also be stated that greater precaution was taken in this last investigation in removing water from the gas stream and from the catalyst for tests made with dry gases.

For activated carbon, values of conversion calculated from these constants deviated by an average of ±1.9% from experimental values; for silica gel the average deviation was ±1.4%. The range of variation for calculated values was ±6% from experimental values.

The effect of water vapor on percentage conversion as a function of catalyst-to-feed ratio or reciprocal space velocity has been calculated and is shown in Figure 6 for activated carbon and in Figure 7 for silica gel at relative humidities up to 20%. The additional catalyst required to compensate for the presence of water vapor, plotted as function of dew point, is shown in Figure 8 for activated carbon and in Figure 9 for silica gel. The additional catalyst is expressed as a fraction of that required when no water vapor is present. These results are given for 95% conversion of nitric oxide with 3% nitric oxide in the entering feed, an isothermal reaction temperature of 30°C., and a reaction pressure of 1 atm. For example, at a dew point of −20°C. 17% more activated carbon is needed than for a dry gas; at a dew point of 0°C. 100% more catalyst is required. For silica gel, 30% more is required at a dew point of −20°C. than for the dry gas and 220% more at a dew point of 0°C. These figures apply to a reaction temperature of 30°C. It is evident that silica gel is much more sensitive to the partial pressure of water vapor than is activated carbon below a relative humidity of 20%.

SUMMARY

In these experiments on the catalytic oxidation of dilute nitric oxide, the apparent rate-controlling chemical step and the corresponding form of the rate equation as obtained by previous investigators has been confirmed. The quantitative effect of water vapor on the reaction rate has been established for both silica gel and activated carbon catalysts. In the presence of water vapor the reaction-rate equation is

$$r = \frac{p_{NO}^2 p_{O_2}}{(a + bp_{NO}^2 + cp_{NO_2} + wp_{H_2O})} \quad (9)$$

The effect of water vapor is to reduce the reaction by reversible adsorption on the active sites of the catalyst. The value of w is dependent on temperature but independent of water-vapor concentra-

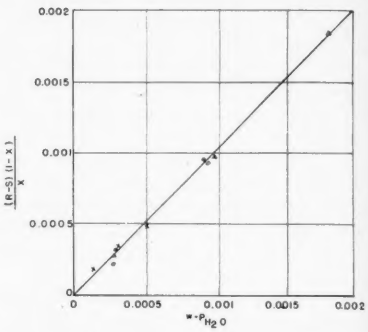

Fig. 5. Water-vapor of adsorption term at relative humidity below 20%; catalyst, activated carbon.

× 30°C., w = 0.0812
○ 45°C., w = 0.0634
△ 60°C., w = 0.0544

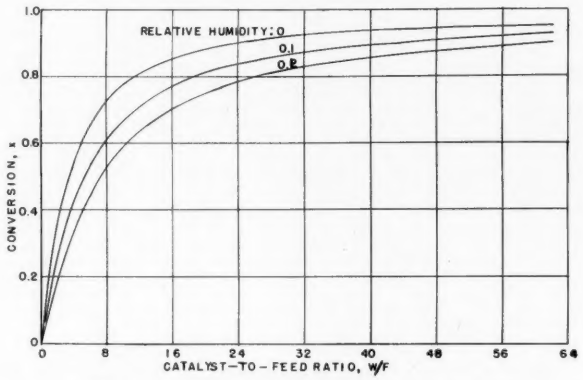

Fig. 6. Effect of water vapor on the conversion of nitric oxide.

Catalyst: activated carbon **Temperature: 30°C.**
Pressure: 1.0 atm. **Feed: 3% nitric oxide in air**

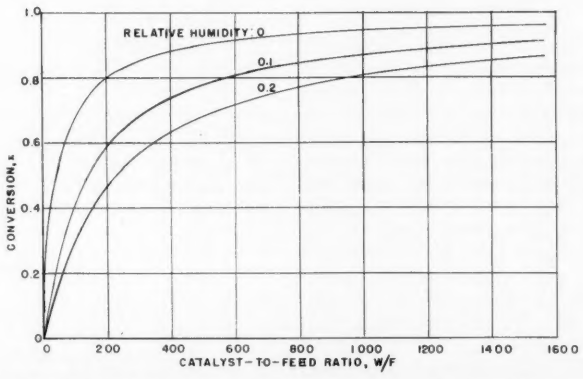

Fig. 7. Effect of water vapor on the conversion of nitric oxide.

Catalyst: Silica gel **Temperature: 30°C.**
Pressure: 1.0 atm. **Feed: 3% nitric oxide in air**

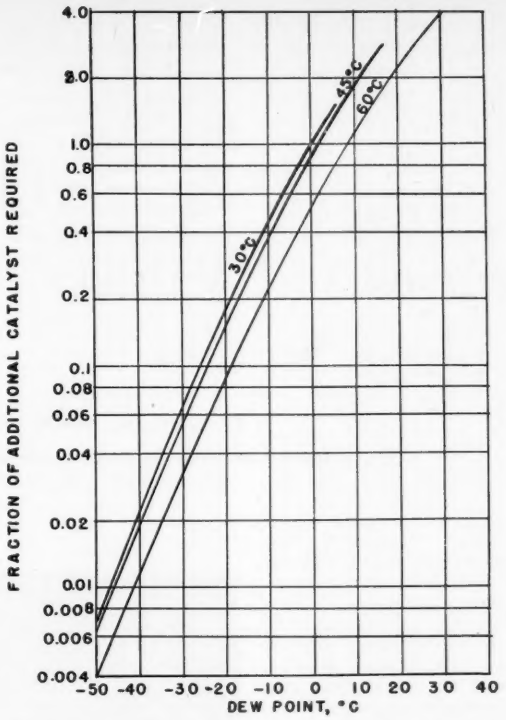

Fig. 8. Effect of dew point on the fraction of additional catalyst required.
Catalyst: activated carbon Feed: 3% nitric oxide in air
Pressure: 1.0 atm. Conversion: 95%

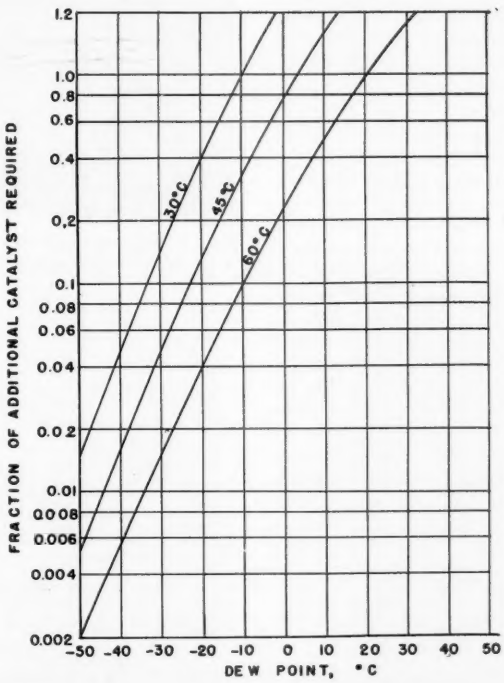

Fig. 9. Effect of dew point on the fraction of additional catalyst required.
Catalyst: silica gel Feed: 3% nitric oxide in air
Pressure: 1.0 atm. Conversion: 95%

tion up to a relative humidity of 20%. At relative humidities above 20% the value of w for activated carbon increases greatly with relative humidity, apparently corresponding to the effect of capillary adsorption.

ACKNOWLEDGMENT

The assistance of Glør Th. Mejdel, Samuel W. McKibbins, and Charles L. Stoner in the experimental work is gratefully acknowledged, as is financial aid through fellowships provided by the Gulf Oil Corporation, the National Science Foundation, and the Engineering Experiment Station of the University of Wisconsin.

NOTATION

a = rate-equation constant
b = rate-equation constant
c = rate-equation constant
F = feed, g.-moles of nitric oxide/hr.
F_t = total feed, g.-moles/hr.
k_H = homogeneous reaction velocity constant
m = initial partial pressure of nitric oxide, atm. $= N_{NO}\pi$
n = average partial pressure of oxygen, atm. $= (N_{O_2} - \frac{1}{4}N_{NO})\pi$
N_A = initial mole fraction of subscript component
π = total pressure, atm.
p_A = partial pressure of subscript component, atm.
p_s = vapor pressure of water, atm.
R = $m^2n(W/F)_w$ (experimental value in the presence of water vapor)
r = catalytic rate of reaction, g.-moles of nitric oxide reacted/(g. of catalyst)(hr.)
S = $m^2n(W/F)_0$ (calculated value, absence of water vapor assumed)
V = volume of reactor, liters
W = mass of catalyst, g.
w = rate-equation constant
x = conversion, moles of nitric oxide reacted/mole of nitric oxide feed
y_A = mole fraction of subscript component

LITERATURE CITED

1. Baker, R. W., H. N. Wong, and O. A. Hougen, *Chem. Eng. Progr. Symposium Series* No. 4, **48**, 103 (1952)
2. Bickling, C. R., Ph.D. thesis, Univ. Wisconsin, Madison (1950).
3. Bodenstein, M., *Helv. Chem. Acta*, **18**, 743 (1935).
4. Ermenc, E. D., *Chem. Eng. Progr.*, **52**, 149 (1955).
5. Hasche, R. L., and W. A. Patrick, *J. Am. Chem. Soc.*, **47**, 1207 (1925).
6. Kircher, Omer, Ph.D. thesis, Univ. Wisconsin, Madison (1955).
7. Rao, M. N., and O. A. Hougen, *Chem. Eng. Progr. Symposium Series* No. 4, **48**, 110 (1952).
8. Trautz, M., *Z. Elektrochem.*, **22**, 104 (1916).
9. Treacy, J. C., and Farrington Daniels, *J. Am. Chem. Soc.*, **77**, 2033 (1955).

Measured Plate Efficiencies and Values Predicted from Single-phase Studies

F. E. RUSH, JR., and CLIFFORD STIRBA

E. I. du Pont de Nemours and Company, Inc., Wilmington, Delaware

Plate efficiencies measured on 18-in.-diam. sieve plates are reported for the acetic acid–water system and for the methyl isobutyl ketone–water system at atmospheric pressure. In the former system the major resistance to mass transfer is in the gas phase; liquid-phase resistance to mass transfer is controlling in the latter. Efficiencies are also reported for the aniline-nitrobenzene system (gas-phase resistance controlling) at 5 mm. Hg absolute on 6-in.-diam. sieve plates. Pure gas- and liquid-phase efficiencies for both plate designs were determined by the adiabatic humidification of air and the desorption of oxygen from water into air. Predicted values of plate efficiency for each of the binary systems studied were computed from the pure phase efficiencies according to the procedure outlined by Gerster et al. A comparison between measured and predicted efficiencies is presented as a guide for future research in this field.

The greatest uncertainty in the design of absorption and distillation columns today is in the conversion from theoretical to actual plates, that is, the problem of plate efficiency. This is true regardless of the type of contactor employed, whether bubble-cap plates, sieve plates, or some modification of these. Fortunately, however, this problem is recognized, and more and more work is being aimed at its solution. Perhaps the largest single effort in this endeavor is the A.I.Ch.E. research program on plate efficiency which is currently in progress at three universities.

Many methods for predicting mass-transfer efficiencies have been proposed (*2, 5, 6, 15*). Some emphasize the importance of a certain variable or group of variables which are known to influence the final efficiency attained; others stress the importance of a different set of variables. None of these methods, however, take into account the variables concerned with changes in plate design, that is, the physical dimensions of the plate and its components.

A few years ago Gerster and others (*7, 8, 9*) proposed a method for predicting plate efficiencies by the addition of the separate gas- and liquid-phase resistances. This method takes into account all the factors now known to affect plate efficiency; furthermore, it permits allowances to be made for variations in plate design. Although Gerster's method is believed to be the best available, there actually has been very little confirmation of its accuracy and reliability in the literature, particularly for liquid-phase–controlled systems. Those applications which have been reported are confined to bubble-cap plates.

The authors have used this method with a reasonable degree of success for sieve plates, especially for systems in which the major resistance to mass transfer is in the gas phase. The purpose of this paper is to report some experiences with this method of predicting plate-efficiency values from single-phase studies. It is hoped that the results of this work will serve as somewhat of a guide for future research in this field. The experimental work reported herein covers three binary systems: acetic acid–water at atmospheric pressure, a gas-phase–controlled system; aniline-nitrobenzene at 5 mm. Hg absolute, another gas-phase-controlled system; and methyl isobutyl ketone–water at atmospheric pressure, a liquid-phase–controlled system. The atmospheric-pressure studies were made with 18-in.-diam. sieve plates; the vacuum study utilized 6-in.-diam. sieve plates.

BACKGROUND

The Gerster method of predicting plate efficiency involves, first, determining the number of pure gas-phase transfer units N_{Go} and the number of pure liquid-phase transfer units N_{Lo} for a given plate, at the

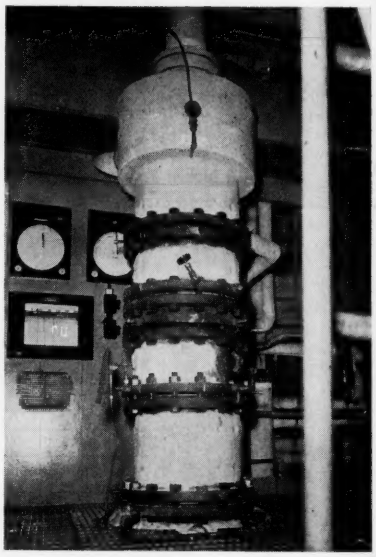

Fig. 1. Eighteen-inch–diameter stainless steel tower and control panel.

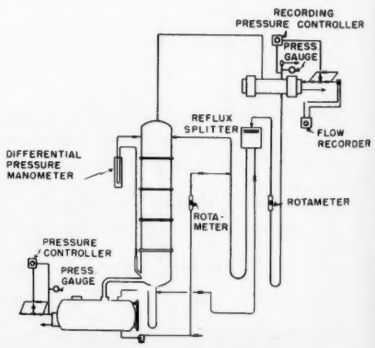

Fig. 2. Schematic arrangement of 18-in.–diam. stainless steel tower.

specified conditions of vapor and liquid flow, by the adiabatic humidification of air and the desorption of oxygen from water into air, respectively. These pure-phase transfer-unit values are then converted, by means of Schmidt-number ratios, to the individual transfer-unit values N_G and N_L, which should exist on the given plate at the specified flow conditions with the system of interest. Equations (1) and (2) illustrate this conversion.

$$N_G = N_{Go}\left(\frac{N_{Sc,Go}}{N_{Sc,G}}\right)^{2/3} \quad (1)$$

$$N_L = N_{Lo}\left(\frac{N_{Sc,Lo}}{N_{Sc,L}}\right)^{1/2} \quad (2)$$

The gas- and liquid-phase Schmidt numbers are defined in Equations (3) and (4):

$$N_{Sc,G} = \frac{\mu_G}{\rho_G D_G} \quad (3)$$

$$N_{Sc,L} = \frac{\mu_L}{\rho_L D_L} \quad (4)$$

In this way the effect of physical properties, including viscosity, density, and molecular diffusivity, for both the liquid and the gas phases is recognized. The effect of variations in plate design on plate efficiency is accounted for in this method by determining values of N_{Go} and N_{Lo} for the basic designs of interest. Finally, the converted transfer-unit values N_G and N_L are added together to yield an over-all transfer efficiency for the plate at the specific conditions, according to either Equation (5) or (6).

$$\frac{1}{-2.3\log(1-E_{OG})} = \frac{1}{N_G} + \frac{mG/L'}{N_L} \quad (5)$$

$$\frac{1}{-2.3\log(1-E_{OL})} = \frac{L'/mG}{N_G} + \frac{1}{N_L} \quad (6)$$

Equation (5) relates the individual transfer units N_G and N_L, the vapor rate G, the liquid rate L', and the slope of the equilibrium curve m for the system of interest to the transfer efficiency of the plate E_{OG}, expressed as an over-all gas-phase efficiency. Equation (6) is the same type of relationship for the over-all liquid-phase efficiency E_{OL}. In Equation (5), the term $1/N_G + (mG/L')/N_L$ is a measure of the total resistance to mass transfer, $1/N_G$ representing the gas-phase resistance and $(mG/L')/N_L$ representing the liquid-phase resistance. Similarly, in Equation (6) $(L'/mG)/N_G$ represents the gas-phase resistance to mass transfer and $1/N_L$ represents the liquid-phase resistance. The values of E_{OG} and E_{OL} obtained in this manner are transfer efficiencies; the Lewis (*12*) equations must be used to obtain the corresponding Murphree values.

APPARATUS

The work at atmospheric pressure, that is, the study of the acetic acid–water system and the methyl isobutyl ketone–water system, was carried out in an 18-in.-diam. stainless steel tower. This unit, shown in Figures 1 and 2, was designed to accommodate one to five plates at place spacings varying from 6 to 24 in. In this study, however, only three plates were employed. Plate spacing was altered by changing the order of the tower sections or by using special sections, depending on the spacing requirement. An 18-in. plate spacing was used with the acetic acid–water system and a 24-in. spacing with the methyl isobutyl ketone–water system. The tower was equipped with a shell-and-tube condenser, and the total condensate flowed from the condenser to a rotameter and then to a reflux splitter. The reflux leaving this splitter entered the tower just behind the inlet weir of the top plate. During the study of the methyl isobutyl ketone–water system additional reflux liquid was pumped from the boiling kettle, which was located directly beneath the tower, and joined the overhead reflux stream. The vapor from the kettle entered the side of the tower through a 6-in. pipe. The liquid overflow from the tower passed through a U-bend seal and returned to the top of the boiling kettle.

The 18-in.-diam. sieve plates (Figure 3) used in these studies had ⅛-in.-diam. holes on ⅜-in. equilateral triangular centers and provided a free area (total area of the holes) equal to 6.7% of the superficial tower area. The discharge weir height was adjusted to provide a minimum static seal of 1.5 in. for the acetic acid–water tests. A constant outlet weir height of 9/16 in. was used for all the methyl isobutyl ketone–water tests. Splash baffles were located ½ in. ahead of the discharge weir and their minimum clearance from the plate surface was ⅜ in. The tops of the splash baffles extended to within 3 to 4 in. of the plate above. These splash baffles were found necessary by actual experimentation. Without them the relatively small liquid flow across the plate in some of the runs was inadequate to maintain a constant seal depth.

For the measurement of the individual-phase efficiencies, one of the 18-in.-diam. plates was set up in a special apparatus designed to accommodate only one test plate. In order to procure reliable data from adiabatic humidification and oxygen desorption, the tests should be carried out across one plate only. If more than one plate is used, the approach to equilibrium conditions is so close that the resulting calculated individual-phase efficiencies have low precision.

The work at 5 mm. Hg abs., that is, the study of the aniline-nitrobenzene system, was carried out in a 6-in.-diam. stainless steel column. This unit was simply a 10-ft. section of 6-in. pipe without intermediate-section flanges. Since this unit was designed for high-vacuum studies down to 1 mm. Hg absolute, flanges and connections were kept at a minimum. The plates (Figure 4) were slipped into the column and spaced on 12-in. centers by three support posts between each plate. The plates were sealed to the column with an O-ring–packing arrangement. This tower was also equipped with a shell-and-tube condenser, and the total condensate flowed from the condenser, through a gas-disengaging chamber to allow inerts to go to the jets, to a rotameter, and then to the top of the column behind the inlet weir on the top plate. Vacuum was supplied by a four-stage jet arrangement, and the desired absolute pressure was maintained by a controlled air bleed.

Six 6-in.-diam. sieve plates on 12-in. plate spacing were used in the study of the aniline-nitrobenzene system. These plates also had ⅛-in. holes on ⅜-in. equilateral triangular centers. The free area (total area of the holes) for the 6-in.-diam. plates was 5% of the superficial tower area. The

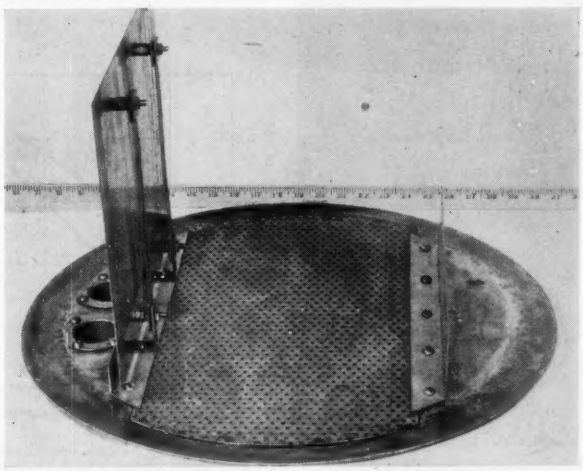

Fig. 3. Sieve plate tested in the 18-in.-diam. tower.

circular discharge downpipe on each plate was adjusted to provide a minimum static seal of ¾ in. Splash baffles in the form of tubes concentric with the downpipes and slotted at the base for the passage of liquid were found to be necessary to maintain a constant seal on the plates.

One of these plates was set up in a 6-in.-diam. Lucite acrylic-resin tower for the measurement of the individual-phase efficiencies. Here again, a single plate was found necessary, particularly for the region of low liquid rates encountered in vacuum distillation.

BASIC DATA

The vapor-liquid equilibrium data for the acetic acid–water system at atmospheric pressure which were used in the calculation of the actual efficiencies represent an average of those found in the literature supplemented by data obtained from unpublished information. These data are shown in Table 1 for the concentration range covered in this study.

Table 1
Vapor-Liquid–Equilibrium Data for Water and Acetic Acid

Mole fraction of water in Liquid	Vapor
0.9200	0.9424
0.9300	0.9493
0.9400	0.95635
0.9500	0.9636
0.9600	0.97085
0.9700	0.9782
0.9800	0.98545
0.9900	0.9927
1.0000	1.0000

Table 2
Schmidt Numbers Used in Plate-efficiency Predictions

System	$N_{Sc,G}$	$N_{Sc,L}$	Temperature, °C.
Oxygen-water	—	344	25
Air-water vapor	0.60	—	25
Water-acetic acid	1.12	82.7	100
Aniline-nitrobenzene	0.47	1,050	56
Methyl isobutyl ketone–water	1.65	90.2	100

Vapor-liquid equilibrium data for the methyl isobutyl ketone–water system were computed, according to equations in Perry (*13*), from solubility data measured at 20°, 40°, 60°, 80°, and 87.5°C. and from measured vapor-pressure values. In the dilute methyl isobutyl ketone concentration range, the region used in this experiment, the slope of the equilibrium curve m is essentially constant at 200. Hence, this constant value was used throughout in all efficiency calculations.

Vapor-liquid equilibrium data for the aniline-nitrobenzene system at 5 and 10 mm. Hg absolute were calculated from total-pressure measurements of mixtures of these two compounds and from vapor-pressure measurement of the pure components according to a method outlined by Holtzlander and Riggle (*10*). These data are shown in Figures 5 and 6.

TEST PROCEDURE

For all the runs made in this investigation with the acetic acid–water system the tower was operated at atmospheric pressure and total reflux. At the beginning of each run the boil-up was adjusted to the desired rate as indicated by the condensate rotameter. This established rotameter reading was held within ±5% for an hour to ensure equilibrium before sampling procedures were started. When any significant fluctuations in the boil-up rate occurred during the waiting period, the column was brought back to the desired rate and a full hour was allowed to elapse before sampling. This period ensured a minimum of four complete changes of holdup at the desired vapor rate.

The runs with the methyl isobutyl ketone–water system were also made at atmospheric pressure, but liquid-to-vapor ratios in the range of 1:1 to 40:1 were studied. After the boil-up had leveled off at total reflux, the pump which recirculated liquid from the boiler to the reflux inlet was started and the flow was adjusted to the desired reading on a rotameter. After steady operation had been attained, approximately 1 hr. elapsed before liquid samples for efficiency determinations were taken.

The boil-up rates for all tests in the 18-in.-diam. tower were computed from recorded inlet and outlet condenser cooling-water temperatures and a direct weighing measurement of the cooling-water rate. The steam condensate from the reboiler was measured as an additional check. The temperatures of the reflux, condensate, and boiling kettle were also recorded. The differential pressure drop across the three plates was measured by a water manometer. All recorded data were taken in duplicate, one set immediately preceding the efficiency samples and one set following. With the methyl isobutyl ketone–water system, two sets of liquid samples were taken about 1 hr. apart to ensure that steady state conditions prevailed.

Only liquid samples were taken for the efficiency determinations. Since the overhead vapor was totally condensed, a sample was taken from the reflux line to determine the composition of the liquid entering the top plate, which for the ketone-water runs was a composite of the totally condensed overhead vapor and the liquid reflux being pumped from the reboiler. A second sample, taken from the U leg leading back to the reboiler, determined the composition of liquid leaving the bottom of the tower. All samples from the 18-in.-diam. column were taken through chilled copper coils to prevent flashing. The sampling connection and line were thoroughly flushed before the sample was taken.

The procedure followed with the aniline-nitrobenzene system in the 6-in.-diam.

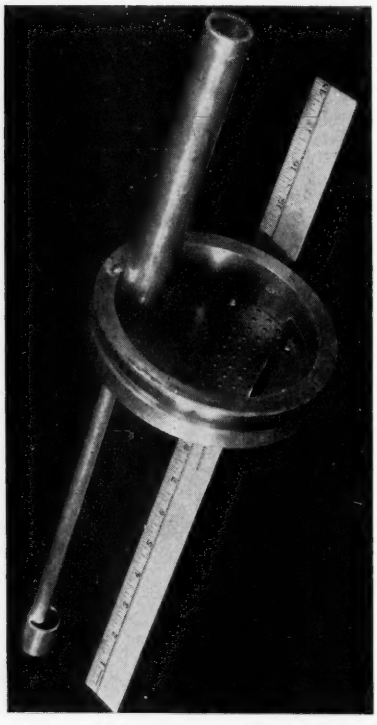

Fig. 4. Sieve plate tested in the 6-in.-diam. tower.

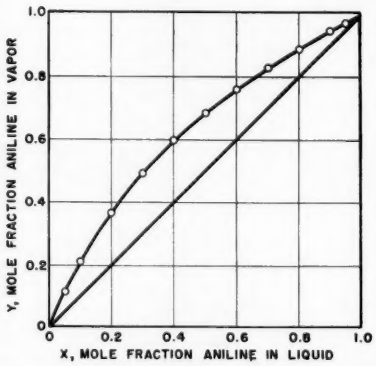

Fig. 5. Vapor-liquid–equilibrium data for aniline nitrobenzene at 5 mm. Hg abs.

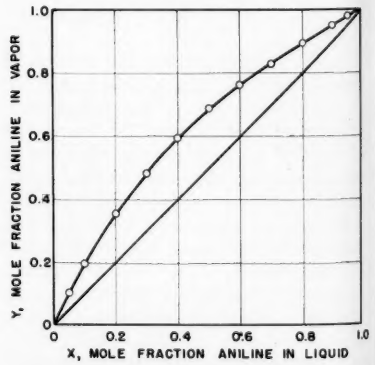

Fig. 6. Vapor-liquid–equilibrium data for aniline nitrobenzene at 10 mm. Hg abs.

column at 5 mm. Hg abs. was similar to that for acetic acid–water. In the vacuum studies, however, the desired top-column pressure was established and under control before heat was applied to the reboiler. Temperatures were measured in the reboiler, bottom column, top column, overhead vapor line, and condensate line. Boil-up was determined by a calibrated rotameter in the overhead condensate line. The differential pressure drop across the six plates was measured by a dibutyl phthalate manometer. Liquid samples for efficiency determination were taken from the overhead condensate line and from the U leg leading back to the reboiler.

As stated above, the adiabatic-humidification tests and the oxygen-desorption tests had to be carried out across one plate only. The oxygen-desorption runs were made by dissolving oxygen in water and pumping the solution to a calming section. Calming sections extended 2 ft. from either side, upstream and downstream, of the test section which held the 18-in.-diam. test plate. The calming sections allowed a reasonably accurate measure of the clear liquid head at each end of the unit and provided a good sample of liquid. With a blank plate in place, oxygenated water was passed through the unit in order to measure the extent to which oxygen was lost from the water in the calming sections. The loss of oxygen was found to be negligible. Samples taken at the center line and near the side wall of the calming sections showed that the liquid composition was uniform across the channel. In the case of the 6-in.-diam. plates no calming section was used; the liquid entered the plate behind an inlet weir, flowed across the plate, under the splash baffle, and over into the cylindrical downpipe. The air and water temperatures were controlled in all runs so that the wet-bulb temperature of the entering air was at the inlet-water temperature to ensure a constant water temperature across the plate and thus no change in the oxygen solubility.

Adiabatic-humidification runs were made in the same way as the oxygen-desorption runs, except that the inlet and exit dry- and wet-bulb temperatures of the air were noted for each test condition. In all cases the water and air temperatures were set so that the wet-bulb temperature of the air was at the temperature of the water. The dry-bulb temperature of the exit air was measured sufficiently far downstream so that there was no appreciable liquid entrainment to the thermometer; furthermore, the wet- and dry-bulb thermometers were located behind a baffle in the outlet duct.

ANALYTICAL PROCEDURE

The acetic acid–water samples used to determine plate efficiency were titrated to a phenolphthalein end point with 0.1*N* sodium hydroxide solution. Results of the titration were converted to mole fractions of water.

The aniline-nitrobenzene samples were analyzed for aniline by titration with 0.1*N* perchloric acid in a glacial acetic acid medium. Crystal violet dissolved in glacial acetic acid was the indicator. The results of these titrations were converted to mole-fraction units.

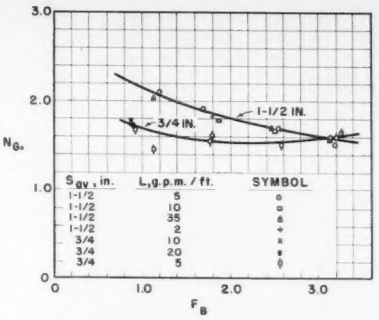

Fig. 7. Number of gas-phase transfer units for 18-in.-diam. sieve plate.

The methyl isobutyl ketone–water samples were analyzed for the ketone by means of the iodoform reaction. An excess of iodine added to a weighed sample formed a precipitate with the ketone, and the unreacted iodine was titrated with 0.1*N* sodium thiosulfate solution to a starch-solution end point. Analyses were computed in mole-fraction units. Oxygen analysis was made by the Winkler method.

EFFICIENCY CALCULATIONS

The average actual plate efficiency for the three plates operating at total reflux on the acetic acid–water system was calculated according to the method of Baker and Stockhardt (*1*). This procedure involves the assumption that Murphree efficiency does not vary from one plate to the next and that only two liquid samples are required: condensate and run-off from the bottom plate. The concentrations of these two samples were plotted on a McCabe-Thiele diagram, and the efficiency was determined by trial and error. Three fractional plates were stepped off by means of proportional dividers, the plate efficiency fraction being changed on each successive trial until the fraction was found which gave the experimentally determined separation in three steps. This fraction then represented the average Murphree vapor efficiency E_{MV} of the three plates.

The average actual plate efficiency for the three 18-in.-diam. plates operating at various reflux ratios on the methyl isobutyl ketone–water system was determined analytically by means of Silver's (*14*) modifications of Colburn's (*4*) equations, which are valid for cases in which the operating and equilibrium lines are straight. Efficiency values for this system were computed as E_{MV}, Murphree vapor efficiency.

For the aniline-nitrobenzene system, a plot was made of theoretical plates vs. composition, with a very low concentration of aniline (0.0001 mole fraction) used as a base point. The theoretical plate value corresponding to the aniline concentration in the liquid leaving the bottom plate of the column was subtracted from the theoretical plate value corresponding to the aniline concentration in the liquid reflux to the top plate of the column. This gave the total number of theoretical plates achieved across the six actual plates, and the ratio of theoretical plates to actual plates was taken as the average plate efficiency. Actually an efficiency calculated in this manner may not be the same numerically as a Murphree vapor efficiency. Several runs, covering the complete range of the experiments, were also reevaluated by means of the Baker and Stockhardt (*1*) method as used on the acetic acid–water system. In the case of the aniline-nitrobenzene system, the maximum deviation between efficiencies computed by these two methods was 1 to 3%. The use of over-all plate efficiencies, as the ratio of theoretical to actual plates, is not recommended for column design unless some check with the Baker and Stockhardt (*1*) method is made.

RESULTS

Data on the number of pure-gas-phase transfer units on the 18-in.-diam. plate are shown in Figure 7 as N_{G_o} vs. the

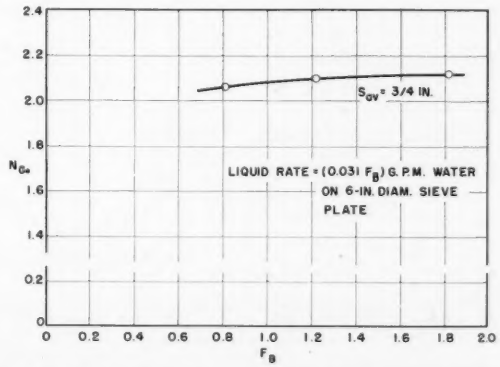

Fig. 8. Number of gas-phase transfer units for 6-in.-diam. sieve plate.

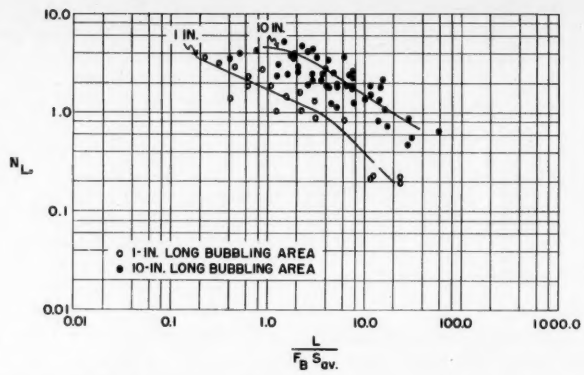

Fig. 9. Number of liquid-phase transfer units as measured on 18-in.-diam. sieve plate.

F factor in the bubbling area F_B, with average clear-liquid-seal depth S_{avg} as a parameter. The average clear-liquid-seal depth for the single 18-in.-diam. test plate was taken as the arithmetic average of the clear liquid depths in the upstream and downstream calming sections, measured directly as clear-liquid depths. In the case of the 18-in.-diam. plates in the column, where no calming sections could be used, the average clear-liquid-seal depth was calculated as the height of the outlet weir plus the computed crest of clear liquid over the weir plus one-half the hydraulic gradient across the plate. (Hydraulic gradient across plates of this diameter at the liquid rates employed in these tests is usually negligible.) It is assumed that liquid flows over the outlet weir as a clear liquid, as a splash baffle was used on all plates in the columns. For the 6-in.-diam. plates, where no calming sections could be used either, the seal was adjusted to give the same pressure-drop curve as measured with an S_{avg} of $\frac{3}{4}$ in. on the single 18-in.-diam. test plate with calming sections. The F factor is defined as the product of the linear vapor velocity, expressed in feet per second and based upon the total cross-sectional area of the column and the square root of the vapor density, the density being expressed as pounds per cubic foot. F_B, the F factor in the bubbling area, is based upon the cross-sectional area of the bubbling zone. The bubbling area on the 18-in.-diam. plates was about 62.5% of the total cross-sectional area of the column; on the 6-in.-diam. plates, the bubbling area was about 54% of the total column area. It is interesting to note that the curve for either seal depth is made up from data taken at several different liquid rates. This indicates that the number of gas-phase transfer units is independent of liquid rate L, expressed as gallons per minute per foot of plate width. The number of gas-phase transfer units is also practically independent of F_B, a direct measure of the vapor rate.

The same type of data were measured on the 6-in.-diam. sieve plates at a nominal seal of $\frac{3}{4}$ in. and they are shown on Figure 8. The difference in the number of gas-phase transfer units for the 18- and the 6-in.-diam. plates at the same average seal of $\frac{3}{4}$ in. is undoubtedly the result of discrepancies in the measurement of the clear-liquid seal on these plates. As explained above, calming sections were used with the 18-in.-diam. test plate but not with the 6-in.-diam. test plate.

Data on the number of pure liquid-phase transfer units on the 18-in.-diam. plates used in these tests are shown in Figure 9 as N_{L_o} vs. a term $L/(F_B S_{avg})$. For this correlation, it was assumed that the interfacial area for mass transfer is directly proportional to F_B, the F factor in the bubbling area, and that the liquid-phase mass transfer coefficient, usually indicated as $k_L a$, is constant across the plate. The liquid-phase transfer units are shown for a 10-in. length of liquid path, which was the dimension of the perforated section in the direction of net liquid flow. When similar measurements were made on the 6-in.-diam. plate, it was found that the oxygen content of the water was reduced to the equilibrium value (within the precision of analysis) for all conditions. The length of liquid path on the 6-in.-diam. plates was 3 in. Since the 6-in.-diam. plates were being used for vacuum studies, the liquid reflux rates were quite small. According to the theory and basic assumptions made in the development of the Gerster approach, the number of liquid-film transfer units on a plate is proportional to the length of liquid path. Hence all but a 1-in. length of perforations on the 18-in.-diam. plate were blanked off, and the oxygen-desorption tests were repeated with the results as shown. These values of the number of liquid-phase transfer units for a 1-in. length of liquid path, multiplied by 10 in the case of the 18-in.-diam. plates and by 3 in the case of the 6-in.-diam. plates, were used in all efficiency predictions.

Values in Figures 7, 8, and 9 were used at the appropriate gas rate, liquid rate, and seal depth, along with Equations (1), (2), and (5) to predict values of E_{OG}, the transfer efficiency based upon over-all gas-film driving force for each of the systems studied. The calculated values of the Schmidt numbers which were used for the conversions indicated in Equations (1) and (2) are given in Table 2.

The comparison between predicted and measured plate efficiency values for the acetic acid–water system at atmospheric pressure and total reflux is shown in Figure 10. This system is predominantly gas-phase controlled, with more than 90% of the total resistance in the gas phase at the conditions studied. The agreement between predicted and measured plate efficiency over the entire range studied is seen to be very good. The maximum difference is about 3%. Since the plate spacing was 18 in., some correction for entrainment effects might be applied to the predicted values at the higher vapor rates.

For the aniline-nitrobenzene system at 5 mm. Hg abs. and total reflux, the same comparison is made in Figure 11. Since only a 12-in. spacing separated the plates

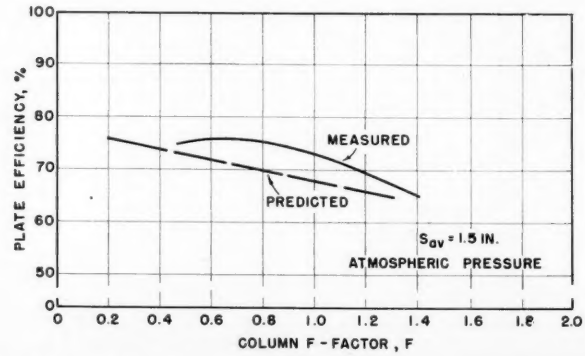

Fig. 10. Comparison of measured and predicted plate efficiencies; 18-in.-diam. column, acetic acid–water system.

during the vacuum tests, corrections for entrainment effects on the predicted efficiency were made according to the equation derived by Colburn (*3*). Entrainment values were estimated from data measured and reported by Jones and Pyle (*11*). In this system approximately 75% of the resistance to mass transfer occurs in the gas phase at the conditions maintained in our tests. Here again the agreement between predicted and measured plate efficiency is quite good. In this case adiabatic-humidification data and oxygen-desorption data, both measured at atmospheric pressure, were used, together with physical-property data, to predict plate efficiencies for the aniline-nitrobenzene system at 5 mm. Hg abs.

The comparison between predicted and measured efficiencies for the methyl isobutyl ketone–water system at atmospheric pressure and at varying reflux ratios is shown in Figure 12. In this system 70 to 80% of the total resistance to mass transfer is in the liquid phase for the operating conditions which were maintained during these tests. The upper curves are for an average seal depth of 1.3 to 1.4 in. of clear liquid, and the lower curves are for an average clear-liquid-seal depth of 0.9 to 1.0 in.

At the higher seal the liquid rate L was approximately 25 (gal./min.)(ft.) of plate width, and the liquid-to-vapor reflux ratio L'/G varied from about 40:1 at the low vapor rate to about 8:1 at the high vapor rate. At the higher seal fairly good agreement exists between the predicted and measured efficiency values at the lower vapor rates. As the vapor rate increases, the difference between predicted and measured efficiency widens as a result of a substantial drop in the measured values.

At the lower seal the liquid rate L was approximately 10 (gal./min.)(ft.) of plate width, and the liquid-to-vapor reflux ratio L'/G varied from about 10:1 to about 3:1. At the lower liquid rate and low vapor rates, measured efficiencies are somewhat higher than the predicted values. As the vapor rate increases, this situation reverses and the predicted values are much greater than the measured ones. Since a 24-in. plate spacing was used in the ketone-water tests, very little of the difference between the predicted and measured values can be attributed to entrainment effects, even at the higher vapor rates.

The experimental data which form the basis of the measured plate-efficiency curve in Figure 10 are taken from Table 1 of Jones and Pyle (*11*). The experimental data for the measured efficiency curves in Figures 11 and 12, respectively, are contained in Tables 3 and 4* of this paper. These tabulations include temperatures, pressure, pressure drop, sample compositions, boil-up rate, F factor, reflux ratio, and plate efficiency.

*Tabular material has been deposited as document 5310 with the American Documentation Institute, Photoduplication Service, Library of Congress, Washington 25, D. C., and may be obtained for $1.25 for photoprints or 35-mm. microfilm.

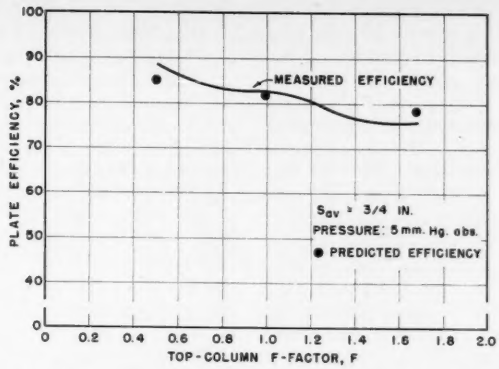

Fig. 11. Comparison of measured and predicted plate efficiencies; 6-in.-diam. column, aniline-nitrobenzene system.

DISCUSSION OF RESULTS

It is to be noted that in all the results a comparison is made between a predicted transfer efficiency and a measured Murphree efficiency, or its equivalent in the case of the aniline-nitrobenzine system.

Early in this work it became apparent that mixing of the liquid in the direction of net liquid flow was taking place on the sieve plates. It was found that the number of liquid-phase transfer units calculated from the oxygen-desorption tests was not directly proportional to length, as theory would predict. It can be seen from Figure 9 that the number of liquid-phase transfer units for a 10-in. liquid path is not ten times the number of liquid-phase transfer units measured for a 1-in. liquid path. This deviation from theory is attributed to liquid mixing in the direction of net liquid flow. Such mixing would be expected to be more pronounced at low liquid flows and high vapor rates. This variation in the number of liquid-phase transfer units per unit of length

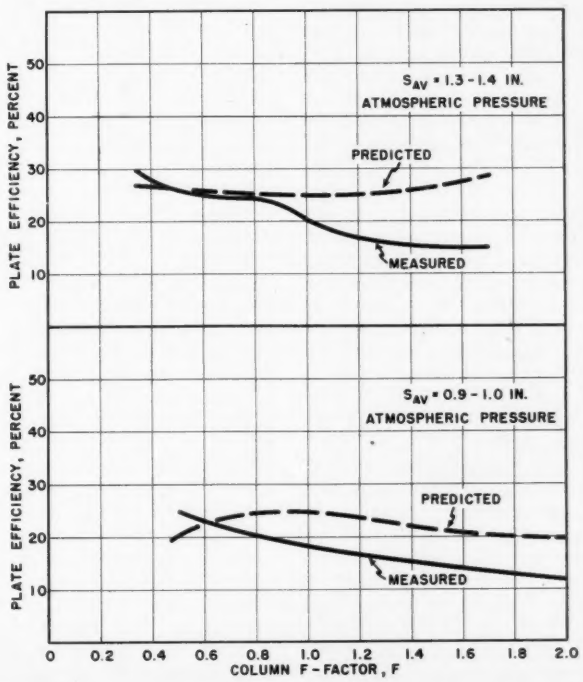

Fig. 12. Comparison of measured and predicted plate efficiencies; 18-in.-diam. column, methyl isobutyl ketone–water system.

with length does not seem to be particularly serious for systems with high gas-phase resistance. In the case of the acetic acid–water system the predicted E_{OG} would have been about 2% lower if calculated from the 10-in. curve rather than the 1-in. curve. In the case of liquid-phase–controlled systems, however, this difference can be quite large. For the methyl isobutyl ketone–water system at S_{avg} of 1.3 to 1.4 in. the predicted transfer efficiencies E_{OG} calculated from the 1-in. oxygen-desorption data are about 25% (Figure 12). When calculated from the 10-in. oxygen data, the predicted transfer efficiencies become 12 to 15%. At the lower seal, S_{avg} of 0.9 to 1.0 in., the predicted efficiencies based upon the 1-in. oxygen data are 20 to 25% but only 8 to 10% based upon the 10-in. oxygen data.

It was found that the predicted transfer efficiencies E_{OG} for the acetic acid–water system, as calculated from the 1-in. oxygen data, agreed quite well with the measured Murphree efficiencies E_{MV} (Figure 10). If the predicted transfer efficiencies had been corrected for cross flow by the Lewis (*12*) equations, with no liquid mixing assumed in the direction of net liquid flow, the resulting predicted Murphree efficiency curve would have been about 15% higher than the measured curve. Hence, it was concluded that a great amount of liquid mixing did occur during the acetic acid–water tests. For this reason, the procedure of calculating sieve-plate transfer efficiencies based upon the 1-in.–long experimental plate with no correction made for cross-flow effects was adopted. All the predicted efficiencies shown in Figures 10, 11, and 12 were computed in this manner.

This procedure has been quite satisfactory for gas-phase–controlled systems (Figures 10 and 11). On larger diameter plates, where liquid mixing might be less than on the smaller plates, such a procedure should give conservative values for predicted plate efficiencies. In the case of a liquid-phase–controlled system, however, this procedure gives predicted plate efficiencies higher than measured. Hence at the present time it should be used only as a rough estimate of plate efficiency for liquid-phase–controlled systems.

As mentioned before, the Gerster approach takes into account all the factors now known to affect plate efficiency, including variations in plate design. When this approach was first presented, it appeared that after the effects of operating and design variables on the individual-phase efficiencies were determined on small-scale plates, it would then be possible to predict from such data efficiencies for any system on any size plate. Although the Gerster approach may still basically have such a potentiality, its utility is somewhat limited, for the present at least, because no quantitative value has been placed on the effect of the various degrees of liquid mixing which are encountered. On large-diameter plates operating with low vapor rates and high liquid rates, liquid mixing in the direction of net liquid flow is expected to be at a minimum, but on small plates operating with high vapor rates and low liquid rates, liquid mixing will be essentially complete. The former situation is handled by the Lewis (*12*) equations; in the latter situation the Murphree efficiency and the transfer efficiency are identical. The vast majority of cases of interest, however, will be somewhere between these two extremes.

Actually, mixing of liquid probably does not change the true efficiency of the plate. It does, however, reduce the total separation achieved across a plate because a reduction in the total driving force for mass transfer results from the mixing. It now appears that some quantitative definition of mixing, expressed as a function of plate design and operating variables, will have to be developed and related to concentration gradients on an an active plate before plate-efficiency predictions can be made with confidence for both gas- and liquid-phase–controlled systems from single-phase studies.

SUMMARY

Murphree vapor efficiencies have been measured on 18-in.-diam. sieve plates for the acetic acid–water system and for the methyl isobutyl ketone–water system at atmospheric pressure. In the former system the major resistance to mass transfer is in the gas phase; liquid-phase resistance to mass transfer is controlling in the latter. Murphree vapor efficiencies have also been determined for the aniline-nitrobenzene system, gas-phase resistance controlling, at 5 mm. Hg abs. on 6-in.-diam. sieve plates. Predicted values of over-all gas-phase transfer efficiency for each of these binary systems have been computed from pure-phase efficiencies according to the method suggested by Gerster et al. (*7, 8, 9*). A comparison between predicted and measured values shows good agreement for those cases in which the major resistance to mass transfer is in the gas phase. In the case of liquid-phase–controlled systems it is recommended that for the present this method be used only for obtaining a rough estimate of the actual plate efficiency. It is suggested that an unknown amount of liquid mixing in the direction of net liquid flow is the main factor contributing to the discrepancy between predicted and measured plate-efficiency values for liquid-phase–controlled systems. Further research on the mixing phenomena will be required before plate-efficiency predictions can be made with confidence for both gas- and liquid-phase–controlled systems from single-phase studies.

NOTATION

D = molecular diffusivity, sq. ft./hr.
E_{MV} = Murphree plate efficiency, over-all gas-concentration basis
E_{ML} = Murphree plate efficiency, over-all liquid-concentration basis
E_{OG} = transfer efficiency, over-all gas-concentration basis
E_{OL} = transfer efficiency, over-all liquid-concentration basis
F = F factor based on tower cross-section area, $F = v\sqrt{\rho_G}$
F_B = F factor based on bubbling area
G = gas mass velocity, lb. moles/(hr.)(sq. ft. of tower cross-sectional area)
L = liquid rate, (gal./min.)(ft. of plate width)
L' = liquid mass velocity, lb. moles/(hr.)(sq. ft. of tower cross-sectional area)
m = slope of equilibrium curve
N_G = number of gas-phase transfer units
N_L = number of liquid-phase transfer units
N_{Sc} = Schmidt number, $\mu/\rho D$
S_{avg} = average seal depth, in. of clear liquid
v = superficial linear vapor velocity, ft./sec.
x = mole fraction of designated component in liquid
y = mole fraction of designated component in vapor
μ = viscosity, lb./(ft.)(hr.)
ρ = density, lb./cu. ft.

Subscripts

L = liquid
G = vapor
o = pure-phase measurements

LITERATURE CITED

1. Baker, Theodore, and J. S. Stockhardt, *Ind. Eng. Chem.*, **22**, 376 (1930).
2. Chu, J. C., *Petroleum Proc.*, **6**, 39 (1951).
3. Colburn, A. P., *Ind. Eng. Chem.*, **28**, 526 (1926).
4. *Ibid.*, **33**, 459 (1941).
5. Drickamer, H. G., and J. R. Bradford, *Trans. Am. Inst. Chem. Engrs.*, **39**, 319 (1943).
6. Geddes, R. L., *ibid.*, **42**, 79 (1946).
7. Gerster, J. A., A. P. Colburn, W. E. Bonnet, and T. W. Carmody, *Chem. Eng. Progr.*, **45**, 716 (1949).
8. Gerster, J. A., W. E. Bonnet, and I. Hess, *Chem. Eng. Progr.*, **47**, 523 (1951).
9. *Ibid.*, **47**, 621 (1951).
10. Holtzlander, G. W., and J. W. Riggle, *A.I.Ch.E. Journal*, **1**, 312 (1955).
11. Jones, J. B., and C. Pyle, *Chem. Eng. Progr.*, **51**, 424 (1955).
12. Lewis, W. K., Jr., *Ind. Eng. Chem.*, **28**, 399 (1936).
13. Perry, J. H., "Chemical Engineers' Handbook," 3 ed., McGraw-Hill Book Company, Inc., New York (1950).
14. Silver, Leonard, *Trans. Inst. Chem. Engrs.* (*London*), **12**, 64 (1934).
15. Walter, J. F., and T. K. Sherwood, *Ind. Eng. Chem.*, **33**, 493 (1941).

Drying of Sand on a Hot Surface

R. W. LUDT

Michigan State University, East Lansing, Michigan

Constant layer moisture at the hot surface is found to exist during the constant-rate period of drying of sand on a hot surface in still air. It accounts not only for the constant-rate period of drying itself but also largely for the length of the period.

Temperature of the air-surface interface usually has minor effects on the rate of vaporization because equilibrium between vapor and the bed is not established during periods of rapid vaporization.

Numerical relationships have not been established.

Even though drying on a hot surface is used extensively in industry there seems to be no explanation of the mechanism in the literature. Further understanding of this mechanism could lead to the development of more efficient applications of hot-surface drying.

The theories of air drying have only limited application to hot-surface drying because of fundamental differences in the application of heat and the flow of material. In air drying, heat is supplied at the same surface from which vapor leaves, but in hot-surface drying it is supplied from the other side. In spite of this difference, it has been shown (*10*) that hot-surface drying as well as air drying gives drying-rate curves with constant-rate, first falling-rate, and second falling-rate periods. There must however be different reasons for this similarity. The purpose of these tests is to determine important factors which govern the drying of granular solids on a hot surface in still air and to show why hot-surface drying gives a drying-rate curve of the same general form as that for air drying.

Materials which may be dried include both hygroscopic and nonhydroscopic substances. In order to eliminate the effects that bound water might have upon the process, sand, a nonhygroscopic material of relatively uniform size and shape, is used to begin the study of hot-surface drying. The results can be regarded as applying to the pore moisture between small granules in a bed of material.

PREVIOUS WORK

Air Drying

Rates and theory for the air drying of numerous substances have been quite thoroughly investigated and reported (*1, 2, 13, 14, 16*). Ceaglske and Hougen (*3*) showed that water flow in sand during air drying is due primarily to capillary forces. They used the method of Haines (*6*) to determine the effect of suction in the sand on percentage of saturation, and Haine's terminology to explain how water is held between sand particles at different stages of drying. Complete saturation of the cells between particles is called the *capillary state*. The *funicular state* occurs when the pores are emptied but the particles are covered by a continuous water film. The *pendular state* is formed in the last stages of drying when the small amount of water present is held at the points of contact of the particles. Pearse, Oliver, and Newitt (*12*) summarized and expanded the theory of air drying the granular materials and of the movement of water within the bed. They explained how the movement of water between particles in the bed depends upon gravitational, capillary, and frictional forces, the relative effect of which is determined by particle size and shape.

From the work referred to, an outline of the mechanism during the air drying of sand can be stated much as follows.

The bed is made up of fine particles between which are interconnecting cells or pores of various size. Evaporation during the capillary state causes a curvature of the water surface in the pores and sets up suction within the bed. When "entry suction" is attained, the continuous water film is broken and water is pulled down the large capillaries and supplied to the surface through the small capillaries. As the capillaries are emptied of water, liquid is replaced by vapor and air. Constant-rate drying occurs during this period and continues until surface particles are no longer supplied with enough water to cover them.

The first falling-rate period begins with this critical moisture content, which often occurs when the larger pores are emptied but the smaller cells still contain water. The second falling-rate period occurs when the remaining water is in the pendular state. Since the water does not present a continuous film in the pendular state, heat for vaporization must be transferred from the heated air down through the bed. Vaporization takes place within the bed and vapor passes out to the air surface.

Hot-surface Drying

For the vacuum drying of Prussian blue on heated shelves Ernst, Ardern, Schmied, and Tiller (*4*) found a constant-rate period followed by a variable rate. At lower vacuum the variable rate is irregular until a definite falling-rate period is reached. At higher vacuum the customary falling rate immediately follows the constant-rate period. In the vacuum drying of Sil-O-Cel, Ernst, Ridgway, and Tiller (*5*) obtained the customary type of drying curves. They showed that in vacuum shelf drying heat is supplied not only from the bottom but also from the top of the cake.

Hougen, McCauley, and Marshall (*8*) presented a limited number of curves for the moisture distribution in sand and in lead shot while drying on a hot surface but did not give pertinent information with regard to conditions. McCready (*10*), using a hot surface for drying paper pulp, showed a constant-rate period followed by first and second falling-rate periods. King and Newitt (*9*) reported a pseudoconstant rate in place of a constant rate while drying glass beads on a hot surface and in a stream of air. The pseudoconstant rate, which is a very gradual falling rate, is followed by first and second falling-rate periods.

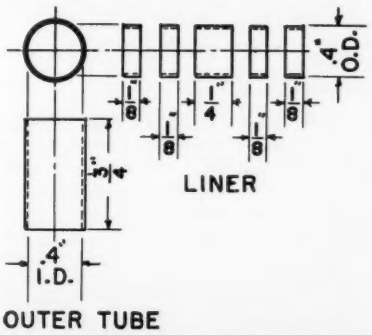

Fig. 1. Sampler for sand-layer moisture.

EQUIPMENT

Drying was carried out on a ¾-in. thick by 12-in.-diam. steel heating plate. The heating plate rested on a similar steel plate, which in turn rested on an electric hot plate. Insulation around the plate edges helped to give an even temperature distribution across the plate. Small holes were drilled radially halfway between the two faces of the heating plate. One hole terminated at the center of the plate and the others on graduated radii at 1-in. intervals. At the end of each hole was welded a 20-gauge fiber-glass–covered copper-constantin thermocouple. The thermocouple wells within the plate were packed with asbestos fiber.

The hot-plate temperature was regulated by resistance coils in series with the hot plate. A voltmeter across the hot-plate coils indicated voltage to the hot plate.

PROCEDURE

Ottawa sand of 40-60 U. S. standard mesh with a void volume of 40.6% was used in all tests. Most of the data were taken with a sand-bed thickness of ¾ in. One drying-rate and one temperature-distribution series were run with a sand bed ¼-in. thick.

Wetted-sand samples were put in a steel ring of 6.25-in. diameter and then placed on the heating surface. Since movement of the sand disturbed the even distribution of moisture, the bed was again saturated while it was on the hot plate. A cardboard cover was then supported 6 in. above the sand surface.

Atmospheric pressure, temperature, and wet-bulb temperature of the surrounding air were taken and reported with the data.

On the basis of the work of McCready

(*10*), atmospheric conditions above the sample are of little importance. When using variations of air temperature, humidity, and velocity, he found that temperature of the air had little effect and that, provided that the difference in temperature between hot surface and drying air was large, humidity had little effect.

The present data were also used to find the effects of atmospheric conditions. Plots of drying rate vs. temperature and drying rate vs. atmospheric pressure indicated no correlation. A plot of rate vs. relative humidity indicated a slight trend toward variation that was within variations of the data. Since the effects of all these variables seemed insignificant with respect to the accuracy of the data, they were neglected. These plots are not shown.

Moisture

While the sand was drying, samples were removed at intervals to determine moisture. It was found that any pressure on the sand changed the moisture distribution in the surrounding sand. Sampling tubes were placed in the sand at the beginning of the run and were spaced to avoid moisture changes in surrounding rings. Eight or nine glass sampling tubes were used for an individual run on drying rate.

Sampling tubes were also used to determine the moisture of the layers. The assembly, shown in Figure 1, was made up of a brass tube of 0.4-in. diameter by ¾-in. length into which were fitted five sectional micarta tubes or liners. When a sample was taken, the entire sampling unit was removed from the sand and the micarta tubes were slipped from the brass tube and separated in individual-layer samples. Results with the brass-micarta unit were compared with those with glass tubes and found to be within the general accuracy. The greatest source of error seemed to be caused by exposure of the sand between time of removal from the hot plate and time that the sample was placed in a closed weighing bottle. Manipulation was speeded up with the use of the brass-micarta unit.

All moisture values were reported on the dry basis.

The method of Haines (*6*) was used to determine the suction-moisture relationship for sand of ¾-in. thickness at room temperature. This method was used and described by Ceaglske and Hougen (*3*).

Temperatures

Temperatures were taken with no. 20 copper-constantin thermocouples provided with a cold junction. Readings, made on a Leeds and Northrup Portable Precision Potentiometer, were recorded to the nearest degree. Thermocouples for the measurement of layer temperatures in the sand were mounted in a frame built of micarta and brass. The hot junctions extended ¾ in. from the micarta face into the sand. The entire frame was covered with sand and the wires were passed through the sand at the same level for 4 in. The same thermocouples suspended vertically in the sand at different levels gave errors up to 6°F.

Layer temperatures were taken in separate tests in a range approaching temperatures used in the drying-rate tests. Plate temperatures midway between the faces of the heating plate were taken at the center and at radii of 1 and 2 in. The three values were averaged and reported to the nearest degree as plate temperature. This plate temperature did not give surface temperatures and should be regarded as approximate surface temperature.

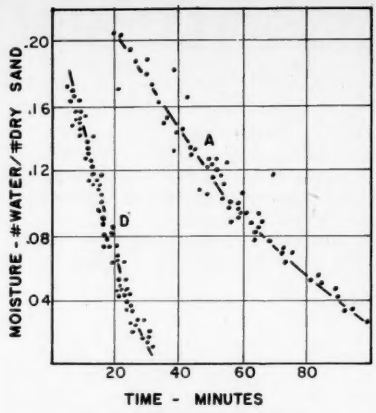

Fig. 2. Drying-rate data.

	Curve *A*	Curve *D*
Average hot-plate temperature	165°F.	168°F.
Surroundings:		
Barometer, mm.	740, +6, −11	740, +16, −9
Temperature, °F.	79, +9, −7	74, +4, −3
Relative humidity, %	38, +26, −22	24, +13, −9
Bed depth, in.	3/4	1/4

Presentation of Data*

From six to nine drying tests were used for each series of drying-rate data. Data from each of these tests were plotted individually and also on a common moisture-time graph. The composite data only are shown in Figures 2 and 3. Drying rates were obtained by measuring the slopes. Rates from the composite data were compared with the averages of the individual runs and were found to be within reasonable agreement. The drying rates are plotted in Figures 4 and 5 with points from the composite data.

From two to four runs were used for each series of layer moisture. The data for a given sand depth were plotted on a common-layer-moisture–compositive-moisture graph, a typical example of which is shown in Figure 6. A curve was drawn through the points; from the smoothed curve, readings were taken at given moisture contents to give the values shown in Tables 1, 2, and 3.

RESULTS

Drying Rates

Drying-rate curves for sand of ¾-in. thickness (Figure 4) show constant-rate periods followed by falling-rate periods. At the lower plate temperatures the constant-rate period terminates at about 10% moisture, as compared with 6% moisture for a plate temperature of 220°F. This agrees with the conclusions of Ernst, Ardern, Schmied, and Tiller (*4*) on Prussian-blue vacuum drying. They found that increased plate temperatures give a longer constant-rate period.

The drying-rate curve for sand of ¼-in. thickness and 168°F. plate temperature (Figure 5) also has a critical point at about 6% moisture. A comparison with the curve for sand of ¾-in. thickness in this temperature range shows that the thinner bed gives a longer constant-rate period but about the same constant rate. This is a conclusion that should not be extended to other bed

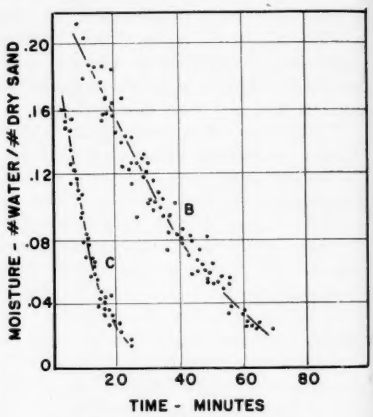

Fig. 3. Drying-rate data.

	Curve *B*	Curve *C*
Average hot-plate temperature	182°F.	220°F.
Surroundings:		
Barometer, mm.	740	739, +7, −11
Temperature, °F.	80	77, +6 −14
Relative humidity, %	26	35, +24, −14
Bed depth, in.	3/4	3/4

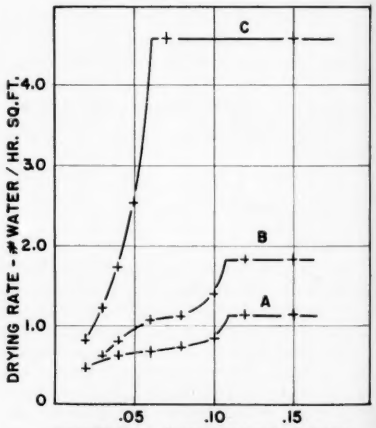

Fig. 4. Hot-surface drying rates.

Curve	Bed depth, in.	Plate temperature, °F.
A	3/4	165
B	3/4	183
C	3/4	220

*Tabular material has been deposited as document 5301 with the American Documentation Institute, Photoduplication Service, Library of Congress, Washington 25, D. C., and may be obtained for $2.50 for photoprints or $1.75 for 35-mm. microfilm.

thicknesses because thickness is probably a factor in this type of drying.

Increased plate temperature increases the value of the constant rate, but other factors also appear to influence the rate.

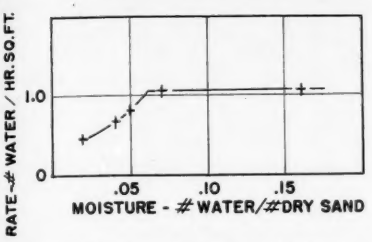

Fig. 5. Hot-surface drying rate: plate temperature, 168°F.; bed depth, 1/4 in.

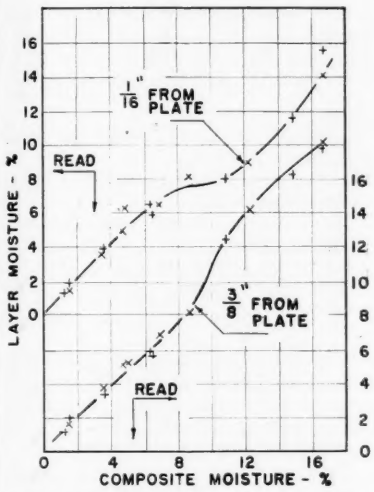

Fig. 6. Typical layer moisture: average hot-plate temperature, 213°F.; sand depth, 3/4 in.; moisture, lb. water/lb. dry sand.

A direct correlation is not apparent from the data on drying rates alone.

Moisture Distribution

Values for the moisture-distribution curves (Figures 7, 8, and 9) are taken from Tables 1, 2, and 3. Plate temperatures for the runs average 161°, 204°, and 213°, respectively, but the sand thickness for each is 3/4 in.

Table 1.—Smoothed Layer Moistures

Average Plate Temperature: 161°F.

Surroundings: 739 mm., 74°F. (+15°, −2°), 46% relative humidity (+3, −4)

Composite moisture Distance from plate, in.	0.190	0.180	0.160	0.140	0.120	0.100	0.080	0.060
1/16	0.194	0.170	0.152	0.144	0.136	0.120	0.096	0.072
3/16	0.193	0.183	0.162	0.136	0.110	0.090	0.070	0.053
6/16	0.199	0.193	0.168	0.133	0.108	0.085	0.068	0.059
9/16	0.190	0.180	0.162	0.147	0.128	0.105	0.081	0.060
11/16	0.175	0.163	0.148	0.140	0.134	0.120	0.088	0.062

Table 2.—Smoothed Layer Moistures

Average Plate Temperature: 204°F.

Surroundings: 734 mm. (+3, −3), 84°F. (+4°, −7°), 50% relative humidity (+13, −10)

Composite moisture Distance from plate, in.	0.170	0.150	0.130	0.110	0.090	0.070	0.050	0.030	0.010
1/16	0.158	0.142	0.128	0.114	0.098	0.078	0.057	0.033	0.008
3/16	0.166	0.147	0.125	0.100	0.075	0.057	0.042	0.029	0.016
6/16	0.185	0.163	0.130	0.102	0.082	0.064	0.047	0.030	0.012
9/16	0.172	0.154	0.135	0.116	0.097	0.077	0.056	0.034	0.007
11/16	0.152	0.145	0.137	0.127	0.107	0.083	0.056	0.029	0.006

Table 3.—Smoothed Layer Moistures

Average Plate Temperature: 213°F.

Surroundings: 738 mm. (±4), 79°F. (±3°), 53% relative humidity (±11)

Composite moisture Distance from plate, in.	0.170	0.150	0.130	0.110	0.090	0.070	0.050	0.030	0.010
1/16	0.160	0.120	0.099	0.086	0.082	0.071	0.054	0.033	0.013
3/16	0.166	0.147	0.108	0.083	0.078	0.060	0.043	0.025	0.008
6/16	0.182	0.168	0.150	0.125	0.077	0.065	0.047	0.030	0.011
9/16	0.171	0.161	0.148	0.125	0.098	0.075	0.053	0.031	0.010
11/16	0.161	0.150	0.136	0.120	0.103	0.083	0.047	0.021	0.007

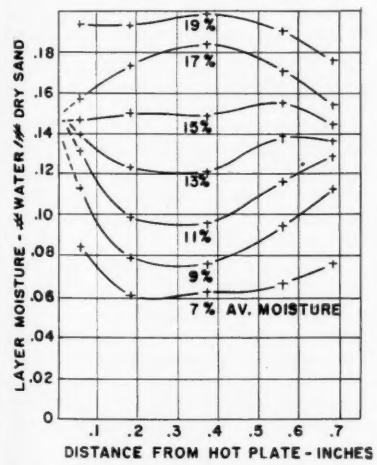

Fig 7. Moisture distribution in sand bed.

Average hot-plate temperature	161°F.
Surroundings:	
Barometer, mm.	739
Temperature, °F.	78, +11, −6
Relative humidity, %	46, +3, −4
Bed depth, in.	3/4

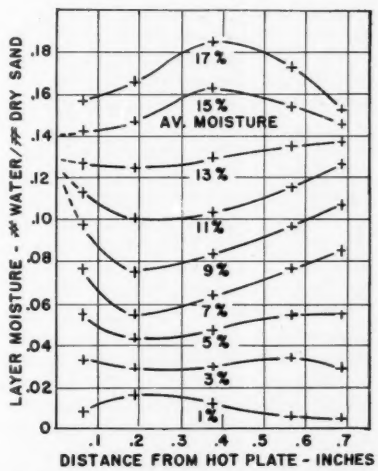

Fig. 8. Moisture distribution in sand bed.

Average hot-plate temperature	202°F.
Surroundings:	
Barometer, mm.	734, +3, −3
Temperature, °F.	84, +4, −7
Relative humidity, %	50, +13, −10
Bed depth, in.	3/4

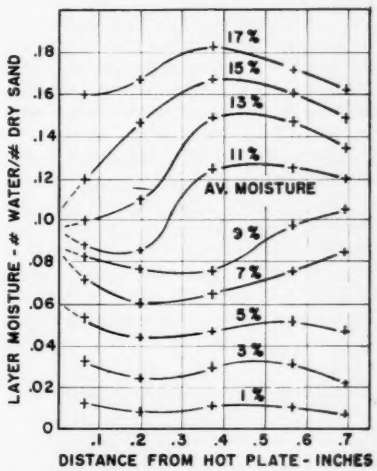

Fig. 9. Moisture distribution in sand bed.

Average hot-plate temperature	213°F.
Surroundings:	
Barometer, mm.	738, +4, −4
Temperature, °F.	80, +2, −3
Relative humidity, %	53, +11, −11
Bed depth, in.	3/4

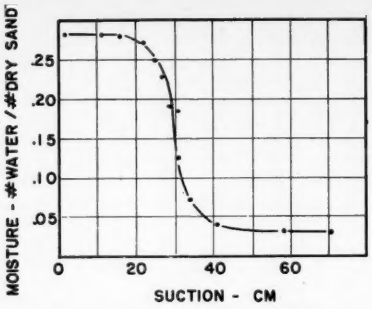

Fig. 10. Suction potential–moisture.

Surroundings:	
Barometer, mm.	738
Temperature, °F.	87
Relative humidity, %	70
Bed depth, in.	3/4

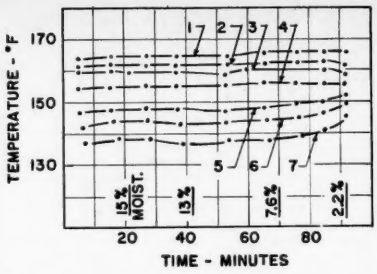

Fig. 11. Typical plate and sand temperatures.

Curve	1	2	3	4	5	6	7
Distance from plate, in.	Plate	0.06	0.15	0.28	0.45	0.56	0.71

Moisture is expressed in lb. water/lb. dry sand

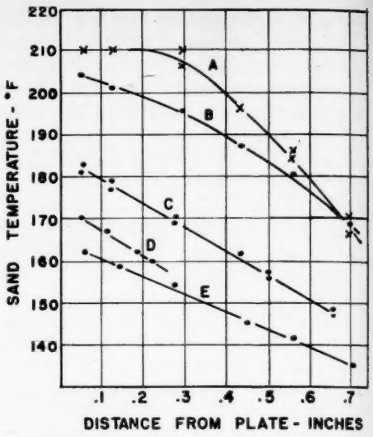

Fig. 12. Sand temperatures above hot plate.

Curve	A	B	C	D	E
Bed depth, in.	3/4	3/4	3/4	1/4	3/4
Plate temperature, °F.	211	208	181-83	175-76	165-66
Range, % moisture	19-11	6	17-3	16-6	17-3
Surroundings:					
Barometer, mm.	746	746	740	742	736
Temperature, °F.	92	92	88	84	78
Relative humidity, %	42	42	29	24	39

Moisture is expressed in lb. water/lb. dry sand.

At high moistures, above 18%, the bed tends to rise from the plate owing to the formation of vapor. At about 16% moisture the bed settles down and the normal constant-rate period begins. The moisture-distribution curves become convex with the maximum moisture near the center of the bed. At intermediate moistures they become or tend to become concave. At very low moistures the curves again become convex. The last case is not clearly shown on the charts but is apparent from inspection of samples tested. Moisture right at the hot surface and at the air surface of the bed is not measured directly, but extrapolation gives an indication of the values.

With a plate temperature of 161°F. moisture at the hot surface appears to remain constant at about 15% between the composite moisture contents of 17 and 10%. A constant layer moisture at the hot surface during the period of constant-rate drying is evident in the runs at other temperatures.

Extrapolated values of moisture at the hot surface for all plate temperatures are tabulated in Table 4. The constant hot-surface layer moisture decreases with increased plate temperature and persists during the period of constant-rate drying as indicated by the drying-rate curves.

Vaporization takes place at the hot surface where heat is supplied. The rising vapor displaces water from the large pores in an amount which depends upon the amount of vapor flowing. At higher plate temperatures more water is displaced, resulting in a lower constant hot-surface layer moisture.

Water displaced from the region of the hot surface is forced to the center of the bed, which then acts as a reservoir to supply the hot surface through the small pores. As long as a sufficient supply of water exists and the rate of vaporization is constant, constant hot-surface layer moisture is maintained.

Inspection of the moisture-distribution curves shows that a concave curve with low moisture near the center of the bed is the forerunner of the first falling-rate drying period. The location of the critical point is a function of both the constant hot-surface moisture and the moisture supply at the center of the bed. Under the conditions of these moisture-distribution tests, low hot-surface moisture corresponds to low critical moisture and a long constant drying-rate period.

Table 4.—Moisture During Constant-rate Drying

Bed Thickness: 3/4 in.

Plate temperature, °F.	Moisture: lb. water/lb. dry sand Hot-surface layer	Range for constant layer moisture	Range for constant rate
213	0.09	0.15–0.07	0.16–0.06
203	0.13	0.15–0.10	0.17–0.105
161	0.15	0.17–0.10	0.17–0.11

Suction Potential

The suction–water-content curve (Figure 10) is shown for sand of 3/4-in. thickness at room temperature. It can be expected to give an indication of the location of critical points in the drying-rate curves, but correlation with hot-surface drying is limited. First it was run at room temperature and not at the drying temperature. Second, the moisture distribution in sand is not the same for the test as for hot-surface drying.

The suction-moisture curve shows that the sand is saturated at about 28% moisture. Between 28 and 11% moisture the large pores are being emptied of water. Between 20 and 6% the curve approaches a straight line with only a small increase in suction. It represents a period when constant-rate drying should be possible if other influences are not more important. All these experimental drying-rate data show a constant rate in this range of moisture.

Between 10 and 4% moisture, suction increases quite rapidly with decrease in moisture because the smaller capillaries are being emptied. It is the period during which the critical point of the drying-rate curve can be expected to occur. The exact location of the critical point will be determined by the constant layer moisture at the hot surface. At 9% constant layer moisture the critical point occurs at about 6%; at 15% critical layer moisture it occurs at about 10%.

Between 4 and 3% moisture, suction increases very rapidly with decrease in moisture. The smallest capillaries are about empty. In a very short time liquid water will touch the particles only at points of contact of the particles. The second falling-rate period will have begun.

Temperature

Temperature-time data for sand of 3/4-in. thickness at a plate temperature of 165°F. are shown in Figure 11. These data as well as those for other runs are shown by temperature-sand depth plots in Figure 12.

Curve *A* of Figure 12 shows the temperature-depth relationship for sand at a plate temperature of 211°F. between moisture contents of 19 and 11%. The distance that the uniform temperature extends up in the sand decreases with decrease in moisture. The curve gradually changes to the form of curve *B* at 6% moisture.

At plate temperatures of 165° and 185°F. the sand temperatures are essentially linear with sand depth and at given depths remain nearly constant over moisture ranges of 15 to about 3%. This range of moisture includes both constant- and first falling-rate periods. Below 3% moisture, which represents the pendular

state of moisture, the temperature-depth relationship becomes nonlinear.

During the constant- and first falling-rate periods heat is transmitted through the bed principally by the latent heat of the vapor. The vapor at a given point tends to go to physical and thermal equilibrium with the wet bed. This results in the condensation of some vapor as it rises through the bed because of decreasing temperatures. The gradual condensation of vapor combines with liquid in the bed and flows down to the hot surface to help replace liquid which has been vaporized. A large flow of liquid to the hot surface is indicated by Tambling (*15*), who by using salt solution in place of water showed that at 12% moisture 60% of the salt is concentrated near the hot surface and about 15% at the air surface. The flow of liquid concentrates most of the soluble material at the hot surface, where most of the vaporization takes place. Some movement of liquids to the air surface also occurs.

The temperature-depth relationship for sand of ¼-in. depth at a plate temperature of 176°F., shown with curve *D*, is also linear until the moisture is decreased to about 6%. This curve may be compared with curve *E* for sand of ¾-in. depth. Plate temperatures for the two are different but are within the same range and should give about the same constant-rate drying. For sand of ¼-in. depth the air interface temperature is about 159°F., corresponding to a vapor pressure of 4.6 lb./sq. in. abs. For sand of ¾-in. depth, the air interface temperature is about 133°F.; if an adjustment is made for difference in plate temperatures, 141°F. can be used. It corresponds to a vapor pressure of 2.9 lb./sq. in. abs. These vapor pressures represent the partial pressure of water vapor at saturation at the temperature of the respective air-sand interfaces. Vapor in excess of these relative amounts would be condensed in the bed if equilibrium were established. Under this condition the drying rates should tend to be proportional to 4.6 and 2.9, the vapor pressures. Actually the vapor does not condense to that extent, for the constant drying rates are shown by the drying-rate curves to be about the same. This comparison indicates that equilibrium between the vapor and the sand is not established during periods of high rate of vaporization; it emphasizes the importance of plate temperature during hot-surface drying.

Drying Process

Combining the results of previous work with the foregoing results gives a description of the mechanism of the drying of sand on a hot surface.

When the bed is saturated with water, the pores between the sand particles are filled with water. Contact with the hot surface causes an evolution of vapor which may lift the bed from the plate. At higher plate temperatures blow holes, which allow much of the vapor to escape, may form. After sufficient water has been vaporized, the bed settles and the normal constant rate of drying begins.

During the constant-rate period vapor formed at the hot surface forces its way up through the large pores of the sand by displacing water. The extent of water displacement governs the moisture content of the sand in contact with the hot surface. Since the rate of vaporization is constant, constant hot-surface layer moisture persists throughout this constant-drying-rate period. This accounts for the constant drying rate which exists during hot-surface drying.

At a higher plate temperature more vapor is formed and must force its way through the large pores by displacing more water from them. The constant hot-surface moisture decreases with increase in plate temperature and is automatically regulated to allow free passage of the vapor formed.

Vapor rising from the hot surface passes through sand of decreasing temperature as it approaches the air interface. Some of the vapor is condensed and the condensate combines with water in the bed to increase the supply available for flow through the small pores to the hot surface. The constant rate period continues as long as sufficient water is available in the center of the bed to maintain the constant hot-surface moisture.

At high rates of vaporization the vapor passes through the sand at such a rate that it does not go to physical and thermal equilibrium with the sand bed. The result is that plate temperatures rather than air-interface temperature are the controlling factor for constant drying rate. Influences such as conduction of heat through the sand, convection from the air interface, and the passage of air through the bed can be expected to have some effects but they are minor.

Besides the cycle for the circulation of water within the bed, there must also be a cycle for air. The large pores contain not only vapor but also air. Air enters the top of the bed, mixes with vapor in the large pores, and flows out into the air as a mixture.

The first falling-rate period begins when a constant hot-surface moisture can no longer be maintained. If the constant hot-surface moisture is high, there is a tendency for the critical moisture to be high; if the constant hot-surface moisture is low, the critical moisture of the drying-rate curve is low.

The second falling-rate period begins when the pendular state of water is reached. Vaporization then occurs to a great extent by heat of conduction through the bed. Heat transfer through the bed is a function of not only the normal heat of conduction but also the flow of hot vapors to a zone of lower temperatures. Harbert, Cain and Huntington (*7*) show that when heat is transferred from a hot surface through wet sand the flow of heat cannot be accounted for entirely by conduction.

CONCLUSIONS

1. Constant layer moisture at the hot surface during constant-rate drying is instrumental in maintaining the constant rate during hot-surface drying.
2. The constant hot-surface layer moisture is an important factor in determining the critical moisture of the drying-rate curve.
3. Plate temperature is normally the most important factor in determining the constant drying rate. It also determines the constant hot-surface layer moisture.
4. Bed thickness influences the critical moisture but within the limits of these tests has little effect on the constant drying rate.
5. Equilibrium between the vapor rising through the bed and the water on the wet sand does not exist during periods of high vaporization rate.

LITERATURE CITED

1. Badger, W. L., and W. L. McCabe, "Elements of Chemical Engineering," 2 ed., McGraw-Hill Book Company, Inc., New York (1936).
2. Brown, G. G., and associates, "Unit Operations," John Wiley and Sons, New York (1950).
3. Ceaglske, N. H., and O. A. Hougen, *Trans. Am. Inst. Chem. Engrs.*, **33**, 283 (1937).
4. Ernst, R. C., D. B. Ardern, O. K. Schmied, and F. M. Tiller, *Ind. Eng. Chem.*, **30**, 1119 (1938).
5. Ernst, R. C., J. W. Ridgway, and F. M. Tiller, *ibid.*, **30**, 1122 (1938).
6. Haines, W. B., *J. Agr. Sci.*, **17**, 264 (1927); **20**, 97 (1930).
7. Harbert, W. D., D. C. Cain, and R. L. Huntington, *Trans. Am. Inst. Chem. Engrs.*, **37**, 267 (1941).
8. Hougen, O. A., H. J. McCauley, and W. R. Marshall, Jr., *ibid.*, *Am. Inst. Chem. Engrs.*, **36**, 183 (1940).
9. King, A. R., and D. M. Newitt, *Trans. Inst. Chem. Engrs.*, **33**, 64 (1955).
10. McCready, D. W., *Paper Trade J.*, **101**, 66 (September, 1935).
11. Oliver, T. R., and D. M. Newitt, *Trans. Inst. Chem. Engrs.*, **27**, 9 (1949).
12. Pearse, J. F., T. R. Oliver, and D. M. Newitt, *ibid.*, **27**, 1 (1949).
13. Perry, J. H., "Chemical Engineers' Handbook," 3 ed., McGraw-Hill Book Company, Inc., New York (1950).
14. Sherwood, T. K., *Trans. Am. Inst. Chem. Engrs.*, **32**, 150 (1936).
15. Tambling, T. N., M.S. thesis, Mich. State U., East Lansing (1953).
16. Walker, W. H., W. K. Lewis, W. H. McAdams, and E. R. Gilliland, "Principles of Chemical Engineering," 3 ed., McGraw-Hill Book Company, Inc., New York (1937).

Presented at A.I.Ch.E. Pittsburgh meeting

Heat Transfer Coefficients for Condensing Organic Vapors of Pure Components and Binary Mixtures

BERNARD S. PRESSBURG and JAMES B. TODD,

Louisiana State University, Baton Rouge, Louisiana

The behavior of the film coefficient of heat transfer for the condensation of organic vapor mixtures was investigated experimentally to establish a satisfactory basis for applying the Nusselt equation to binary systems. Five ideal and nonideal pairs, all of which gave miscible condensates, were studied; the work was carried out under conditions of almost total condensation on a horizontal condensing surface designed to comply as rigidly as possible with the conditions for which Nusselt's equation is valid.

The same behavior was observed for all systems and all concentrations studied: the experimental coefficients fell between those for the pure components and followed the behavior pattern for pure components when the temperature difference was taken as that between the *bubble point* of the condensate and the surface temperature, rather than between the dew point or the measured vapor temperature and the surface temperature. Correlation of the film coefficient showed it to vary approximately linearly with composition if the coefficients were compared at a constant value of the temperature difference, defined as above. This permits determination of the coefficient for a mixture by interpolation between the coefficients for the pure components, which are easily obtained, in preference to making the calculations with the properties of the mixture obtained by laborious and uncertain weighting of the corresponding properties of the pure components.

When results are interpreted in the light of the theories of Colburn and Drew, the presence of a vapor-phase resistance to heat and mass transfer, as postulated by them, is indicated.

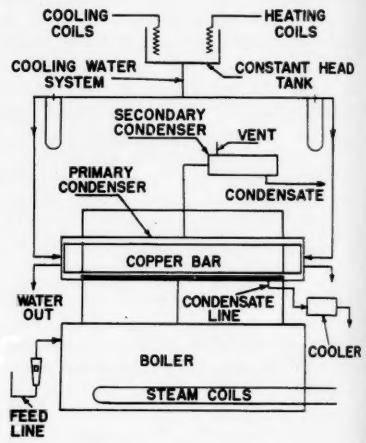

Fig. 1. Test assembly.

The Nusselt equation (*8*) is the most widely used method for predicting the coefficient of heat transfer for condensing vapors. Its validity for pure materials has been established by many investigators (*9, 10, 13*) and its concepts have been extended to apply to mixtures in which one component is noncondensable and to mixtures in which the condensate consists of two immiscible liquids (*1, 2*). However, the condensation of mixtures which give a condensate with a single liquid phase has received a minimum of attention despite the frequency with which this situation occurs in industry. Colburn and Drew (*3*) analyzed the principles involved and developed theoretical relations predicting the behavior of condensing mixtures; Wallace and Davidson (*18*) reported data for the system ethanol-water which gave limited verification to the Colburn-Drew theories. Accordingly, this research was undertaken to provide additional data which would test the Colburn-Drew theory and to establish an accurate and practical method of applying it to design.

APPARATUS AND PROCEDURE

The test assembly, shown in Figure 1, consisted of a boiler which generated the vapors, a horizontal primary condenser on which the test data were obtained, a secondary condenser into which a small amount of excess vapor was vented, and a water-coolant system.

The primary condensing surface was a 4-in. copper cylinder 3 ft. long, installed concentrically in a 6-in. insulated steel pipe which formed the vapor space as shown by Figure 2. Coolant circulated through six $\frac{5}{8}$-in. holes drilled longitudinally through the cylinder, entering three of the channels at one end and three at the other in accordance with the method first used by Othmer and White (*11*) to approach isothermal conditions. As shown by Figure 2, end effects were minimized by collecting the condensate from the center 28 in. and withdrawing this for weighing and analysis.

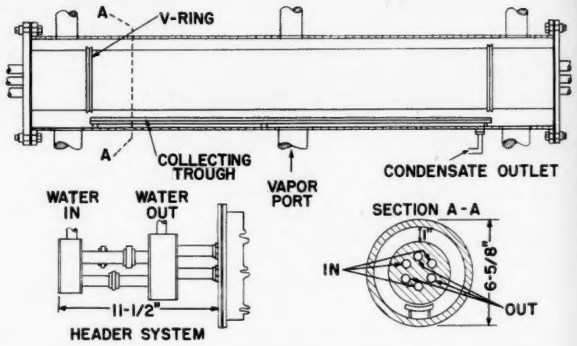

Fig. 2. Condensing surface.

Surface temperatures were measured by ten embedded thermocouples located at various circumferential and longitudinal positions as shown in Figure 3. Installation and additional mechanical details are given in the Appendix.*

All work was carried out at atmospheric pressure plus the 1 or 2 in. of water pressure necessary to maintain the excess vapor flow to the secondary condenser. For each material and concentration a series of tests was made with the temperature difference across the condensate film as the primary variable. This could be controlled over the

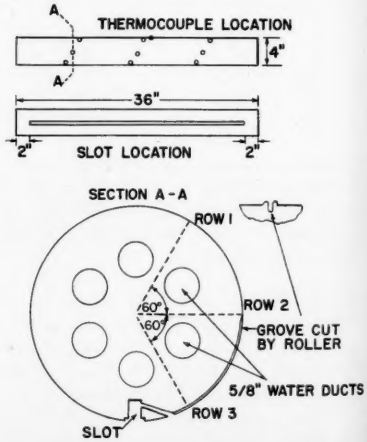

Fig. 3. Thermocouple installation.

*The Appendix has been deposited as document 5302 with the American Documentation Institute, Photoduplication Service, Library of Congress, Washington 25, D. C., and may be obtained for $1.25 for photoprints or 35-mm. microfilm.

J. B. Todd is now with the Kaiser Aluminum and Chemical Corporation, New Orleans, Louisiana.

range of 7° to 50°F. by regulating the coolant-water temperature and rate. During each test all thermocouple readings and condensation rates were observed at frequent intervals and any tests showing a significant variation between start and finish were discarded.

Seven organic materials and five binary mixtures of these were studied. To minimize the possibility of fouling of the surface with time, the general procedure followed was to test two pure materials, then mixtures of these. The source and properties of the materials used are shown below; because of the quantities required, technical grades were used in preference to reagent grade.

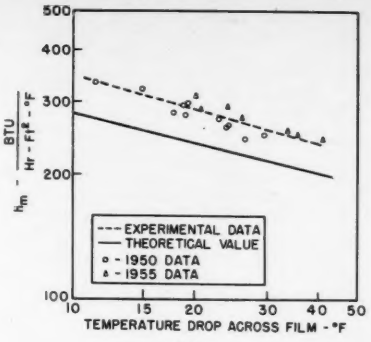

(4)

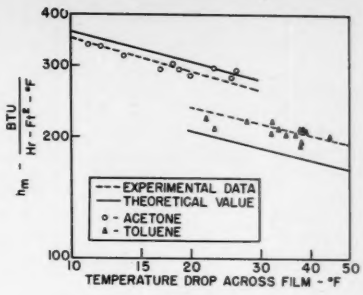

(5)

Figs. 4, 5, 6. Variation of heat transfer coefficient with temperature drop across film: (4) benzene, (5) toluene and acetone, (6) alcohols.

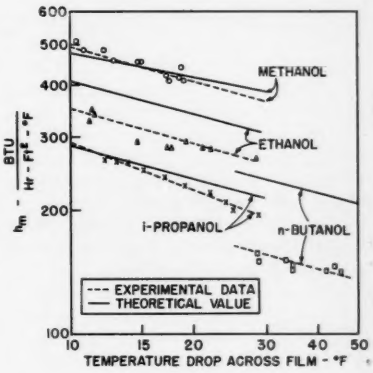

(6)

Physical Properties

Material	Source	Density, g./cc. at 25°C. Literature	Density, g./cc. at 25°C. As used	Refractive index N_D^{25} Literature (*12, 15*)	Refractive index N_D^{25} As used
Benzene	Matheson Chem. Co.	0.879	0.8773	1.4980	1.4875
Toluene	General Chem. Co.	0.8623	0.8635	1.4941	1.497
Acetone	U. S. I. Chem. Co.	0.7920 at 20°	0.7917 at 20°	1.3566	1.3555
Methanol	Allied Chem. & Dye	0.7866	0.7868	1.3267	1.3268
Ethanol	U. S. I. Chem. Co.	0.7894	0.7897	1.3595	1.3588
i-Propanol	Allied Chem. & Dye	0.7812	0.7814	1.3758	1.3750
n-Butanol	Carbide & Carbon Chem.	0.8096	0.8091	1.3990	1.3966

RESULTS

General Observations

As observed through sight glasses in the vapor jacket, the condensate formed a continuous film which drained from the bar in a smooth, uniform manner in most tests. Exceptions were noted in the case of methyl alcohol–benzene mixtures, which gave an uneven drainage pattern at low condensation rates, and in many tests in which the temperature difference was about 40° to 50°F.; in the latter case the condensate could be seen to swirl and otherwise deviate from smooth flow.

Vapor velocities in the annulus around the condensing surface were calculated and found to have a maximum value less than 1 ft./sec.; the more usual value was about 0.5 ft./sec. at the inlet and must have fallen off rapidly as the vapors condensed. In general, the vapor rate to the secondary condenser was adjusted to be approximately 10% of that on the primary surface to prevent the accumulation of any noncondensables evolved from the boiling liquid and also to provide a slight positive pressure to prevent the entry of air. Thus the velocity of the vapor leaving the primary condenser was about 0.05 ft./sec.

The temperature distribution shown in Table 1 is typical of that found in the course of the work. In ten tests, chosen at random, the highest difference between any two thermocouple readings was 5+°F.; more commonly, the range was less than 3°F. between extremes, or approximately 18% of the average Δt, the standard deviation varying from 0.5° to 3°F., or 3 to 17% of the average Δt. Further analysis of these tests was made to determine the mean deviation of each thermocouple position from the average of all ten embedded thermocouple readings for that test; the results are summarized:

Position	Average deviation, °F.
Top of cylinder (1 thermocouple)	+1.37
First horizontal row (3 thermocouples)	+0.32
Middle horizontal row (3 thermocouples)	+0.06
Bottom horizontal row (3 thermocouples)	−0.79

Table 1. Typical Temperature Distribution and Test Data

	163.6°F.	
162.7	162.7	163.8
162.5	162.5	163.2
161.9	160.8	162.3

(Note: temperatures shown above correspond to thermocouple locations shown in Figure 3)

Condensing vapor	Benzene
Average surface temperature	162.6°F.
Observed vapor temperature	176.7°F.
Δt	14.1°F.
Condensation rate	434 g./min. = 57.5 lb./hr.
Reynolds number ($4\Gamma'/\mu$)	121.5
Heat flow	9,750 B.t.u./hr.
h_m (experimental	289 B.t.u./(hr.)(sq. ft./°F.)
h_m (calculated for same condensation rate)	266 B.t.u./(hr.)(sq. ft./°F.)

This temperature pattern is explainable by the variation in the local coefficient with radial position around the bar. If, as Nusselt predicted, the coefficient is highest at the top, where the cumulative amount of condensate is a minimum, the total thermal resistance between the vapor and an isothermal plane within the copper bar is a minimum, and the local heat flux is a maximum. As the condensate runs down the face of the cylinder, it increases in thickness and thermal resistance, and the heat flux decreases; since the metal resistance is substantially the same at all radial positions, the temperature difference across it decreases and the surface temperature is thus cooler, as indicated.

Since the magnitudes of these deviations was generally small relative to the average temperature difference, and since average, rather than point, coefficients were desired, the arithmetic average of the ten embedded thermocouples was used as the surface temperature in determining the temperature difference for use in Newton's equation:

$$h_m = q/A\Delta t \qquad (1)$$

PURE COMPONENTS

Tests were made with pure components for two reasons: to compare the results

Table 2. Summary of Results—Pure Compounds

Material	Δt, °F.	Range of values $4\Gamma'/\mu$	h_m, B.t.u./(hr.)(sq. ft./°F.)	Correlation of experimental data
Benzene	7.0–29.5	105–203	251–480	$h_m = 289(\Delta t)^{-0.284}$
Toluene	21.9–53.6	146–377	186–239	$h_m = 477(\Delta t)^{-0.235}$
Methanol	8.3–18.8	42–75	409–517	$h_m = 1059(\Delta t)^{-0.336}$
Ethanol	11.2–28.3	35–62	266–350	$h_m = 652(\Delta t)^{-0.270}$
i-Propanol	12.2–28.8	32–48	194–264	$h_m = 684(\Delta t)^{-0.372}$
n-Butanol	28.2–49.9	62–80	133–158	$h_m = 401(\Delta t)^{-0.277}$
Acetone	9.7–26.0	102–208	282–362	$h_m = 659(\Delta t)^{-0.275}$

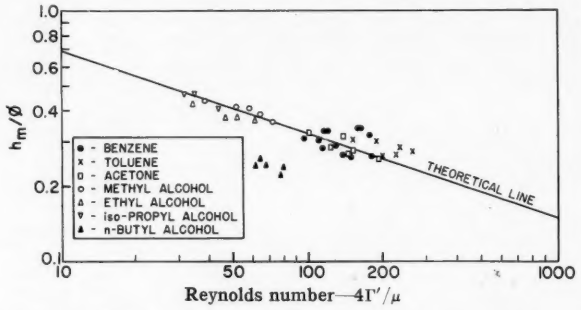

Fig. 7. Generalized correlation of heat transfer coefficient with Reynolds number.

obtained with this apparatus with the theoretical values predicted by the Nusselt equation and to provide experimental values for the pure components against which their mixtures could be compared under the same conditions.

Results are summarized in Table 2; typical test results are shown graphically for the various materials as Figures 4, 5, and 6. Of primary interest is the agreement between the observed and the theoretical values, which can be seen visually in Figures 4 to 6 and is summarized statistically in Table 3.

Figures 4 to 6 test the agreement of the data with one form of Nusselt's equation:

$$h_m = 0.725(k^3\rho^2 g\lambda/D\mu\Delta t)^{0.25} \qquad (2)$$

Since Δt was the controlled variable, for Equation (2) to be valid the logarithmic plot should show a linear variation of h with Δt and should have a slope approximating -0.25. Deviation from 0.25 is to be expected since the physical properties of the condensate vary with temperature; the properties are evaluated at a film temperature, $t_f = t_s - 0.75\,\Delta t$, and would, therefore, vary with the value of Δt.

As shown in Table 2, values of the slope in Figures 4 to 6 varied from -0.24 to -0.37. Although it was essentially parallel to the theoretical line in all cases, the best statistical line fell significantly above the theoretical for benzene and toluene and below the theoretical for ethanol, butanol and acetone. High values may be attributed to turbulence induced by the vapor velocity and low values to the fouling of the condenser surface; however, since both high and low results were obtained and the averages shown in Table 3 are in good quantitative agreement with the corresponding values reported in McAdams (*6*), it is more probable that the difference represents a variance between the physical properties of the actual materials tested and the values reported for these in the literature and used in calculating the theoretical values of the coefficient. Whatever the cause of this discrepancy, the mutual consistency and reproducibility of the results lend confidence to their value and the use of the apparatus for the binary studies.

Figure 7 represents the alternate, generalized form of Nusselt's equation:

$$h_m/\phi = 1.51(4\Gamma'/\mu_f)^{0.333} \qquad (3)$$

where

$$\phi = (k^3\rho^2 g/\mu^2)^{0.333} \qquad (3a)$$

$4\Gamma'/\mu_f$ is the Reynolds number for the drainage of the condensate film from a horizontal tube. Its critical value is generally accepted to be about 4,200, but it will be noted in Figure 7 that there is an indication that turbulence begins at a lower value, possibly as low as 200, and that at Reynolds numbers above this the coefficient increases, rather than decreases, with increasing condensation rates; this behavior has been established for condensation on vertical tubes (*7*) and has been suggested for other transfer phenomena (*14*). Additional data at higher condensation rates, not obtainable with this apparatus, are needed to establish this quantitatively.

Table 3. Statistical Analysis of Results—Pure Compounds

Material	Standard deviation in h_m: From experimental correlation, B.t.u./(hr.)(sq.ft.)(°F.)	From theoretical value for same Δt, B.t.u./(hr.)(sq.ft.)(°F.)	$\left[\frac{h_m \text{ expt'l.}}{h_m \text{ theor.}}\right]_{avg.}$ Experimental	Literature (*9*)
Benzene	17.8	66.2	1.27	0.84–1.22
Toluene	21.3	38.1	1.16	0.76–1.04
Methanol	19.9	24.5	1.00	1.06
Ethanol	11.7	66.1	0.85	1.02
i-Propanol	3.6	15.8	0.95	0.73–0.94
n-Butanol	5.3	85.8	0.65	0.85
Acetone	10.8	17.6	0.97	

BINARY MIXTURES

To apply Equation (1) and determine h_m for the binary mixtures q was evaluated by multiplying the difference between the enthalpies of a saturated vapor and a saturated liquid of the condensate composition by the weight rate at which the condensate was collected; the enthalpy chart and the vapor-liquid equilibrium diagram for each system, needed for this purpose, were prepared from the best available equilibrium and thermal properties data (*12, 15*). Typical results are given in Table 4.

As shown by Figure 8 and as considered speculatively by Colburn and Drew (*3*) and Wallace and Davidson (*18*), three choices exist as to the correct temperature to be used with the surface temperature to establish Δt for use in Equation (1). These are t_v, the vapor temperature, measured by a thermocouple in the line between the reboiler and the vapor jacket around the bar; t_{DP}, the dew point of the vapor, read from the temperature-composition diagram for the system; and t_{BP}, the bubble point of the condensate, also read from the temperature-composition diagram. By definition these give

$$\Delta t_v = t_v - t_{surface} \qquad (4a)$$

$$\Delta t_{DP} = t_{DP} - t_{surface} \qquad (4b)$$

$$\Delta t_{BP} = t_{BP} - t_{surface} \qquad (4c)$$

Values of the film coefficient were calculated for each set of data, by use of each of these choices of Δt. The results obtained with *n*-butanol–benzene are typical and are shown in Figure 9. If the three lines obtained from the same experimental data are studied in relation to the corresponding lines for the pure components, it will be noted that the definition of Δt by Equation (4c) was the only one which gave a slope approxmating that of the pure components. Further, the line based on Δt_{BP} is the only one to fall between the pure com-

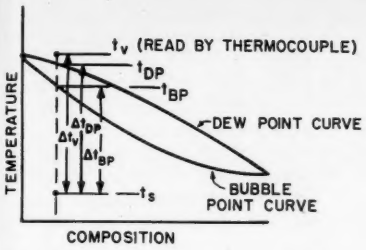

Fig. 8. Definitions of Δt for binary mixtures.

ponents over the entire range of Δt's studied.

The *n*-butanol–benzene system for which the data were plotted in Figure 9 is nonazeotropic, if not ideal. When ideal mixtures are considered, the physical properties of the mixture are the weighted average of those of the pure components and must fall between them; therefore, the heat transfer coefficient based on these should also fall between the limiting values established by the pure components at the same Δt. The conclusion follows that the correct Δt to use is that based on the bubble point of the condensate.

Figure 10 shows the same results for ethanol-benzene, a nonideal mixture.

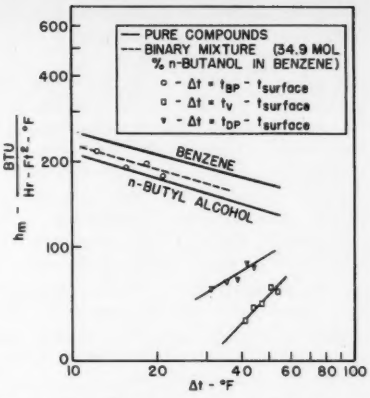
PURE COMPOUNDS
BINARY MIXTURE (34.9 MOL % n-BUTANOL IN BENZENE)
o - $\Delta t = t_{BP} - t_{surface}$
□ - $\Delta t = t_v - t_{surface}$
▽ - $\Delta t = t_{DP} - t_{surface}$
BENZENE
n-BUTYL ALCOHOL
h_m - BTU / Hr - Ft² - °F
Δt - °F

Fig. 9. Correlation of film coefficient with temperature difference for binary mixtures (*n*-butyl alcohol–benzene system).

Again, the coefficient calculated with a Δt based on the bubble point was the only one to fall between the values for the pure components and the only one with a slope approximating -0.25. Although the physical properties of a nonideal mixture are not necessarily additive and the coefficient need not fall between those for the pure components, the slope should nevertheless be essentially -0.25

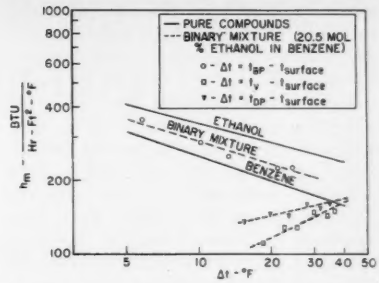
PURE COMPOUNDS
BINARY MIXTURE (20.5 MOL % ETHANOL IN BENZENE)
o - $\Delta t = t_{BP} - t_{surface}$
□ - $\Delta t = t_v - t_{surface}$
▽ - $\Delta t = t_{DP} - t_{surface}$
ETHANOL
BINARY MIXTURE
BENZENE
h_m - BTU / Hr - Ft² - °F
Δt - °F

Fig. 10. Correlation of film coefficient with temperature difference for binary mixtures (benzene-ethanol system).

since all tests were made with the same mixture and, within a few degrees, for the same film temperature.

For each of the binary systems studied, the experimental coefficient was correlated with composition. This is shown in Figure 11, for the system ethanol-benzene; temperature difference is used as a parameter to put all mixtures on a comparable basis. The resulting plot approaches linearity, particularly at the higher values at Δt. Even at lower Δt's, where the plot deviated markedly from a straight line, 7% was the maximum difference found between the observed

TABLE 4. TEST RESULTS*

System	Condensate composition	Avg. surface temperature, °F.	Observed vapor temperature, °F.	Bubble point, °F.	Δt_{BP}, °F.	Condensate rate, lb./hr.	Experimental coefficient, B.t.u./(hr.)(sq. ft./°F.)
Methanol-benzene	0.0 mole % alcohol	158.0	176.7	175.3	17.3	77.1	293
	0.0	150.6	176.8	175.3	24.7	100.9	273
	0.0	140.5	177.3	175.3	34.8	125.2	242
	17.7	114.9	165.8	137.1	22.2	60.5	273
	46.5	115.6	143.7	136.0	20.4	46.1	310
	61.2†	117.7	136.7	135.7	17.9	37.3	317
	83.0	129.1	142.4	136.9	13.3	18.6	436
	100.0	128.9	147.3	148.1	19.2	38.9	418
	100.0	136.8	147.5	148.1	11.3	26.4	487
Ethanol-Benzene	20.5 mole % alcohol	138.2	167.9	155.4	17.5	50.3	285
	44.8†	140.8	153.8	153.8	13.0	34.6	289
	57.5	127.5	158.6	154.1	26.7	52.8	239
	81.3	141.2	166.7	158.3	17.5	30.9	250
	100.0	144.5	172.9	173.3	28.8	48.6	266
	100.0	155.2	172.9	173.3	18.1	33.6	284
n-Butanol-benzene	20.9 mole % alcohol	167.0	195.2	178.4	11.2	31.4	224
	34.9	160.4	213.5	181.3	21.0	42.7	179
	58.5	169.8	228.0	189.6	18.6	29.6	158
	83.7	200.6	237.2	210.0	8.9	14.6	179
	100.0	197.8	243.2	243.9	46.1	60.9	143
	100.0	210.0	243.2	243.9	33.9	47.5	153
Methanol-acetone	0.0 mole % alcohol	114.6	132.6	133.0	18.4	58.0	302
	0.0	123.4	133.1	133.0	9.6	37.8	362
	17.7	114.9	165.8	137.1	22.2	60.5	273
	20.0†	115.7	131.3	131.3	15.6	45.9	348
	42.7	124.0	133.5	131.6	7.6	24.9	468
	57.7	108.2	137.1	132.6	24.4	46.3	307
	82.5	120.9	143.4	138.4	17.5	25.4	372
Methanol-isopropanol	0.0 mole %	158.3	180.2	180.5	22.2	40.1	220
	0.0 methanol	168.0	180.2	180.5	12.5	26.8	264
	27.5	161.0	173.5	167.8	6.8	21.1	408
	42.5	140.3	169.9	162.0	21.7	41.8	273
	62.8	142.7	165.5	156.2	13.5	34.9	399
	80.0	144.5	159.6	152.0	7.5	26.5	603

*Typical results only. Complete data available in references *5, 8, 16, 17,* and/or research records.
†Azeotrope composition.

coefficient and the corresponding value predicted by linear interpolation between the values for the pure components at the same Δt.

In both these regards—the correlation with Δt_{BP} and the linearity of h_m with composition—all binary systems investigated behaved similarly. Since these included methanol-isopropanol (ideal), butanol-benzene (nonideal, but nonazeotropic), methanol-benzene, acetone-methanol, and ethanol-benzene (minimum boiling azeotropes), the conclusions appear to apply to all types of mixtures.

These experimental results can be considered in terms of the theoretical relations developed by Colburn and Drew (*3*) to predict interface concentrations and temperatures as the rate of condensation and the conductance of the gas and liquid films varied.

First the fact that the bubble-point temperature exists at the liquid-vapor interface requires that there be a gas-phase resistance to account for the difference in the vapor temperature and the bubble point: were this resistance negligible, the vapor temperature or the dew point would determine the temperature driving force across the condensate film; however, as shown, this did not correlate the results.

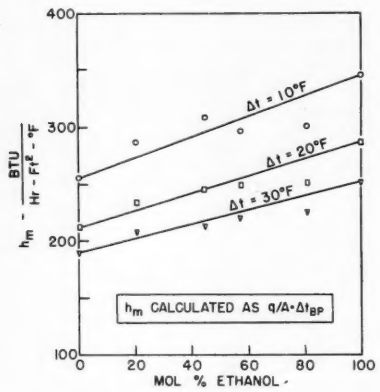

Fig. 11. Variation of coefficient with composition of binary mixtures (ethanol-benzene system).

Colburn and Drew postulated that higher rates of condensation would tend to give total condensation (no fractionation) and lower rates for the same system would tend to give equilibrium condensation, with a corresponding variation in the interface temperature. No such variation was observed; in all tests the use of bubble point gave the most consistent results, with no obvious difference in the deviation from the best correlations at either high or low deltas, as would be expected if the use of the bubble point did not hold throughout the range studied. This, of course, does not repudiate the theory of Colburn and Drew but does indicate that, for the materials studied in this work, a wider range of temperature differences must be investigated to verify it.

Kent and Pigford (*4*) extended the Colburn-Drew work in considering the fractionation effected in condensation. Specifically, they postulated that the interfacial concentration depended on the relative values of the gas- and liquid-phase mass transfer coefficients. The calculations made in the present work assumed that there was no difference in the composition of the condensate from the vapor-liquid interface to the wall. This may be taken as evidence that the gas film controlled in this system. Were there any significant change in composition across the liquid film, the bubble point at the vapor-liquid interface would be different from that based on the average condensate composition; the temperature difference would vary accordingly and would show in the correlations made, particularly at low values of the temperature difference.

In considering these observations, one must keep in mind that the research was carried out at almost total condensation. Since the primary interest was in the liquid film coefficient, the composition of the residual vapor was not ascertained as a routine; however, in the few cases where it was determined, it was consistently richer in the more volatile component than was the condensate obtained at the same time. This enrichment appeared to resemble that predicted by the equilibrium diagram for the condensate composition, but additional study is needed to verify this and ascertain the limits under which it holds true.

ACKNOWLEDGMENT

The authors wish to acknowledge use of data obtained by Jacob J. Trachtenberg (*17*), James A. Malone (*5*), and Habib Labbauf as part of their respective thesis researches while graduate students at Louisiana State University. The latter two were holders of the Dow Research Fellowship in Chemical Engineering during the period of their research. Recognition is due also to Jesse Coates, who directed the research of Dr. Todd (*16*) and Mr. Trachtenberg.

NOTATION

A = heat transfer area, πDL, sq. ft.
D = outside diameter of condensing surface, ft.
g = acceleration of gravity, ft./hr.^{2}
h_m = average coefficient of heat transfer, B.t.u./(hr.)(sq. ft. °F.)
k = thermal conductivity of condensate, B.t.u./(hr.)(sq. ft.)(°F./ft.)
L = length of condensing surface, ft.
q = rate of heat transfer,—B.t.u./hr.
t = temperature, °F.
t_{BP} = bubble point of mixture, as determined by temperature-composition diagram
t_{DP} = dew point of mixture, as determined by temperature-composition diagram
t_f = temperature of condensate film
t_s = temperature of condensing surface as measured experimentally
t_{sv} = temperature of saturated vapor
t_v = temperature of vapor phase as measured experimentally
W = rate of condensate formation, lb./hr.
Δt = temperature difference, °F.

$$\Delta t_{BP} = t_{BP} - t_s$$

$$\Delta t_{DP} = t_{DP} - t_s$$

$$\Delta t_v = t_v - t_s$$

Γ' = rate of condensate drainage, W/L, lb./(hr.)(ft.), for horizontal surfaces
λ = latent heat of vaporization, B.t.u./lb.
μ = viscosity of condensate, lb.(ft.)(hr.)
μ_f = viscosity of condensate, lb./(ft.)(hr.) at t_f
ρ = density of condensate, lb./cu. ft.
ϕ = physical property group, $(k^3\rho^2 g/\mu^2)^{1/3}$, B.t.u./(hr.)(sq. ft./°F.)

LITERATURE CITED

1. Baker, E. M., and A. C. Mueller, *Ind. Eng. Chem.*, **29**, 1065 (1937); *Trans. Am. Inst. Chem. Engrs.*, **33**, 531 (1937).
2. Baker, E. M., and U. Tsao, *Ind. Eng. Chem.*, **32**, 1115 (1940); *Trans. Am. Inst. Chem. Engrs.*, **36**, 517 (1940).
3. Colburn, A. B., and T. B. Drew, *Trans. Am. Inst. Chem. Engrs.*, **33**, 197 (1937).
4. Kent, E. R., and R. L. Pigford, *A.I.Ch.E. Journal*, **2**, 363 (1956).
5. Malone, J. A., M.S. thesis, Louisiana State Univ., Baton Rouge (1955).
6. McAdams, W. H., "Heat Transmission," 3 ed., Chap. 13, McGraw-Hill Book Company, Inc., New York (1954).
7. Monrad, C. C., and W. L. Badger, *Trans. Am. Inst. Chem. Engrs.*, **24**, 84 (1930); *Ind. Eng. Chem.*, **22**, 1103 (1930).
8. Nusselt, W., *Ver. Deut. Ing.*, **60**, 569 (1916).
9. Othmer, Donald F., *Ind. Eng. Chem.*, **21**, 576 (1929).
10. ———, and Saul Berman, *Ind. Eng. Chem.*, **35**, 1068 (1943).
11. Othmer, D. F., and R. E. White, *Trans. Am. Inst. Chem. Engr.*, **37**, 135 (1941).
12. Perry, J. H., ed., "Chemical Engineers' Handbook," 3 ed., McGraw-Hill Book Company, Inc., New York (1950).
13. Rhodes, F. H., and K. R. Younger, *Ind. Eng. Chem.*, **27**, 957 (1935).
14. Stirba, Clifford, and D. M. Hurt, *A.I.Ch.E. Journal*, **1**, 178 (1955).
15. Timmermans, Jean, "Physico-Chemical Constants of Pure Organic Compounds," Elsevier Publishing Co., New York (1950).
16. Todd, James B., M.S. thesis (1950) and Ph.D. dissertation (1953), Louisiana State Univ., Baton Rouge.
17. Trachtenberg, J. J., M.S. thesis, Louisiana State Univ., Baton Rouge (1952).
18. Wallace, J. L., and A. W. Davison, *Ind. Eng. Chem.*, **30**, 948 (1938).

Graphical Solution of Turbulent-flow Diffusion Equations

P. A. LONGWELL

California Institute of Technology, Pasadena, California

Linear partial-differential equations are often encountered when thermal or material diffusion in flowing systems is considered. Analytic solutions of such equations are known for only the simplest situations. In two examples a graphical method of solution is presented and demonstrated which makes feasible, without excessive labor or special computing facilities, the use of available knowledge concerning turbulent flow in the prediction of thermal or material transfers in complex situations involving linear steady flow.

Prediction of the distribution of temperature or concentration in flowing streams is of interest in industrial applications. In recent years studies of turbulence have led to means of estimating eddy properties (*4*), which permit the solution of differential equations, at least in principle, to yield the desired information for any particular situation. In practice the solution of differential equations involving eddy properties has proved difficult, but a straightforward and relatively easy method of obtaining solutions of certain types of differential equations which apply to heat transfer and material transfer in flowing streams has been devised.

DIFFERENTIAL EQUATIONS FOR THERMAL AND MATERIAL TRANSPORT

If there is thermal transport between the parallel plates shown in Figure 1 and a fluid which is flowing turbulently between them, the over-all energy balance may often be expressed accurately by the equation

$$u_x \frac{\partial T}{\partial x} = \frac{\partial}{\partial y}\left[\epsilon_{cy} \frac{\partial T}{\partial y}\right] \qquad (1)$$

when the eddy conductivity in the y direction is defined (*4*) by the relation

$$\epsilon_{cy} = \epsilon_{cy} + K = \frac{-\mathring{Q}_y}{\sigma C_P \left(\frac{\partial T}{\partial y}\right)} \qquad (2)$$

In the derivation of Equation (1) it is assumed that conditions are steady and that the velocity is a function only of the y coordinate. It is further assumed that the specific heat and weight of the fluid are constant, that there are no temperature gradients in the z direction, and that there are no energy sources in the fluid. Changes in potential and kinetic energy, viscous dissipation, and conduction in the x direction are neglected.

For thermal transport in a fluid flowing through a circular section of constant diameter, assumptions analogous to those made above lead to the relationship

$$r u_x \frac{\partial T}{\partial x} = \frac{\partial}{\partial r}\left(r \epsilon_{cr} \frac{\partial T}{\partial r}\right) \qquad (3)$$

Turbulent diffusion may be described by use of an eddy diffusivity defined in the y direction, for example, by the equation

$$\epsilon_{Dky} = \epsilon_{Dky} + D_{ky} = \frac{c_k u_y - \mathring{m}_{ky}}{\frac{\partial c_k}{\partial y}} \qquad (4)$$

in which u_y is the hydrodynamic velocity of the fluid in the y direction. Equation (4) is an extension of the relationships of Opfell and Sage (*15*).

Simplifying assumptions, which are often appropriate, give differential equations for turbulent diffusion that are similar to Equations (1) and (3) but have c_k substituted for T and ϵ_{Dk} in place of ϵ_c.

GENERAL FORM OF SIMPLIFIED DIFFERENTIAL EQUATION

If it is assumed that the eddy conductivity and diffusivity are functions only of the coordinate normal to the direction of flow, Equations (1) and (3) and the analogous ones for material transport are all of the form

$$\frac{\partial \phi}{\partial x} = f_1(y) \frac{\partial}{\partial y}\left[f_2(y) \frac{\partial \phi}{\partial y}\right] \qquad (5)$$

The coordinate y in Equation (5) is generalized to include the radial coordinate for cylindrical symmetry. While the eddy properties are probably functions of variables other than this one coordinate, the approximation seems adequate in view of the present state of knowledge regarding these eddy properties.

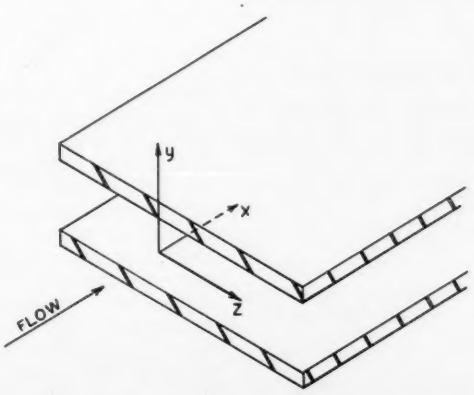

Fig. 1. Flow between parallel plates.

Equation (5) is a linear partial-differential equation but is not susceptible to analytic solution except in the simplest situations. For the case of plug flow with constant conductivity or diffusivity, the solutions are analogous to those for transient heating or cooling of a solid, given by Carslaw and Jaeger (*3*) for both the infinite slab and infinite cylinder for a variety of boundary conditions. Graetz (*5*) found the solution for plug flow in a pipe with uniform wall temperature and (*6*) also found a series-expansion analytic solution for the case of laminar flow with parabolic velocity distribution in a pipe with uniform wall temperature; this solution is given by Jakob (*7*). Berry (*1*) obtained formal solution to Equations (1) and (3) as an infinite series of solutions to a Sturm-Liouville problem, but for any specific instance these solutions must be obtained by lengthy numerical computations. Butler and Plewes (*2*) found a series solution for the case of diffusion in laminar flow between parallel plates. However even the analytic solutions for laminar flow with simple boundary conditions are very complicated, and it becomes necessary to find better methods for the solution of more complex problems.

Numerical methods have been applied to heat transfer with streamline flow by Norris and Streid (*14*), Kays (*8*), Schenk (*19*), and others. The use of electrical analogy to solve the turbulent heat transfer problem between parallel plates has been described by Schlinger et al. (*16*). Schmidt (*17*) described a graphical method for the solution of transient-heat-conduction problems in solids, which was extended to cylindrical and spherical bodies by Nessi and Nisolle (*13*). This method is described by McAdams (*11*), Jakob (*7*), and many others. Later Schmidt (*18*), in a paper which did not become well known in this country, described a graphical method for solution of partial-differential equations of the type shown in Equation (5). Schmidt's method, which differs in detail from the one shown in this paper, is described by Mickley (*12*). Schmidt gave no examples and Mickley does not take an example to the point where results are obtained.

DERIVATIONS FOR GRAPHICAL METHOD

The graphical method of solution of Equation (5) is derived as follows. First, in order to remove $f_2(y)$ from inside the differential, a change in variable is made:

$$dw = \pm\frac{dy}{f_2(y)} \tag{6}$$

In Equation (6) the sign may be selected for convenience in the particular problem. Then

$$\frac{\partial\phi}{\partial w} = \left(\frac{\partial\phi}{\partial y}\right)\left(\frac{dy}{dw}\right) = \pm f_2(y)\,\frac{\partial\phi}{\partial y} \tag{7}$$

and

$$\frac{\partial}{\partial y}\left(\frac{\partial\phi}{\partial w}\right) = \left(\frac{dw}{dy}\right)\frac{\partial}{\partial w}\left(\frac{\partial\phi}{\partial w}\right) = \frac{1}{f_2(y)}\,\frac{\partial^2\phi}{\partial w^2} \tag{8}$$

Substitution of Equations (7) and (8) in Equation (5) gives

$$\frac{\partial\phi}{\partial x} = f_3(w)\left(\frac{\partial^2\phi}{\partial w^2}\right) \tag{9}$$

when

$$f_3(w) = \frac{f_1(y)}{f_2(y)} \tag{10}$$

Equation (9), which is a linear partial-differential equation of simpler form than Equation (5), then is expressed in finite difference form. Partial derivatives are expressed as

$$\left(\frac{\partial\phi}{\partial x}\right)_{m,n} = \frac{\phi_{m+1,n} - \phi_{m,n}}{\Delta x} \tag{11}$$

and

$$\left(\frac{\partial^2\phi}{\partial w^2}\right)_{m,n} = \frac{1}{\Delta w_n}\left[\frac{\phi_{m,n+1} - \phi_{m,n}}{\Delta w_{n+1/2}} + \frac{\phi_{m,n-1} - \phi_{m,n}}{\Delta w_{n-1/2}}\right] \tag{12}$$

The subscript m pertains to the coordinate x and subscript n pertains to coordinate w, as shown in Figure 2. Equation (11) is conventional, and the representation of the second derivative in Equation (12) is a logical extension of conventional formulas for the case in which unequal intervals of the independent variable are used. Equation (12) may be shown by Taylor's series expansion to be a correct representation using three unequally spaced points. The intervals of w are defined in Figure 2, in which it is seen that

$$\Delta w_n = \tfrac{1}{2}[\Delta w_{n+1/2} + \Delta w_{n-1/2}] \tag{13}$$

Substitution of Equations (11) and (12) in Equation (9) gives the equation

$$\phi_{m+1,n} - \phi_{m,n} = \frac{(\Delta x)f_3(w_n)}{\Delta w_n}\left[\frac{\phi_{m,n+1} - \phi_{m,n}}{\Delta w_{n+1/2}} + \frac{\phi_{m,n-1} - \phi_{m,n}}{\Delta w_{n-1/2}}\right] \tag{14}$$

Use of Equation (13) in Equation (14) leads to

$$\phi_{m+1,n} = \left[1 - \frac{2(\Delta x)f_3(w_n)}{(\Delta w_{n+1/2})(\Delta w_{n-1/2})}\right]\phi_{m,n} + \frac{(\Delta x)f_3(w_n)}{\Delta w_n}\left[\frac{\phi_{m,n+1}}{\Delta w_{n+1/2}} + \frac{\phi_{m,n-1}}{\Delta w_{n-1/2}}\right] \tag{15}$$

The finite increments in x and w are now constrained to satisfy the relationship

$$\frac{2(\Delta x)f_3(w_n)}{(\Delta w_{n+1/2})(\Delta w_{n-1/2})} = 1 \tag{16}$$

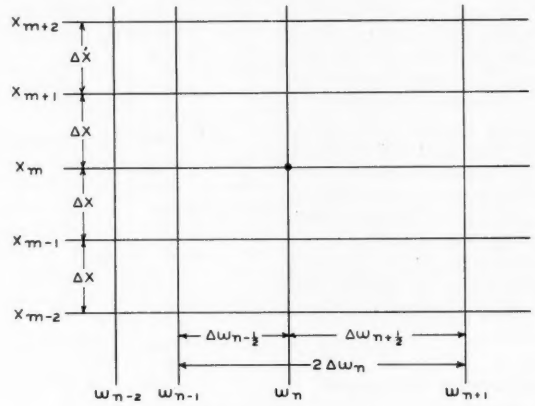

Fig. 2. Finite-difference grid.

If Equation (16) is substituted in Equation (15) and the result rearranged, the following is obtained:

$$\phi_{m+1,n} = \frac{1}{2(\Delta w_n)}\left[(\phi_{m,n+1})(\Delta w_{n-1/2}) + (\phi_{m,n-1})(\Delta w_{n+1/2})\right] \tag{17}$$

Equation (17) is satisfied by the geometry of a Schmidt-type construction, as can be easily demonstrated in Figure 3 by use of the relationships for similar triangles.

The spacing of the discrete values of w is determined by solution of Equation (16). This solution must have appropriate numbers of intervals in both the x and w coordinates, and the size of the intervals in w should increase or decrease smoothly. Intervals must also be placed as required to establish boundary conditions.

The application of boundary conditions is similar to that with conventional

Schmidt plots. Boundary conditions of the type

$$\phi = \phi_a \quad \text{at} \quad y = y_a \qquad (18)$$

become

$$\phi = \phi_a \quad \text{at} \quad w = w_a \qquad (19)$$

where w_a is the value of w corresponding to y_a.

If

$$\frac{\partial \phi}{\partial y} = 0 \quad \text{at} \quad y = y_a \qquad (20)$$

use of Equation (7) gives

$$\frac{\partial \phi}{\partial w} = 0 \quad \text{at} \quad w = w_a \qquad (21)$$

as long as $f_2(y_a)$ is finite. This boundary condition is imposed by imagining a mirror image on the other side of w_a and is illustrated in two examples which follow.

Another boundary condition which commonly arises owing to the finite thermal conductivity of a wall and to finite heat transfer coefficients is

$$\frac{\partial \phi}{\partial y} = C_1(\phi_a - \phi_s) \quad \text{at} \quad y = y_a \qquad (22)$$

With Equation (7) substituted, the boundary condition becomes

$$\frac{\partial \phi}{\partial w} = \pm C_1 f_2(y_a)[\phi_a - \phi_s] \quad \text{at} \quad w = w_a \qquad (23)$$

which is satisfied by the construction shown in Figure 4. A point at the level ϕ_s is placed a distance $1/C_1 f_2(y_a)$ measured in the units of w from w_a and is used as a constant-temperature point.

Extensions of the method to match other boundary conditions such as variable temperatures may be made.

USE OF GRAPHICAL METHOD

There follows an outline of the method of solution of a differential equation of the type shown by Equation (5). ϕ is to be determined as a function of x and y, and it is presumed that the functions $f_1(y)$ and $f_2(y)$ are known in at least tabular form.

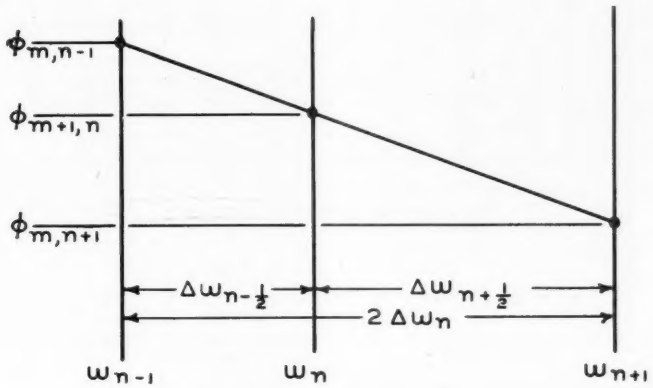

Fig. 3. Schmidt-type construction.

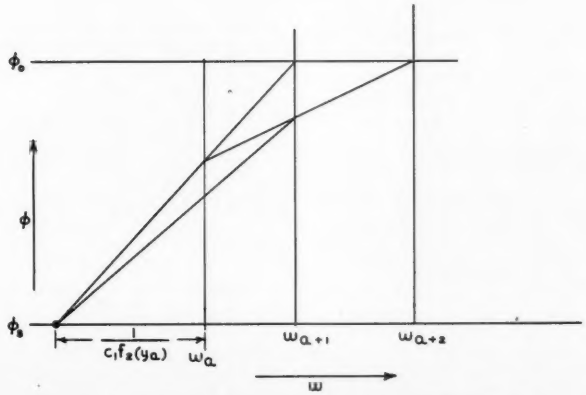

Fig. 4. Construction for boundary condition of Equation (23).

1. The new variable w should be calculated as a function of y by integration of Equation (6) between appropriate limits. This integration may well be done numerically or graphically.

2. $f_3(w)$ as defined by Equation (10) is to be calculated as a function of y and, by use of the relationship obtained above between w and y, $f_3(w)$ should be plotted as a function of w.

3. Equation (16) and the graph of $f_3(w)$ are used to calculate the intervals in w. In essence this amounts to writing Equation (16) for each interior point and, by trial and error, finding a set of w coordinates which satisfies the equation and has a suitable number of intervals. The solution can be systematized, however, so that the labor of obtaining such a set is not great. In the author's experience with this method there has always been evident a suitable place on the plot of $f_3(w)$ at which to start the calculation. For Equation (1), if the velocity and eddy conductivity are symmetrical about the center line, $f_3(w)$ will be likewise symmetrical, and a start is made at the center line by letting the intervals in w be symmetrical; that is, at the center line, Equation (16) becomes

$$(\Delta w_{n-1/2})^2 = 2(\Delta x) f_3(w_n) \qquad (24)$$

A trial value of Δx is selected, and Δw for either side of the center line is calculated. Then, by use of Equation (16), Δw's and therefore w's are calculated step by step toward the wall. If, as is generally the case for a first iteration, the boundary does not coincide with a calculated w, the value of Δx is adjusted and the calculation repeated until a suitable value of Δx is found.

For Equation (3), $f_3(w)$ goes to infinity at the center line of the pipe and also at the wall. In this case the minimum in $f_3(w)$ is a suitable starting point, and the intervals $\Delta w_{n-1/2}$ and $\Delta w_{n+1/2}$ are taken as equal for w_n at this minimum. The procedure is illustrated in the examples below.

4. A graph of a size suitable for Schmidt-type constructions is made, with ϕ as the ordinate and w as the abscissa. Vertical lines are drawn at the values of w calculated above. The boundary conditions are converted from the original form to those pertaining to ϕ as a function of w and entered or used accordingly. A conventional Schmidt-type construction (*7, 11*) is then made. This is illustrated in Figure 5, which shows the construction for boundary conditions involving a step function in ϕ at one boundary and $(\partial\phi/\partial w)$ of zero at the second boundary, which might well be a center of symmetry. The value of ϕ at the end of the fourth interval in x is shown dotted.

5. Values of ϕ at the desired intervals of x are read as functions of w and converted to a basis of y by use of the plot of w vs. y previously made.

Example 1. Heat Transfer with Laminar Flow and Parabolic Velocity Distribution

As a first example a fluid flowing in a laminar fashion in a pipe is considered. The velocity distribution is taken to be parabolic and invariant, and the fluid, which is at a uniform temperature T_0, enters a section having a wall temperature T_s. The temperature of the fluid as a function of position is desired.

The differential equation is

$$ru_x \frac{\partial T}{\partial x} = K \frac{\partial}{\partial r}\left[r \frac{\partial T}{\partial r}\right] \qquad (25)$$

with the boundary conditions

$$T = T_0 \quad \text{at} \quad 0 \leq r \leq r_0 \quad \text{for} \quad x < 0 \qquad (26)$$

and

$$T = T_s \quad \text{at} \quad r = r_0 \quad \text{for} \quad x > 0 \qquad (27)$$

The velocity distribution is given by

$$u_x = 2U\left[1 - \frac{r^2}{r_0^2}\right] \qquad (28)$$

Dimensionless variables may be defined:

$$\eta = \frac{r}{r_0} \qquad (29)$$

$$\phi = \frac{T - T_0}{T_s - T_0} \qquad (30)$$

$$\lambda = \frac{Kx}{r_0^2 U} \qquad (31)$$

Substitution of Equations (28) to (31) in Equations (25) to (27) gives

$$\frac{\partial \phi}{\partial \lambda} = \frac{1}{2\eta(1 - \eta^2)} \frac{\partial}{\partial \eta}\left[\eta \frac{\partial \phi}{\partial \eta}\right] \qquad (32)$$

with boundary conditions

$$\phi = 0 \quad \text{at} \quad 0 \leq \eta \leq 1 \quad \text{for} \quad \lambda < 0 \qquad (33)$$

and

$$\phi = 1 \quad \text{at} \quad \eta = 1 \quad \text{for} \quad \lambda > 0 \qquad (34)$$

By symmetry a further boundary condition is known:

$$\frac{\partial \phi}{\partial \eta} = 0 \quad \text{at} \quad \eta = 0 \qquad (35)$$

To prepare for graphical treatment, the change of variable shown in Equation (6) is used. For this case the change of variable becomes

$$dw = -\frac{d\eta}{\eta} \qquad (36)$$

The negative sign was selected in order to make w positive. Integration of Equation (36) gives

$$w = -\ln \eta \qquad (37)$$

The function defined by Equation (10) for this case is

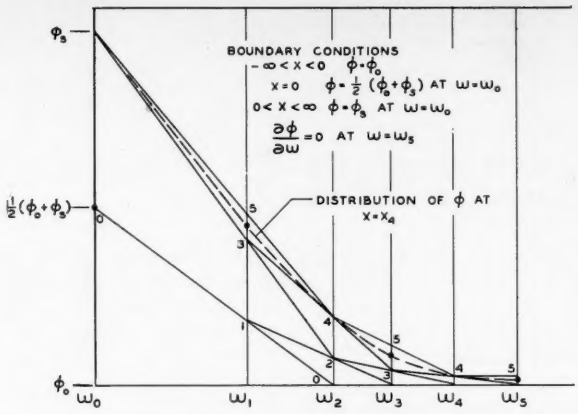
BOUNDARY CONDITIONS
$-\infty < X < 0 \quad \phi = \phi_0$
$X = 0 \quad \phi = \frac{1}{2}(\phi_0 + \phi_s)$ AT $\omega = \omega_0$
$0 < X < \infty \quad \phi = \phi_s$ AT $\omega = \omega_0$
$\frac{\partial \phi}{\partial \omega} = 0$ AT $\omega = \omega_s$
DISTRIBUTION OF ϕ AT $X = X_4$
ϕ_s
$\frac{1}{2}(\phi_0 + \phi_s)$
ϕ_0
ω_0
ω_1
ω_2
ω_3
ω_4
ω_5

Fig. 5. Construction showing method of evaluating ϕ.

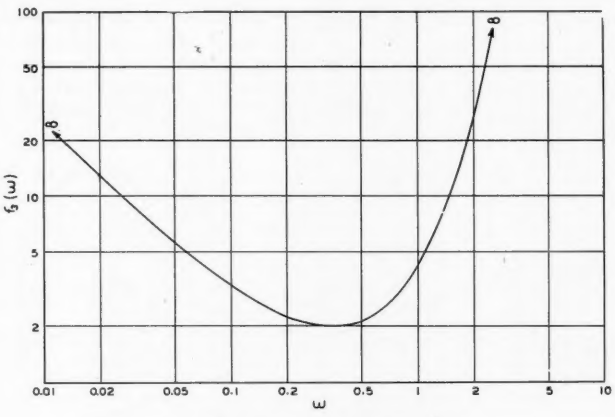

Fig. 6. The function $f_3(w)$ in Example 1.

$$f_3(w) = \frac{1}{2\eta^2(1 - \eta^2)} \qquad (38)$$

Equations (37) and (38) were used to calculate w and $f_3(w)$, and in Figure 6, $f_3(w)$ is shown as a function of w. As can be seen, a minimum in $f_3(w)$ occurs at a w of about 0.35, and this was used as the starting point of calculations for the intervals Δw. A value of 2.66×10^{-3} for $\Delta\lambda$ was found, by trial, to be satisfactory in that an interval ended at $w = 0$ and that a suitable number of intervals Δw were formed. With this value of $\Delta\lambda$ Equation (24) becomes

$$(\Delta w_{n-1/2})^2 = 2(\Delta\lambda) f_3(w_n) = 0.01064 \qquad (39)$$

which applies only for w_n corresponding to the minimum value of $f_3(w)$. Equation (16), which applies everywhere, becomes

$$(\Delta w_{n+1/2})(\Delta w_{n-1/2}) = 5.32 \times 10^{-3} f_3(w_n) \qquad (40)$$

The values of w_n which satisfy these equations and the corresponding values of η_n have been tabulated (*10*). Since the transformation of Equation (37) has the characteristic that

$$w \to \infty \quad \text{as} \quad \eta \to 0 \qquad (41)$$

the intervals are not extended to $\eta = 0$; however since η can be made as small as is desired, no real difficulty is introduced. In this case a minimum value of η of 0.0348, with fifteen intervals, was deemed adequate.

The boundary conditions must be expressed in terms of w. These are

$$\phi = 0 \quad \text{at} \quad 0 \leq w < \infty \quad \text{for} \quad \lambda < 0 \qquad (42)$$

$$\phi = 1 \quad \text{at} \quad w = 0 \quad \text{for} \quad \lambda > 0 \qquad (43)$$

and

$$\frac{\partial \phi}{\partial w} \to -0 \quad \text{as} \quad w \to \infty \qquad (44)$$

The boundary conditions of Equations (42) and (43) are easily handled, and the one of Equation (44) is approximated in this case by

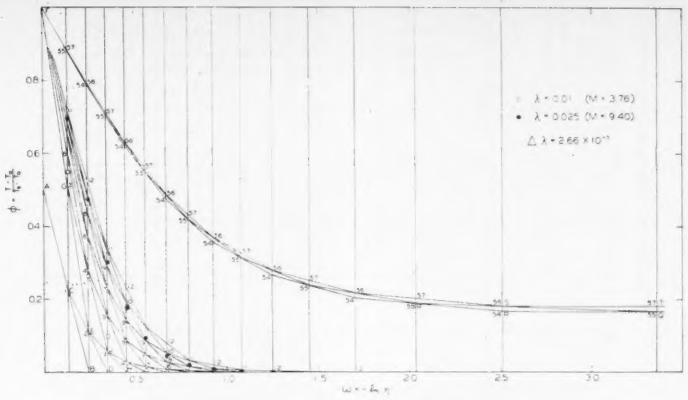

Fig. 7. Graphical construction for Example 1.

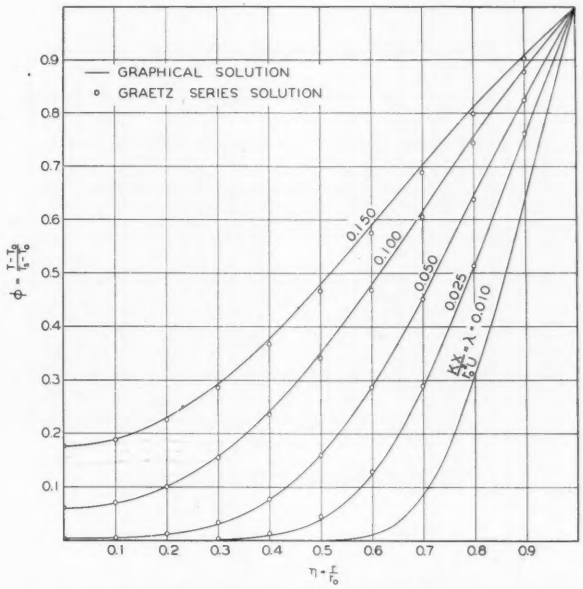

Fig. 8. Solutions for Example 1.

$$\frac{\partial \phi}{\partial w} = 0 \quad \text{at} \quad w = 3.36 \qquad (45)$$

A Schmidt-type plot was made of ϕ against w on large cross-section paper, and vertical lines were entered at the values of w calculated by use of Equation (40). Figure 7 is a reproduction of this plot showing the spacing of the lines and the construction for the first few intervals $\Delta\lambda$. The boundary condition for $\lambda = 0$ is interpreted as $\phi = 0.5$ at the boundary $w = 0$, since this is the average of the values of ϕ for $\lambda < 0$ and $\lambda > 0$. Construction is started by drawing a line between the points labeled A and B, which are conditions at $\lambda = 0$. The condition at $\Delta\lambda$ is given by point C, in accordance with Equation (17) and Figure 3. Construction of the line CD gives point E as a condition at $2\Delta\lambda$. Since point F represents the condition at the boundary for $\lambda > 0$ it is now used, and lines EF and EH are drawn, points G and J being given as points for $3\Delta\lambda$. The numbers at the points in Figure 6 correspond to M in the equation

$$\lambda = M\Delta\lambda \qquad (46)$$

The construction for a few intervals at higher values of λ, $M = 55$, 56, and 57, is shown to illustrate the treatment of the boundary condition of Equation (45). The points at $M = 54$ are from previous construction. For $M = 55$ a horizontal line is drawn from P intersecting the line $w = 3.36$ at Q, which becomes the value for $M = 55$. This construction satisfies the boundary condition of Equation (45). Point S, for $M = 56$, is obtained conventionally by drawing a line between R and Q, and point T, for $M = 57$, is again obtained by drawing a horizontal line, this time from point S.

Points interpolated for two even values of λ, 0.01 and 0.025, are indicated on Figure 7. The numerical values of ϕ found for even values of λ are available (*10*).

COMPARISON WITH ANALYTIC SOLUTION

The results of this graphical solution of the differential Equation (25), as described above, are shown in Figure 8. Graetz (*6*) found an analytic solution to this problem which is described by Jakob (*7*) and others. The temperature is expressed as an infinite series for which the coefficients of only the first few terms are known. If the dimensionless variables of Equations (29) through (31) are used, the Graetz solution as given by Jakob is

$$\phi = 1 - 1.477e^{-3.658\lambda}R_0(\eta) + 0.810e^{-22.178\lambda}R_1(\eta) - 0.385e^{-53.05\lambda}R_2(\eta) + \cdots \qquad (47)$$

whereas Lee, Nelson, Cherry, and Boelter (*9*) give

$$\phi = 1 - 1.476e^{-3.656\lambda}Y_1(\eta) + 0.807e^{-22.305\lambda}Y_2(\eta) - 0.589e^{-56.956\lambda}Y_3(\eta) + 0.479e^{-107.619\lambda}Y_4(\eta) - \cdots \qquad (48)$$

Equation (48) has one more term of the series than does Equation (47). The coefficients and exponents are somewhat different in these two equations, as are also the functions R_n and Y_n as tabulated by the respective authors. The truncated series is not useful for low values of λ, since it converges too slowly and is reported (*8*) as being invalid for $\lambda < 0.03$.

Points calculated by use of Equation (48) are shown for four values of λ in Figure 8. Equation (48) was selected instead of (47), because Equation (47) was found to diverge from the graphical solution for $\lambda = 0.05$. Both equations gave essentially identical results for $\lambda = 0.10$ and 0.15. Points for values of r/r_0 of less than 0.3 are not shown for $\lambda = 0.025$, because these values oscillate about zero and would cause confusion.

Agreement between the graphical solution and the Graetz series solution is seen to be very good for $\lambda = 0.025$ and $\lambda = 0.05$. For $\lambda = 0.10$ and $\lambda = 0.15$ there are some differences, although central temperatures agree. The maximum deviation of a point from the graphical solution is 0.014 in terms of ϕ, occurring for $\eta = 0.7$ and $\lambda = 0.15$. This accuracy is considered more than adequate for engineering purposes.

Example 2. Heat Transfer with Turbulent Flow

Heat transfer to a turbulently flowing liquid is treated as a second example of the application of this graphical method of solution of the governing differential equations. The problem selected concerns water, initially at a uniform temperature of 200°F., flowing with a bulk velocity of 10 ft./sec. in a pipe 4.00 in. in internal diameter. The water enters a section of heated copper pipe having a wall thickness of 0.25 in. Saturated steam at an absolute pressure of 25 lb./sq. in. is condensing on the exterior of the pipe with a heat transfer coefficient

of 3,000 B.t.u./(hr.)(sq. ft.)(°F.). The radial temperature distributions in the water at positions 5, 10, and 15 ft. from the entrance to the heated section are desired. It is assumed that fully developed turbulence exists at the entrance section.

Equation (3) is the differential equation describing this situation. Boundary conditions are

$$T = 200°F. \quad \text{for} \quad 0 \leq r \leq r_0 \quad \text{at} \quad x < 0 \qquad (49)$$

$$T_s = \text{temp. steam} = 240°F. \quad \text{for} \quad x > 0 \qquad (50)$$

and by symmetry

$$\frac{\partial T}{\partial r} = 0 \quad \text{at} \quad r = 0 \qquad (51)$$

The functions for the general form of Equation (5) are

$$f_1(r) = \frac{1}{u_x r} \qquad (52)$$

$$f_2(r) = r\varepsilon_c \qquad (53)$$

and

$$f_3(w) = \frac{1}{u_x r^2 \varepsilon_c} \qquad (54)$$

The variable w is defined by

$$dw = -\frac{dr}{r\varepsilon_c} = +\frac{d(r_0 - r)}{r\varepsilon_c} \qquad (55)$$

Before Equations (54) and (55) can be applied, the velocity distribution and the point values of the total conductivity must be known. The velocity distribution was estimated by use of the relationships (*4*)

$$u^+ = \frac{1}{0.0695} \tanh (0.0695 r^+) \quad \text{for} \quad r^+ \leq 26.7 \qquad (56)$$

$$u^+ = 5.5 + 2.5 \ln r^+ \quad \text{for} \quad r^+ > 26.7 \qquad (57)$$

The eddy viscosity was determined by use of

$$\frac{\varepsilon_m}{\nu} = \frac{r}{r_0} \cosh^2 [0.0695 r^+] \quad \text{for} \quad r^+ \leq 26.7 \qquad (58)$$

$$\frac{\varepsilon_m}{\nu} = 0.4 \frac{r}{r_0} r^+ \quad \text{for} \quad r^+ > 26.7 \qquad (59)$$

Because the Reynolds number is very high, 10^6, the eddy conductivity was determined by use of the approximation

$$Pr_{eddy} = \frac{\epsilon_m}{\epsilon_c} = 1 \qquad (60)$$

The calculated values of the velocity, the total conductivity, the new variable w, and the function $f_3(w)$ were tabulated (*10*) as functions of the radius. Figure 9 shows

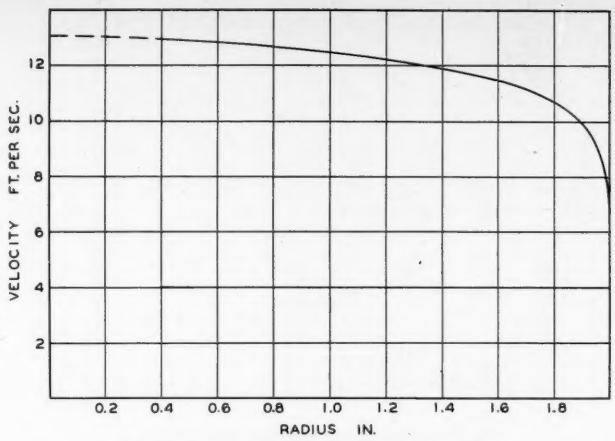

Fig. 9. Velocity distribution for Example 2.

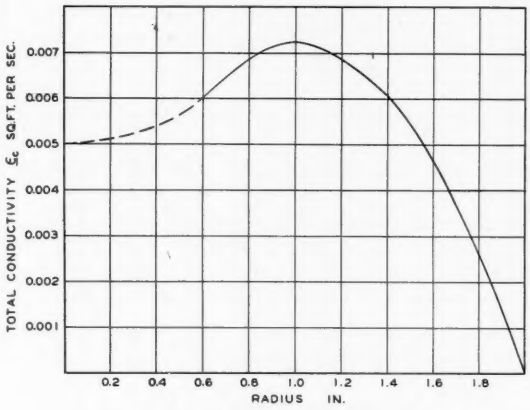

Fig. 10. Total conductivity for Example 2.

the estimated velocity distribution, the dotted portion representing a departure from Equation (57), because the latter erroneously gives a nonzero slope at the center line. The estimated total conductivity is shown in Figure 10, in which the dotted portion represents a departure from values calculated by use of Equations (59) and (60), because the eddy conductivity is known (*4*) to remain fairly large near the center of the channel. In Figure 11 the variable w is shown as a function of the radius deficiency $(r_0 - r)$. The behavior of the function $f_3(w)$ is shown in Figure 12, in which it is plotted as a function of w. A minimum in $f_3(w)$ occurs at a value of w of 505 sec./sq. ft.

Solution for a suitable set of values of w was carried out by use of Equation (24) for the value of w of 505 sec./sq. ft. and Equation (16) for the other values of w. By trial, a value of Δx of 0.569 ft. was found to give ten intervals, which was considered appropriate, including an interval ending at $w = 0$.

The boundary condition of Equation (50) leads to an equation of the form of Equations (22) and (23). If conduction in the metal wall parallel to the axis is neglected, the thermal flux from the steam may be equated to that through the wall and to that entering the water:

$$\left(\frac{\partial T}{\partial r}\right)_{r_0} = \frac{T_s - T_{r_0}}{(\sigma C_P \varepsilon_c) r_0 \left[\frac{r_0}{h r_1} + \frac{r_0}{k_m} \ln \frac{r_1}{r_0}\right]} \qquad (61)$$

Use of Equations (23) and (53) with Equation (61) shows that the construction distance in w units is

$$\frac{1}{C_1 f_2(r_0)} = (\sigma C_P) \left[\frac{1}{r_1 h} + \frac{1}{k_m} \ln \frac{r_1}{r_0}\right] \qquad (62)$$

which was found to be 502 sec./sq. ft.

A large-scale plot was made on cross-section paper with temperature as the ordinate and w as the abscissa. Vertical lines were drawn at the calculated values of w (*10*) and the graphical solution was performed. Figure 13 is a reproduction of this plot showing the construction. The construction for the Δx intervals 9 through 26 is omitted in the interest of clarity. The points are numbered to correspond to M in

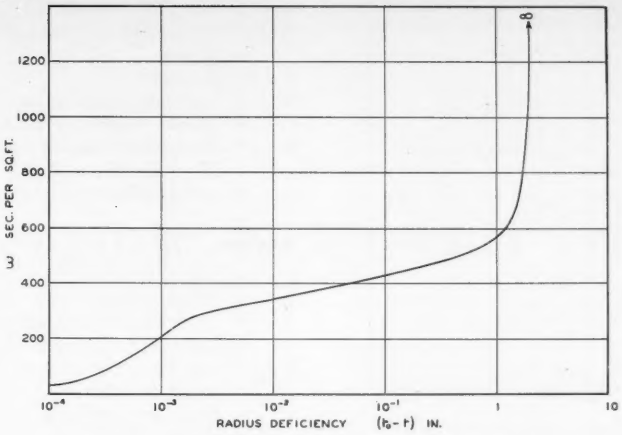

Fig. 11. Transformation variable w for Example 2.

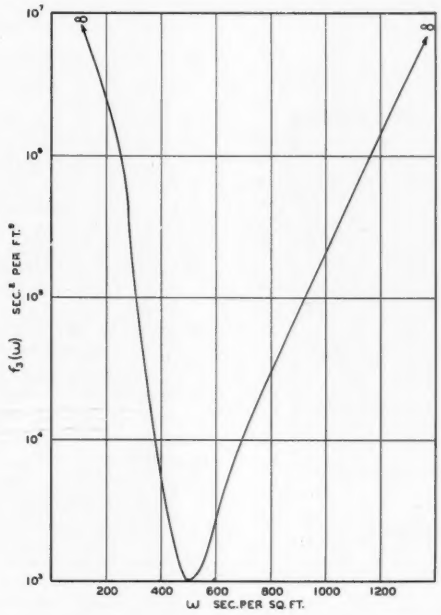

Fig. 12. Function $f_3(w)$ for Example 2.

$$x = M\Delta x \qquad (63)$$

Values of the radius are indicated at the top of Figure 13 in order to show the extreme variation in the intervals of radius which are used to satisfy the equations governing the graphical solution.

The temperatures for the downstream distances of 5, 10, and 15 ft. (*10*) were read from Figure 13. The temperature distributions for bulk of the stream are shown in Figure 14 and the distributions close to the wall are presented in Figure 15.

DISCUSSION

The procedure demonstrated is a straightforward method of solving differential equations of the form of Equation (5). The method does not require specialized equipment such as analogue or digital computers or excessive amounts of time.

The examples selected were taken from the field of heat transfer to flowing fluids, but the derivations of Equations (6) through (24) are more general and the method may well be applied to any differential equation which can be expressed in the form of Equation (5). The examples demonstrate that no undue difficulty is caused by enormous variation in the functions $f_1(y)$ and $f_2(y)$.

The method is demonstrated as a graphical one and indeed the graphical solution appears advantageous. There may be situations, however, in which a numerical solution is to be preferred. Numerical solution can be accomplished by use of Equation (17), the weighting factors of which can be calculated for each interval in w and then used to evaluate values of ϕ.

ACKNOWLEDGMENT

The assistance of W. N. Lacey in reviewing the manuscript is gratefully acknowledged.

NOTATION

C_1 = a constant
c_k = concentration of component k, (lb.)/(cu. ft.)
C_P = specific heat at constant pressure, B.t.u./(lb.)(°F.)
cosh = hyperbolic cosine
D_{ky} = Fick diffusion coefficient for component k in y direction
d = differential operator
e = base of natural logarithms, 2.71828—
f = Fanning friction factor
$f_1(y)$ = function of y [Equation (5)]
$f_2(y)$ = function of y [Equation (5)]
$f_3(w)$ = $f_1(y)/f_2(y)$
h = heat transfer coefficient, B.t.u./(sq. ft.)(sec.)(°F.)
k_m = thermal conductivity of wall, B.t.u./(ft.)(sec.)(°F.)
ln = natural logarithm
M = number of intervals in x or λ
$\mathring{m}$ = weight rate of transport, lb./(sq. ft.)(sec.)
Pr = Prandtl number
$\mathring{Q}$ = thermal flux, B.t.u./(sq. ft.)(sec.)
R_n = coefficient in Graetz series given by Jakob (*7*)
r = radius, ft.
r^+ = distance parameter $(r_0 - r)U\sqrt{f/2}/\nu$
r_0 = internal radius of pipe, ft.
r_1 = external radius of pipe, ft.
T = temperature, °F.
T_0 = original temperature of fluid, °F.
T_s = temperature at one boundary, °F.
tanh = hyperbolic tangent
U = gross velocity, ft./(sec.)
u = point velocity, ft./(sec.)
u^+ = velocity parameter $u/U\sqrt{f/2}$
w = transformation variable (varying units)
x = Cartesian coordinate in direction of flow, ft.
Y_n = coefficient in Graetz series given by Lee et al. (*9*)
y = generalized distance coordinate; Cartesian coordinate, ft.
z = Cartesian coordinate, ft.
Δ = increment in
ϵ_c = eddy conductivity, sq. ft./sec.
ξ_c = total conductivity, $(\epsilon_c + K)$, sq. ft./sec.
ϵ_D = eddy diffusivity, sq. ft./sec.
ξ_D = total diffusivity, $(\epsilon_D + D)$, sq. ft./sec.
ϵ_m = eddy viscosity, sq. ft./sec.
ξ_m = total viscosity, $(\epsilon_m + \nu)$, sq. ft./sec.

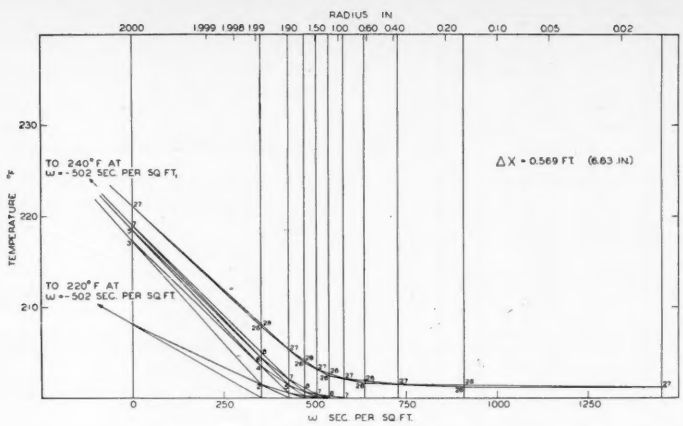

Fig. 13. Graphical construction for Example 2.

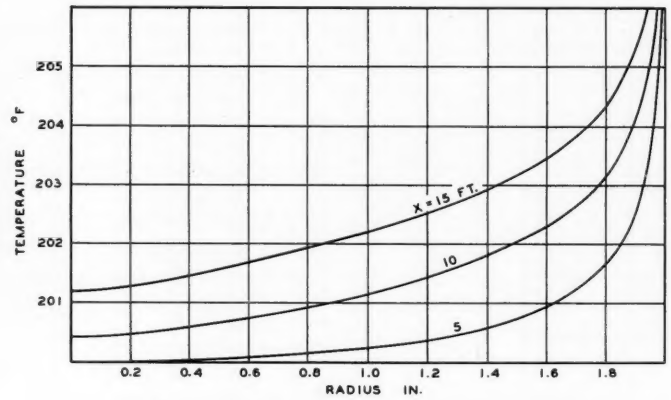

Fig. 14. Temperature distributions determined in Example 2.

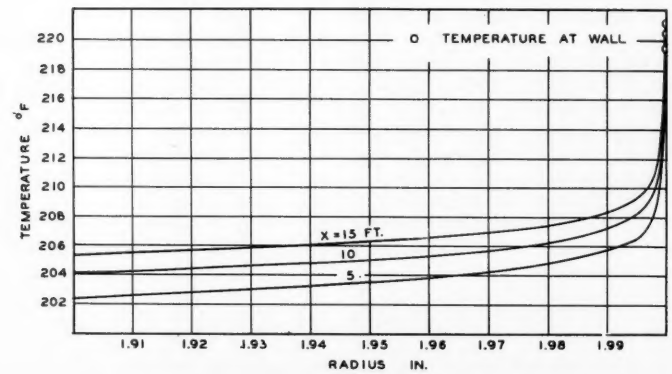

Fig. 15. Temperature distributions close to wall in Example 2.

η = r/r_0
K = thermometric conductivity, sq. ft./sec.
λ = Kx/r_0^2U
ν = kinematic viscosity, sq. ft./sec.
σ = specific weight, lb./cu. ft.
ϕ = dependent variable; also $(T - T_0)/(T_s - T_0)$
∂ = partial-differential operator

Subscripts

a = boundary
k = diffusing component
m = intervals in x or λ direction
n = intervals in y, r or w direction
0 = bulk condition at $x = 0$
r = radial direction
s = boundary condition
x, y = x, y directions

LITERATURE CITED

1. Berry, V. J., *Appl. Sci. Research* (*A*), **4**, 61 (1953).
2. Butler, R. M., and A. C. Plewes, *Chem. Eng. Progr. Symposium Ser.* No. 10, **50**, 121 (1954).
3. Carslaw, H. S., and J. C. Jaeger, "Conduction of Heat in Solids," Clarendon Press, Oxford (1947).
4. Corcoran, W. H., and B. H. Sage, *A.I.Ch.E. Journal*, **2**, 251 (1956).
5. Graetz, L., *Ann. Physik*, **18**, 79 (1883).
6. *Ibid.*, **25**, 337 (1885).
7. Jakob, Max, "Heat Transfer," vol. I, John Wiley and Sons, Inc., New York (1949).
8. Kays, W. M., *Tech. Report No. 20*, Contract N60NR-251, T.O.6, Stanford Univ., Stanford, Calif. (1953).
9. Lee, A., W. O. Nelson, V. H. Cherry, and L. M. K. Boelter, *Proc. Fifth Internatl. Congress Appl. Mech.*, p. 571, (1938).
10. Longwell, P. A., Document 5304, American Documentation Institute Auxiliary Publications Project, Library of Congress, Washington 25, D. C., $1.25 for photostat or 35-mm. microfilm.
11. McAdams, W. H., "Heat Transmission," 3 ed., McGraw-Hill Book Company, Inc., New York (1954).
12. Mickley, H. S., T. K. Sherwood and C. E. Reed, "Applied Mathematics in Chemical Engineering," 2 ed., McGraw-Hill Book Company, Inc., New York (1957).
13. Nessi, A., and L. Nissole, "Méthodes Graphiques pour l'étude des Installations de Chauffage et de Réfrigération en Régime Discontinu," Dunod, Paris (1929).
14. Norris, R. H., and D. D. Streid, *Trans. Am. Soc. Mech. Engrs.*, **62**, 525 (1940).
15. Opfell, J. B., and B. H. Sage, *Ind. Eng. Chem.*, **47**, 918 (1955).
16. Schlinger, W. G., V. J. Berry, J. L. Mason, and B. H. Sage, *Ind. Eng. Chem.*, **45**, 662 (1953).
17. Schmidt, E., "Festschrift zum Siebzigsten Geburtstag August Foeppls," p. 179, Julius Springer, Berlin (1924).
18. ———, *Forsch. Gebiete Ingenieur.*, **13**, 177 (1942).
19. Schenk, J., *Appl. Sci. Research* (*A*), **5**, 241 (1955).

Two-phase, Steam-water Critical Flow

H. S. ISBIN, J. E. MOY, and A. J. R. DA CRUZ

University of Minnesota, Minneapolis, Minnesota

Two-phase critical flow of steam-water mixtures has been investigated over a pressure range from 4 to 43 lb./sq. in. abs. and a quality range from saturated vapor to 1% (weight) vapor. Discharges were measured from 1/4-, 1/2-, 3/4-, and 1-in. pipes and from annuli of intermediate cross-sectional areas. The experimental mass flow rates are always greater than the values calculated on the basis of a homogeneous flow model. Several empirical methods for correlating the data were determined, and comparisons are presented of the predictions of several analytical flow models.

Critical flow occurs when the velocity of the fluid is equal to that of the propagation of the pressure wave. Single-phase critical flow can be predicted, but thus far no reliable theory has been established for two-phase. This study is concerned with the concurrent flow of steam-water mixtures.

The flow of flashing-water mixtures has received considerable attention (*1* to *5*, *8*, *10*, *12*, *17*, *18*, *19*) and the existence of two-phase–critical-flow behavior has been noted (*1*, *3*, *4*, *5*, *7*, *12*, *15*, *16*, *18*), but with the exception of the flow tests undertaken by C. Robbins* this investigation represents the first study undertaken explicitly to measure critical flows of steam-water mixtures over a wide range of quality. Critical flow of vapor-liquid mixtures occurs in many engineering and industrial applications, such as the handling of condensed gases and refrigerants, drains, and blow-offs from boilers and turbines, and in coolant designs for nuclear reactors.

EXPERIMENTAL

Figure 1 is a schematic sketch of the flow equipment used to investigate the critical flow behavior of steam-water mixtures. Steam and water flows were mixed, passed through a horizontal test section, and then discharged into an enlarged pipe which was connected directly to a condenser. The total mass flow to the test section was readily set and controlled—independent of the pressure regulation in the condenser—by throttling separately the supply of steam and water to the mixer. Changes in the downstream pressure (in the expansion section) served to change only the axial pressure distribution in the test section and not the discharge rates. The pressure drops along the length of the test section were measured to about 1 diam. of the discharge end. Figure 2 illustrates the pressure profiles for the test section for changes in downstream pressure. Nearly all runs were made with a downstream pressure of 1 lb./sq. in. abs., and the critical pressure in the test section at the discharge was determined by extrapolating the pressure profiles to the end of the pipe; however, it is to be noted that even at this low downstream pressure the effects on the pressure profile did not entirely disappear. The propagation of pressure disturbances through a thin liquid annulus is not unexpected.

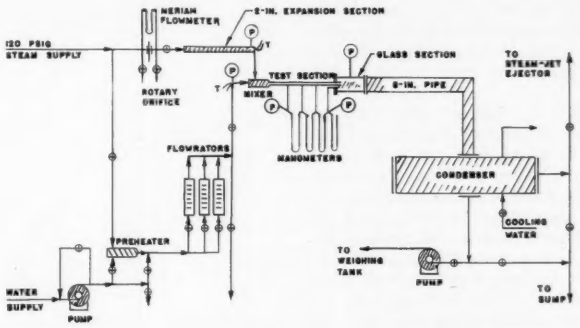

Fig. 1. Schematic sketch of critical steam-water flow equipment.

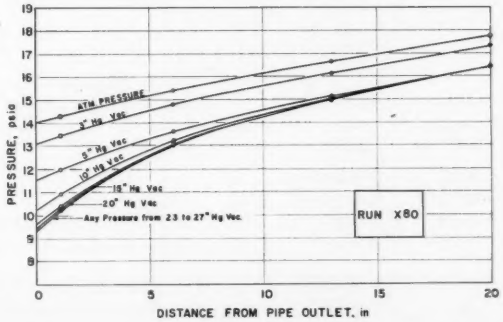

Fig. 2. Variation in pressure profile as downstream pressure varies between atmospheric and 27 in. Hg.

J. E. Moy is now with the Glenn L. Martin Company, Baltimore, Maryland, and A. J. R. da Cruz is completing U. S. Army service.

*Classified studies at the General Electric Company, Richland, Washington.

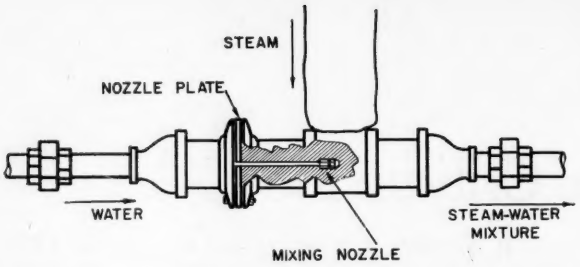

Fig. 3. Diagram of steam-water mixer showing installation of nozzle.

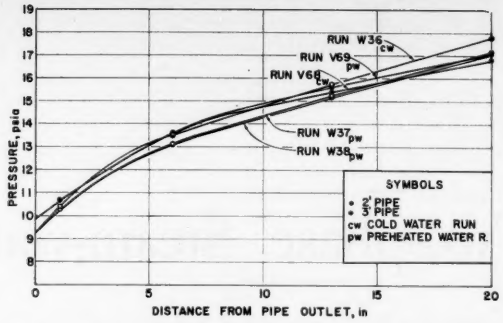

Fig. 4. Comparison of cold-water runs with preheated-water runs.

Considerable attention was directed to the method of mixing the steam and water flows. The diagram of the steam-water mixer is given in Figure 3. Mixing conditions included a variety of spray nozzles, 2- and 3-ft. test sections, and cold and preheated water with proportionately different steam flows to provide the same desired exit quality. Typical comparisons of the effects of pipe length and water preheat are shown in Figure 4. The effect of mixing on the evaluation of the critical discharge pressure was found to be within the experimental error of extrapolating the pressure profile curves (about 0.1 lb./sq. in. abs. in the 5 to 20 lb./sq. in abs. range, and about 0.5 lb./sq. in. abs. in the 25 to 45 lb./sq. in. abs. range). The method of mixing affected the pressure profiles, but the 2-ft. test section was sufficiently long so that the values determined for the critical pressure were independent of the method of mixing.

The total energy of the discharge stream was determined by measuring separately the flow rates and enthalpies of the steam and water feeds to the mixer. Calculated kinetic-energy terms were included when significant.

Four full-bore test sections were used consisting of stainless steel pipes ¼, ½, ¾, and 1 in. in diam.; and two annuli were formed by placing a ¼-in. brass pipe inside the ¾- and 1-in. pipes and supporting it by three brass pins. The discharge of each test section had a sharp, flat cross section. Data for the test sections are summarized in Table 1. Critical flow occurred within the test section at the discharge end. The experimental critical two-phase flow conditions were defined by the total measured flow rate of water and steam to the test section, calculated total energy of the flowing stream in the test section, and the extrapolated pressure in the test section at the discharge for a downstream pressure of 1 lb./sq. in. abs

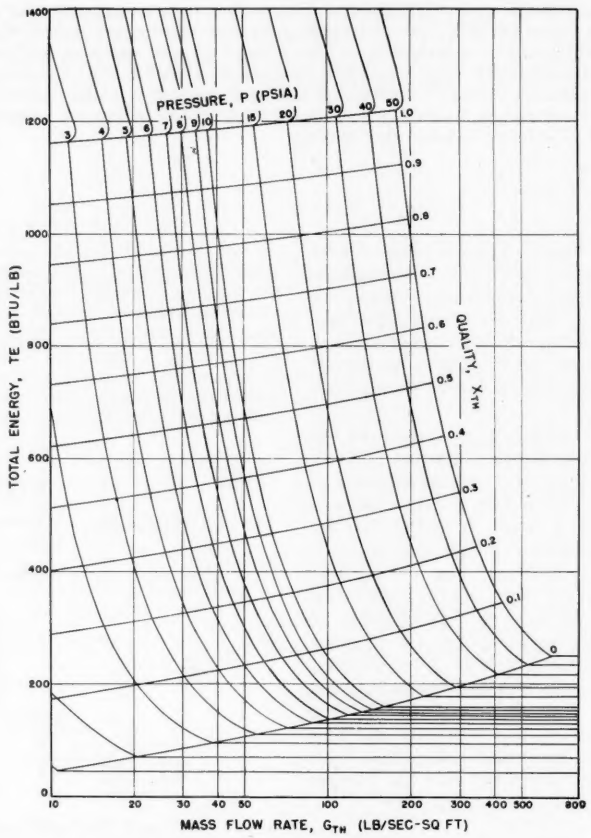

Fig. 5. Theoretical critical discharges for steam-water mixtures (homogeneous model).

Table 1. Test Sections

Nominal pipe size, full-bore	Inside diameter, in.	Cross-sectional area, sq. ft.	I.D.,† in.	Pressure taps Distance from discharge end, in. Tap number 1	2	3	4
1/4	0.3743	0.0007641	1/16	1/2	5	11	18-1/2
1/2	0.6249	0.002130	1/16	1/2	5	11	18-1/2
3/4	0.8188	0.003657	3/32	3/4	5-1/2	11-1/4	18-3/4
1	1.0425	0.005927	1/8	1-3/32	6-1/32	13	20
Annulus 3/4–1/4*		0.002068		Same as 3/4-in. full bore			
1–1/4		0.004324		Same as 1-in. full bore			

*¼ brass pipe, 0.5398 in. O.D. The distances of the supporting pins from the pipe outlet were 9.937 and 8.550 in. for the 1—¼ = and ¾—¼ annuli, respectively. (The inlet ends were separately supported.)
†I. D. of pressure tap.

EXPERIMENTAL DATA

The extensive data of Cruz for the 1-in.–diam. test section are tabulated in reference *6*, and the data of Moy (*14*) are summarized in Table 2. Values tabulated are as follows: G, critical mass flow rate (total flow rate); P, critical pressure; TE, total specific energy of the two-phase flow; and x_{th}, a calculated value which

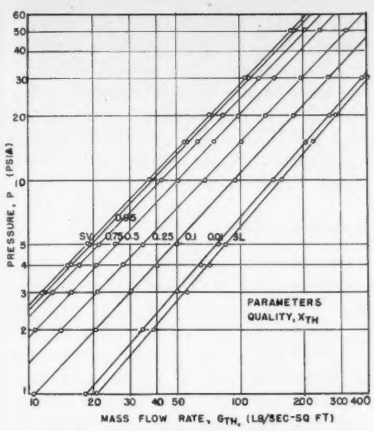

Fig. 6. Theoretical critical mass flow rates of steam-water mixtures as a function of critical pressure (homogeneous model).

represents the quality of the two-phase flow for the given conditions of P and TE, on the assumption that the flow is a homogeneous mixture at a uniform velocity and with the liquid and vapor at equilibrium. The evaluation of a true quality at the discharge end of the test requires detailed information on the kinetic energies of each of the phases.

CORRELATION OF DATA

Homogeneous Model

The application of single-phase theory to the homogeneous model requires the following assumptions: (1) the flow mixture is homogeneous and is flowing at a uniform velocity with the phases in equilibrium and (2) the critical-flow condition is defined under the restraints that the change in mass flow rate with respect to the pressure is zero at constant entropy. Under these conditions the critical mass flow rate is defined by the relation

$$G^2 = -g_c\left(\frac{dp}{dv}\right)_s \qquad (1)$$

where v is the mixture specific volume and is equal to $v_f + xv_{fg}$. Values for G calculated with Equation (1) are referred to as theoretical values, or G_{th}. Figure 5 illustrates the relations between total specific energy TE, critical mass flow rate G, critical pressure P, and quality x for steam-water flows based upon the homogeneous model. The quality is calculated through the use of the total energy relation:

$$TE = h_f + xh_{fg} + [(v_f + xv_{fg})]G^2/2g_cJ \qquad (2)$$

The logarithmic plot of G vs. P yields nearly parallel straight lines with the quality as a parameter (see Figure 6), and the logarithmic plot of $G/P^{0.96}$ vs. x (Figure 7) serves to bring the curves together over the range of quality from 1 to 0.1. The points indicated on Figures 6 and 7 are calculated values.

Empirical Correlations

Cruz noted that the plot of $[(G_{OB} - G_{TH})/G_{OB}]$ 100, percentage of deviation, vs. quality, x_{th}, served to correlate his data for the 1-in.-diam. test section, independent of the critical pressures. The subscript OB refers to the experimental (observed) data, and TH refers to the homogeneous-flow-model calculations (theoretical). Moy's data, to-

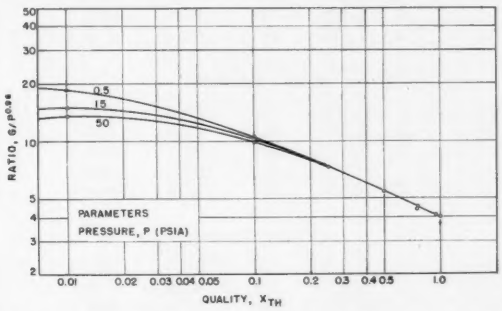

Fig. 7. Empirical representation of theoretical critical mass flow rates of steam-water mixtures (homogeneous model).

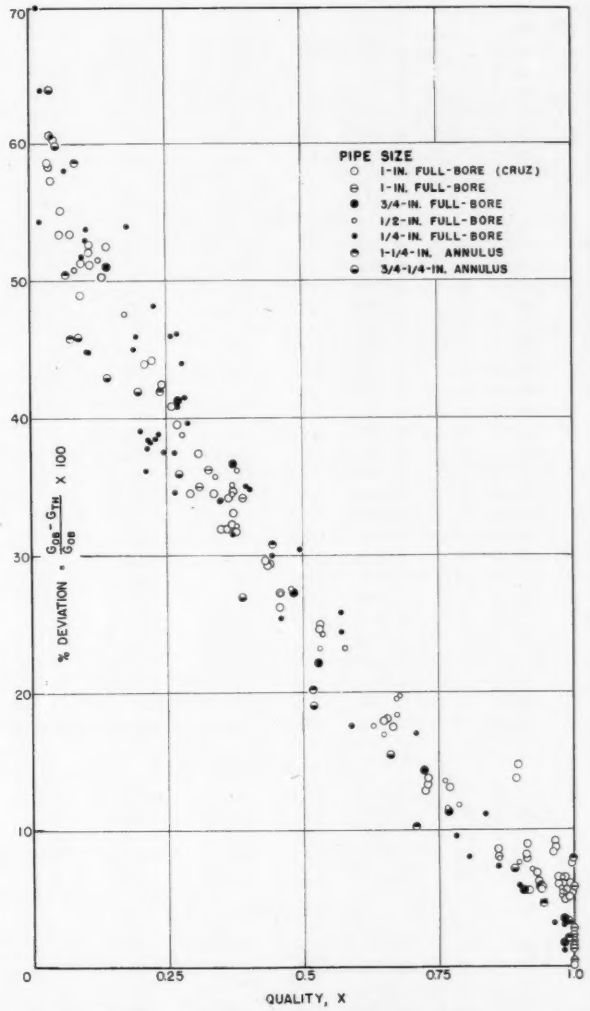

Fig. 8. Empirical correlation of experiment ' data on critical steam-water mass-flow-rate deviations from theoretical values.

TABLE 2. TWO-PHASE, STEAM-WATER, CRITICAL-FLOW DATA
(Downstream pressure at 1 lb./sq. in. abs.)

Run	G	TE	P	x_{th}	Run	G	TE	P	x_{th}
				1-in. full bore					
91	26.2	1175.6	6.9	0.999	96	34.5	1180.9	8.75	1.000
92	32.4	1177.7	8.5	0.996	97	22.4	1170.1	5.75	0.998
93	20.8	1177.1	5.4	1.000	98	80.5	557.2	9.4	0.390
94	22.5	1177.7	5.8	1.000	99	92.6	492.6	9.5	0.327
95	22.8	1179.4	7.4	1.000	100	92.4	473.8	9.4	0.310
				3/4-in. full bore					
194	66.1	1180.4	18.2	0.985	199	96.3	666.0	13.7	0.484
195	66.3	1180.3	17.8	0.985	200	78.9	532.9	8.5	0.372
196	110.5	722.3	17.8	0.530	201	46.7	899.6	9.3	0.725
197	82.3	962.5	18.1	0.770	202	100.6	432.1	8.9	0.272
198	71.0	1099.2	17.7	0.908	203	148.8	294.8	8.5	0.140
				1/2-in. full bore					
160	79.5	536.6	9.0	0.372	177	98.0	660.9	13.8	0.479
161	80.1	536.0	8.9	0.373	178	81.0	546.4	9.5	0.378
162	73.4	857.3	13.5	0.675	179	51.7	823.3	9.5	0.650
163	66.6	1178.5	17.5	0.985	180	104.6	445.7	9.7	0.280
165	56.0	750.1	9.0	0.580	181	168.9	283.4	9.2	0.125
166	79.8	543.5	8.8	0.380	182	168.9	283.5	9.2	0.125
167	73.9	861.3	13.4	0.675	183	348.9	269.8	17.6	0.081
168	79.9	541.4	8.8	0.380	184	257.8	360.5	17.6	0.173
169	74.7	865.1	13.6	0.680	185	160.3	529.3	17.6	0.340
170	67.6	1176.5	17.7	0.980	186	126.4	648.9	17.7	0.460
171	112.1	726.3	17.7	0.538	187	95.8	845.4	17.8	0.630
172	83.7	960.7	17.8	0.770	188	80.5	969.9	17.6	0.790
173	67.5	1175.9	17.8	0.980	189	73.8	1058.1	17.7	0.865
174	112.0	726.0	17.8	0.533	190	71.0	1120.1	17.8	0.924
175	83.3	958.7	17.8	0.766	191	68.4	1174.0	17.7	0.980
176	72.5	1090.7	17.6	0.900					
				1/4-in. full bore					
230	90.0	1180.8	23.8	0.980	239	565.5	231.2	19.2	0.039
231	102.2	1039.0	23.2	0.838	240	638.3	211.5	18.1	0.022
232	114.4	912.3	22.4	0.710	241	691.3	192.2	15.0	0.010
233	133.5	769.9	21.6	0.573	242	895.0	238.8	33.2	0.017
234	173.4	599.5	20.6	0.405	243	562.8	333.1	36.0	0.107
235	213.5	485.4	20.4	0.290	244	370.1	435.6	34.5	0.212
236	275.6	389.2	20.3	0.195	245	343.9	483.5	34.0	0.265
237	401.0	293.6	20.9	0.095	246	292.6	596.3	36.8	0.372
238	477.5	264.5	21.3	0.063	247	249.3	681.4	37.0	0.460
248	213.5	811.7	39.7	0.590	284	62.2	411.0	5.0	0.270
249	179.0	1001.7	40.8	0.783	285	35.0	1165.0	9.0	0.985
250	173.9	1025.5	40.8	0.808	286	68.9	511.0	7.6	0.350
251	168.3	1079.0	41.1	0.862	287	46.5	735.0	7.2	0.572
252	165.7	1116.4	41.9	0.900	288	38.4	644.0	5.2	0.495
253	159.9	1180.0	43.0	0.965	289	51.0	496.0	5.07	0.350
275	362.8	421.5	31.7	0.202	290	79.1	312.0	4.5	0.180
276	316.7	428.6	28.5	0.215	292	46.2	509.0	4.4	0.370
277	290.7	420.6	25.6	0.215	293	206.0	265.0	10.2	0.102
278	254.7	420.2	22.7	0.220	294	206.0	264.0	10.0	0.102
279	217.9	423.0	19.6	0.230	295	111.2	341.0	7.9	0.190
280	179.7	421.0	16.0	0.235	296	90.0	430.0	8.0	0.272
281	144.1	422.3	13.2	0.245	297	80.5	412.5	6.4	0.260
282	109.4	433.6	10.7	0.264	298	60.8	423.0	5.15	0.280
283	73.6	439.0	6.6	0.285	299	56.5	354.0	3.9	0.227
				1-1/4 in. annulus					
209	184.6	233.8	9.6	0.075	214	73.4	1140.0	18.9	0.945
210	59.4	1181.1	16.0	0.991	215	76.6	616.0	9.9	0.445
211	191.5	428.0	16.9	0.240	216	35.3	1186.2	8.8	1.000
212	115.2	711.0	18.6	0.518	217	185.8	238.8	8.3	0.085
213	89.1	904.0	18.9	0.710	218	185.9	218.8	8.3	0.067
				3/4–1/4 in. annulus					
219	58.9	1184.1	15.7	0.993	225	189.5	382.8	15.1	0.200
220	64.6	1083.0	15.6	0.893	226	221.0	328.8	15.1	0.145
221	82.7	851.8	16.0	0.663	227	285.5	261.0	15.3	0.080
222	96.3	703.9	15.9	0.520	228	350.2	220.8	12.5	0.050
223	119.1	570.7	15.5	0.390	229	390.4	201.3	11.5	0.036
224	156.4	459.9	15.4	0.275					

gether with those of Cruz, are given in Fig. 8. The empirical relation noted for the homogeneous flow model, Figure 7, was used to plot the experimental critical mass flow rate and critical pressure data as a function of the calculated quality, x_{th}. Figure 9 illustrates the effectiveness of this empirical correlation.

Analytical Models

One simple approach to the critical two-phase flow is to assume an annular flow with a central gas core with the sonic velocity of the gas core limiting the total flow. If the void fraction data of Martinelli (*13, 9*) or the estimated values of Levy (*11*) are used, it is found that this approach leads to values for the critical flow which are well above the experimental measurements. For example, the value of R_g would have to be about 0.3 to conform to the observed discharges for qualities as low as 0.050; whereas the Martinelli and Levy R_g values are 0.9 and 0.7.

A more detailed approach is based upon a momentum balance initially derived by Linning (*12, 9*), which incorporates several simplifying assumptions. In an annular flow model with gas flowing at a uniform velocity in the core and the liquid flowing at a uniform velocity in an annulus at the wall, the pressure at a cross section is considered to be uniform. For the conditions of steady and isentropic flow (to evaluate maximum flow).

$$d(W_g u_g + W_f u_f) = -A\,dp \qquad (3)$$

The phase velocities are expressed in terms of the void fractions, quality, and the total mass flow rate:

$$u_g = \frac{x G v_g}{R_g} \qquad (4)$$

$$u_f = \frac{(1-x) G v_f}{(1-R_g)} \qquad (5)$$

Further, $W_g = xGA$ and $W_f = (1-x)GA$. With these substitutions and the differentiation carried out under constant entropy, Equation (3) becomes

$$-1 = \frac{G^2}{g_c}\left[\left\{\frac{2xv_g}{R_g} - \frac{2(1-x)v_f}{1-R_g}\right\}\left(\frac{dx}{dp}\right)_s + \left\{\frac{(1-x)^2}{1-R_g}\right\}\left(\frac{dv_f}{dp}\right)_s + \frac{x^2}{R_g}\left(\frac{dv_g}{dp}\right)_s + \left\{\frac{(1-x)^2 v_f}{(1-R_g)^2} - \frac{x^2 v_g}{R_g^2}\right\}\left(\frac{dR_g}{dp}\right)_s\right] \qquad (6)$$

Martinelli's correlation of R_g may be represented by a straight line over limited ranges:

$$R_g = aX + b \qquad (7)$$

where a and b are constants to be determined for each range and

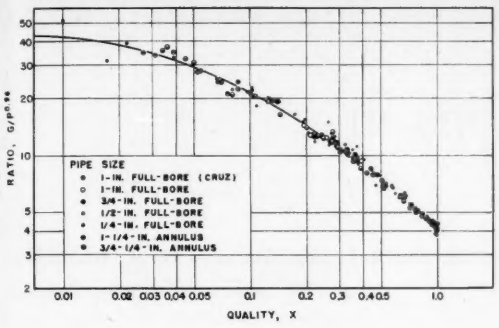

Fig. 9. Empirical correlation of experimental data on critical steam-water mass flow rates.

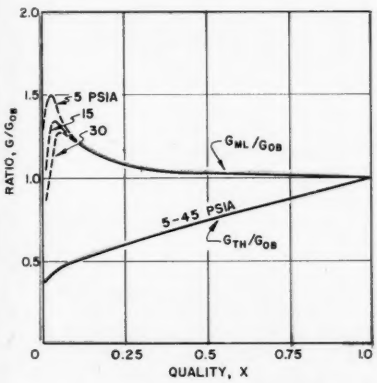

Fig. 10. Comparison of calculated mass flow rates with observed values.

$$X^2 = \left(\frac{1-x}{x}\right)^{1.8}\left(\frac{v_f}{v_g}\right)\left(\frac{\mu_f}{\mu_g}\right)^{0.2}$$

$$= f(x, p) \text{ for steam-water} \qquad (8)$$

An approximation of the term $(dR_g/dp)_s$ is then

$$\frac{1}{a}\left(\frac{dR_g}{dp}\right)_s = \left(\frac{dX}{dx}\right)_p\left(\frac{dx}{dp}\right)_s + \left(\frac{dX}{dp}\right)_x \qquad (9)$$

Thus with the use of the steam tables and the empirical evaluations from the Martinelli correlation, Equation (6) can be solved for G for given values of x and p. The use of the modified momentum model leads to results shown in Figure 10. Agreement is good at the higher qualities and the predicted values become increasing larger than the observed values as the quality is decreased. At 10% quality the ratio of the predicted to the observed value is as high as 1.24. The ratio G_{TH}/G_{OB} is included in Figure 10 for comparison of the modified momentum model and the homogeneous model.

COMPARISON WITH OTHER INVESTIGATORS

Benjamin and Miller's data on flashing water for 4-in. pipes (*3*) are closely approximated by the homogeneous model and thus are not in agreement with the empirical correlations given in Figures 8 and 9. Similarly, the Bottomley mass flow data (*4*) for 3 to 4% quality at critical pressures from 35 to 53 lb./sq. in. abs. are significantly lower than the observed values in this paper.

Burnell's data (*5*) for boiling-water discharge from ½- to 1½-in. pipes agreed within ±10% with the discharges calculated from the empirical correlations for a pressure range from 6 to 15 lb./sq. in. abs. and were 20 to 35% lower for a pressure range from 25.4 to 58.5 lb./sq. in. abs. The Burnell nozzle-discharge data ranged from 3.4 to 34.1% less than the empirical values based upon the correlations.

Comparisons were made with Linning's predicted discharge values (*12*) for qualities from 1 to 10%. The Linning values were about 40 to 50% less than the observed values in this paper.

SUMMARY

A new method of measuring the critical flow behavior of steam-water mixtures has been described. In general, the critical flows measured are higher than the results reported previously by investigators studying the flow of flashing water. The inadequacy of the homogeneous model for evaluating critical discharges for low qualities has been demonstrated. Two empirical correlations were developed, but these correlations should be limited to the range of variables studied. Several analytical approaches were tried and a modified momentum model yielded the best results over a quality range from 1 to 0.1. Considerable progress has yet to be made in defining and understanding the two-phase critical-flow phenomena.

ACKNOWLEDGMENT

The investigations reported were made possible through an Atomic Energy Commission contract AT-(11-1)-210, 211 with the Chemical Engineering Department, University of Minnesota.

NOTATION

A = flow cross-sectional area, sq. ft.
a, b = empirical constants
G = mass flow rate, lb./(sec.)(sq. ft.)
g_c = gravitational constant, 32.2 lb.$_m$-ft./lb.$_f$-sec.^{2}
h = enthalpy, B.t.u./lb.
J = conversion factor, 778 ft.-lb./B.t.u.
P = critical pressure, lb./sq. in. abs.
R_g = void fraction, fraction of cross-sectional area occupied by the gas
s = entropy, B.t.u./(lb.)(°F.)
TE = total specific energy, B.t.u./lb.
u = velocity, ft./sec.
v = specific volume, cu. ft./lb.
W = mass rate, lb./sec.
x = quality
μ = viscosity, lb.$_m$/(ft.)(sec.)

Subscripts

f = saturated liquid phase
fg = change by evaporation
g = gas phase
OB = observed or experimental
TH or th = theoretical (calculated on basis-of homogeneous model)

LITERATURE CITED

1. Allen, W. P. Jr., *Trans. Am. Soc. Mech. Engrs.*, **73**, 257 (1951).
2. Bailey, J. F., *ibid.*, 1109 (1951).
3. Benjamin, M. W., and J. G. Miller, *Trans. Am. Soc. Mech. Engrs.*, **64**, 657 (1942).
4. Bottomley, W. T., *Trans. Northeast Coast Institution of Engineers and Shipbuilders*, **53**, 65 (1936–7).
5. Burnell, J. G., *Engineering*, **164**, 572 (1946).
6. Cruz, A. J. R., M.S. thesis, Univ. of Minnesota, Minneapolis (1953).
7. Harvey, B. F., and A. S. Foust, *Chem. Eng. Progr. Symposium Ser.* No. **5**, **49**, 91 (1953).
8. Hodkenson, B., *Engineering*, **143**, 629 (1937).
9. Isbin, H. S., R. Moen, and D. R. Mosher, *AECU-2994* (1954).
10. Kittredge, A. E., and E. S. Dougherty, *Combustion*, **6**, 14 (1934).
11. Levy, S., *Proc. Second Midwestern Conference on Fluid Mechanics*, p. 237, Ohio State University, Columbus (1952).
12. Linning, D. L., *Proc. Inst. Mech. Engrs. (B)*, **1**, 64 (1952).
13. Martinelli, R. O., and R. W. Lockhart, *Chem. Eng. Progr.*, **45**, No. 1, 39 (1949).
14. Moy, J. E., M.S. thesis, Univ. of Minnesota, Minneapolis (1955).
15. Rateau, A., "Experimental Researches on the Flow of Steam Through Nozzles and Orifices and the Flow of Hot Water," trans. by H. B. Brydon, Constable, London (1905).
16. Schweppe, J. L., and A. S. Foust, *Chem. Eng. Progr. Symposium Ser.* No. 5, **49**, 77 (1953).
17. Silver, R. S., *Proc. Roy. Soc. (London)* **A194**, 464 (1948).
18. Silver, R. S., and J. A. Mitchell, *Trans. Northeast Coast Institution of Engineers and Shipbuilders*, **62**, 51, D15-30 (1945–6).
19. Stuart, M. D., and D. R. Yarnall, *Mech. Eng.*, **58**, 481 (1936); *Trans. Am. Soc. Mech. Engrs.* **66**, 387 (1944).

Catalyzed Gas-liquid Reactions in Trickling-bed Reactors

B. D. BABCOCK, GLØR T. MEJDELL and O. A. HOUGEN

University of Wisconsin, Madison, Wisconsin

Kinetic studies were made in a differential flow reactor of the hydrogenation of α-methylstyrene with the liquid trickling over a bed of catalyst pellets countercurrent to a stream of hydrogen. The catalysts consisted of palladium, platinum, rhodium, ruthenium, and nickel supported on the external surfaces of alumina pellets.

With palladium at pressures above 3 atm. the apparent rate-controlling step was a surface reaction between dissociated hydrogen and α-methylstyrene both adsorbed on different types of active sites. Below 3 atm. pressure the reactants competed for similar active sites. With platinum the apparent rate-controlling step was a surface reaction between dissociated hydrogen and α-methylstyrene on similar active sites. Rhodium and nickel catalyzed the polymerization α-methylstyrene together with slow hydrogenation. Ruthenium had negligible activity for catalyzing the hydrogenation under the moderate conditions used in this work.

In all cases mass transfer resistances were negligible.

Part I. Hydrogenation of α-Methylstyrene Catalyzed by Palladium

This study was undertaken to demonstrate the utility of applying established concepts of mass transfer and chemical kinetics to the correlation of reaction-rate data obtained on a three-phase system in a flow reactor. The particular system chosen for study was a liquid-gas reaction catalyzed by a bed of solid particles, that is, a trickling-bed reactor. The chemical reaction studied in this investigation was the hydrogenation of liquid α-methylstyrene to form liquid cumene. The reaction was carried out in a fixed bed of catalyst pellets consisting of palladium deposited on the external surfaces of alumina pellets. A flow system in a differential bed was selected with the liquid trickling over the pellets and with hydrogen flowing countercurrently. The accuracy of the analysis permitted the use of a thin-bed reactor, which resulted in small changes in temperature, pressure, and composition across the bed. Such conditions allowed the use of arithmetic mean values of these properties calculated from the terminal conditions of the bed for correlation with reaction rates.

SELECTION OF THE SYSTEM

A gas-liquid reaction was desired which would proceed rapidly to completion at moderate temperatures and pressures in the presence of a solid catalyst and which would proceed at a negligible rate in the absence of a solid catalyst. Alphamethylstyrene was selected as the liquid reactant for its low volatility, ease of hydrogenation, ease of accurate analysis of reaction products, and completeness of reaction at moderate temperatures. It proved to be an ideal compound for kinetic studies of a gas-liquid reaction although the reaction itself is of no commercial importance.

Palladium supported on alumina pellets was chosen as the catalyst for its ability to hydrogenate liquid α-methylstyrene rapidly to a single product, cumene, at moderate temperatures and pressures. In the manufacture of this catalyst the palladium was deposited on the exterior surfaces of ⅛- by ⅛-in. cylinders as a thin layer making up 0.5 weight % of the pellets.

PREVIOUS WORK

Trickling Reactors

Previous experiments on the kinetics of trickling-bed reactors were reported by Miller (*6*) and Klassen (*5*). Miller used an integral reactor for the hydrogenation of cottonseed oil over a pelletted nickel catalyst. Mass transfer resistances were reported to be negligible. Klassen used a differential reactor for the air

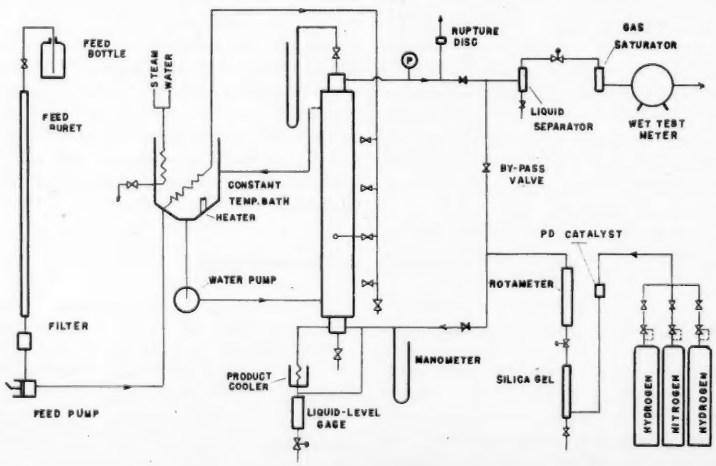

Fig. 1. Flow diagram.

B. D. Babcock is with E. I. duPont de Nemours and Co., Inc., Parkersburg, West Virginia, and G. T. Mejdell is with Norges Tekniske Høgskole, Trondheim, Norway.

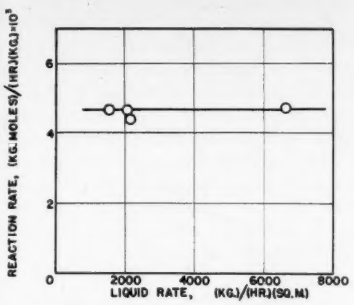

Fig. 2. Dependence of reaction rate on liquid rate; G = 16.6 kg./(hr.)(sq. meter), T = 39.5°C., and π = 1.93 atm.

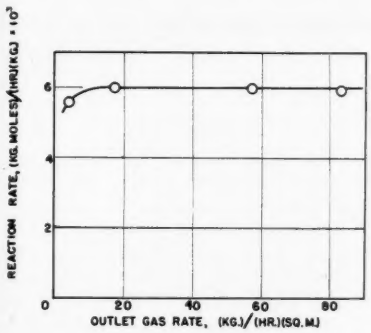

Fig. 3. Dependence of reaction rate on gas rate; T = 39.5°C. and π = 1.93 atm.

oxidation of ethanol to acetic acid in the presence of a palladium catalyst. He found that the apparent rate-controlling chemical step was the reaction between adsorbed molecular ethanol and adsorbed molecular oxygen. Mass transfer coefficients were calculated for the transfer of oxygen through the gas and liquid phases to the catalyst surface.

Palladium-hydrogen System

Palladium has an unusual capacity for dissolving and transmitting hydrogen. Below 300°C. two palladium-hydrogen phases exist, the α phase, low in hydrogen, and the β phase, rich in hydrogen (*7*). Palladium has a face-centered cubic structure with a lattice constant which is increased by the adsorption of hydrogen as follows:

Palladium	3.883 Å.
α-Pd-H	3.894 Å.
β-Pd-H	4.018 Å.
Excess hydrogen in Pd-H	> 4.018 Å.

The adsorption and occlusion of hydrogen by palladium occurs as atomic hydrogen, as is demonstrated by the observation that the amount adsorbed or occluded is proportional to the square root of the pressure.

In the vapor-phase hydrogenation of benzene on palladium Alchudzhan (*1*) found that the α-phase palladium-hydrogen crystal was an active catalyst whereas the β phase was relatively inactive. The β phase was formed by prolonged exposure of palladium to hydrogen at room temperature. The α phase was restored by subsequent displacement of hydrogen by contact with either nitrogen or oxygen.

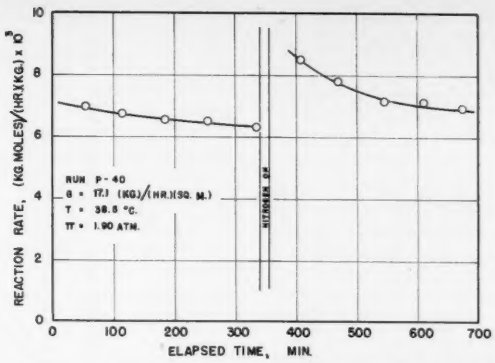

Fig. 4. Variation of catalyst activity with time at the beginning of a run.

EXPERIMENTAL EQUIPMENT

A flow diagram of the experimental equipment is shown in Figure 1. The reactor consisted of a stainless steel pipe 49 in. long by 1½ in. I.D. jacketed with a 3-in. steel pipe. A flow of water through the annulus maintained the desired temperature in the reactor, which was packed with an 8-in. depth of inert alumina pellets both immediately above and below the catalyst bed to distribute the liquid feed and to mix the reaction products thoroughly. Thirty grams of catalyst were used throughout this work. Surface-area measurements of the catalyst pellets were not attempted, as only the exterior areas of the pellets were covered with active catalyst.

Liquid feed was pumped into the reactor by a Hills-McCanna duplex pump with a delivery rate variable from 0 to 11 liters/hr. Pulsation in the flow of the liquid over the catalyst was minimized by the superimposed inert packing.

Commercial α-methylstyrene was used in these studies without further purification. The feed and product of the various runs were tested for polymers by the method of Boundy and Boyer (*2*), and in no case was any polymer detected.

The hydrogen was purified to remove traces of oxygen by passing the gas over a palladium catalyst to convert the oxygen to water and then through a silica gel bed to remove the water. Only a small fraction of the hydrogen stream fed to the reactor was consumed; therefore calculation of the hydrogen consumption by difference was not attempted.

Temperature measurements were made with bare thermocouples extending into the reactor both above and below the catalyst. The wires were sealed in steel tubes with an epoxy resin, and the resin exposed to the process was coated with Sauereisen cement to prevent contamination of the catalyst. Despite attempts to maintain isothermal operation, some temperature rise through the catalyst bed was unavoidable. For adiabatic operation this temperature rise is about 5.8°C. for each 1% conversion. The actual rise through the bed averaged 3°C. for each per cent of conversion, an indication that the operation was between adiabatic and isothermal. An arithmetic average value of temperature across the bed was used in correlating rate data. Since the reaction rate was nearly linear with temperature over the small ranges of temperature rise which occurred in the reactor, no significant errors are introduced through use of the arithmetic mean valves.

Pressures were measured both above and below the bed with mercury manometers and Bourdon gauges. The pressure drop through the reactor did not exceed 5 mm. Hg in any of the runs.

Pure cumene, which was needed for preparation of the various feed compositions between 10 and 90% α-methylstyrene, was prepared by complete hydrogenation of α-methylstyrene and was purified by simple distillation.

The extent of conversion in the reactor was determined by the difference in refractive indexes between feed and product samples as measured with a dipping refractometer. The refractive indexes of the three related hydrocarbons at 30°C. are as follows:

		n_D
α-methylstyrene	(*2*)	1.5331
Cumene	(*3*)	1.4865
Isopropylcyclohexane	(*3*)	1.4364

Complete hydrogenation of the α-methylstyrene yielded a product with the refractive index of cumene thus demonstrating that the benzene ring is not hydrogenated under the conditions used in this work.

Reaction rates were calculated as

$$r = -\frac{F\Delta x}{W} \qquad (1)$$

For the thin catalyst bed Δx ranged between 0.01 and 0.03 and could be determined with a precision of ±0.0005.

PRELIMINARY EXPERIMENTS

To establish the limitations of experimental procedures several preliminary experiments were performed. With nickel as a catalyst extensive polymerization of the α-methylstyrene took place, whereas with palladium only hydrogenation of the side chain occurred.

The homogeneous reaction rate was found to be negligible in the temperature and pressure ranges under study. Further tests showed that the reaction was not catalyzed by the catalyst support, alumina, or by the walls of the reactor.

Feed Flow Rates

Preliminary tests to determine the effects of gas and liquid flow rates showed that reaction rates were independent of the flow rates of either the gas or the liquid provided that these rates exceeded 1,500 kg./(hr.)(sq. meter) for the liquid and 15 kg./(hr.)(sq. meter) for the gas (Figures 2 and 3). These results are partial proof that under these conditions mass transfer resistances are of negligible importance in controlling the reaction rate.

Catalyst Activity

Several months of experimentation was carried out before techniques for securing reproducible catalyst activity were acquired. Poisoning of the palladium catalyst, caused by the epoxy resin used to seal the thermocouples, was prevented by covering the exposed resin with Sauereisen cement.

The activity of fresh catalyst was initially high but decreased to a constant value after several hours. Exposure of the catalyst to nitrogen, oxygen, or argon caused a temporary increase in the activity of the catalyst, as shown in Figure 4. This effect was due to the displacement of hydrogen from the palladium structure with a resulting change of phase to a more active catalytic form. The catalyst was therefore kept wetted with feed stock and in contact with hydrogen at atmospheric pressure when the unit was not in operation.

Fresh feed or feed stock that had been stored for some time gave unusually high reaction rates when first passed through the reactor, probably owing to the presence of dissolved oxygen or oxidation products. After the feed had been circulated through the reactor for several hours the reaction rate returned to normal.

Following this preliminary work it was possible to make a complete study of the effects of pressure, temperature, and feed composition on reaction rates at a constant level of catalyst activity.

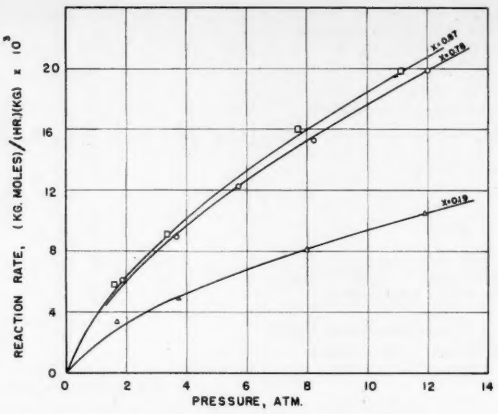

Fig. 5. Reaction rate as a function of pressure at 38.2°C.

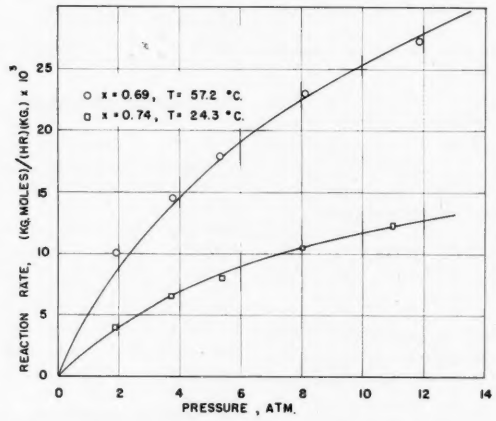

Fig. 6. Reaction rate as a function of pressure at 57.2° and 24.3°C.

CORRELATION OF EXPERIMENTAL DATA

The following conclusions were drawn from the experimentally determined reaction rates, plotted as functions of concentration, temperature, and pressure in Figures 5 to 8.*

1. Mass transfer resistance in the gas phase is nonexistent, as the phase is pure hydrogen.

2. Mass transfer resistance in the liquid surrounding the pellets is negligible as evidenced by the independence of reaction rates of liquid and gas flow rates. Furthermore at low pressures a maximum is observed in the reaction rate plotted as a function of mole fraction of α-methylstyrene (Figure 7), an impossible condition if mass transfer were rate controlling.

3. Mass transfer resistance inside the catalyst pellets is small, as the reaction is restricted to the exterior surface where the catalyst resides. A rough calculation by the Thiele method gave an effectiveness factor of 80% if it was assumed that hydrogen must diffuse through liquid α-methylstyrene and of 99% if it is assumed that the diffusion of α-methylstyrene is limiting. It is likely that hydrogen enters the catalyst by diffusion through the palladium structure as well as through portions of the catalyst surface which are not wetted by liquid. The actual effectiveness factor is therefore between 80 and 99%.

4. Adsorption rates of the reactants or desorption rates of the product cannot be rate controlling because if (*a*) adsorption of hydrogen were rate controlling, the reaction rate would be proportional to hydrogen pressure; (*b*) adsorption of α-methylstyrene were rate controlling, the reaction rate would be proportional to the first or higher power of the concentration of α-methylstyrene, depending on the adsorption equilibrium constant for cumene; and (*c*) desorption of cumene were rate controlling, the reaction rate would be nearly independent of the concentration of α-methylstyrene and of hydrogen pressure.

It was concluded therefore that the surface reaction is rate controlling. A consideration of possible surface-reaction steps showed that previously formulated rate equations were not satisfactory over the entire range of pressure. None of the mechanisms postulated by Hougen and Watson (*4*) explained the difference in the effects of liquid feed composition on reaction rate at 1.9 and 3 atm. pressure, as shown in Figure 7. At a hydrogen pressure of 1.9 atm. the maximum rate occurred at a mole fraction of α-methylstyrene of 0.5. At increased pressures the maximum rate occurred at increasingly higher mole fractions of α-methylstyrene.

*These data in tabular form have been deposited as document 5307 with the American Documentation Institute, Photoduplication Service, Library of Congress, Washington 25, D. C., and may be obtained for $1.25 for photoprints or 35-mm. microfilm.

The most satisfactory interpretation of the experimental results for pressures above 3 atm. postulates that the reaction rate is controlled by a surface reaction between adsorbed α-methylstyrene and two adsorbed hydrogen atoms where the two reactants are adsorbed on different types of active sites. The rate equation corresponding to this rate-controlling step, with Langmuir type of adsorption isotherms assumed, is

$$r = k_s K_H K_\alpha \pi x \left[\frac{1}{1 + \sqrt{K_H \pi}}\right]^2 \cdot \left[\frac{1}{1 + K_\alpha x + K_c(1 - x)}\right] \quad (2)$$

This equation was rearranged into the form

$$r = A\pi x \left[\frac{1}{1 + B\sqrt{\pi}}\right]^2 \left[\frac{1}{1 + Cx}\right] \quad (3)$$

for convenience in evaluating the constants. The three constants, which are functions of temperature only, were calculated at the three temperatures by the method of least squares. It was next assumed that K_c, the adsorption constant for cumene, is much less than K_α, the adsorption constant for α-methylstyrene. With this assumption the logarithms of the three constants should be linear functions of the reciprocal absolute temperatures. This relationship is shown in Figure 9. Again the best straight line was determined by the method of least squares. The solid lines shown in Figures 5 to 8 are the values of the reaction rates calculated from Equation (3) by use of the calculated constants. The final form of the rate equation is then

$$r = k_s K_H K_\alpha \pi x \left[\frac{1}{1 + \sqrt{K_H \pi}}\right]^2 \cdot \left[\frac{1}{1 + K_\alpha x}\right] \quad (4)$$

$$\ln k_s = -\frac{1225}{RT} + 0.17$$

$$\ln K_H = -\frac{5780}{RT} + 6.16$$

$$\ln K = \frac{1325}{RT} - 0.98$$

A comparison of the experimental and calculated results is shown in Table 1.

TABLE 1

Temperature, °C.	Average deviation of a single measurement, %	Maximum deviation, %	Number of experimental points
24.3	3.0	5.6	8
38.2	2.3	5.3	18
57.2	2.7	5.3	9

DISCUSSION OF RESULTS

Selection of Rate-controlling Step

The proposed rate equation fits the experimental data with an average deviation of a single measurement of less than 3% for pressures above 3 atm. Below 3-atm. pressure the proposed equation is not so accurate. The data indicate that below 3-atm. pressure the α-methylstyrene and hydrogen compete for the same active sites. Such an assumption results in a rate equation of the form

$$r = \frac{A\pi x}{(1 + B\sqrt{\pi} + Cx)^3} \quad (5)$$

Sufficient data were not taken to evaluate the constants of this equation because the available catalyst volume in the reactor was too low to permit sufficient conversion for accurate analysis.

The change in the apparent rate-controlling step as pressure is increased is consistent with the observations of Alchudzhan (*1*) concerning the activity of the two palladium-hydrogen phases. At higher pressures the β phase would be present which could have markedly different adsorption characteristics from the α phase.

Heats of Reaction and Adsorption

The energy of formation of the activated complex was found to be 1,225 cal./g.-mole. This is consistent with the endothermic nature of the formation of an activated complex.

The observed heat of adsorption of α-methylstyrene, $-1{,}325$ cal./g.-mole, is consistent with the exothermic nature of molecular adsorption. The relatively small value suggests that physical adsorption may be involved rather than chemisorption.

The observed heat of adsorption of hydrogen, $+5{,}780$ cal./g.-mole, does not agree with the exothermic behavior reported by Smith (*7*). However, the nature of the adsorption on the restricted areas of the surface of the catalyst cannot be expected to be directly comparable with adsorption in the bulk of the metal. The endothermic nature of the adsorption observed in this work is in agreement with the observation that the heat of dissociation of the hydrogen molecule is greater than the heat of adsorption of molecular hydrogen.

Errors

Errors in measuring the various experimental quantities are estimated as follows:

	Estimated error
Liquid flow rate	±2%
Gas flow rate	±2%
Temperature	±0.2°C.
Pressure	± 15 mm. Hg (1 to 3 atm.) ± 0.07 atm. (3 to 12 atm.)
Conversion	±0.03%
Reaction rate	±5%

SUMMARY

1. The catalytic activity of palladium for hydrogenation is increased by pretreatment with air or nitrogen. Subsequent exposure to hydrogen reduces the activity.

2. All mass transfer resistances were negligible under the conditions of operation.

3. Above 3-atm. pressure the apparent rate-controlling step is a surface reaction between adsorbed α-methylstyrene and adsorbed atomic hydrogen on different types of active sites. A rate equation is presented which fits the experimental data with an average deviation of 3%. The maximum deviation of a single measurement is 5.6%.

4. Below 3-atm. pressure the mechanism of the reaction changes, owing to a phase change in the palladium-hydrogen catalyst system. Insufficient experimental data were obtained to formulate a rate equation in this region.

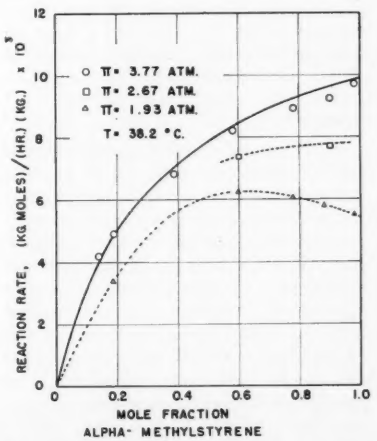

Fig. 7. Reaction rate as a function of conversion at 38.2°C.

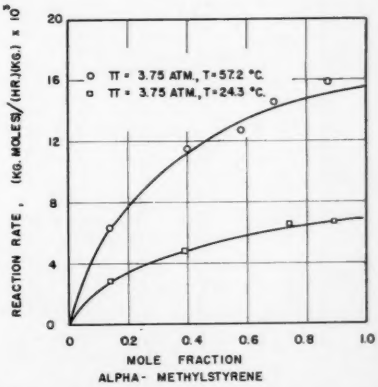

Fig. 8. Reaction rate as a function of conversion at 57.2° and 24.3°C.

Part II. Hydrogenation of α-Methylstyrene Catalyzed by Platinum

GLØR T. MEJDELL AND O. A. HOUGEN

University of Wisconsin, Madison, Wisconsin

This second investigation on the kinetics of catalyzed gas-liquid reactions in trickling-bed reactors is similar to that described in Part I except that platinum was used as the catalyst instead of palladium. A few exploratory experiments were also made with ruthenium, rhodium, and nickel.

CATALYST

A platinum catalyst supported on 1/8- by 1/8-in. cylindrical pellets of alumina was used. The platinum appeared as a fine-grain deposit on the exterior surfaces of the pellets, which had the following properties:

Bulk density	0.91 ± 0.01 g./cc.
Pellet density	1.39 ± 0.01 g./cc.
Platinum content	2%

Interior surface areas of the pellets were not measured, as only the external surfaces of the pellets were covered with the active catalyst and hence involved in the reaction.

To obtain sufficient conversion for reliable determinations of reaction rates 100 g. of catalyst was used for runs Pt-12 to Pt-15 and 350 g. for the remaining runs. The catalyst bed was replaced after runs Pt-15 and Pt-20. Between runs the catalyst was kept wetted with the liquid feed and in contact with hydrogen at 1 atm.

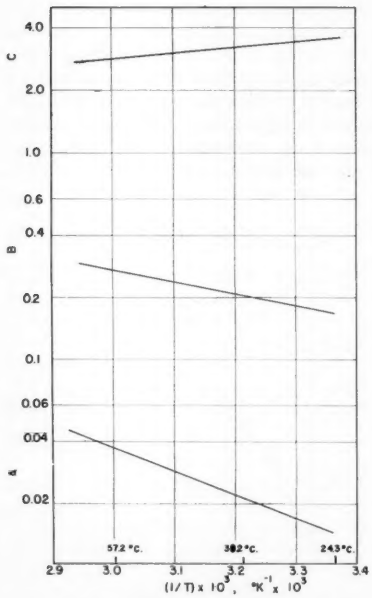

Fig. 9. Temperature dependence of constants of Equation (3).

EXPERIMENTAL OBSERVATIONS

Compared with the palladium catalyst the activity of the platinum was much more difficult to reproduce and did not reach a constant value within 100 hr. of operation.

The observed behavior of the platinum catalyst is summarized as follows:

1. The catalyst activity showed an irreversible decline with time of operation and did not attain a constant value as was the case with palladium. After an initial rapid rate of decline the catalyst activity continued to decline indefinitely at a slow rate.
2. In contrast to the behavior of palladium, the reduced activity of platinum after storage under hydrogen was not restored by exposure to air or nitrogen.
3. The activity of a fresh supply of catalyst decreased rapidly during the first 16 hr. of operation, dropping to less than 10% of its initial value during operation at constant pressure and feed composition. With a fresh supply of catalyst, experimental runs were continued for at least 20 hr. before samples and data were taken for correlation.
4. An increase in the pressure of hydrogenation produced a considerable decrease in catalyst activity. Further variations in pressure did not alter this activity unless the former highest pressure was subsequently exceeded. Any increase in pressure above this former highest pressure caused a further decrease in activity. These results are shown in Figure 10. In any given series of pressure runs the experiments were, therefore, started with the highest pressure of the planned series in order that runs at subsequent pressures would be made at nearly the same activity.

Standard Run

In the course of making experimental runs at variable conditions of pressure and composition, the extreme sensitivity of the catalyst activity made it necessary to make intermediate runs at frequent intervals under some arbitrary standard conditions of operation. From the decline in activity between two succeeding standard runs the catalyst activities of intermediate runs at variable pressure and composition were estimated. This standard run was chosen at the arbitrary conditions of 40°C., 3.7 atm., and a liquid feed composition of 60 mole % α-methylstyrene.

To secure several data at nearly constant activity the experimental operation was continued for 30 to 80 hr. in each series without interruption.

CORRELATION OF DATA

All experimental data on significant runs are tabulated in Table 1.* The reaction rates. adjusted to a standard activity are plotted in Figures 11 and 12 as functions of liquid composition at different pressures. From these data the following conclusions were drawn:

1. Mass transfer resistances were negligible, as the reaction rates were independent of the flow rates of either gas or liquid. This conclusion is supported by the results of the first investigation using palladium catalyst, where although the reaction rate was ten times faster than with platinum the mass transfer resistances were negligible. In this investigation the resistance to the mass transfer of hydrogen was much less than 1% of the resistance imposed by the chemical reaction.
2. The adsorption rate of hydrogen is not rate controlling. If it were, the reaction rate would be directly proportional to the pressure of hydrogen, whereas the observed rate varied with a fractional power of pressure much less than unity.
3. The adsorption of α-methylstyrene is not rate controlling, as this would require a rate proportional to the concentration to a first or higher power depending upon the adsorption constant of cumene. The reaction rate was a complex function of liquid composition, reaching a maximum rate at compositions below unit mole fraction of α-methylstyrene.
4. The desorption of cumene is not rate controlling, as this would require a rate nearly independent of pressure and concentration, contrary to observations.
5. The rate-controlling step does not involve the impact of one unadsorbed reactant with the other adsorbed. This would give a reaction rate proportional to the concentration of the unadsorbed reactant, contrary to observations.

Development of Equations of Rate-controlling Step

The experimental data combined with the observations above indicate that the rate-controlling step is a surface

*See footnote on page 368.

reaction between the adsorbed α-methylstyrene and adsorbed atomic hydrogen on adjacent sites. By the methods outlined by Hougen and Watson (*4*), extended to gas-liquid reactions, this postulation results in the following rate equations:

$$r=\frac{k_s(L-c_p)^3K_\alpha K_H x\pi}{(1+K_\alpha x+K_c(1-x)+\sqrt{K_H\pi})^3} \quad (1)$$

Equation (1) may be written in the following form:

$$r = \frac{A\pi x}{(1 + B\sqrt{\pi} + Cx)^3} \quad (2)$$

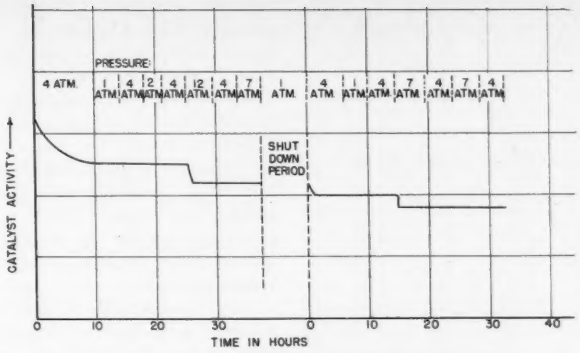

Fig. 10. Typical behavior of platinum catalyst.

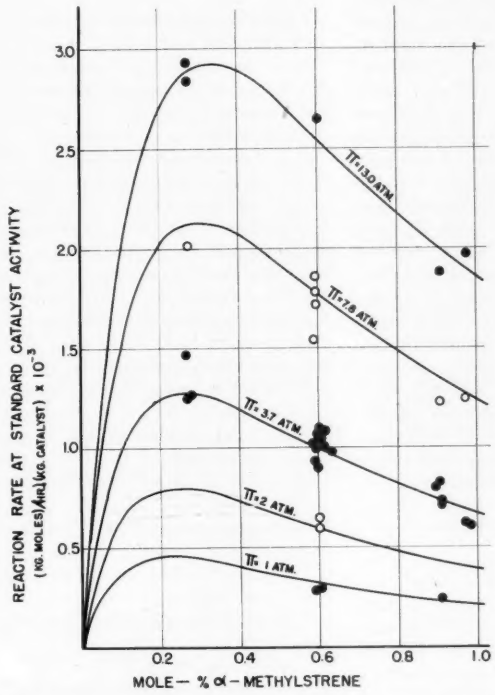

Fig. 11. Reaction rate as a function of liquid composition at standard catalyst activity.

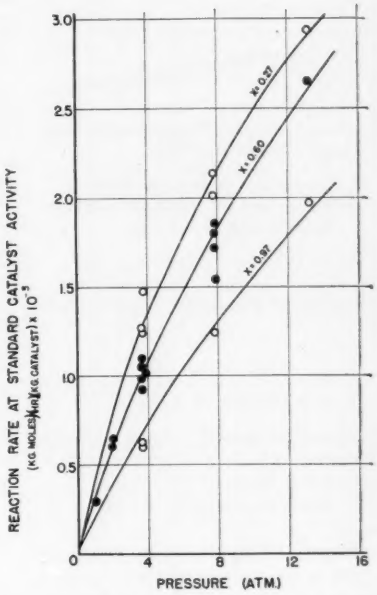

Fig. 12. Reaction rate as a function of hydrogen pressure at standard catalyst activity.

where

$$A = \frac{k_s K_H K_\alpha (L - c_p)^3}{(1 + K_c)^3} \quad (3)$$

$$B = \frac{\sqrt{K_H}}{1 + K_c} \quad (4)$$

$$C = \frac{K_\alpha - K_c}{1 + K_c} \quad (5)$$

The values of B and C are constant for all experimental runs at constant temperature, whereas A is a function of the catalyst activity.

Standard Activity

If A_s is the value of A for a "standard activity," arbitrarily defined as the catalyst activity having a reaction rate of 1×10^{-3} (kg-moles)/(hr.)(kg. catalyst) under standard conditions, namely, 40°C., 60 mole % α-methylstyrene, and a hydrogen pressure of 3.7 atm., from this definition and Equation (2),

$$A_s = \frac{1(10^{-3})}{(3.7)(0.6)} \cdot (1 + B\sqrt{3.7} + 0.6C)^3 \quad (6)$$

The value of A at any other catalyst activity will then be given as

$$A = A_s\alpha \quad (7)$$

where

$$\alpha = \frac{A}{A_s} = \left(\frac{L - c_p}{L - c_{p_s}}\right)^3 = r_s \times 10^3 \quad (8)$$

Introducing the activity factor in Equation (2) gives

$$r = \frac{\alpha A_s \pi x}{(1 + B\sqrt{\pi} + Cx)^3} \quad (9)$$

Evaluation of Constants in Rate Equation (1)

Rearrangement of Equation (2) gives

$$\sqrt[3]{\frac{\pi x}{r}}\,\frac{1}{\sqrt[3]{A}} + \frac{B\sqrt{\pi}}{\sqrt[3]{A}} + \frac{Cx}{\sqrt[3]{A}} \quad (10)$$

The constants A, B, and C were determined from Equation (10) by the method of least squares, and the value of A_s was calculated from Equation (6). At a temperature of 40°C.

$$A_s = 1.155 \times 10^{-2}, \quad B = 0.195,$$

and $$C = 2.623.$$

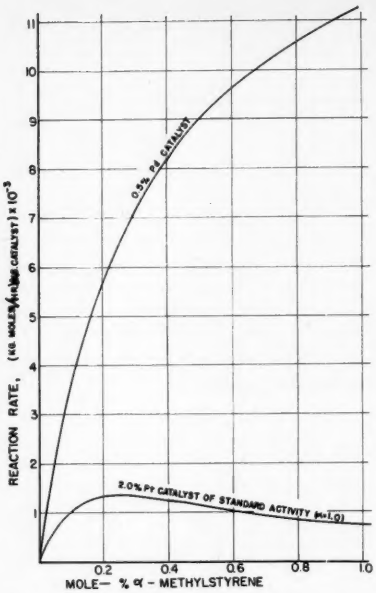

Fig. 13. Comparison of reaction rates with 0.5% palladium and 2% platinum catalysts at 40°C. and $\pi = 4$ atm.

Inserting these values in Equation (9) gives

$$r = \frac{\alpha 0.01155 \pi x}{(1 + 0.195\sqrt{\pi} + 2.623x)^3} \quad (11)$$

The catalyst activity factor defined by Equation (8) is a function of the history of the catalyst. The values of α used in these correlations are given in Table 1.*

In Figure 12 the reaction rates at standard activity are plotted against hydrogen pressure π at three values of liquid composition, namely, at $x = 0.27$, 0.6, and 0.97. In Figure 11 the reaction rates at standard activity are plotted against liquid composition at five pressures: 1, 2, 3.7, 7.8 and 13.0 atm. The unusual and unexpected effect of liquid concentration is shown in Figure 11, where for any given pressure the maximum rate does not occur at a mole fraction of unity, but at a mole fraction ranging from 0.2 to 0.35. The constants k_s, k_α, k_H, and K_c in Equation (1) are exponential functions of temperature. The constants A_s, B, and C in Equation (2) were evaluated only at 40°C. Evaluation of A_s, B, and C at other temperatures did not seem warranted unless the variables influencing the activity factor L-c_p were also formulated in terms of the past history of the catalyst and operating variables.

Comparison of Catalysts

In this investigation on the catalytic hydrogenation of α-methylstyrene five catalysts were used. A comparison of the reaction rates obtained at 40°C. and 3-atm. pressure as a function of liquid feed composition is shown in Figure 13. These results are based upon unit mass of catalyst. It will be observed that palladium is fully ten times as effective as platinum. With palladium a constant activity is obtainable; with platinum, the results are based upon a standard activity. Actually the activity of platinum steadily declined without reaching a constant value.

At pressures below 3 atm. both platinum and palladium exhibited similar behavior where the rate-controlling chemical step was the surface reaction between adsorbed α-methylstyrene and adsorbed atomic hydrogen. The effect of composition was remarkable in exhibiting a maximum rate at mole fractions of α-methylstyrene less than unity. With platinum, pressures were increased to 12 atm. without reaching a maximum rate at a concentration of unity. With palladium the rate-controlling step changed at pressures above 3 atm., corresponding to a phase change in the palladium-hydrogen alloy. The initial reaction rate with rhodium as a catalyst was of the same order of magnitude as that of palladium. However, the catalyst activity decreased so rapidly that the reaction rate was almost negligible after 10 hr. of operation. The reaction rates with rhodium and ruthenium were too slow for study, and nickel caused a polymerization of the α-methylstyrene. Because of polymerization or low rates no data were correlated for these three catalysts.

SUMMARY

1. With platinum as a catalyst the apparent rate-controlling chemical step in the hydrogenation of α-methylstyrene consisted of a surface reaction between adsorbed α-methylstyrene and adsorbed atomic hydrogen.

2. At a given temperature and pressure the maximum rate occurred at a mole fraction below unity. With palladium similar concentration effects were observed; however, the maximum rate occurred at a mole fraction of unity at about 3 atm. and above.

3. Platinum showed extreme variation in activity, depending upon pressure, temperature, time, and past history. A condition of constant activity was not obtained within running times of 100 hr. Rate equations were, therefore, expressed in terms of a standard activity or activity factor.

4. For the same condition of temperature, pressure, and concentration the reaction rates were at least ten times faster with palladium than with platinum.

5. Rhodium and ruthenium reaction rates were too slow for study in the available apparatus.

ACKNOWLEDGMENT

The authors wish to express their appreciation to the Wisconsin Alumni Research Foundation, the Celanese Corporation of America, E. I. du Pont de Nemours and Company, and the Foreign Operations Administration through the National Academy of Sciences for the financial support of this project through grants-in-aid for personnel, supplies, and equipment; to the Dow Chemical Corporation for donation of α-methylstyrene; to the International Nickel Company through the courtesy of E. M. Wise for the donation of rare metal catalysts; and to Willard H. Sawyer, Hirotaro Saito, and D. L. Johnson for their scientific collaboration.

NOTATION

A = constant in rate equation
A_s = value of constant in rate equation at standard catalyst activity
B = constant in rate equation
C = constant in rate equation
c_p = diminished number of active sites due to deactivation of catalyst or to gradual and irreversible accumulation of adsorbed poisons
F = liquid feed rate, kg.-moles/hr.
G = gas flow rate, kg./(hr.)(sq. meter)
K_c = adsorption constant for cumene
K_H = Adsorption constant for hydrogen
K_α = adsorption constant for α-methylstyrene
k_s = surface reaction velocity constant, kg.-moles/(hr.)(kg. of catalyst)
L = total number of active sites/g. of catalyst
L = liquid flow rate kg./(hr.)(sq. meter)
R = gas constant = 1.987 cal./(°K.)(g.-mole)
r = reaction rate, kg.-moles/(hr.)(kg. of catalyst)
r_s = reaction rate under standard conditions
T = temperature, °K.
W = mass of catalyst pellets, kg.
x = mole fraction α-methylstyrene in an α-methylstyrene–cumene mixture
α = catalyst activity factor
π = hydrogen pressure, atm.

LITERATURE CITED

1. Alchudzhan, A. A., *Zhur. Fiz. Khim.*, **26**, 1591 (1952) (*Chem. Abs.*, **47**, 6235c).
2. Boundy, R. H., and R. F. Boyer, "Styrene," Reinhold Publishing Corp., New York (1952).
3. Forziati, A. F., *J. Research Nat. Bur. Standards*, **44**, 373 (1950).
4. Hougen, O. A., and K. M. Watson, "Chemical Process Principles," Part III, John Wiley and Sons, New York (1947).
5. Klassen, J., Ph.D. thesis, Univ. Wisconsin (1953).
6. Miller, E. W., Ph.D. thesis, Case Inst. Technol., Cleveland (1952).
7. Smith, D. P., "Hydrogen in Metals," The University of Chicago Press, Chicago (1948).

*See footnote on page 368.

Studies on Effective Thermal Conductivities in Packed Beds

SAKAE YAGI and DAIZO KUNII

University of Tokyo, Tokyo, Japan

Applying both their own assumptions and the mechanism of lateral mixing proposed by Ranz (20), the authors obtained theoretical formulas for effective thermal conductivities k_e in packed beds. Previously reported experimental data were analyzed with these equations, and the usable data for prediction of k_e were shown.

In order to see the influence of both packing characteristics and temperature on the effective thermal conductivities, experimental data were obtained with air for beds with various kinds of packing, i.e., iron spheres, porcelain packings, cement clinker, insulating fire brick, and Raschig rings. Correlation of these data with Equation (15) showed that this equation adequately expressed the heat transfer mechanisms in packed beds with motionless gases, especially at high temperatures.

In the design of equipment for gas-solid reactions the proper values of the effective thermal conductivities must be estimated as simply as possible. On the basis of theoretical studies of heat transfer in these systems reported by Wilhelm (*22, 27*), Ranz (*20*), Damköhler (*7*), and Smith (*2*), the authors find that effective thermal conductivities can be separated into two terms, one of which is independent of fluid flow and the other dependent on the lateral mixing of the fluid in the packed beds. Thus theoretical equations of the effective conductivities in packed beds can be obtained that are simpler than equations previously reported. This paper reports four studies: first, the derivation of theoretical equations presented by Yagi and Kunii (*28*); second, an analysis of experimental data presented by several investigators; third, an outline of experiments on effective thermal conductivities in various kinds of packed beds with motionless air; and, fourth, an analysis of the experimental data by means of the authors' theoretical equations.

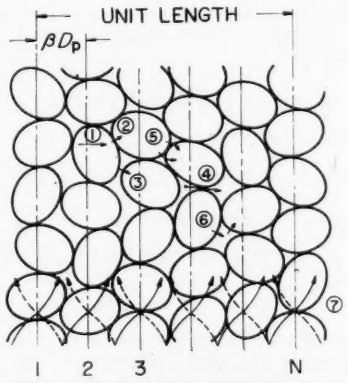

Fig. 1. A model of heat transfer in a packed bed. 1, heat transfer through solid; 2, heat transfer through the contact surface of solid; 3, radiant heat transfer between surfaces of solid (in case of gas); 4, radiant heat transfer between adjacent voids (in case of gas); 5, heat transfer through the fluid film near the contact surface; 6, heat transfer of convection, solid-fluid-solid; 7, heat transfer by lateral mixing of fluid, proposed by W. E. Ranz (20).

THEORETICAL EQUATIONS

Fundamental Assumptions

A model of heat transfer in packed beds is shown in Figure 1. Seven processes are discussed as follows:

Heat transfer mechanisms independent of fluid flow

1. Thermal conduction through solid
2. Thermal conduction through the contact surfaces of two packings
3. Radiant heat transfer between sur-

Table 1. Analytical Results of Experimental Data of Effective Thermal Conductivities in Packed Beds with Fluid Flow

$$k_e/k_g = k_e^\circ/k_g + (\alpha\beta)N_{pr}N_{ReM} = k_e^\circ/k_g + (\alpha\beta)N_{peM}$$
$$N_{ReM} = GD_p/\mu$$

Reference	Solid Gas	Diam. of solid, mm.	Diam. of bed, mm.	Data obtained N_{ReM}	k_e°/k_g	$(\alpha\beta)$	D_p/D_T
9	Catalyst cylinder Air	3.6 6.0 10.5	25.4 50 100	0∼ 1,000	5.5	0.10	0.036∼ 0.24
3	Alumina cylinder Air	3.18	51	0∼ 100	5.0	0.0833	0.0624
5	Celite cylinder Air	3.18 12.7	127	70∼ 3,500	10.4	0.136	0.025∼ 0.10
4	Silica-alumina, alumina, glass, cylinder, tablet, sphere Air, natural gas	4.9 25.4	51 102 153	0∼ 140	10.0	0.10	0.32∼ 0.37
	Glass, metal sphere Air, H_2, CO	2.46 7.42			—	0.090	0.246∼ 0.0742
1	Catalyst Air	10	100	0.1∼ 3,000	—	0.110	∼0.10
	Raschig ring Air	15×15			—	0.226	0.15
	Broken solid marble, etc. Air	2.85 16.5	52 154	30∼ 630	10	0.13	0.03∼ 0.17
15	Raschig ring (Fig. 7) Air	6.74 25	52 154	60∼ 650	3	0.24 0.17 0.12	0.10 0.15 0.20
	Berl saddle (Fig. 7) Air	12.5 25	100 154	70∼ 970	6	0.165 0.138 0.109	0.081 0.162 0.250
15	Catalyst cylinder annular space Air	3.6 6.0 10.5	154/48.5 100/34 154/27	20∼ 700	5.5	0.10	0.02∼ 0.105
21	Catalyst cylinder Air	3.18 4.76 6.36	50.8	0∼ 400	3.4 4.6 4.6	0.14 0.12 0.10	0.0625 0.0935 0.125
19	Glass sphere Air	13.3 18.2	205.0	100∼ 2,000	25.6	0.102	0.065 0.088
29	Iron sphere glass sphere insulating firebrick sphere, Air	11.0 6.0 10.0	52.9	50∼ 400	k_e°/k_g by Eq. (15)	0.12	0.114∼ 0.208

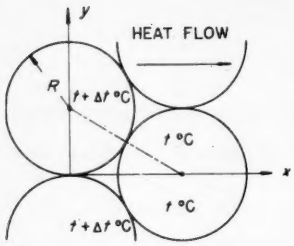

Fig. 2. Two-dimensional model of heat transfer through the fluid film in the void of packed bed.

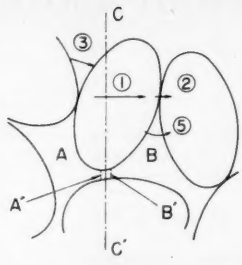

Fig. 3. A model of heat transfer without flowing fluid. A': black body surface representing void A; B': black body surface representing void B; CC': cross section perpendicular to the direction of heat flow.

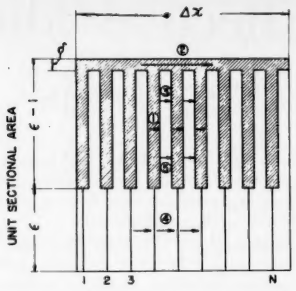

Fig. 4. Simplified model of heat transfer in packed bed without flowing fluid.

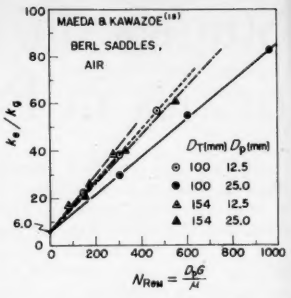

Fig. 5. Data for Berl saddles, by Maeda and Kawazoe (*15*).

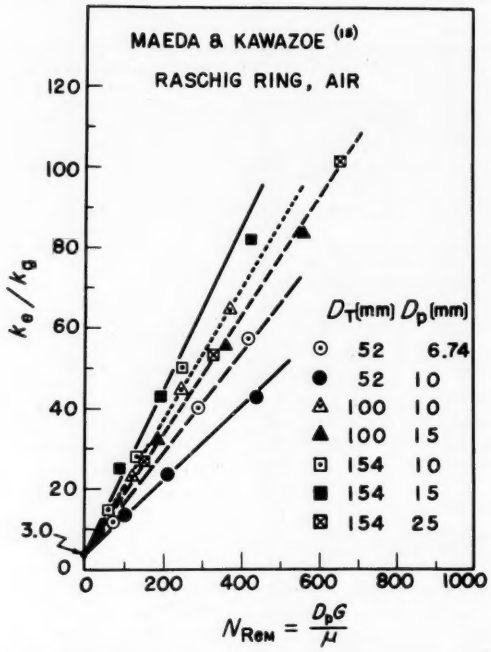

Fig. 6. Data for Raschig rings, by Maeda and Kawazoe (*15*).

faces of two packings (in the case of gas)

4. Radiant heat transfer between neighboring voids (in the case of gas)

Heat transfer mechanisms dependent on fluid flow

5. Thermal conduction through the fluid film near the contact surface of two packings
6. Heat transfer by convection, solid-fluid-solid
7. Heat transfer by lateral mixing of fluid

Mechanism 5 is calculated theoretically in the case of a two-dimensional model as shown in Figure 2, and it is found that nearly all the heat flows through the thin films of fluid near the contact point or surface of the two solids. Therefore it can be assumed that fluid flow has little effect on mechanism 5, because the fine interstices near the contact surfaces are embedded in the boundary layers except in the case of large Reynolds number.

When the Reynolds number is small, the boundary layers around the solid packings are thick; therefore mechanisms 1, 3, 4, and 5 are predominant. However, in the case of a large Reynolds number, process 7 controls the heat flux in any packed bed, and therefore the effect of mechanism 6 on the total rate of heat flow is slight. The theoretical equations containing mechanism 6, as well as the other processes, show that the effects of the convectional heat transfer mechanism solid-fluid-solid are small at all Reynolds numbers; the authors assume therefore that (1) thermal conduction through the thin film of fluid near the contact surfaces is not affected by fluid flow and (2) the convectional heat transfer mechanism solid-fluid-solid is less important than the other mechanisms and can be safely neglected.

Effect of Fluid Flow

Effective thermal conductivity caused by the lateral mixing of fluid is presented by Ranz (*20*) as the following equation:

$$(k_e)_t = \alpha C_p G/N \qquad (1)$$

The factor β is defined as the ratio of the average length l_p between the centers of two neighboring solids in the direction of heat flow to the mean diameter of packing D_p.

$$\beta = l_p/D_p \qquad (2)$$

In practical packed beds β takes a limited value between 0.82 and 1.0 for the wide ranges of packing characteristics. According to the definitions of both N and l_p,

$$N = 1/l_p = 1/\beta D_p \qquad (3)$$

From Equations (1) and (3),

$$(k_e)_t/k_g = (\alpha\beta)N_{pr} \cdot N_{Re_M} = (\alpha\beta)N_{pe_M}$$

$$N_{pr} = C_p\mu/k_g,$$

$$N_{Re_M} = D_p G/\mu, \qquad (4)$$

$$N_{pe_M} = D_p C_p G/k_g$$

The effective thermal conductivity, caused by the heat transfer mechanisms (1 to 5 in Figure 1) in the packed beds with motionless fluid, is defined by k_e°, a value that, according to assumptions 1 and 2 above, can be considered to remain constant and in parallel with the mechanism of lateral mixing when the fluid flows through the packed bed. Therefore, the effective thermal conductivity in packed beds is formulated as follows:

$$k_e = k_e^\circ + (k_e)_t \qquad (5)$$

Applying Equation (4) gives

$$\frac{k_e}{k_g} = \frac{k_e^\circ}{k_g} + (\alpha\beta)N_{pr}N_{ReM} = \frac{k_e^\circ}{k_g} + (\alpha\beta)N_{peM} \quad (6)$$

Although the value of α is 0.179 in case of the rhombohedral packing of spheres (*20*), such values seem to change considerably in an actual packed bed according to the shape of the packings, the fraction void, and the ratio of the packing diameter to the bed diameter.

Motionless Fluids

In Figure 3 the heat transfer mechanisms in the series containing the thermal conduction in the solid phase arise in the fraction $(1 - \epsilon)$ of the sectional area $C - C'$ and then the radiant heat flows from one void to another through the fraction ϵ of the sectional area.

The heat transfer coefficient of thermal radiation can be formulated as the following equations, with the two parallel surfaces of black body A' and B' near the section $C - C'$ as shown in Figure 3 assumed to represent the two voids A and B respectively:

from solid surface to solid surface

$$h_{rs} = 0.1952\{p/(2 - p)\} \cdot \{(t + 273)/100\}^3 \quad (7)$$

from void to void

$$h_{rv} = \left[0.1952 \Big/ \left\{1 + \frac{\epsilon}{2(1 - \epsilon)} \cdot \frac{1 - p}{p}\right\}\right]\{(t + 273)/100\}^3 \quad (8)$$

Then the over-all heat transfer rate q [kcal./(sq. m.)(hr.)] is formulated as Equation (9) by application of a model of heat transfer in a packed bed with motionless fluid as shown in Figure 4.

$$q = \frac{k_e^\circ}{\Delta x}\Delta t = \delta\frac{k_s}{\Delta x}\Delta t + U_s(1 - \epsilon - \delta)\Delta t + V_v\epsilon\Delta t \quad (9)$$

$$\frac{1}{U_s} = (N\Delta x)\left\{\frac{l_s}{k_s} + \frac{1}{k_g/l_v + h_{rs}}\right\} = (N\Delta x)\left\{\frac{\gamma D_p}{k_s} + \frac{1}{k_g/(\varphi D_p) + h_{rs}}\right\} \quad (10)$$

$$\frac{1}{U_v} = N\Delta x\frac{1}{h_{rv}} \quad (11)$$

where

γ = length of solid affected by thermal conductivity/mean diameter of solid = l_s/D_p

δ = total area of perfect contact surfaces as solid phase in sectional area of section $C - C'$/sectional area of section $C - C'$

φ = effective thickness of fluid film in void in relation to thermal conduction/mean diameter of solid = l_v/D_p (12)

The general equations are derived from Equations (9) through (12).

General equation

$$\frac{k_e^\circ}{k_g} = \delta\left(\frac{k_s}{k_g}\right) + \frac{(1 - \epsilon - \delta)\beta}{\gamma\left(\frac{k_g}{k_s}\right) + \frac{1}{\frac{1}{\varphi} + \frac{D_p h_{rs}}{k_g}}} + \epsilon\beta\frac{D_p h_{rs}}{k_g} \quad (13)$$

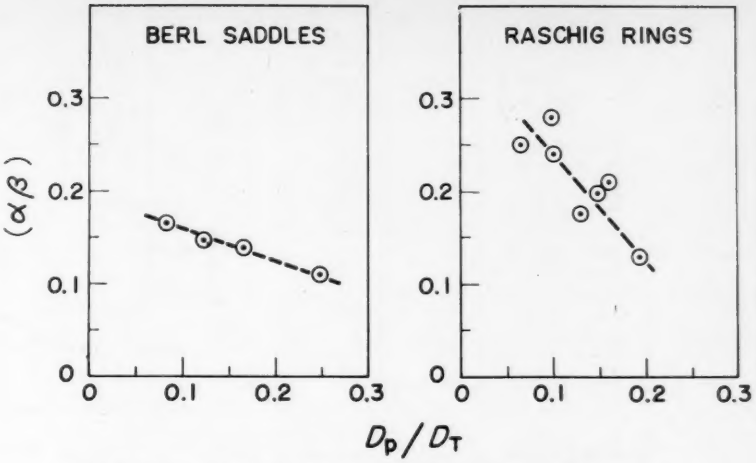

Fig. 7. Values of $(\alpha\beta)$ obtained from data by Maeda and Kawazoe (*15*).

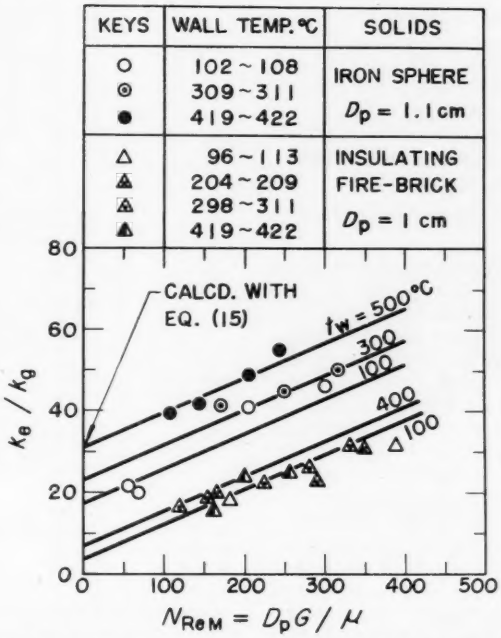

Fig. 8. Effects of wall temperature and thermal conductivities of solid particles on the effective thermal conductivities, by Yagi, Kunii and Shimomura (*29*).

Equations for special cases can be derived from Equation (13) as follows:

In vacuum

$$\frac{k_e^\circ}{k_g} = \delta + \frac{(1 - \epsilon)\beta}{1 + k_g/(D_p h_{rs})} + \epsilon\beta\frac{D_p h_{rs}}{k_g} \quad (14)$$

In case of gas-filled voids

$$\frac{k_e^\circ}{k_g} = \frac{\beta(1 - \epsilon)}{\gamma\left(\frac{k_g}{k_s}\right) + \frac{1}{(1/\varphi) + (D_p h_{rs}/k_g)}} + \epsilon\beta\frac{D_p h_{rs}}{k_g} \quad (15)$$

Table 2. Observers and Experimental Conditions in Figures 9 and 10.

Observer	Solid	Average diam.	Keys in Figures 9 and 10
Kling (*14*)	Steel sphere	3.8	(1)
Schuman and Voss (*24*)	Steel sphere	1.27	(2)
	Lead sphere	2.62	(2)
Waddems (*26*)	Steel sphere	1.59 ~ 7.94	(3)
Waddems (*26*)	Lead sphere	1.59 ~ 7.94	(4)
Waddems (*26*)	Steel cylinder, hexagonal prism		(5)
Kannuluick (*13*)	Carborundum	40 ~ 600	(6)
Schuman and Voss (*24*)	Quartz		(7)

In case of fine particles with motionless gas

$$\frac{k_e^\circ}{k_g} = \beta \frac{1-\epsilon}{\frac{k_g}{k_s} + \varphi} \qquad (16)$$

Equation (16) can be used for the packed bed of highly conductive solids with voids filled in with liquid. For practical purposes the values of both β and γ can be assumed as approximately unity.

ANALYSIS OF DATA PREVIOUSLY REPORTED WITH THEORETICAL EQUATIONS

Fundamental Data ($\alpha\beta$) for Beds with Fluid Flow

Experimental data previously reported concerning the effective thermal conductivities in packed beds with fluid flow can be separated into two groups:

1. k_e^∞, over-all thermal conductivities, the values of which incorporate the resistance to heat transfer within the bed, as well as at the walls of the confining tube (*10, 14, 16, 23, 25*).

2. k_e, the mean value in packed bed, the heat transfer resistance at the walls of the confining tube being removed (*1, 3, 4, 5, 8, 9, 15, 19, 21*).

According to the results of Hatta and Maeda (*9*), the value of k_e^∞ is about half that of k_e when $N_{ReM} = 800$; therefore the experimental data of k_e^∞ are omitted here.

When given experimental equations or data are transformed into standard form, i.e., Equation (6), the most important values of $(\alpha\beta)$ in packed beds can be obtained as summarized in Table 1. For example, some data by Maeda and Kawazoe (*15*) for Berl saddles and Raschig rings are shown in Figures 5 and 6 respectively, where the value of $(\alpha\beta)$ varies considerably with the ratio of solid diameter D_p to tube diameter D_T as shown in Figure 7. For spheres, cylinders, pellets, or broken granules the values of $(\alpha\beta)$ cover a narrow range, i.e., 0.1 to 0.14 for the different packing conditions. Since the Raschig ring has a hole through which the fluid may flow, the probability of lateral mixing in a bed packed with these rings can be assumed to be about twice that for ordinary solid packing.

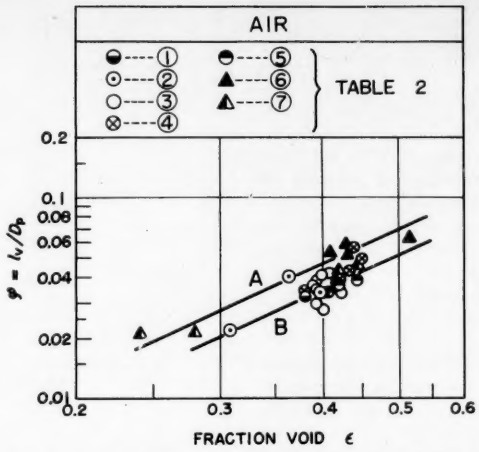

Fig. 9. Values of φ, calculated from experimental data previously reported (for air).

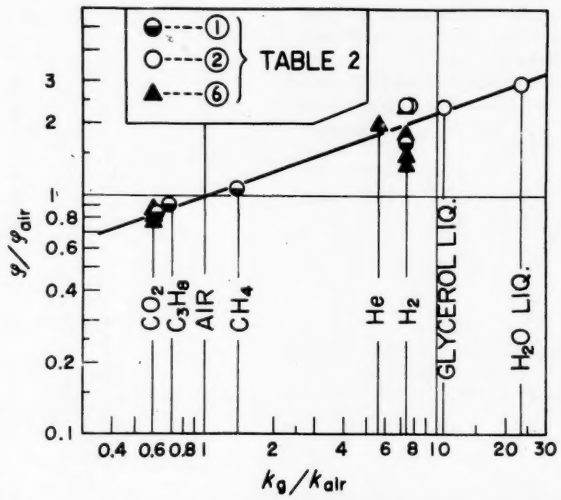

Fig. 10. Ratio (φ/φ_{air}) obtained from experimental data previously reported (for various kinds of fluid).

Being affected by the physical characteristics of solid packing, the values of k_e/k_g for iron spheres differ considerably from those for insulating fire bricks as shown in Figure 8, where the calculated values of k_e°/k_g derived with Equation (15) coincide fairly well with the experimental data obtained by the authors.

Effective Thermal Conductivities k_e° with Motionless Fluid

When experimental data for k_e° previously reported are analyzed by means of Equation (14) in packed beds of powdery materials, i.e., quartz, zinc, and iron, under reduced pressure of 0.05 to 0.20 mm. Hg, it is found that the values of δ are smaller than 10^{-5}. Therefore, it is reasonable to eliminate δ in Equation (13) under atmospheric pressure.

Analyzing the experimental data of k_e° reported by Kling (*14*), Schuman and Voss (*24*), Waddems (*26*), and Kannuluick (*13*) for solid packings of high thermal conductivities, i.e., steel, lead, Carborundum, and quartz, by means of Equation (15) or (16) yields the fundamental data of φ, shown in Figure 9 for air and in Figure 10 for the various fluids.

According to curve *B* for cylinders or spheres in Figure 9, the value of φ is 0.034 for the fraction void $\epsilon = 0.4$; then the effective thickness of fluid film in voids seems much smaller than the nominal length of the void, an indication of the importance of the thin film of fluid near the contact surfaces of two solids, as shown above.

Experimental data for effective thermal conductivities in a packed bed with motionless fluid, which the thermal conductivities of solids affect seriously, are compared with the calculated value by use of Equation (15), the values of φ being obtained from Figures 9 and 10 for the given values of fraction void ϵ. The results of this calculation are sum-

marized in Table 3, which indicates that theoretical equations (15) can correlate with the experimental data under different experimental conditions.

EXPERIMENTS

Apparatus

The experimental equipment (Figure 11) is similar to that used by other workers (*11, 12, 17*) for measurement of effective thermal conductivities in packed beds with motionless air. The column is constructed from a stainless steel tube with a Carborundum electric heater held in a coaxial silica tube. The solids are packed in the space between the two tubes, and the heat losses along the axis are obviated by the almost constant temperature distribution achieved by the adjustment of compensating electric heaters. Equally spaced chromel-alumel thermocouples are installed in the positions shown in Figure 11.

Procedure

Three to six hours after the electric heaters are switched on, heat flow attains steady state, and temperature, electric current, and voltage may be measured. Intervals between measurements under the same conditions are nearly 20 or 30 min. for all operating runs. The physical characteristics of the solid used for these experiments are shown in Table 4.

Experimental Results*

The values of effective thermal conductivities $k_e°$ in packed beds with motionless air are calculated by the following equations:

$$(0.860)\,VI = \frac{\pi l k_e° \,\Delta t}{2.3 \log_{10}(D_0/D_i)} \qquad (17)$$

$$\Delta t = t_{B3} - t_{A3} \qquad (18)$$

On application of the following values, Equation (19) is derived from Equation (17):

$$l = 0.25,\ D_0 = 0.146,\ D_i = 0.0375$$

$$k_e° = 0.743(VI)/\Delta t \qquad (19)$$

Several examples of radial distribution of temperature are shown in Figure 12, where the distribution seems nearly straight; therefore, the mean temperature of the packed bed t_m, based on the volume of the solids, can be obtained easily. The ratio of $k_e°$ to the thermal conductivity of the air k_g is plotted with respect to the mean temperature of the packed bed t_m, as shown in Figures 13 to 17, where the following values of k_g are used for numerical calculations:

*Complete tabular material has been deposited as document 5305 with the American Documentation Institute, Photoduplication Service, Library of Congress, Washington 25, D. C., and may be obtained for $2.50 for photoprints or $1.75 for 35-mm. microfilm.

Table 3. Comparison of Calculated Values of $k_e°/k_g$ with Experimental Data Previously Reported

Reference	Solid	Fluid	Avg. Diam., D_p mm.	Exp. $k_e°/k_g$	Temp., °C.	Fraction void ϵ	k_g, kcal./(m.)(hr./°C.)	Calcd. $k_e°/k_g$
	Glass	He	—	2.60	10	0.35	0.60*	2.42
13	Glass	Air	—	6.62	10	0.35	0.60*	9.30
	Diphenylamine	H_2	—	1.00	10	0.513	0.189	0.48
	Diphenylamine	Air	—	3.30	10	0.513	0.189	2.68
24	Coal	Air	—	5.23	40*	0.437	0.60*	6.15
		H_2	—	1.53	40*	0.437	0.60*	1.46
	Catalyst	Air	3.6	5.40†	130	0.40	0.30*	5.48
9	cylinder	Air	6.0	5.98†	130	0.40	0.30*	5.98
		Air	10.5	6.20†	130	0.40	0.30*	6.00
14	Glass sphere	Air	4.06	12.0	60*	0.40	1.0*	11.0
3	Alumina pellet	Air	3.18	5.0†	300	0.40	0.30	5.04
		Air	0.64	9.8	140	0.39	1.6*	9.7
18	Sand	Air	0.13	9.8	140	0.37	1.6*	10.9
		Air	0.73	7.7	140	0.41	1.6*	8.95
	Hydrated alumina	Air	8	10†	50*	0.40*	0.92	11.3
4	alumina, sphere, pellet	Air	12		50*	0.40*	2.68	15.2
5	Celite	Air	3.18	11.4†	80*	0.40*	0.30*	5.5
	cylinder	Air	12.7				0.30*	8.0
15	Broken	Air	2.85	10†	140	0.45	2.2*	8.7
	solid	Air	16.5		140	0.45	2.2*	13.8

*Estimated values.
†Extrapolated values, $N_{Re\,M} \to 0$.

t, °C.	0	200	400	600	800	1,000	1,200
k_g	0.0211	0.0338	0.0447	0.0534	0.0602	0.0655	0.0696

Data from Cowling (*6*).

Table 4. Characteristics of Solids Used for Experiments on Effective Thermal Conductivities with Motionless Air

Solid	Nominal diam., mm.	Fraction void ϵ	Data used for calculation of $k_e°/k_g$: D_p, mm.	k_s, kcal./(m.)(hr./°C.)	k_s/k_g	φ*	β	γ
Iron sphere	11.0	0.40	11.0	45 const.	—	0.034	1.0 and 0.9	1
Porcelain cylinder	9.6×8.5	0.43	9.05†	1.4 const.	—	0.040	1	1
Porcelain granule	6.0	0.43	6.0	1.4 const.	—	0.040	1	1
Cement clinker	5.0	0.50	5.0			0.050		
	3.6	0.50	3.6	1.7 const.	—	0.050	1	1
	2.6	0.50	2.6			0.050		
	0.35 ~ 0.01	0.54	0.18			0.060		
Insulating fire brick, cube	10	0.40	10.0	0.20 at 400°C.	4.48 const.	0.034	1	1
Insulating fire brick, sphere	5.0	0.50	5.0	0.20 at 400°C.	4.48 const.	0.050	1	1
Raschig ring								
Regularly packed	9 × 9 thickness	0.67	9.0	1.40 const.	—	0.034	$1/\sqrt{3}$	1.2/9
Randomly packed	1.2	0.72	9.0		—	0.034	$1 \times 1/3 + (1/\sqrt{3}) \times 2/3$	1.2/9

*The values of φ are obtained from B line in Figure 9.
†Mean value.

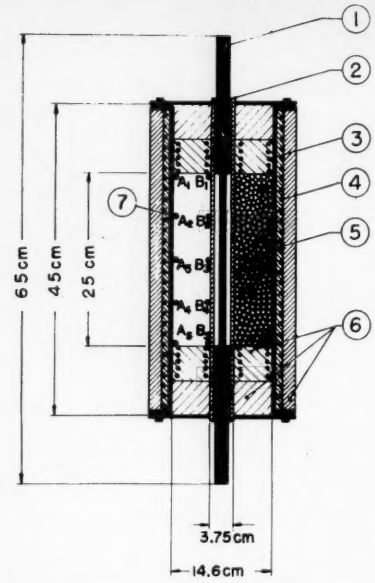

Fig. 11. Experimental packed bed with stagnant air, for measurement of effective thermal conductivities. 1, SiC electric heater; 2, silica tube; 3, Nichrome wire for compensation of lateral heat loss; 4, Nichrome wire for adjustment of bed temperature; 5, packed bed; 6, insulating fire brick; 7, position of thermocouples.

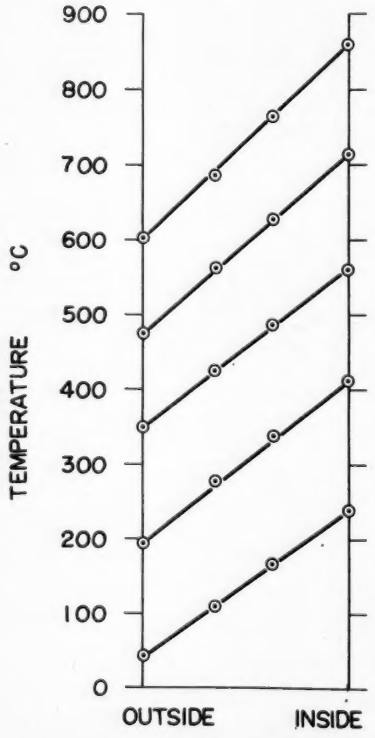

Fig. 12. Example of radial temperature distribution in the experimental packed bed without flowing fluid.

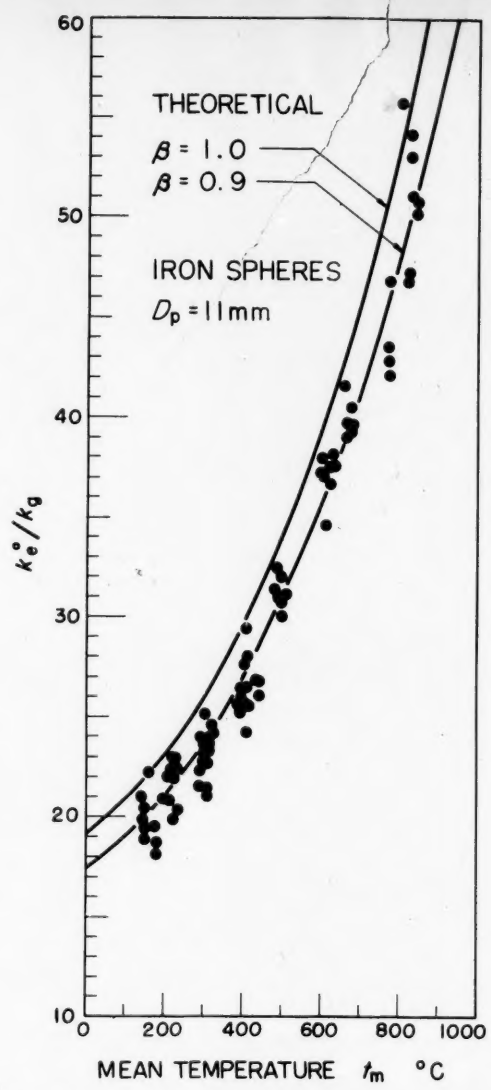

Fig. 13. Data obtained for packed beds of iron sphere, D_p = 11 mm.

Discussion

Since the values of $k_e°/k_g$ increase with the increase of the mean temperature of the packed bed t_m, radiant heat transfer seems to predominate when the mean temperature is high and the diameter and thermal conductivity of solids are large.

It is natural that the radiant heat transfer from solid to solid seriously affects the total heat flow in the case of iron spheres (Figure 13), because of the high conductivity of the solid phase. On the other hand, thermal radiation from void to void causes considerable heat flux even in the case of poorly conductive solids when the mean temperature of the packed bed is higher than 400°C., as shown in Figure 16.

The mean diameter of the solid greatly affects thermal conductivity, especially in the case of high temperature, as plotted in Figure 15, where the values of $k_e°/k_g$ are nearly constant for beds of particles smaller than 0.35 mm., an indication that thermal radiation can be neglected in such cases.

In Figure 17 the values of $k_e°/k_g$ for Raschig rings packed randomly are shown to be about 20% greater than those for rings packed regularly, because of the increase in the mean length of voids, which increases thermal radiation.

THEORETICAL VALUES COMPARED WITH EXPERIMENTAL DATA

In order to discuss the adequacy of the models of heat transfer mechanisms proposed by the authors, the theoretical

values of $k_e°/k_g$ are calculated from Equation (15) by taking the numerical values of the thermal conductivities of solid k_s and the factors β or γ as shown in Table 4 and comparing the results of calculation with the experimental data in Figures 13 to 17.

Although the equations derived by the authors are simple and contain some assumptions, they explain the experimental data fairly well, and the heat transfer models applied by the authors are sufficient to express the phenomena occurring in packed beds. Selection of the factors β, γ, and φ for beds packed with spheres, cylinders, or granules is easy, as shown in Table 4, but it is more difficult to select these values in the case of beds packed with Raschig rings. The thickness of the Raschig rings used in the experiment was $l_s = 1.2$ mm.

$$\gamma \doteqdot l_s/D_p$$

$$= 1.2 \text{ mm.}/9.0 \text{ mm.} = 0.0134$$

In beds packed regularly as shown in Figure 18, thermal radiation must pass through three voids in order to reach the point B from A or point B' from A'. Therefore, for the effective mean length of void l_p concerning the thermal radiation beam, the following value is assumed:

$$l_p = \sqrt{3}D_p/3 = D_p/\sqrt{3}$$

then

$$\beta = l_p/D_p = 1/\sqrt{3}$$

(regularly packed)

In the case of Raschig rings packed randomly, the possibility that the axis of the ring turns in the same direction as the heat flow is roughly considered as one-third, and so the value is assumed as

$$\beta = 1 \times (1/3) + (1/\sqrt{3}) \times (2/3)$$

Since the void spaces within the Raschig rings are fairly large, it can be considered that thermal radiation is superior to conduction through the air in the hollow spaces of the Raschig rings at temperatures above 300°C.; only the thin film of air between two rings effectively permits thermal conduction through the air. Therefore the value of φ selected is the same as for ordinary cylinders. The deviation of the experimental data from the calculated line in Figure 17 may be caused by the free convection in the wide spaces of the large fraction void $\epsilon = 0.67$ to 0.72.

CONCLUSIONS

1. In the study of the mechanisms of heat transfer in packed beds with fluid flow and with motionless fluid in voids, several models of heat transfer mechanisms were applied and general equations of effective thermal conductivities in packed beds were obtained as Equations (6), (15), and (16).

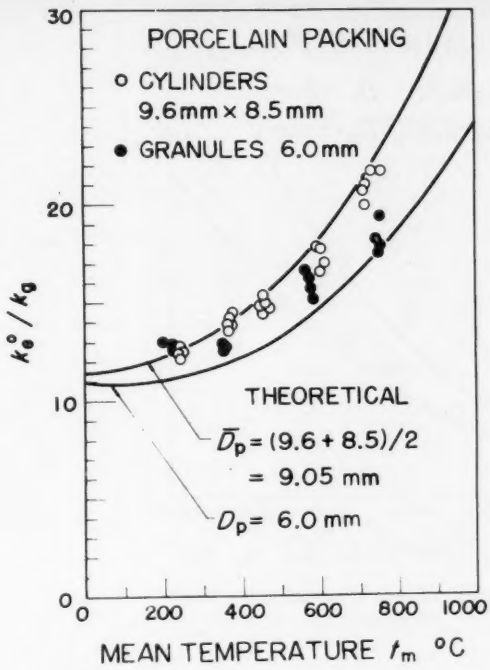

Fig. 14. Data for packed beds of porcelain packings.

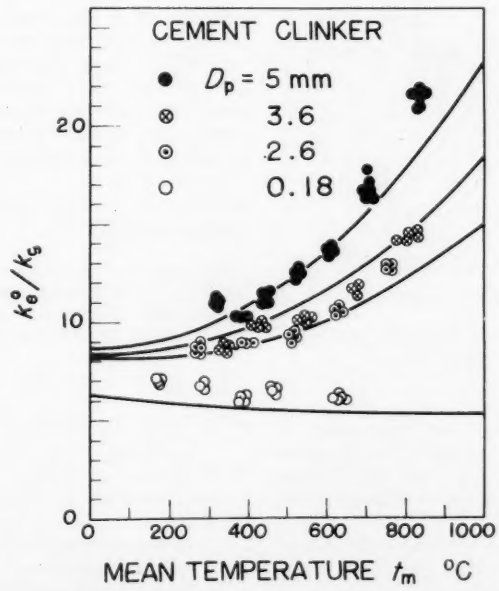

Fig. 15. Data for packed beds of cement clinker.

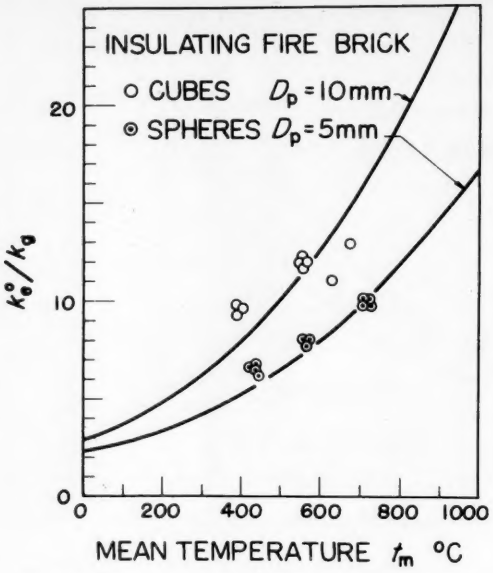

Fig. 16. Data for packed beds of insulating-fire-brick particles.

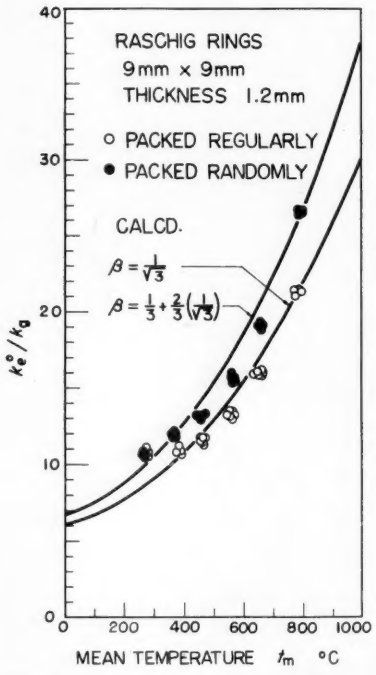

Fig. 17. Data for packed beds of Raschig rings.

2. Experimental data previously reported in cases of relatively low temperature were analyzed, and fundamental values for the calculation of the effective thermal conductivities by the authors' theoretical equations, i.e., α β and φ, were obtained as shown in Table 1 and Figures 7, 9, and 10.

3. Effective thermal conductivities in packed beds with motionless air were measured by collaborators of the authors for relatively high temperatures, and the radiant heat transfer mechanism was found to be most effective when the temperature of the bed was higher than 400°C. Both the diameters and the thermal conductivities of solid particles seriously affect the values of effective thermal conductivities in packed beds.

4. When results calculated from the authors' theoretical equation are compared with the experimental data presented, Equation (15) seems adequately to predict effective thermal conductivities in packed beds.

ACKNOWLEDGMENT

The authors wish to express their appreciation to Mitsuhiro Nakamura, Tomohiro Ito, and Shuichi Igarashi for their assistance in performing the experimental work.

NOTATION

C_p = specific heat of fluid, kcal./(kg.)(°C.)
D_p = nominal or average diameter of packing, m.
G = mass velocity of fluid, based on empty tube, kg./(sq. m.)(hr.)
I = electric current, amp.
h_{rs} = heat transfer coefficient for radiation, solid to solid, kcal./(sq. m.)(hr./°C.)
h_{rv} = heat transfer coefficient for radiation, void to void, kcal./(sq. m.)(hr./°C.)
k_e = effective thermal conductivity of packed bed with flowing fluid, kcal./(m.)(hr./°C.)
k_e° = effective thermal conductivity of packed bed with motionless fluid, kcal./(m.)(hr./°C.)
k_g = thermal conductivity of fluid, kcal./(m.)(hr./°C.)
k_s = thermal conductivity of packing material, kcal./(m.)(hr./°C.)
l = length of packed bed, m. of two neighboring solids in the direction of heat flow, m.
l_p = effective length between the centers
l_s = effective length of solid relating to thermal conduction, m.
l_v = effective thickness of fluid film adjacent to contact surface of two solid particles, m.
N = number of solids in the unit length of packed bed, measured in the direction of heat flow
p = emissivity of solid surface
t = temperature, °C.
t_m = mean temperature of packed bed, °C.
V = voltage, volt

Greek Letters

α = mass velocity of fluid flowing in the direction of heat or mass transfer/

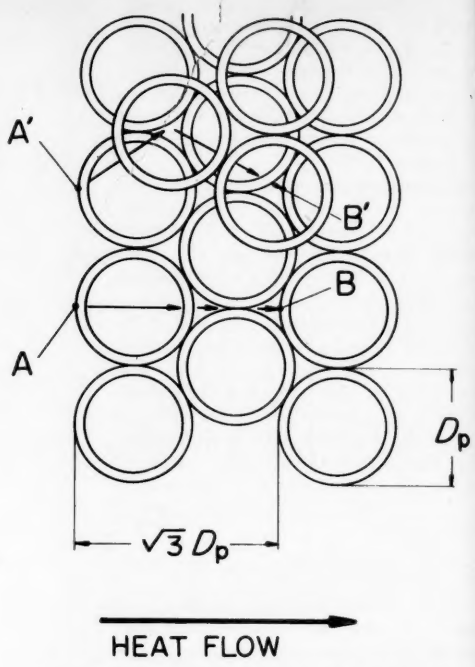

Fig. 18. Model of heat transfer in beds of Raschig rings packed regularly.

mass velocity of fluid based on sectional area of empty tube in the direction of fluid flowing

$\beta = l_p/D_p$

$\gamma = l_s/D_p$

$\varphi = l_v/D_p$

ϵ = fraction void

LITERATURE CITED

1. Aerov, M. E., and N. N. Umnik, *J. Appl. Chem. (U.S.S.R.)*, **27**, No. 3, 265 (1954).
2. Argo, W. E., and J. M. Smith, *Chem. Eng. Progr.*, **49**, 443 (1953).
3. Bunnell, D. G., H. B. Irvin, R. W. Olson, and J. M. Smith, *Ind. Eng. Chem.*, **41**, 1977 (1949).
4. Campbell, J. M., and R. L. Huntington, *Petroleum Refiner*, **30**, 127 (1951); **31**, 123 (1952).
5. Coberly, C. A., and W. R. Marshall, Jr., *Chem. Eng. Progr.*, **47**, 141 (1951).
6. Cowling, C., "Mathematical Theory of Non-Uniform Gases," Cambridge University Press (1952).
7. Damköhler, G., "Der Chemie Ingenieur 'Eucken Jakob,' " Vol. 3, Part 1, 441.
8. Felix, J. R., and W. K. Neill, Paper presented at A.I.Ch.E. Atlantic City meeting (1951).
9. Hatta, S., and S. Maeda, *Chem. Eng. (Japan)*, **12**, 56 (1948); **13**, 79 (1949).
10. Hougen, J. O., and E. L. Piret, *Chem. Eng. Progr.*, **47**, 287 (1951).
11. Igarashi, S., B.S. thesis, Univ. Tokyo (1956).
12. Ito, T., B.S. thesis, Univ. Tokyo (1955).
13. Kannuluick, W. G., and L. H. Martin, *Proc. Roy. Soc. (London)*, **A141**, 144 (1933).
14. Kling, G., *Forsch. Gebiete Ingenieuerw.*, **9**, 82 (1938).
15. Maeda, S., and K. Kawazoe, *Chem. Eng. (Japan)*, **15**, 5, 9, 312 (1951); **17**, 276 (1953); **18**, 279 (1954).
16. Molino, D. F., and J. O. Hougen, *Chem. Eng. Progr.*, **48**, 147 (1952).
17. Nakamura, M., B.S. thesis, Univ. Tokyo (1954).
18. Okada, S., and R. Toyabe, B.S. thesis, Univ. Tokyo (1953, 1954).
19. Plautz, D. A., and H. F. Johnstone, *J. Am. Inst. Chem. Engrs.*, **1**, No. 2, 193 (1955).
20. Ranz, W. E., *Chem. Eng. Progr.*, **48**, 247 (1952).
21. Schuler, R. W., V. P. Stallings, and J. M. Smith, *Chem. Eng. Progr. Symposium Ser.* No. 4, **48**, 19 (1952).
22. Singer, E., and R. H. Wilhelm, *Chem. Eng. Progr.*, **46**, 343 (1950).
23. Sugawara, W., and S. Sato, *Trans. Soc. Mech. Engr. (Japan)*, **13**, No. 45, 164 (1947).
24. Schuman, T. E. W., and V. Voss, *Fuel*, **13**, 249 (1934).
25. Verschoor, H., and G. Schuit, *Appl. Sci. Research*, **42**, A2, No. 2, 97 (1950).
26. Waddems, A. L., *J. Soc. Chem. Ind.*, **63**, 337 (1944); *Chemistry & Industry*, 206 (1944).
27. Wilhelm, R. H., W. C. Wynkoop, and D. W. Collier, *Chem. Eng. Progr.*, **44**, 105 (1948).
28. Yagi, S., and D. Kunii, *Chem. Eng. (Japan)*, **18**, 576 (1954).
29. Yagi, S., D. Kunii, and Y. Shimomura, *Chem. Eng. (Japan)*, **21**, 342 (1957).

Behavior of Suspended Particles in a Turbulent Fluid

S. K. FRIEDLANDER

Columbia University, New York, New York

Heat and mass transfer and coagulation are considered as related to the mean-square relative velocity between particle and fluid $\overline{u_R^2}$ and eddy diffusion as described by the mean-square particle displacement, $\overline{X_P^2}$. The mathematical methods used are similar to those employed in the early calculations of the Brownian motion.

The mean-square relative velocity is obtained as a function of particle characteristics, intensity of turbulence, and a fluid correlation coefficient. In the limiting case of equal particle and fluid density $\overline{u_R^2} = 0$, and for very heavy particles $\overline{u_R^2} \rightarrow \overline{u_P^2}$.

A general expression for the eddy diffusivity is obtained which reduces to the same form as that of the fluid for the stationary state. However, the correlation coefficient to be used in the calculations depends on $\overline{u_R^2}$. As a first approximation, it can be assumed that at a sufficiently long time from the introduction of the particles, fluid and particle diffusivities are equal.

For short times after injection, the particle spread may be much less than that of the fluid. An illustrative calculation for the initial spreading of a jet of suspended particles is offered. In all cases an effort is made to organize the available experimental data within the framework of the theory.

The behavior of dilute suspensions of small particles in a turbulent fluid is of interest in agitation, fuel injection, erosion, silt transport, and cloud formation. During these processes a number of related effects may occur including (1) heat and mass transfer to the suspended particles, (2) eddy diffusion of the dispersed material, and (3) coagulation or collision.

Practically all the available experimental data are concerned with the second effect, eddy diffusion. The com-

S. K. Friedlander is now at The Johns Hopkins University, Baltimore, Maryland.

bined settling and diffusion of particles in water has been studied by Rouse (*11*) and Kalinske and Pien (*7*). Longwell and Weiss (*9*) have studied initial spreading of fuel droplets injected into turbulent air, and Friedlander (*3*) has investigated the deposition of suspended particles from turbulent air. Theories of particle diffusion have been derived in an interesting monograph by Tchen (*14*) and, more recently, in a study by Soo (*12*). A theory of turbulent coagulation has been advanced by Frisch (*5*).

This paper considers heat and mass transfer and coagulation as related to the relative velocity between particle and fluid, and eddy diffusion as described by the mean-square particle displacement. The mathematical methods used were originally developed for the calculation of the Brownian motion (*16*) and random noise in electrical devices. An effort is made to organize the available experimental data within the framework of the theory, with the emphasis, in general, on quantitative explanation rather than mathematical rigor.

As is common in the treatment of turbulent phenomena, handling the problem mathematically requires the consideration of simple systems. In this case, a homogeneous turbulent field containing particles smaller than the microscale of the fluctuating motion being assumed, the results will be best applied to such regions as the center of a pipe or to the atmosphere and with more difficulty to agitated tanks or boundary layers; however, even in the more complicated cases qualitative conclusions are possible.

MEAN-SQUARE RELATIVE-VELOCITY AND TRANSFER RATES

Rates of heat and mass transfer to dilute suspensions of small particles in a turbulent fluid are of determining influence in such phenomena as the growth of organisms in stirred tanks, the evaporation of droplets in spray drying and in fuel injection, and the formation of clouds. The usual theoretical or empirical correlations for transfer rates to small particles apply to spheres in an *infinite* body of fluid which moves past the particle with a *constant* velocity. If the relative velocity between a particle and the fluid around it is known, the transfer coefficient can be obtained.

Clearly, however, the requirements of a large body of fluid moving at constant velocity past the particle are not fulfilled in the case of particles suspended in a turbulent fluid. In the atmosphere and in large ducts it is often the case that the particles together with their associated thermal or concentration boundary layers are smaller than the Eulerian microscale of turbulence, the distance over which velocity differences are high. Mickelsen (*10*) found that for air flow in an 8-in. duct at velocities ranging from 50 to 160 ft./sec. the Eulerian microscale at the pipe axis was approximately 4,500μ. This is considerably larger than the usual drop size encountered, for example in fuel injection. Thus in this instance there is some justification for assuming that the particle moves in a large, uniform field of flow.

There is, however, little justification for assuming that the velocity past the particle is constant, since it must vary with time for each particle and over all the particles at any time. Therefore the root-mean-square relative velocity between particle and fluid is assumed to represent the characteristic value for transfer calculations. If values of this parameter were available, the mean Reynolds number could be estimated and the Nusselt number obtained from correlations such as that of Friedlander (*4*) for low Reynolds numbers. The transfer coefficient might then be used with a driving force based on the concentration or temperature difference between the bulk of the fluid and the surface of the particle to determine the transfer rate.

Evidently such a calculation hinges on a method for obtaining the root-mean-square relative velocity, which can be estimated in the following manner for a fluid in homogeneous turbulence containing a large number of small, rigid, noninteracting spheres.

The particles have been in the fluid long enough to have reached a steady statistical configuration. They are much smaller than the Eulerian microscale of turbulence but large enough for their Brownian motion to be negligible. (There is no correlation between the turbulent and Brownian fluctuations, and the approach which follows can easily be modified to take both into account.)

Each particle is assumed to be contained within a large packet of fluid, an "eddy," having a velocity u_F and an acceleration a_F. One might picture, for example, a particle of sand in a thimbleful of fluid. Both the fluid velocity and the fluid acceleration vary with time; moreover, the particle may move gradually from packet to packet, and this movement is more pronounced the larger and heavier the particle.

A force balance may now be written on the particle in the x direction, taken perpendicular to the gravitational field. Provided that the Reynolds number $d_P\sqrt{\overline{u_R^2}}\rho/\mu$ is 1 or less, the resistance of the fluid to the particle motion will be governed by Stokes's Law:

$$F_f = -f(u_p - u_F) \tag{1}$$

This expression is adequate for small particles in gases but may be inaccurate for large accelerations in liquids. [See, for example, Hughes and Gilliland (*6*).]

In addition to the frictional resistance, the particle will be subjected to a "buoyant" force because of the pressure gradient within the packet of fluid. In general, the fluctuating pressure gradients will be related to the fluctuating fluid accelerations through the equations of fluid motion. If the Reynolds number of turbulence is sufficiently high, however, it appears that the frictional terms in these equations may be neglected (*1, 13*). In this case the pressure gradient is related to the acceleration by the expression

$$\frac{\partial p}{\partial x} = -\rho_F a_F \tag{2}$$

and the buoyant force acting on the particle will be

$$F_b = m_F a_F \tag{3}$$

Thus the force balance describing the motion of the particles takes the form

$$m_p a_p = m_F a_F - f(u_p - u_F) \tag{4}$$

or

$$\frac{du}{dt}u_p + \beta u_p = \beta u_F + \gamma\frac{du_F}{dt} \tag{5}$$

Physically, β^{-1} is a measure of particle inertia; it represents the time necessary for the velocity of a particle injected into a stagnant fluid to reach $1/e$ of its initial value.

As the fluid-particle system is in a steady, homogeneous, and isotropic turbulence, the fluid velocity (and, in a related manner, its acceleration) possesses the following characteristics:

1. The mean value of the fluid velocity taken over all the particles at any instant is zero:

$$\bar{u}_F(t) = 0 \tag{6}$$

2. There exists some correlation between the values of the fluctuating fluid velocity at any two times t_1 and t_2 such that

$$\overline{u_F(t_1)u_F(t_2)} = \overline{u_F^2}R(t_2 - t_1) \tag{7}$$

where

$\overline{u_F^2}$ = mean square fluid velocity summed over all particles

This correlation is finite only for very small values of $t_2 - t_1$. In other words, there is little relation between the velocities of the fluid surrounding the particle at any two times unless these times are close to each other. It should be noted that this correlation coefficient relates the velocities of the fluid in the neighborhood *of the particle* at different times. For a given turbulent fluid it is a function of the size and density of the particle; these determine the "slip" or motion relative to the fluid. In general, the coefficient will vary from approximately the Lagrangian fluid correlation for extremely small

particles to the Eulerian time coefficient for large, heavy particles.

Proceeding with the calculation of the mean velocity, upon integrating Equation (5) one obtains

$$u_p = u_{p0}e^{-\beta t} + \beta e^{-\beta t}\int_0^t e^{\beta T}u_F\,dT + \gamma e^{-\beta t}\int_0^t e^{\beta T}a_F\,dT \qquad (8)$$

Integrating the last term by parts, subtracting $u_F - u_{F0}e^{-\beta t}$ from both sides, and rearranging yields

$$u_R - u_{R0}e^{-\beta t} = (1-\gamma)[(u_{F0}e^{-\beta t} - u_F) + \beta e^{-\beta t}\int_0^t e^{\beta T}u_F\,dT] \qquad (9)$$

Squaring and taking mean values over all particles at time t gives

$$\overline{u_R^2} - 2\overline{u_R u_{R0}}e^{-\beta t} + \overline{u_{R0}^2}e^{-2\beta t} = (1-\gamma)^2\{\overline{u_{F0}^2}e^{-2\beta t} - 2\overline{u_{F0}u_F}e^{-\beta t} + \overline{u_F^2} + 2\beta e^{-\beta t}\int_0^t e^{\beta T}\overline{u_{F0}u_F(T)}\,dT - 2\beta\int_0^t e^{-\beta(t-T)}\overline{u_F(T)u_F(t)}\,dT + \beta^2 e^{-2\beta t}\overline{\left[\int_0^t e^{\beta T}u_F\,dT\right]^2}\} \qquad (10)$$

From Equation (7)

$$\overline{u_F u_{F0}} = \overline{u_F^2}R(\theta) \qquad (11)$$

and the first integral on the right becomes

$$\overline{I_1} = \overline{u_F^2}\int_0^t e^{\beta\theta}R(\theta)\,d\theta \qquad (12)$$

If $\theta = t - T$, the second integral can be written

$$\overline{I_2} = \overline{u_F^2}\int_0^t e^{-\beta\theta}R(\theta)\,d\theta \qquad (13)$$

To evaluate the last quantity in (10), one writes the mean square of the integral in terms of two independent variables of integration T_1 and T_2:

$$\overline{I_3} = \int_0^t\int_0^t e^{\beta(T_1+T_2)}\cdot\overline{u_F(T_1)u_F(T_2)}\,dT_1\,dT_2 \qquad (14)$$

This integral may be evaluated by letting $\theta_1 = T_2 - T_1$ and $\theta_2 = T_1 + T_2$. The Jacobian for the coordinate transformation is ½; evaluating the new limits of integration and remembering that R is an even function, one may write

$$\overline{I_3} = \overline{u_F^2}\int_0^t R(\theta_1)\,d\theta_1\int_{\theta_1}^{2t-\theta_1} e^{\beta\theta_2}\,d\theta_2 = \frac{\overline{u_F^2}}{\beta}\left\{\int_0^t [R(\theta)]\cdot(e^{-\beta\theta+2\beta t} - e^{\beta\theta})\,d\theta\right\} \qquad (15)$$

In general, the correlation coefficient $R(\theta)$ decreases rapidly with θ. This is a property inherent in the turbulent fluid. Thus integrals of the type of (13) quickly approach a limit, as the effect of the term $e^{-\beta\theta}$ is to make the integrand decrease even more rapidly. Substituting (15), (13), (12), and (11) in (10) and considering the motion as t approaches infinity, one finds that terms with multipliers $e^{-\beta t}$ and $e^{-2\beta t}$ vanish, giving the steady state value

$$\overline{u_R^2} = (1-\gamma)^2\overline{u_F^2}\cdot\left(1 - \beta\int_0^\infty e^{-\beta\theta}R(\theta)\,d\theta\right) \qquad (16)$$

From this result a number of interesting conclusions may be drawn. When particle and fluid are of equal density, $\gamma = 1$ and $\overline{u_R^2} = 0$, as the particle follows the motion of the fluid. When the particle is extremely heavy, β and γ are small and $\overline{u_R^2}$ approaches $\overline{u_F^2}$. If the particle is very small (β very large) but of a density different from that of the fluid ($\gamma \neq 1$), it is necessary to consider the correlation coefficient only in the neighborhood of $\theta = 0$ since $e^{-\beta\theta}$ decreases so rapidly. Expanding $R(\theta)$ [see Frenkiel (*2*), for example] gives

$$R(\theta) = 1 - \frac{\theta^2}{\lambda^2} + \frac{\theta^4\overline{\left(\frac{da_F}{d\theta}\right)^2}}{24(\overline{u_F^2})^2} - \cdots \qquad (17)$$

Substituting in (16) and integrating yields

$$\overline{u_R^2} \approx 2(1-\gamma)^2\frac{\overline{u_F^2}}{\lambda^2\beta^2} \qquad (18)$$

This expression should apply to very small particles in a liquid.

In the general case it is necessary to have values for the correlation coefficient as a function of time. If the particles follow the motion of the fluid approximately, the proper coefficient to use is the Lagrangian correlation. This can be checked by substituting in (15) to see whether $\overline{u_R^2}$ is small. If it is a large percentage of $\overline{u_F^2}$, the Eulerian time coefficient should be used.

There does not seem to be any information available concerning the relationship between these two coefficients although the data on eddy diffusion discussed in the next section indicate that they are probably similar in form. In the absence of more certain information, mean relative velocities may be estimated on the basis of the data of Mickelsen (*10*), who measured turbulence intensity and correlation at the axis for air flow in an 8-in. pipe. On the assumption that the form for the Langrangian coefficient is given by

$$R(\theta) = e^{-a\theta} \qquad (19)$$

the parameter a was found to be 200 sec.$^{-1}$ from Mickelsen's data for $U = 75$ ft./sec. Substituting in (16) and integrating yields

$$\frac{\overline{u_R^2}}{\overline{u_F^2}} = \frac{a}{a+\beta} \qquad (20)$$

In Figure 1 $\overline{u_R^2}/\overline{u_F^2}$ is plotted as function of particle size for air at 20°C. Clearly, for particles larger than about 10μ, "slip" occurs and the mean relative velocity becomes significant. Values for the Nusselt number for mass transfer, a Schmidt group of unity being assumed, are also shown in Figure 1. It is evident that the assumption sometimes made of Nusselt number = 2 (stagnant case) for particles carried along by a turbulent fluid may be in error. The dotted parts of the curves are uncertain because slip occurs (which makes suspect the use of the Lagrangian coefficient) and because the mean relative Reynolds number is greater than 5 (contrary to the assumption of Stokes's Law).

The variation of mean-square velocity among particles of different sizes in the turbulent field will result in collision and, for cases of inelastic impact, in agglomeration or coalescence. A clear picture of this phenomenon can be obtained from a consideration of fog droplets in atmospheric turbulence. In this case scale is very large and the system may be considered to consist of masses of air which contain suspended particles and which move in a random manner. The larger particles, which have high mean-square relative velocities, will tend to sweep out the smaller ones with efficiencies of collision which can be estimated from calculations such as those of Langmuir (*8*). Such an explanation offers a mechanism for rain formation by coalescence of droplets in a turbulent field. The same picture is applicable in agitated systems. Calculations of turbulent coagulation will, of course, depend on information on scale and intensity of turbulence for the system under consideration.

EDDY DIFFUSION OF SUSPENDED PARTICLES

The combined diffusion and settling of suspended particles has been studied by Kalinske and Pien (*7*) and Rouse (*11*), who were particularly interested in problems of silt transport. These investigators studied systems which were in a steady state so that the rate of downward settling was equal to the rate of upward diffusion. Rouse found little variation in diffusivity with particle size; Kalinske and Pien actually used eddy diffusivities determined independently with hydrochloric acid to predict successfully the concentration gradient of fine sand. Friedlander (*3*) studied the deposition of particles from turbulent air on the walls of ducts. Assuming equal particle and fluid diffusivities, he found fair agreement of theory with his data.

Longwell and Weiss (*9*), on the other hand, were interested in the initial spreading of a fuel spray injected at the center of a turbulent pipe flow. Their theory, which was semiquantitative, indicated that particles with relatively high inertia diffuse less rapidly than fluid. The data which they obtained agreed with their qualitative picture.

In addition to these studies of particle motion, there have been efforts to trace turbulent fluid motion by use of small particles. Thus it is of importance to be able to describe the rate of spreading of the particles at various stages after their introduction into the fluid.

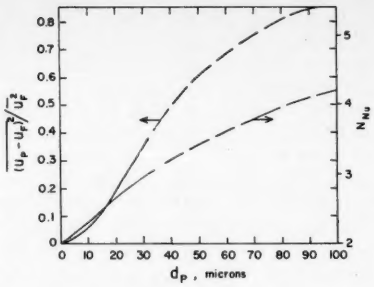

Fig. 1. Predicted relative velocities and mass transfer to particles ($\rho_p = 1$) in 8-in. pipe with $U = 75$ ft./sec.

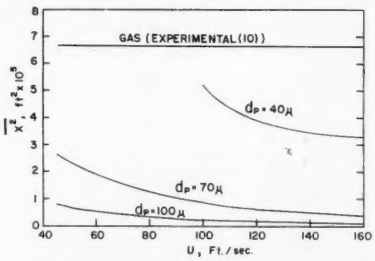

Fig. 2. Predicted spread 4 in. downstream from point of injection for particles ($\rho_p = 1$) in air (20°C.) flowing through an 8-in. pipe.

AN ASYMPTOTIC EXPRESSION FOR THE MEAN-SQUARE DISPLACEMENT

The rate of eddy diffusion of the suspended particles can be described by expressing their mean-square displacement $\overline{X_P^2}$ as a function of time. Again a large number of small, noninteracting spheres may be envisioned in a fluid in homogeneous turbulence. The system has reached a steady statistical configuration. The plane $x = 0$, parallel to the gravitational field, intercepts a large number of marked particles at $t = 0$. The distance traveled by one of these particles in the time t is obtained by integrating Equation (5):

$$X_p + \frac{u_p - u_{p0}}{\beta} = \int_0^t u_F(T)\, dT + \frac{\gamma(u_F - u_{F0})}{\beta} \qquad (21)$$

Squaring both sides of the equation and taking averages over all the particles originally in $x = 0$ gives

$$\overline{X_p^2} + \frac{2}{\beta}\int_0^t \overline{u_p(T)[u_p(t) - u_{p0}]}\, dT + \overline{\frac{(u_p - u_{p0})^2}{\beta^2}} = \int_0^t \int_0^t \overline{u_F(T_1)u_F(T_2)}\, dT_1\, dT_2 + \frac{2\gamma}{\beta}\int_0^t \overline{u_F(T)[u_F(t) - u_{F0}]}\, dt + \frac{\gamma^2\overline{(u_F - u_{F0})^2}}{\beta^2} \qquad (22)$$

According to Frenkiel (*2*), the double integral can be written

$$\overline{I_4} = 2\overline{u_F^2}\int_0^t (t - \theta)R(\theta)\, d\theta \qquad (23)$$

The fact that the correlation coefficient is an even function makes it is easy to show that

$$\int_0^t \overline{u(T)[u(t) - u_0]}\, dT = 0 \qquad (24)$$

Substituting in (22), gives

$$\overline{X_p^2} + \frac{2\overline{u_p^2}}{\beta}(1 - R_p(\theta)) = 2\overline{u_F^2}t\int_0^t (t - \theta)R(\theta)\, d\theta + \frac{2\gamma}{\beta}\overline{u_F^2}(1 - R(\theta)) \qquad (25)$$

As t approaches infinity, this becomes

$$\overline{X_p^2} = 2\overline{u_F^2}t\int_0^{t\to\infty} R(\theta)\, d\theta \qquad (26)$$

This expression, which is identical in form with that of the Taylor diffusion equation, was also obtained by Tchen (*14*), who interpreted it to mean that particles and fluid diffuse at the same rate. However, the correlation coefficient in (26) applies to the fluid velocities *over the path of the particle*. As pointed out above, heavy particles move relatively slowly and cannot follow the fluid eddies which surge around them. Thus the correlation coefficients which should be utilized in (26) range between two extremes: (1) the Lagrangian coefficient for small particles able to follow the fluid and (2) the Eulerian time coefficient for particles which remain almost fixed.

There does not seem to be any information available concerning the relationship between these two coefficients. The data of Kalinske and Pien and those of Rouse for combined eddy diffusion and settling of sand particles in water indicated little variation of the eddy diffusivity with particle size. Thus in their cases, at least, the two types of coefficients were probably similar.

Defining R_p as a correlation coefficient between particle velocities, one may also write the mean-square particle displacement after a sufficiently long times as

$$\overline{X_p^2} = 2\overline{u_p^2}t\int_0^\infty R_p(\theta)\, d\theta = 2\overline{u_F^2}t\int_0^\infty R(\theta)\, d\theta \qquad (27)$$

Thus for heavy particles with low mean-square velocities, the scale as defined by $\int_0^\infty R_p(\theta)\, d\theta$ must be correspondingly large. In other words, heavier particles "remember" for a longer time than lighter ones what has happened to them previously.

This one-dimensional treatment can be extended in the case of nonisotropic turbulence to the Y and Z displacements by defining correlation coefficients in these directions and using the appropriate mean-square velocities. The procedure then is identical with that outlined above, and analogous expressions for the mean-square displacements and velocities will be outlined.

INITIAL SPREADING OF PARTICLES ORIGINALLY AT REST

Although after long periods of time the forms of the equations representing the mean-square particle and fluid displacements are similar, the behavior for short times is quite different. The rate of initial spreading is often of interest when a suspension of particles is injected into a high-velocity gas stream. In the analysis that follows it is assumed that the gas is flowing in a homogeneous, isotropic turbulence. This is approximated near the axis for high-velocity pipe flow. The suspension is introduced at the center of the pipe with the main-stream velocity U in such a way that the characteristics of the turbulence are undisturbed. The initial radial velocity of the particles is zero, and diffusion in the axial direction is negligible in comparison with transport by the fluid.

To find the mean-square lateral displacement of the particles from the axis Equation (5) is integrated with $\gamma = 0$ and with $u_{p0} = 0$, to give

$$X_p = \int_0^t (1 - e^{-\beta(t-T)})u_F\, dt \qquad (28)$$

Squaring and averaging yields

$$\overline{X_p^2} = \int_0^t \int_0^t (1 - e^{-\beta(t-T_1)}) \cdot (1 - e^{-\beta(t-T_2)})\overline{u_F(T_1)u_F(T_2)}\, dT_1\, dT_2 \qquad (29)$$

As in the previous discussion,

$$\overline{u_F(T_1)u_F(T_2)} = \overline{u_F{}^2}R.$$

In this case, however, R is a function not only of $(T_2 - T_1)$ but also of t, as the system is not in a statistically steady state. For large, heavy particles with low mean-square velocities, the variation with t should not be great; as an approximation, it will be assumed that R is an even function of only the time difference.

Letting $P_1 = t - T_1$ and $P_2 = t - T_2$ and expanding the exponentials and the correlation coefficient $R(T_2 - T_1) = R(P_2 - P_1)$ as in (17) gives

$$\overline{X_p{}^2} = \overline{u_F{}^2}\int_t^0\int_t^0\left[\beta^2P_1P_2\frac{-\beta^3}{2}\cdot(P_1{}^2P_2 + P_1P_2{}^2) + \beta^4\left(\frac{P_1P_2{}^3}{6} + \frac{P_1{}^2P_2{}^2}{4} + \frac{P_2P_1{}^3}{6}\right) - \frac{\beta^2}{\lambda^2}(P_1P_2{}^3 - 2P_1{}^2P_2{}^2 + P_1{}^3P_2) + \cdots\right]dP_1\,dP_2 \quad (30)$$

$$= \overline{u_F{}^2}\left[\beta^2\frac{t^4}{4} - \beta^3\frac{t^5}{6} + \left(\frac{5}{72}\beta^4 - \frac{\beta^2}{36\lambda^2}\right)t^6 + \cdots\right] \quad (31)$$

This expression describes the initial spreading of particles issuing with zero velocity from a point source in a turbulent gas. For very short times the correlation coefficient approaches unity, and

$$\overline{X_p{}^2} \approx \beta^2\overline{u_F{}^2}\frac{t^4}{4} \quad (32)$$

The dependence on t^4 is in marked contrast with the behavior of turbulent-fluid particles (*2*), for which

$$\overline{X_F{}^2} \approx \overline{u_F{}^2}t^2 \quad (33)$$

Clearly, then, care must be taken in using particles to trace turbulent motion in gases.

Equation (31) also indicates that the effect of the turbulent field does not become important for a while (only in the sixth-order term). Thus as in the case of the fluid, initial spreading of particles should depend little on the correlation coefficient but very much on the intensity of turbulence. This is the same conclusion to which Longwell and Weiss came on a more qualitative basis.

To continue with the calculation of lateral spread information is needed on turbulence intensities and correlation. Mickelsen (*10*), who measured the diffusion of helium injected from a point source at the center of an 8-in. pipe, found that in the range of 50 to 160 ft./sec. the radial turbulent intensity was about 0.032. For any point L downstream, $t = L/U$, and with $\sqrt{\overline{u_R{}^2}}/U = 0.032$ (31) becomes

$$\overline{X_p{}^2} = \frac{10^{-3}}{4}\frac{\beta^2L^4}{U^2}\left[1 - \frac{2}{3}\beta\frac{L}{U} + \left(\frac{5}{18}\beta^2 - \frac{1}{9\lambda^2}\right)\left(\frac{L}{U}\right)^2 + \cdots\right] \quad (34)$$

To estimate the parameter λ (which is taken to be the Lagrangian microscale) from the diffusion data of Mickelsen, one uses the method of Uberoi and Corrsin (*15*), who write

$$\frac{\overline{X_F{}^2}}{\overline{u_F{}^2}t^2} = 1 - \frac{1}{6}\frac{t^2}{\lambda^2} + \cdots \quad (35)$$

Thus if $\overline{X_F{}^2}/\overline{u_F{}^2}t^2$ is plotted vs. t^2, the slope at $t^2 = 0$ is $-1/6\lambda^2$ and the intercept is unity. In this manner it was found that

$$\frac{1}{\lambda^2} = 18U^2 \quad (36)$$

where λ is in seconds when U is in feet per second. In Figure 2, $\overline{X_p{}^2}$ is plotted as a function of gas velocity with particle size as the parameter for $L = 4$ in. The experimental data of Mickelsen for the diffusion of helium are also shown.

The curves show that for diffusion of gases or very small particles ($\beta \gg 1/t$), $\overline{X_F{}^2}$ measured at a given point varies little with the air velocity. This can be explained if it is remembered that for short times

$$\overline{X_F{}^2} = \overline{u_F{}^2}t^2 = 10^{-3}L^2 \quad (37)$$

On the other hand, for larger particles ($\beta \ll 1/t$) mean-square displacement at a given point decreases rapidly with mainstream velocity. These conclusions are confirmed at least qualitatively by the experimental data of Longwell and Weiss (*9*) for initial spreading of volatile and nonvolatile fuels.

ACKNOWLEDGMENT

The author wishes to acknowledge helpful conversations with Yonathan Bard of the Columbia University Department of Chemical Engineering and J. L. Lebowitz of the Department of Physics, Syracuse University.

NOTATION

a = constant, sec.$^{-1}$
a_F = acceleration, sq. cm./sec.
d_p = particle diameter, cm. or μ
f = resistance coefficient = $3\pi\,\mu d_p$ in Stokes's region, g./sec.
F_b = buoyant force, dynes
F_f = frictional resistance, dynes
$I_{1,2}$... = integrals
L = distance downstream from injection point, in.
m_F = mass of fluid occupying same volume as m_p, g.
m_P = mass of particle, g.
p = pressure, dynes/sq. cm.
P_1, P_2 = variables of integration, sec.
R = fluid correlation coefficient, dimensionless
R_P = particle correlation coefficient, dimensionless
t = time
T, T_1, T_2 = variables of integration, sec.
u_F = fluid velocity, cm./sec.
u_p = particle velocity, cm./sec.
u_{F0} = initial fluid velocity, cm./sec.
u_{p0} = initial particle velocity, cm./sec.
u_R = $u_p - u_F$, cm./sec.
U = pipe mainstream velocity, cm./sec.
x, y, z = coordinate axes
X_p = particle displacement in x direction, cm.
X_F = fluid displacement in x direction, cm.
Y, Z = displacements in y and z directions, respectively, cm.
β = f/m_p, sec.$^{-1}$
γ = $m_F/m_P = \rho_F/\rho_P$, dimensionless
θ, θ_1, θ_2 = variables of integration, sec.
λ = microscale, sec.
μ = fluid viscosity, g./(cm.)(sec.)
ρ_F = fluid density, g./cc.
ρ_P = particle density, g./cc.

LITERATURE CITED

1. Batchelor, G. K., *Proc. Cambridge Phil. Soc.*, **47**, 359 (1951).
2. Frenkiel, F. N., "Advances in Applied Mechanics," vol. III, Academic Press Inc., New York (1953).
3. Friedlander, S. K., *Ind. Eng. Chem.*, **49**, 1151 (1957).
4. ———, *A.I.Ch.E. Journal*, **3**, 43 (1957).
5. Frisch, H. L., *J. Phys. Chem.*, **60**, 463 (1956).
6. Hughes, R. R., and E. R. Gilliland, *Chem. Eng. Progr.*, **48**, 497 (1952).
7. Kalinske, A. A., and C. L. Pien, *Trans. Am. Geophys. Union*, **24**, Part II, 530 (1943).
8. Langmuir, Irving, *J. Meteorology*, **5**, 175 (1946).
9. Longwell, J. P., and Malcolm Weiss, *Ind. Eng. Chem.*, **45**, 667 (1953).
10. Mickelsen, W. R., *Natl. Advisory Comm. Aeronaut. Tech. Note* 3570 (October, 1955).
11. Rouse, Hunter, "Proceedings of the Fifth International Congress of Applied Mechanics," p. 550, John Wiley and Sons, New York (1939).
12. Soo, S. L., *Chem. Eng. Sci.*, **5**, 57 (1956).
13. Taylor, G. I., *Proc. Roy. Soc., (London)*, **A151**, 465 (1935).
14. Tchen, C. M., "Mean Value and Correlation Problems Connected with the Motion of Small Particles Suspended in a Turbulent Fluid," Martinus Nijhoff, The Hague (1947).
15. Uberoi, M. S., and Stanley Corrsin, *Natl. Advisory Comm. Aeronaut. Rept.* 1142 (1953).
16. Uhlenbeck, G. E., and L. S. Ornstein, *Phys. Rev.*, **36**, 823 (1930).

Determination of the Chemical Properties of an Oxide Catalyst in a Closed System

C. D. HOLLAND and P. G. MURDOCH

Texas Agricultural and Mechanical College System, College Station, Texas

The bulk chemical properties of an impregnated chromia-alumina catalyst with respect to several gases, CO, CO_2, C_3H_6, were determined as a function of the degree of oxidation of the surface of the catalyst. The importance of the results lies in the demonstration that a simple method described herein can be used to obtain significant data on catalytic surfaces. Briefly, the prior adsorption of oxygen by the catalyst tended to promote the adsorption of carbon monoxide and to prohibit the adsorption of carbon dioxide. Far more carbon monoxide was adsorbed by the highly oxidized surface than could be accounted for on the basis of adsorbed carbon dioxide. The quantity of propylene adsorbed also increased with an increase in the oxidation of the surface. The results are explained on the basis of two types of adsorbed oxygen atoms.

The importance of catalysts in the chemical industries initiated this investigation, one of the objectives of which was to determine some chemical properties of the surface of an oxide catalyst. Use of a closed system permitted separate examinations of various portions of the catalyst surface. The method of approach described herein is not proposed as a substitute for the flow-type experiments described by Hougen and Watson (*6*). It is instead suggested as an independent approach to be used in conjunction with the usual flow-type experiments to give a better understanding of the manner in which a catalyst participates in a given chemical reaction.

Past investigations of catalysts in closed systems may be divided into two classes, those involving physical adsorption and those involving chemical adsorption. Except in the measurement of the surface area of the catalyst, the adsorptions involved in this investigation were of the chemical type. Most of the previous experimentation concerning this type of adsorption has been pointed toward showing either the heterogeneity or homogeneity of catalyst surfaces. H. S. Taylor and coworkers (*8*, *9*, *10*) have interpreted the results of their investigations, which involved the adsorption of hydrogen by technical catalysts, as showing the heterogeneity of technical catalyst surfaces. On the other hand, Roberts (*7*), Beeck (*2*), and Eucken (*4*) have investigated pure metal catalysts, usually in the form of films, and found that all adsorption sites on them behaved in essentially the same manner, which led them to conclude that the surfaces possessed a high degree of homogeneity.

The oxidized surface of the catalyst investigated here could be described in terms of two basic groups of sites, and within each group these sites appeared to exhibit homogeneous behavior.

Most of the catalysts used commercially contain several components. In view of this a rather complex catalyst was selected for the investigation in order to determine whether or not the bulk chemical properties of its surface could be explained in a relatively simple manner, as described above. The catalyst selected contained oxides of chromium, iron, and potassium supported on alumina. The percentages by weight of Cr_2O_3, Fe_2O_3, K_2O, and Al_2O_3 were 20, 3, 2,

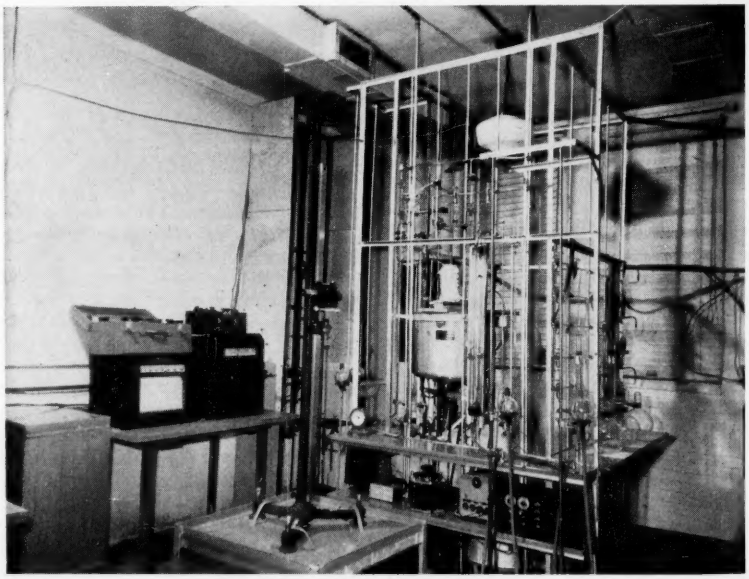

Fig. 1A. Adsorption apparatus.

*P. G. Murdoch is at present with the Dow Chemical Company, Midland, Michigan.

and 75 respectively. The chemical properties of the surface of this catalyst at various degrees of oxidation with respect to carbon dioxide, carbon monoxide, propylene, and oxygen (following the prior adsorption of propylene) were determined.

The importance of the results lies in the demonstration that a simple method can be used to obtain significant data, rather than in the detailed properties of the particular surface used.

DESCRIPTION OF APPARATUS

An adsorption apparatus suitable for measuring the quantities of a gas adsorbed, desorbed, and reacted in the presence of an oxide catalyst was constructed. The arrangement of the apparatus, shown in Figure 1, is in many respects similar to the one proposed by Brunauer, Emmett, and Teller (*3*) for surface-area determinations. The auxiliary equipment consisted of the following: (1) a constant-temperature water bath from which water was circulated through the burette jacket, (2) several appropriate constant-temperature baths used to maintain the catalyst bulb at the desired temperatures, (3) a vapor-pressure thermometer (M_2 was a part of this thermometer) constructed so that it might also be used as a Toepler pump, (4) a pressure controller which maintained the system pressure constant by adjusting the mercury level in the burette, (5) a mercury-condensation pump preceded by a mechanical vacuum pump, and (6) a cathetometer for reading manometers M_1 and M_2. A detailed description of the apparatus is given in reference *5*.

EXPERIMENTAL PROCEDURE

The manipulation of the various stopcocks necessary to effect the adsorption and desorption experiments has been described in reference *5*. It is in many respects similar to that used in the Brunauer, Emmett, and Teller surface-area determinations. The behavior of the catalyst, at various degrees of oxidation, in the presence of each of the gases mentioned previously was determined by adsorption and desorption experiments. When any of the gases reacted with previously adsorbed substances on the surface of the catalyst, the necessary gas samples were analyzed by use of a mass spectrometer. These experiments were performed with the catalyst at a temperature of 550°F. Adsorption experiments were carried out at a constant pressure of 73.2 cm. Hg. abs.

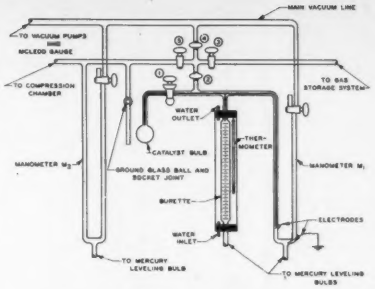

Fig. 1B. Adsorption apparatus.

The catalyst was stabilized by alternately oxidizing and reducing it until the change of its chemical adsorption properties with age (time) was negligible. A surface area of 72.6 sq. m./g. was obtained through the method proposed by Brunauer, Emmett, and Teller (*3*) for a fresh sample of the catalyst and an area of 64.5 sq. m./g. was obtained for the stabilized catalyst. After each experiment the catalyst was thoroughly cleaned by alternately oxidizing and reducing it ten times at 980°F. This process was carried out over a period of about 3 days. After the final reduction, the catalyst was evacuated for approximately 12 hr. for the purpose of removing any hydrogen which might have been adsorbed during the final reduction. Close agreement between oxygen adsorption and the hydrogen uptake during reduction indicated that little or no oxidizable hydrogen was retained on the reduced surface after evacuation. Similar behavior has been observed for chromia supported on alumina (*11*), but not for pure chromic oxide (*12*). In spite of the severity of the cleaning process employed, it was difficult to return the catalyst to the same degree of cleanliness each time. The experimental procedure was repeated precisely, but the cleanliness of the surface of the catalyst could not be.

After the catalyst had been reduced and cleaned, the oxygen was adsorbed on it, the amount being dependent upon both time and temperature. It could be removed quantitatively with hydrogen. Throughout this paper the quantities of gases adsorbed are, for convenience, referred to as 10^5 times the actual values. The results of these experiments are shown in Figure 2. For oxygen adsorptions of about 16.0 g.-atoms/g. of catalyst, an adsorption temperature of 550°F. was employed. Temperatures of 675° and 980°F. were used when it was desired to adsorb quantities of oxygen in the neighborhood of 24 and 45 g.-atoms, respectively. The adsorption of oxygen was essentially irreversible. Each adsorption experiment was followed by a desorption experiment for the purpose of measuring any small quantity of oxygen which could be desorbed. After the oxygen surrounding the catalyst had been removed, the gas to be studied was admitted to the catalyst and the quantity of the gas adsorbed (or the change in volume at constant pressure) was measured. The residual gas surrounding the catalyst and products which desorbed readily from the surface of the catalyst were withdrawn, measured, placed in a sample container, and analyzed by use of a mass spectrometer. The information obtained from the experiments was used to make an over-all material balance, which established quantitatively the final state of the catalyst with respect to adsorbed substances. The results of the experimental investigations follow. The original data are given in reference *5*.

EXPERIMENTAL RESULTS

Carbon Dioxide Experiments

In these experiments the action between carbon dioxide and the catalyst at different degrees of oxidation was determined, and the results of these experiments are shown in Figure 3. The upper curve represents the amount of carbon dioxide adsorbed on the surface of the catalyst, and the lower curve shows the amount remaining after desorption. About 75% of the carbon dioxide was adsorbed during the first 30 sec. of each experiment. The experiments were carried out for several hours, and at the end of that time the rate of adsorption was very nearly zero.

Examination of the results showed that as the amount of oxygen initially adsorbed on the hydrogen-reduced catalyst was increased, the adsorption of carbon dioxide by the catalyst decreased.

Carbon Monoxide Experiments

A set of experiments was devised for the purpose of ascertaining the behavior of carbon monoxide and the catalyst at various degrees of oxidation. The first step in these experiments consisted of the adsorption of the desired quantity of oxygen on the hydrogen-reduced catalyst. Then the catalyst, at the

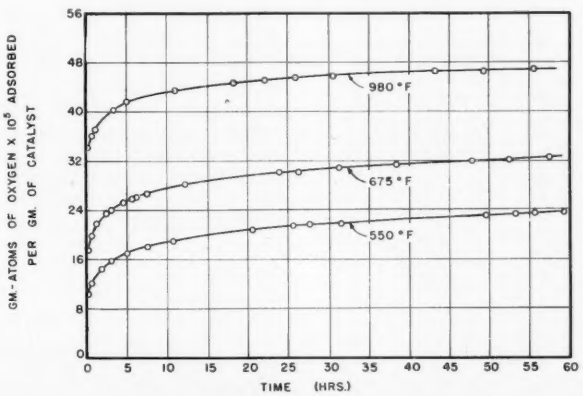

Fig. 2. Adsorption of oxygen.

resulting state of oxidation, was treated with carbon monoxide for a period of 3 min., after which all adsorption and reaction appeared to have been completed. The gas in the dead space (the space bounded by the catalyst bulb and stopcock 1) was then withdrawn, measured, and analyzed. For the lower initial adsorptions of oxygen by the catalyst, a single treatment of the catalyst with carbon monoxide was sufficient. However, in the investigation of the catalyst at its most highly oxidized state, it was necessary to treat it several times with carbon monoxide. The first few times it was treated, the catalyst bulb became filled with carbon dioxide and limited the extent of the adsorption and reaction processes. The results of these experiments are shown in Figure 4. The deviation of the two points from the two curves (at 18.8 g.-atoms of oxygen initially adsorbed) is attributed to the limiting effect of the size of the bulb for the single treatment of carbon monoxide employed in that particular experiment.

In Figure 4 the carbon monoxide which remained adsorbed on the catalyst, in the form of either carbon monoxide or carbon dioxide, was calculated as carbon monoxide and is referred to as *carbon monoxide adsorbed*. Upon examination of the experimental results, it is seen that both carbon monoxide adsorption and the reaction of carbon monoxide with adsorbed oxygen to produce carbon dioxide increased as the previously adsorbed oxygen was increased. In the experiment in which the catalyst contained initially 45.2 g.-atoms of adsorbed oxygen, upon treatment of this catalyst with carbon monoxide, 13.6 g.-atoms reacted to produce carbon dioxide which was evolved to the gas phase; associated with the remaining 31.6 g.-atoms of oxygen was 28.0 g.-atoms of carbon monoxide. On the basis of the ratio obtained, 28/31, one would be led to conclude that carbon monoxide was adsorbed on the catalyst in the form of carbon dioxide. However, from the results of the carbon dioxide experiments, one would not have expected more than 10 g.-moles of carbon dioxide to have been adsorbed. From both sets of experiments, on carbon monoxide and dioxide, it appears that some of the carbon monoxide was adsorbed in some form other than as carbon dioxide.

Propylene Experiments

These experiments consisted of treating the catalyst, at various degrees of oxidation, with propylene. When propylene had been in contact with the catalyst for 8 min., the adsorption appeared to have been completed. Then the gas surrounding the catalyst was withdrawn, measured, and analyzed. The results of these experiments are shown in Figure 5. Upon examination of these results it is seen that the quantity of carbon adsorbed

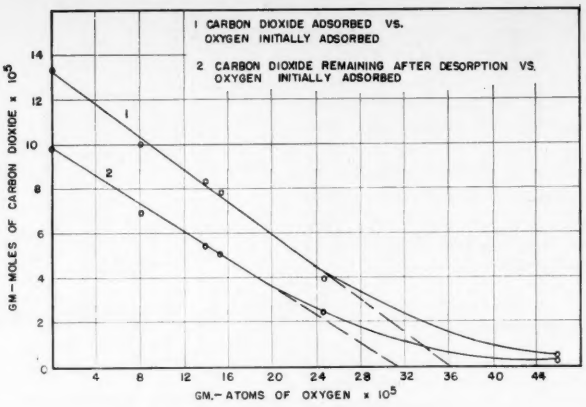
1 CARBON DIOXIDE ADSORBED VS. OXYGEN INITIALLY ADSORBED
2 CARBON DIOXIDE REMAINING AFTER DESORPTION VS. OXYGEN INITIALLY ADSORBED
GM-MOLES OF CARBON DIOXIDE x 10^5
GM.- ATOMS OF OXYGEN x 10^5

Fig. 3. Adsorption of carbon dioxide.

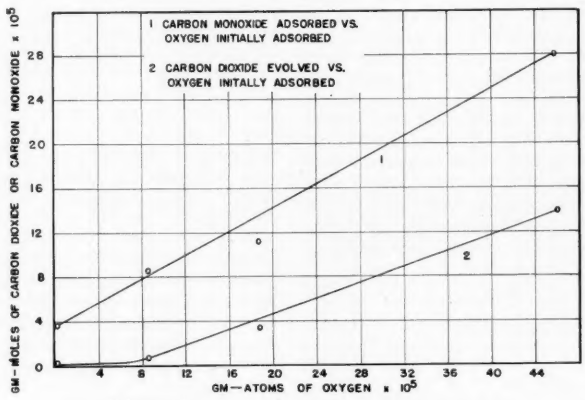
1 CARBON MONOXIDE ADSORBED VS. OXYGEN INITIALLY ADSORBED
2 CARBON DIOXIDE EVOLVED VS. OXYGEN INITALLY ADSORBED
GM-MOLES OF CARBON DIOXIDE OR CARBON MONOXIDE x 10^5
GM—ATOMS OF OXYGEN x 10^5

Fig. 4. Adsorption and reaction of carbon monoxide.

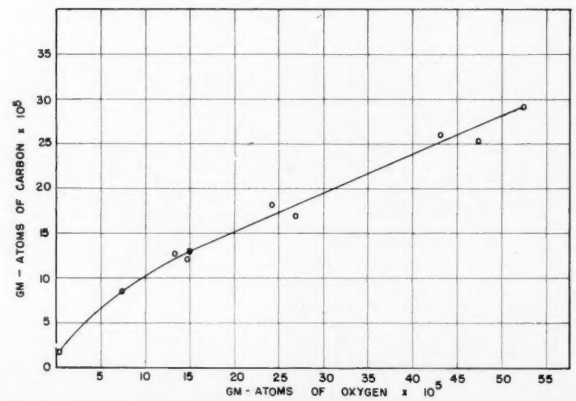

Fig. 5. Adsorption of propylene.

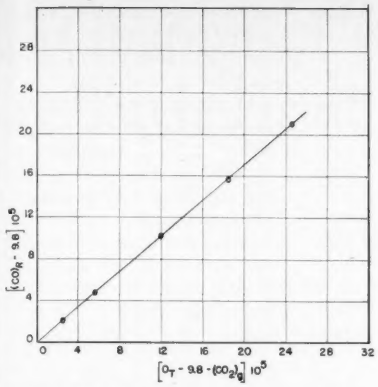

Fig. 6. Test of carbon monoxide correlation.

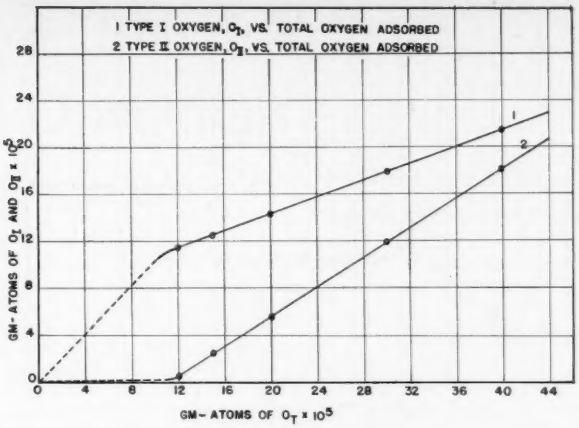
1 TYPE I OXYGEN, O_I, VS. TOTAL OXYGEN ADSORBED
2 TYPE II OXYGEN, O_{II}, VS. TOTAL OXYGEN ADSORBED
GM-ATOMS OF O_I AND $O_{II} \times 10^5$
GM-ATOMS OF $O_T \times 10^5$

Fig. 7. Oxygen distribution.

increased as the amount of oxygen initially adsorbed was increased. In addition to the retention of carbon, the catalyst also adsorbed hydrogen. As the amount of oxygen initially adsorbed was varied from 7.69 to 45.8 g.-atoms, the hydrogen-carbon ratio varied from 1.89 to 1.93. The gas withdrawn from the vicinity of the catalyst contained a corresponding amount of propane, thereby having a hydrogen-carbon ratio greater than 2.0. The reduced catalyst did not promote hydrogen transfer.

Oxidation products such as carbon monoxide and dioxide were not detected in the gas sample. Had an appreciable quantity of carbon dioxide been formed, the results of the carbon dioxide experiments indicate that some of this gas would have been desorbed in the process of the removal of the gas sample. In view of the results of the experiments with carbon monoxide and dioxide and with propylene, it appears that the carbon and hydrogen were adsorbed in the form of a carbon-hydrogen molecule rather than as carbon monoxide and dioxide.

Oxidation of the Catalyst Containing Adsorbed Propylene

After the catalyst had been treated with propylene as described above, oxygen was admitted to it. The principal fact established was that essentially all the adsorbed propylene reacted with the oxygen, giving carbon dioxide, water, and traces of carbon monoxide. Since the gas samples were not analyzed for water, the numerical results are not stated; however, the qualitative result is worthy of mention, in view of the failure of propylene to react with adsorbed oxygen to yield oxidation products.

DISCUSSION AND INTERPRETATION

The results of the carbon monoxide experiments indicate that the oxidized catalyst contained adsorbed oxygen atoms of different character; one type reacted with carbon monoxide to give carbon dioxide, and the other type adsorbed carbon monoxide. These are referred to as types I and II, respectively. In any correlation of the results of the carbon monoxide experiments it apparently would be necessary to use the concept of two types of adsorbed oxygen atoms.

There are perhaps several ways in which the results of the carbon monoxide, carbon dioxide, and propylene experiments could be correlated. One method, believed adequate and representative of the properties of the catalyst, is shown here. Although empirical, it is remarkably simple and straightforward. Other methods are of course not excluded.

Correlation of the Carbon Monoxide Results

Interpretation of the results on carbon monoxide entails the concept of two types of adsorbed oxygen atoms, and the carbon dioxide results are also used, as some of the carbon monoxide which was retained could have been adsorbed in the form of carbon dioxide.

To type II adsorbed oxygen atoms is attributed the adsorption of carbon monoxide as such. Thus,

$$(CO)_a = \alpha O_{II} \qquad (1)$$

Of the total carbon monoxide remaining on the catalyst, not more than 9.8 g.-moles could have remained in the form of carbon dioxide. (See Figure 3.) If it is assumed that these sites were always available for the adsorption of carbon dioxide, then the expression for the total amount of carbon monoxide remaining adsorbed on the catalyst in the form of either carbon monoxide or dioxide is

$$(CO)_R = 9.8 + \alpha O_{II} \qquad (2)$$

This equation is applicable to those experiments where the quantity of oxygen initially adsorbed was sufficient for the production of 9.8 g.-moles of carbon dioxide.

All the carbon dioxide formation is attributed to the adsorbed oxygen of type I. Part of this carbon dioxide, 9.8 g.-moles, was retained by the catalyst and the remainder was evolved to the gas phase, because of the lack of adsorption sites. Thus,

$$O_I = (CO_2)_g + 9.8 \qquad (3)$$

Since only two types of adsorbed oxygen atoms were proposed, the total quantity of oxygen adsorbed prior to a carbon monoxide experiment is given by

$$O_T = O_I + O_{II} \qquad (4)$$

Elimination of O_I and O_{II} from these equations results in

$$(CO)_R - 9.8 = \alpha[O_T - 9.8 - (CO_2)_g] \qquad (5)$$

Values of $(CO)_R$ and $(CO_2)_g$ corresponding to given values of O_T were read from the smooth curves shown in Figure 4. A plot of Equation (5) is shown in Figure 6. Support of the correlation of the carbon monoxide results is given by the linearity and zero intercept of the line shown in Figure 6. The slope α of the line was found to be 0.847.

The oxygen distribution, O_I and O_{II} as functions of O_T (for O_T greater than 9.8), was obtained by use of Equations (3) and (4). Graphical representation of it is given in Figure 7. For oxygen adsorption less than 9.8, O_I was taken approximately equal to O_T, indicated by the broken lines. This distribution was used to correlate the results of the propylene experiments, as shown below.

Correlation of the Propylene Results

If the adsorption of propylene could be attributed to either one of the two types of oxygen, then one of the two

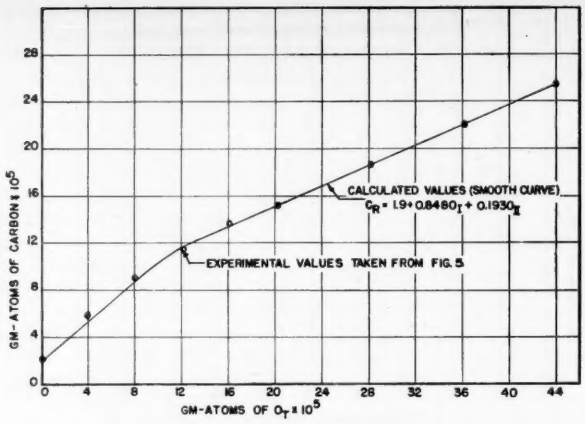
GM-ATOMS OF CARBON x 10^5
GM-ATOMS OF O_T x 10^5
CALCULATED VALUES (SMOOTH CURVE)
C_R = 1.9+0.848O_I + 0.193O_II
EXPERIMENTAL VALUES TAKEN FROM FIG. 5

Fig. 8. Correlation of results of propylene experiments.

constants, β and γ, in the following equation would be equal to zero.

$$C_R = 1.9 + \beta O_I + \gamma O_{II} \qquad (6)$$

The constant, 1.9, represents the quantity of carbon adsorbed on the reduced catalyst. The best correlation of the propylene results was obtained by taking $\beta = 0.848$ and $\gamma = 0.193$. By means of these values and the oxygen distribution, a comparison of the calculated and experimental values of the carbon adsorbed is shown in Figure 8. The agreement of these indicates that both types of oxygen were involved in the adsorption of propylene.

Correlation of the Carbon Dioxide Results

Of the total carbon dioxide adsorbed, part of it was strongly held but the remainder was weakly held and could be desorbed readily. Essentially all the carbon dioxide sites covered by the prior adsorption of oxygen can be accounted for on the basis of the extrapolated straight lines shown in Figure 3. The equations are as follows:

$$(CO_2)_T = 13.62 - 0.361\ O_T \qquad (7)$$

$$(CO_2)_S = 9.8 - 0.331\ O_T \qquad (8)$$

Subtracting Equation (8) from (7) gives the expression for the weakly held carbon dioxide.

$$(CO_2)_W = 3.4 - 0.05\ O_T \qquad (9)$$

These relationships indicate that the carbon dioxide sites were covered indiscriminately by oxygen of types I and II.

It is of interest to compare the coefficients in Equations (1) and (6) with the mole ratio of chromium to iron in the catalyst sample. The latter contained 0.875 atom of chromium/0.125 atom of iron. The experimental coefficients of 0.847, 0.848, and 0.193 are of the same order of magnitude as the chromium-iron ratio. Although this correspondence does not certify the following relationship between the behavior of the catalyst and its composition, it does suggest that about 87% of the O_I was adsorbed on chromium and the remainder of the O_I was adsorbed on iron; whereas, 87% of the O_{II} was adsorbed on iron, while the remainder of the O_{II} was adsorbed on chromium. Furthermore, carbon monoxide was adsorbed by oxygen of type II on iron, and propylene was retained by oxygen of type I on chromium as well as by oxygen of type II on chromium.

It should be pointed out that the determination of the relationship between catalyst behavior and catalyst composition was not an object of the original investigation. The relationship suggested is an interesting consequence of the correlations.

CONCLUSIONS

The chemical properties, as illustrated by use of the surface of an oxide catalyst, are useful in interpreting the catalytic behavior of surfaces. It was possible to explain the behavior of the surface of the catalyst used on the basis of two types of adsorbed oxygen atoms. In view of the information obtained for this technical oxide catalyst, it appears that this method of approach should prove useful in the study of catalysts.

ACKNOWLEDGMENT

This work was supported through the cooperation of the Texas Engineering Experiment Station, The Gulf Oil Company, and the Magnolia Petroleum Company.

NOTATION

C_R = atoms of carbon retained by the catalyst after any given propylene experiment

$(CO)_a$ = moles of carbon monoxide adsorbed on the catalyst in some form other than that of carbon dioxide

$(CO)_R$ = total moles of carbon monoxide adsorbed (in the form of either carbon monoxide or dioxide) by the catalyst during any given carbon monoxide experiment

$(CO_2)_g$ = moles of carbon dioxide formed and evolved to the gas phase during any given carbon monoxide experiment

$(CO_2)_S$ = moles of carbon dioxide strongly adsorbed in any given carbon dioxide experiment

$(CO_2)_T$ = total moles of carbon dioxide adsorbed in any given carbon dioxide experiment

$(CO_2)_W$ = moles of carbon dioxide weakly adsorbed in any given carbon dioxide experiment

O_I = moles of adsorbed oxygen of Type I; this type reacted with carbon monoxide to produce carbon dioxide

O_{II} = moles of adsorbed oxygen of type II; this type was responsible for the adsorption of carbon monoxide in some form other than that of carbon dioxide

O_T = total moles of adsorbed oxygen; it is equal to the sum of types I and II

α = proportionality constant defined by Equation (1)

β, γ = proportionality constants defined by Equation (6)

LITERATURE CITED

1. Beeck, Otto, in "Advances in Catalysis," by W. G. Frankenburg, V. I. Komarewsky and E. K. Rideal, vol. II, pp. 151–194, Academic Press, Inc., New York (1950).
2. ———, *Rev. Mod. Phys.*, **17**, 61 (1945).
3. Brunauer, Stephen, P. H. Emmett, and Edward Teller, *J. Am. Chem. Soc.*, **60**, 309 (1938).
4. Eucken, A., *Discussions Faraday Soc.*, No. 8, p. 128 (April, 1950).
5. Holland, C. D., dissertation, A. & M. College of Texas, College Station (May, 1953).
6. Hougen, O. A., and K. M. Watson, "Chemical Process Principles," Part III, John Wiley & Sons, Inc., New York (1948).
7. Roberts, J. K., *Proc. Roy. Soc. (London)*, **A152**, 445 (1935).
8. Taylor, H. S., *Z. Electrochem.*, **35**, 545 (1929).
9. ———, and S. C. Liang, *J. Am. Chem. Soc.*, **69**, 1306 (1947).
10. Taylor, H. S., *Trans. Far. Soc.*, p. 3 (April, 1950).
11. Voltz, S. E., and W. S. Weller, *J. Am. Chem. Soc.*, **76**, 4701 (1954).
12. Weller, W. S., and S. E. Voltz, *ibid.*, **76**, 4695 (1954).

Evaluation of the Heat Requirements in Batch Distillation Operations

J. G. STIEHL and JAMES H. WEBER

University of Nebraska, Lincoln, Nebraska

A rigorous method is presented for the evaluation of the heat requirements in binary batch fractionations which involve negligible column hold up. The method, in which the additional variables of the discontinuous process are taken into account, is a modification of the methods of Ponchon and Savarit for continuous operation. Two examples, one for a fractionation in which the composition of the product is constant and the other in which the reflux ratio is constant, are given as illustrations of the method.

The application of the method permits more accurate evaluation of reboiler and condenser heat loads and, in turn, better design.

The methods (*1, 6*) which are available for the solution of batch fractionation problems are often modifications of the McCabe-Thiele (*3*) solution for continuous-rectification problems. Consequently, the heat loads at the reboiler and condenser cannot be evaluated rigorously but can be only approximated. The degree of accuracy of the approximation depends upon the validity of the assumptions made in the McCabe-Thiele development: (1) molal latent heat independent of composition, (2) negligible heat of solution, and (3) negligible sensible heat effects. However, since the errors introduced by these individual assumptions may often tend to be compensating, better criteria for the applicability of the McCabe-Thiele method are that the saturated liquid and vapor lines on an enthalpy concentration are straight and, further, that the molal latent heat of vaporization is independent of composition. Either the chemical molecular weight or a fictitious molecular weight may be used as a basis for the determination of the molal latent heat.

Furthermore, when a modified McCabe-Thiele solution is applied to batch-fractionation problems, the condenser and reboiler loads become identical. For reasons cited above, it appears worth while to develop a method whereby the heat effects in batch distillation operations can be determined rigorously.

The methods of Ponchon (*4*) and Savarit (*5*) offer a rigorous means of solving two-component distillation problems in which the composition on a given plate is independent of time, i.e., steady state-operation. To apply this method to batch-fractionation problems, one must allow for the fact that the liquid and vapor compositions are functions of time as well as of plate number. Also one must take into account the fact that a batch fractionation may be carried out under conditions in which the product composition is constant and the reflux ratio varied or in which the reflux ratio is constant and the product composition allowed to change.

J. G. Stiehl is at present at the Wright-Patterson Air Force Base, Ohio.

PROPOSED METHOD

The batch fractional-distillation system is shown diagrammatically in Figure 1. An over-all differential material balance is

$$dL = -dD \qquad (1)$$

and an over-all differential-component material balance is

$$d(x_L L) = -x_D\, dD \qquad (2)$$

Then, substituting Equation (1) into (2) gives

$$d(x_L L) = x_D\, dL \qquad (3)$$

or

$$x_L\, dL + L\, dx_L = x_D\, dL \qquad (4)$$

If Equation (4) is rearranged, an equation similar to the Rayleigh equation is obtained:

$$L^{-1}\, dL = (x_D - x_L)^{-1}\, dx_L \qquad (5)$$

or

$$\ln (L/L_0) = \int_{x_{L_0}}^{x_L} (x_D - x_L)^{-1}\, dx_L \qquad (6)$$

In a batch distillation in which the composition of the overhead production is held constant by variation of the reflux ratio, the preceding equation may be directly integrated. Substituting the integrated form of Equation (1) into this equation gives

$$D = L_0(x_{L_0} - x_L)/(x_D - x_L) \qquad (7)$$

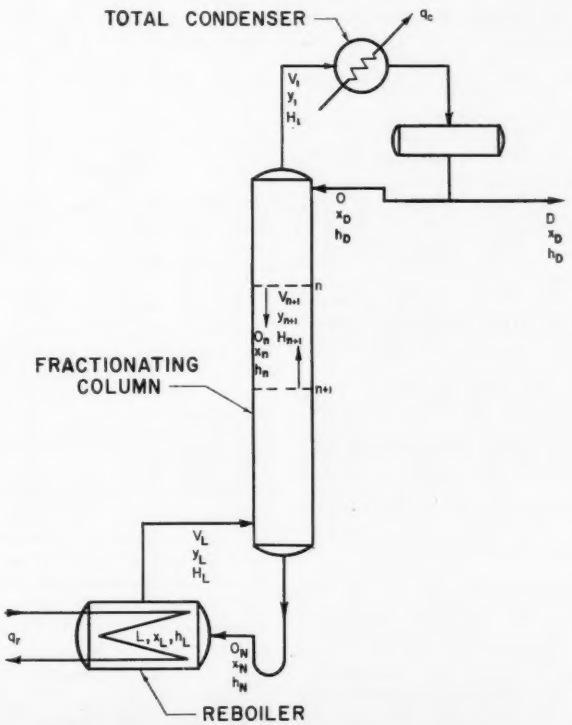

Fig. 1. Schematic diagram of a batch distillation system.

This equation is simply a material balance. If x_D is replaced by $(x_D)_{avg}$ the equation is also valid for a batch distillation which is carried out by use of a constant reflux ratio.

To obtain equations relating the operating conditions in the column to the condenser load and product, heat and material balances are made around the n plate and the top of the column (Figure 1).

$$dD + d0_n = dV_{n+1} \tag{8}$$

$$x_D\, dD + x_n\, d0_n = y_{n+1}\, dV_{n+1} \tag{9}$$

and

$$d'q_c + h_D\, dD + h_n\, d0_n = H_{n+1}\, dV_{n+1} \tag{10}$$

Substituting Equation (8) into Equations (9) and (10) gives

$$d0_n/dD = (x_D - y_{n+1})/(y_{n+1} - x_n) \tag{11}$$

and

$$d0_n/dD = (d'q_c/dD + h_D - H_{n+1})/(H_{n+1} - h_n) \tag{12}$$

If

$$Q_c' = d'q_c/dD + h_D \tag{13}$$

Equation (12) may then be written

$$d0_n/dD = (Q_c' - H_{n+1})/(H_{n+1} - h_n) \tag{14}$$

The combination of Equations (11) and (14) gives

$$d0_n/dD = (x_D - y_{n+1})/(y_{n+1} - x_n) = (Q_c' - H_{n+1})/(H_{n+1} - h_n) \tag{15}$$

Equation (15) is equivalent to the equation developed by Ponchon (*4*) and Savarit (*5*) for the operating line in the rectifying section for the solution of problems involving continuous fractionation processes.

If Equation (15) is applied to the top of the column, the relationship between Q_c' and the reflux ratio is obtained:

$$\frac{d0}{dD} = \frac{Q_c' - H_1}{H_1 - h_D} \tag{16}$$

If the complete system is considered, an over-all heat balance may be written:

$$d'q_r = d'q_c + h_D\, dD + d(h_L L) \tag{17}$$

or

$$d'q_r = Q_c'\, dD + d(h_L L) \tag{18}$$

It should be noted that Equations (17) and (18) imply adiabatic operation of the column and neglect the temperature changes of the materials of construction. Equations (6), (13), (15), and (18) are sufficient to solve rigorously any binary batch distillation problem with negligible liquid holdup.

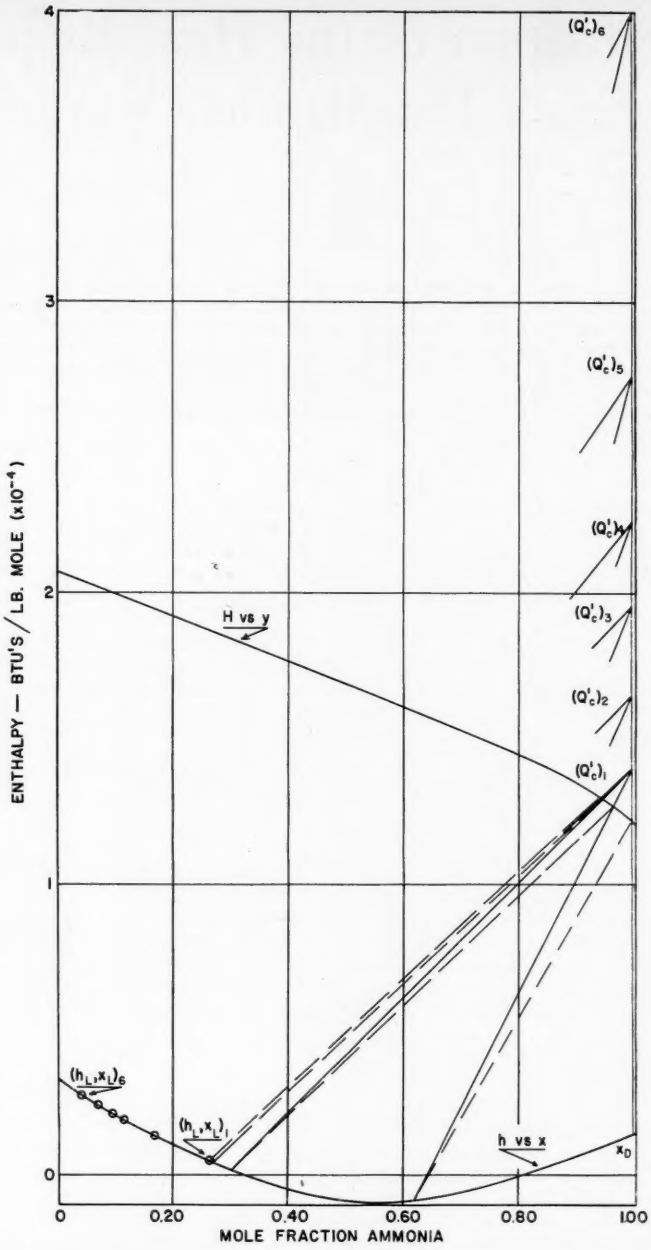

Fig. 2. Enthalpy-concentration diagram for the ammonia-water system showing the variation of Q_c' and x_L when x_D is held constant.

Equation (15) and an enthalpy-concentration diagram for the system under consideration provide a graphical method of determining the relationship between the still composition, the distillate composition, and the reflux ratio as shown by Ponchon and Savarit. Equations (13) and (18) provide the relationships necessary to solve rigorously for the heat requirements.

Equation (18) may be integrated to give

$$q_r = \int_0^D Q_c'\, dD + h_L L - h_{L_0} L_0 \tag{19}$$

Rearranging and integrating Equation (13) results in the following equation:

$$q_c = \int_0^D Q_c'\, dD - \int_0^D h_D\, dD \tag{20}$$

The integration of $Q_c'\, dD$ in Equations (19) and (20) must necessarily be carried out graphically, the relationship between Q_c' and D being found from Equations (1), (6), and (15).

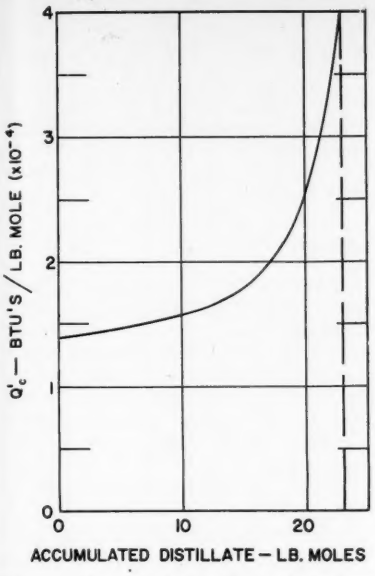

Fig. 3. Q_c' vs. D plot for the evaluation of $\int_0^D Q_c'\,dD$.

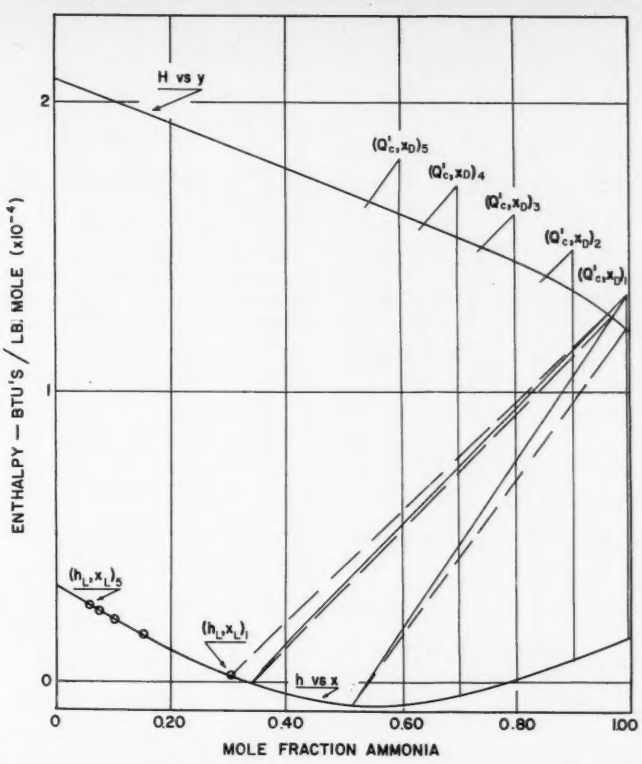

Fig. 4. Enthalpy-concentration diagram for the ammonia-water system showing the variation of Q_c' and x_L when the reflux ratio is constant.

Equation (20) may be simplified when the method of operation is such that the overhead product composition is constant, as h_D is dependent only upon the product composition.

$$q_c = \int_0^D Q_c'\,dD - h_D D \qquad (21)$$

When the method of operation is such that the reflux ratio is constant, $h_D\,dD$ must be graphically integrated for a rigorous solution of Equation (20). However, for some systems the saturated liquid line on an enthalpy-concentration diagram is nearly a straight line. If the enthalpy of the product leaving the system when approximately half the product has been collected can be estimated, Equation (20) may be simplified to give

$$q_c = \int_0^D Q_c'\,dD - (h_D)_{avg} D \qquad (22)$$

Equation (22) should not result in any significant error if the saturated liquid line is nearly horizontal.

ILLUSTRATIONS

Two illustrations, one for the case of constant product composition and the other for the case of constant reflux ratio, are presented here to compare the results obtained by previously developed methods with the results obtained by the rigorous method presented here. The ammonia-water system was used in both illustrations and the data of Merkel and Baznjakowic (*2*) were utilized.

The first problem considered was

L_0 = 100 lb. moles
x_{L_0} = 0.258 NH_3 (mole fraction)
x_D = 0.995 NH_3 (mole fraction)
x_L(final) = 0.039 NH_3 (mole fraction)
Reflux ratio—variable
Number of theoretical plates = 4
Pressure = 14.7 lb./sq. in. abs.

With the information given above and Equation (7), the top product obtained is 22.91 moles.

If this problem is solved by the method of Bogart (*1*), a fictitious molecular weight for one of the components must be used if the necessary assumptions are to be approximately true. No one value for the fictitious molecular weight will satisfy the requirements; consequently, different results will be obtained depending upon the value selected. A fictitious molecular weight of 29.7 for ammonia was chosen for this illustration. This value was determined by making the molal latent heat of vaporization of ammonia equal to the molal latent heat of vaporization of water. The problem was then solved and it was determined that 20.16 fictitious moles of vapor entered the condenser. If the molal latent heat of condensation of water is used, the heat load at the condenser is

$$q_c = (20.16)(17{,}484)$$

$$= 352{,}000 \text{ B.t.u.}$$

The heat load at the reboiler is identical, owing to the assumptions made. In the solution of the problem the operating lines were considered straight, an assumption that is unrealistic for this system.

If this problem is solved by the proposed method, the procedure would be:

1. On an enthalpy-concentration diagram for the ammonia-water system, locate x_D at 0.995 mole fraction ammonia and assume a value for Q_c'. The reflux ratio is then fixed.
2. Step off four theoretical plates and thus determine x_L. (See Figure 2.)
3. Use Equation (6) to determine the amount of distillate obtained.
4. Repeat steps 1 to 3, using different values of Q_c'. This permits the determination of Q_c' as a function of the number of moles of distillate accumulated.
5. Plot Q_c' as a function of the accumulated distillate (Figure 3) and by graphical integration determine the value of $\int_0^D Q_c'\,dD$, the first term in the right-hand member of Equation (21).
6. Determine the condenser heat load by Equation (21).
7. Determine the reboiler heat load by Equation (19).

For the problem in question,

$$\int_0^{22.9} Q_c'\,dD = 426{,}000 \text{ B.t.u.}$$

and

$$q_c = 426{,}000 - (1{,}410)(22.91)$$

$$q_c = 394{,}000 \text{ B.t.u.}$$

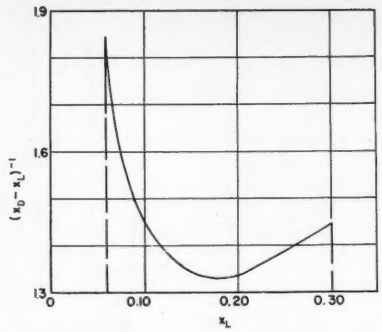

Fig. 5. $(x_D - x_L)^{-1}$ vs. x_L plot for the evaluation of $\int_{x_{L_0}}^{x_L} (x_D - x_L)^{-1}\, dx_L$.

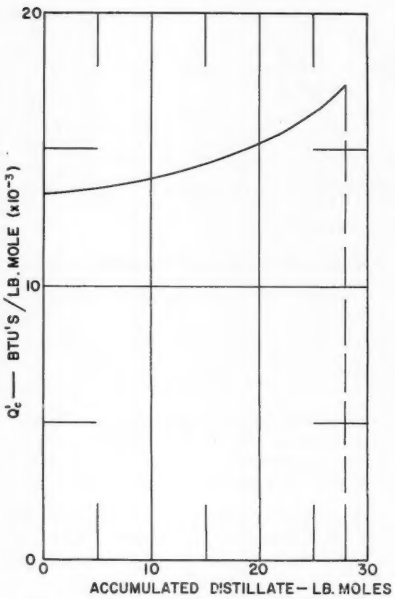

Fig. 6. Q_c' vs. D plot for the evaluation of $\int_0^D Q_c'\, dD$.

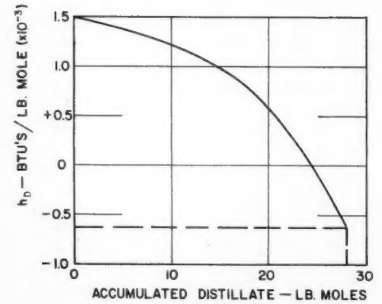

Fig. 7. h_D vs. D plot for the evaluation of $\int_0^D h_D\, dD$.

and

$$q_r = 426{,}000 + (77.09)(2{,}700) - (100)(-890)$$

$$q_r = 723{,}000 \text{ B.t.u.}$$

It will be noted that the reboiler heat loads, as determined by the two methods, are hardly comparable and that the condenser heat loads differ by 10.7%.

The second illustration is one in which the reflux ratio was held constant and the composition of the overhead product allowed to vary. The problem was

$L_0 = 100$ lb. moles
$x_{L_0} = 0.302$ NH_3 (mole fraction)
$(x_D)_{avg} = 0.90$ NH_3 (mole fraction)
$0/V_1 = 0.10$
Number of theoretical plates = 3
Pressure = 14.7 lb./sq. in. abs.

If a fictitious molecular weight of 29.7 for ammonia is assumed and the problem solved by the method of Smoker and Rose (*6*), it is determined that 21.3 fictitious moles of vapor enter the condenser. If the molal latent heat of condensation of water is used, the heat load at the condenser is

$$q_c = (21.3)(17{,}485) = 372{,}000 \text{ B.t.u.}$$

The reboiler and condenser heat loads are identical in this method.

By the proposed method of solution, the following procedure is used:

1. On an enthalpy-concentration diagram for the ammonia-water system, assume a value of x_D (this fixes h_D) and locate Q_c'. Q_c' can be calculated, since the $0/V_1$ ratio is fixed. (See Figure 4.)
2. Step off three theoretical plates and determine x_L and h_L.
3. Use Equation (6) to determine the amount of distillate obtained. (See Figure 5.)
4. Repeat steps 1 to 3 and plot $(x_D)_{avg}$ vs. accumulated distillate. From this plot the amount of product of 0.90 NH_3 can be obtained. This particular step is basically the same procedure as used in the Smoker and Rose method.
5. Plot Q_c' as a function of the amount distilled (Figure 6) and determine the value of $\int_0^D Q_c'\, dD$.
6. Plot h_D as a function of the amount distilled (Figure 7) and determine the value of $\int_0^D h_D\, dD$.
7. Determine the reboiler heat load by Equation (19).
8. Determine the condenser heat load by Equation (20).

For the problem in question:

$$\int_0^{28.0} Q_c'\, dD = 405{,}000 \text{ B.t.u.}$$

$$\int_0^{28.0} h_D\, dD = 11{,}000 \text{ B.t.u.}$$

therefore,

$$q_r = 405{,}000 + (2{,}660)(72) - (195)(100)$$

$$q_r = 577{,}000 \text{ B.t.u.}$$

and

$$q_c = 405{,}000 - 11{,}000$$

$$q_c = 394{,}000 \text{ B.t.u.}$$

Although the heat loads at the condenser, as calculated by the two methods, differ by only 5.6%, the heat loads at the reboiler differ by 35.4%.

SUMMARY

A rigorous method for the determination of the heat requirements in batch fractionation processes has been presented. The method, which is a modification of the methods of Ponchon (*4*) and Savarit (*5*), can be used for the solution of batch-fractionation problems in which the reflux ratio is constant and the overhead product varies or in which the overhead product is constant and the reflux ratio varies.

The proposed method is illustrated and compared with methods which have been presented previously.

NOTATION

D	= amount of product
H	= enthalpy per unit quantity of vapor
L	= amount of liquid in still
O	= amount of liquid overflow
Q_c'	= construction point representing conditions at top of column
V	= amount of vapor flow
d	= differential
d'	= inexact differential
h	= enthalpy per unit quantity of liquid
q_c	= amount of heat removed at the condenser
q_r	= amount of heat added at the reboiler
x	= composition in the liquid phase
y	= composition in the vapor phase

Subscripts

D	= product
L	= still
L_0	= initial still conditions
N	= bottom plate in column
n	= nth plate in column
$n+1$	= $(n+1)$ plate in column
1	= top plate

LITERATURE CITED

1. Bogart, M. J. P., *Trans. Am. Inst. Chem. Engrs.*, **33**, 139 (1937).
2. Merkel, Friedrich, and Franjo Baznjakowic, "Diagrams and Tables for Calculating Absorption Machines," Springer, Berlin (1929).
3. McCabe, W. L., and E. W. Thiele, *Ind. Eng. Chem.*, **17**, 605 (1925).
4. Ponchon, Marcel, *Tech. mod.*, **13**, 20 (1921).
5. Savarit, Paul, *Arts et métiers*, **65**, 142, 178, 241, 266, 307 (1922).
6. Smoker, E. H., and Arthur Rose, *Trans. Am. Inst. Chem. Engrs.*, **36**, 285 (1940).

Gas Mixing in a Square Duct

EUGENE MILLER, S. P. FOSTER, R. W. ROSS, and KURT WOHL

There are numerous practical examples of the importance of gas mixing to the chemical industry and to combustion-engine technology. In the chemical plant good mixing is often a criterion for obtaining profitable yields. In the Diesel and Otto cycle engines, gas turbines, rockets and ramjets, gas mixing has an important bearing on performance. Moreover, poor mixing often causes excessive corrosion or erosion of reactor and combustion chamber walls because of the presence of zones of extreme temperature or chemical concentration.

A number of theoretical and experimental investigations have been reported on the mixing of free and coaxial jets (*5*, *9* to *12*). These studies frequently do not apply to the more complicated mixing conditions encountered in industry.

Chilton and Genereaux (*4*) introduced a sidestream gas containing smoke into a gas mainstream and studied the resultant mixing process visually. They concluded that an ordinary T configuration gave as good mixing as any other simple arrangement having low energy requirements and that the mass velocity ratio of the two gas streams was the controlling variable.

More recently, in a series of papers (*1*, *2*, *3*, *13*, *14*), Callaghan, Ruggeri, and Bowden studied the penetration of a hot-air jet into an air stream flowing perpendicular to it in a narrow, high channel. They followed the limits of jet penetration into the channel by means of a thermocouple rake and measured temperature profiles for various relative angles of the sidestream and for different sidestream-orifice shapes. A jet emerging from a square orifice penetrated further into the channel than one emerging from a circular orifice of the same cross-sectional area.

Ehrich (*6*) analyzed the dynamics of jets entering into a general stream at an oblique angle from slots and orifices, based on simplified two-dimensional potential-flow theory. His study agreed qualitatively with Callaghan and Ruggeri's penetration data (*1*). Frazer (*7*) made a complementary, three-dimensional potential-flow analysis of a round jet penetrating into a main stream at right angles and also obtained qualitative agreement with Callaghan and Ruggeri.

Hawthorne, Rogers, and Zaczek (*8*) studied the penetration and mixing of a jet of cold air issuing through a hole in the wall of a 3-in.-square duct carrying hot air. This work came to the authors' attention after completion of the present work. Measurements were made with a temperature rake with some complementary shadowgraph and schlieren photographs. The duct length required to obtain the same degree of mixing in a 3-in.-square duct was found to be twice that in a 1½-in.-square duct. A correlation of the distance to which the cold jet penetrated the hot air in the main duct was obtained with the factor $R_m R_v / (1 + R_v)^2$ in terms of the present nomenclature. Turbulence in the hot stream reduced the penetration. Also, the penetration increased if another jet or a rod was placed immediately upstream. A jet emerging from a square hole penetrated as far into the duct as did a jet from a circular hole of equal area. A jet emerging from a rectangular hole of the same area penetrated further into the duct when placed with its long side in the direction of the stream and less when placed transversely.

The present study is an extension of the work initiated by Chilton and Genereaux. The characteristics and controlling parameters of gas mixing in a square duct with a sidestream entering at right angles have been examined more completely by means of instantaneous shadow photography and chemical-sampling techniques. It has been possible to obtain a semiquantitative picture of gas mixing under this circumstance which may have application to industrial problems.

SCOPE OF WORK

The main experimental situation chosen for study was the mixing of an air stream flowing in a square duct with a stream of carbon dioxide entering from the side. The sidestream tube was placed perpendicular to the main duct with the exit port ending flush with the main duct inner wall. In a small number of tests the roles of the gases were inverted.

For flow visualization of the mixing process, instantaneous shadow photographs were found superior to smoke photography and chemical or thermal analysis. Although basically a qualitative tool as used, the instantaneous shadowgraph was found unexcelled in its revelation of the turbulent structure of mixing. Measuring on the shadowgraph the distance to which mixing had progressed to some defined degree made it possible to obtain quantitative results as well. Sampling by means of a probe yielded results which were in good agreement with the conclusions drawn from the shadowgraphs.

The following parameters and experimental variables were independently and systematically varied:

1. Main duct size D, 1-, 2-, and 3-in. square
2. Main-gas-stream velocity, V_D, 12.5 to 100 ft./sec.
3. Sidestream: main-stream mass velocity ratio R_m, 2 : 1 to 32 : 1
4. Sidestream: main-stream volume flow ratio R_v, 1 : 50 to 1 : 1.6
5. Sidestream port shape—circular, square, and rectangular (length : width ratio of 1.9 : 1). Also, slits extending over the whole width of the main duct were used.

All possible combinations of the variables however, were not explored. Reference is made to the experimental results for details.

CRITERIA FOR MIXING

A typical example of mixing is shown in the instantaneous shadowgraph, Figure 1. Air is flowing horizontally in the 3-in.-square main duct at a velocity of 49 ft./sec. with carbon dioxide entering sidewise at the bottom wall from a cylindrical tube. R_m is 4.6 and R_v is 1 : 12.2. Typically for these conditions, the entering carbon dioxide jet first is bent by the mainstream, then spreads, reaches the opposite duct wall, distributes itself across the duct more or less evenly, and finally blends completely with the main stream.

After an examination of shadowgraphs taken for various mixing conditions, four parameters were chosen as descriptive of the mixing process. These can be understood from Figure 1.

Penetration distance P is defined as the longitudinal distance between the upstream edge of the sidestream-jet shadow image at the side tube port and the plane where the jet shadow just reaches the opposite wall. This parameter is a measure of the "stiffness" of the sidestream jet or its resistance to being bent. It is related to the problem of distributing the sidestream over the cross section of the duct. Penetration is the first requirement for complete mixing of the two streams. Penetration distance, as defined here, is different from the penetration described by Callaghan et al. and Hawthorne et al. These authors measured the transverse distance to the outer edge of the sidestream jet from the bottom wall of the main duct as a function of the

E. Miller is at present with Redstone Arsenal, Huntsville, Alabama; S. P. Foster with E. I. du Pont de Nemours Company, Inc., Wilmington, Delaware; R. W. Ross with Shawinigan Resins Corporation, Springfield, Massachusetts; and Kurt Wohl at the University of Delaware, Newark, Delaware.

distance down the main duct from the sidestream inlet.

Bulk mixing distance B is defined as the longitudinal distance between the center of the side tube port and the plane where the schlieren are distributed (but not necessarily uniformly) over the whole duct. At this distance, bulky and nonuniform schlieren are visible. The bulk mixing distance is at least as large as the penetration distance but is usually larger.

Macromixing distance M is defined as the longitudinal distance between the center of the side tube port and the plane where a roughly even distribution of the schlieren is accomplished over the cross section of the duct. The schlieren intensity and scale, i.e., "graininess," are uniform over the cross section at this distance. Coarse mixing has been accomplished, but molecular mixing has not yet been completed. Molecular mixing also takes place during this interval, but macrodistribution is the dominant operation. The macromixing distance is at least as long as the bulk mixing distance but is usually longer.

Micromixing distance, to be consistent, should be defined by the longitudinal distance from the center of the side tube port to a plane where the schlieren have become invisible. The shadowgraph method though capable of defining the scale of the schlieren, cannot accurately resolve the plane at which the schlieren have disappeared because of the secondary patterns superimposed by the glass walls of the duct. Instead of a distance parameter, a scale of grading the quality of micromixing has been chosen which provides a method for describing the micromixing in a semiquantitative manner.

Grade A: excellent; very faint schlieren present after 3.5 duct diam. and none at 7 duct diam.

Grade B: good; distinct schlieren at 3.5 diam. and none or faint at 7 diam.

Grade C: fair, medium-scale schlieren present at 7 duct diam.

Grade D: poor; bulky, large-scale schlieren at 7 duct diam.

It would be difficult to ascertain the difference between the micro- and macromixing by another method such as chemical analysis. It is a virtue of the shadowgraph method to be able to discriminate between the two.

Shadowgraphs taken through the top and bottom duct walls (both of glass) and probe samplings indicated that the sidewise spreading and mixing of the sidestream jet with the main stream were completed before completion of the mixing viewed from the side. This was the case in all duct sizes studied. Since the side plane thus represented the controlling plane of mixing, the major portion of the shadowgraphs were taken in this plane.

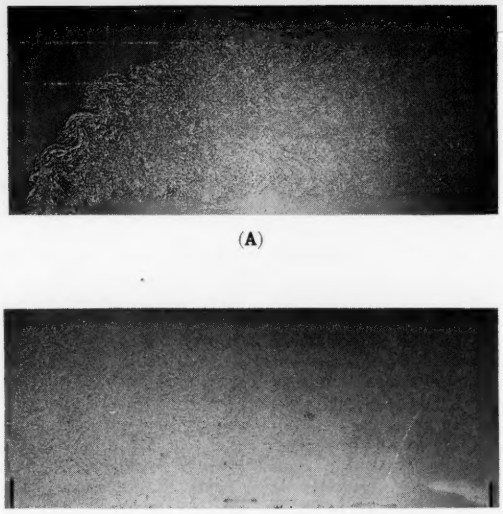

(A)

(B)

Fig. 1. Mixing of air flowing in a 3-in. square duct with carbon dioxide entering sidewise from tube. R_v = 1:12.2, R_m = 4.6, V_D = 49 ft./sec.

A. Upstream section, 0 to 2.3 duct diam. B. Downstream section, 2.3 to 4.6 duct diam.

ANALYSIS

Qualitative consideration of the mixing problem predicts that mixing is largely controlled by the size of the duct and side port and by the velocities and densities of the mainstream and sidestream jet. Viscous-force effects have been neglected.

For penetration distance P, there can be written:

$$P = f(D, d, V_D, u, \rho_D, \rho_d) \qquad (1)$$

If

$$\frac{P}{D} = K_p\left(\frac{V_D}{u}\right)^a\left(\frac{D^2}{\pi d^2/4}\right)^b\left(\frac{\rho_D}{\rho_d}\right)^c \qquad (2)$$

then

$$\frac{P}{D} = K_p\left(\frac{V_D\rho_D}{u\rho_d}\right)^{a-b}\left(\frac{V_D D^2}{u\pi d^2/4}\right)^b\left(\frac{\rho_D}{\rho_d}\right)^{c-a+b} \qquad (3)$$

or

$$\frac{P}{D} = K_p\frac{(\rho_D/\rho_D)^\gamma}{R_m{}^\alpha R_v{}^\beta} \qquad (4)$$

where

$$R_m = u\rho_d/V_D\rho_D \quad \text{and} \quad R_v = \frac{u\pi d^2/4}{V_D D^2}$$

The ratio D/d was a dependent variable in these experiments, since R_m and R_v were varied independently; by definition,

$$R_m = \frac{\rho_d}{\rho_D}\left(\frac{D^2}{\pi d^2/4}\right)R_v \qquad (5)$$

Similarly,

$$\frac{B}{D} = \frac{K_b(\rho_D/\rho_d)^\delta}{R_m{}^\epsilon R_v{}^\kappa} \qquad (6)$$

and

$$\frac{M}{D} = \frac{K_m(\rho_D/\rho_d)^\eta}{R_m{}^\theta R_v{}^\iota} \qquad (7)$$

It may be mentioned at this point that, at least for small ducts, $\gamma = \delta = \eta = 0$; i.e., the effect of density ratio is taken care of by the term R_m.

The quality of micromixing is necessarily affected by the mass velocity and volume flow ratios since penetration, bulk mixing, and macromixing take place before completion of micromixing. However, final micromixing is molecular in nature and such factors as diffusivity would have to enter into the analysis as well. Since micromixing could be graded only qualitatively, no correlation was attempted.

APPARATUS AND PROCEDURE

Three different mixing chambers were used. They were square wooden ducts 1 in. square by 36 in. long, 2 in. square by 55 in. long, and 3 in. square by 85 in. long, with two side walls of special plate glass, Libby-Owens-Ford OS 1076. The 1- and 2-in. square ducts had glass walls for the last 20 in. of length, the 3-in. square duct for 39 in. Provision was made for introducing the mainstream gas into one end of the square duct and for the sidestream gas to enter through the bottom wall near the beginning of the glass-walled section, equidistant from the two side walls.

The flow length before the glassed section

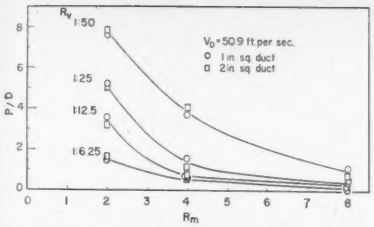

Fig. 2. Penetration distance: duct width as a function of mass velocity and volume flow ratios, 1- and 2- in. square ducts, cylindrical side tube.

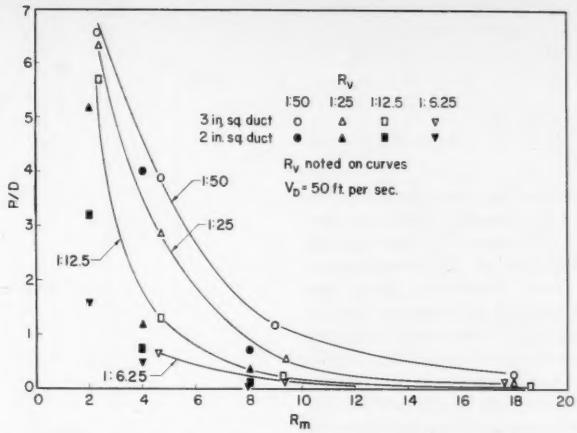

Fig. 3. Penetration distance: duct width as a function of mass velocity and volume flow ratios, 2- and 3-in. square ducts, cylindrical side tube.

of the 1- and 2-in. square ducts, 20 diam., was sufficient to smooth out entrance disturbances. The 3-in. square duct was somewhat short because of space limitations, 15 diam.; a 32-mesh screen was placed at the entrance to correct this deficiency. It was found experimentally, however, that flow disturbances produced at the entrance were negligible compared with the turbulence generated by the jet interaction.

The cylindrical tubes used for the sidestream were machined on a lathe. Rectangular and square tubes were formed from cylindrical brass tubes over previously machined mandrels. Dimensions of the various ports were measured with a traveling microscope.

The sampling probe consisted of a steel tube 0.047 in. I.D. by 0.004 in. wall by 12 in. long. Samples were withdrawn with the probe positioned parallel to the main gas stream. The holder was graduated in divisions of 0.01 in. for movement in horizontal and vertical directions perpendicular to the axis of the duct. The duct cross section was divided arbitrarily into nine equal sections, and for each sampling the probe was located at the center of a section. Samples were drawn into a burette with mercury as the working fluid. The sampling velocity through the probe was 25 ft./sec.

The sample was analyzed for carbon dioxide with a potassium hydroxide solution. A thin layer of water was kept on top of the mercury in the burette to keep the water-vapor content of the sample constant.

EXPERIMENTAL RESULTS

Shadowgraphic Studies

Cylindrical Side Tube. PENETRATION DISTANCE. In Figures 2 and 3, P/D measurements for the 1-, 2-, and 3-in. square ducts are correlated as a function of R_m and R_v at a main duct velocity of about 50 ft./sec. It may be seen that P/D decreases with an increase in R_m and R_v. At low values of R_m and R_v, e.g., 2 : 1 and 1 : 50 respectively, the carbon dioxide jet offers little resistance to the air stream and is swept down the duct for a relatively long distance before reaching the upper wall. At the highest values of R_m and R_v studied, e.g., 18 : 1 and 1 : 6.25 respectively, the sidestream jet offers so much resistance to the air stream that the penetration distance is almost zero. In between these extremes the penetration distance decreases continuously with increasing R_m and R_v.

In Figure 2 the data for both the 1- and 2-in.-square ducts are correlated by the same curves. Therefore, it may be concluded that P/D is independent of duct size in this range. In Figure 3 the data for the 3-in.-square duct are compared with the data for the 2-in.-square duct. It is evident that the values for the 3-in.-square duct are consistently higher. P/D is not independent of scale, therefore, above the 2-in.-square duct size.

In order to check on the validity of R_m and R_v as controlling variables for penetration distance, the roles of the gases were inverted in the 1-in.-square duct, carbon dioxide becoming the mainstream and air the sidestream. At this duct size at least, the data are correlated by R_m and R_v independent of the density of the gases. It was not possible to repeat these tests in the larger ducts because of limitations of the carbon dioxide supply.

The penetration distance data for all three ducts were correlated by

$$P/D = K_p/R_m{}^2 R_v \qquad (4a)$$

the exponent of the density ratio γ being zero. Equation (4*a*) applies to a fixed duct velocity and duct size in which R_m and R_v are independently varied. The results of the correlation are shown graphically in Figures 4 and 5.

The values of K_p, given in Figure 5*a*, were obtained from the data by the method of least squares. The independence of both duct size and role of the gases in the 1- and 2-in.-square ducts is evident from the identical values of K_p obtained. At every duct velocity studied the K_p values for the 3-in.-square duct are larger than for the 1- and 2-in.-square duct. Generally, it is seen from the figure that K_p decreases with an increase in duct velocity, although for the 3-in.-square duct data a single value of $K_p = 1.6$ adequately correlates all the data. In general, the duct velocity, compared with the other variables, has only a small effect on the penetration distance.

Equation (4*a*), with these values of K_p, correlates the results by approximately $\pm 20\%$. The largest deviations from the correlation are found for the smallest and largest values of P/D. At the smallest distances the relative error of measurement is, of course, large, and at the largest distances dilution effects make the measurements relatively doubtful.

Callaghan and Ruggeri's measurements of the "penetration" of air jets issuing from circular orifices into a 2- by 20-in. duct were correlated by

$$\left(\frac{l}{d}\right)^{1.65} = KR_m\left(\frac{S}{d}\right)^{0.5} \quad \text{in reference } 1 \qquad (8)$$

and as

$$\frac{l}{d} = K\left(\frac{\rho_d}{\rho_D}\right)^{0.52}\left(\frac{u}{V_D}\right)^{0.59} \cdot \left(\frac{S}{d}\right)^{0.26} \quad \text{in reference } 3 \qquad (9)$$

for large values of the ratio of the width of the jet to the orifice diameter d. In these correlations, l is the penetration and S is the distance downstream of the jet entrance at which penetration is measured. If special pairs of values of l and S are interpreted as D and P respectively, in terms of the present definition of penetration distance the following expressions result:

$$\frac{P}{D} = \frac{K_p(D/d)^{2.3}}{R_m{}^2} = \frac{K_p(\rho_D/\rho_d)(D/d)^{0.3}}{R_m R_v} \qquad (8a)$$

and

$$\frac{P}{D} = \frac{K_p(D/d)^{2.3}}{R_m{}^2 R_v{}^{0.3}} =$$

$$\frac{K_p(\rho_D/\rho_d)(D/d)^{0.3}}{R_m R_v{}^{1.3}}, \text{ respectively} \quad (9a)$$

The differences between these results and those of the present paper are due probably to differences in experimental configuration. Also, in the cited experiments the duct boundary layer was removed by suction upstream of the jet orifice to minimize wall boundary-layer effects. This was not done in this work.

Bulk Mixing Distance. A correlation of B/D as a function of R_m and R_v for the 2- and 3-in.-square ducts is shown in Figure 6. Nominal duct velocity is 50 ft./sec. Approximately the data for the 2- and 3-in.-square ducts may be represented by the same curve. Data taken with the 1-in.-square duct also fall quite close except for low mass velocity ratios near 2 : 1 where the values for the 1-in.-square duct are somewhat lower. B/D may be considered independent of duct size and density ratio within the range of these tests. It was found that the duct velocity has only a slight effect on the parameter B/D, apparently less than observed for P/D.

A logarithmic plot of B/D vs. R_m at constant R_v merely produces a family of nonlinear curves. Bulk mixing distance is not, therefore, a simple exponential function of mass velocity and volume flow ratios as was proposed by Equation (6).

Macromixing Distance, M/D. Figure 7 is a plot of M/D as a function of R_m and R_v at a constant duct velocity of 50.9 ft./sec. for the 1- and 2-in.-square ducts. The points for both ducts are satisfactorily correlated by the same curves, an indication that M/D is independent of duct size in this scale.

This independence does not extend to the 3-in.-square duct, as is seen in Figure 8. The data for the 3-in.-square duct are mostly higher than for the 1- and 2-in.-square ducts. Further, at higher R_m and R_v ratios the entire pattern of variation of M/D is reversed. At $R_m \leq 8$, M/D decreases with an increase in R_m and R_v, just as in the 1- and 2-in.-square ducts. At $R_m \geq 14$, M/D increases with an increase in R_m and R_v. Shadowgraphs show that as the sidestream volume flow rate and velocity are increased, a portion of the sidestream gas tends to hover at the upper wall.

When the sidestream jet strikes the opposite wall with force, it spreads out forward, backward, and sidewise in the plane of the wall. When the sidewise-spreading gases meet the side walls, they flow down to the bottom wall and finally fill the whole duct. During this distribution process turbulent mixing is of course taking place—not only in the distributed gas, but, prior to wall colli-

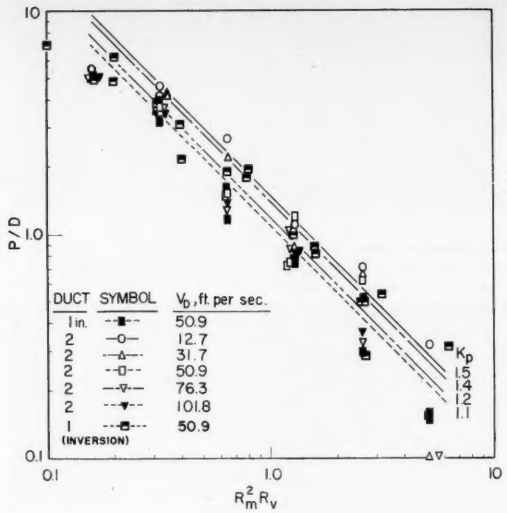

Fig. 4. Correlation of penetration distance: duct width with mass velocity and volume flow ratios, 1- and 2-in. square ducts, cylindrical side tube.

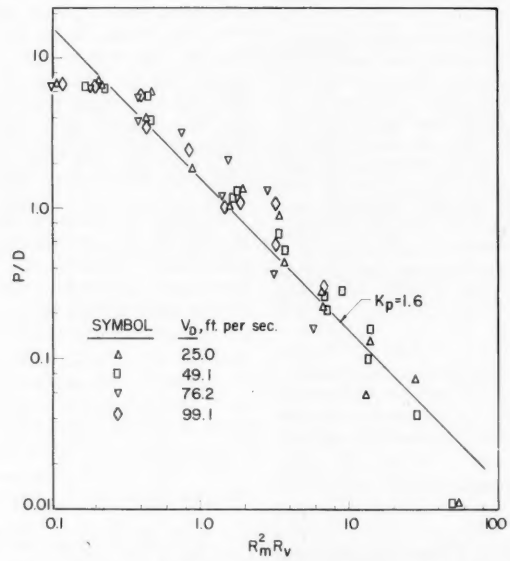

Fig. 5. Correlation of penetration distance: duct width with mass velocity and volume flow ratios, 3-in. square ducts, cylindrical side tube.

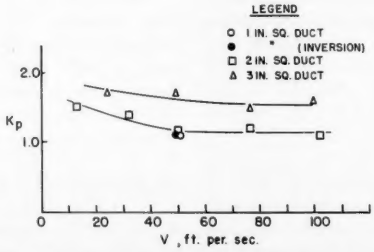

Fig. 5a. K_p as a function of duct velocity and duct size.

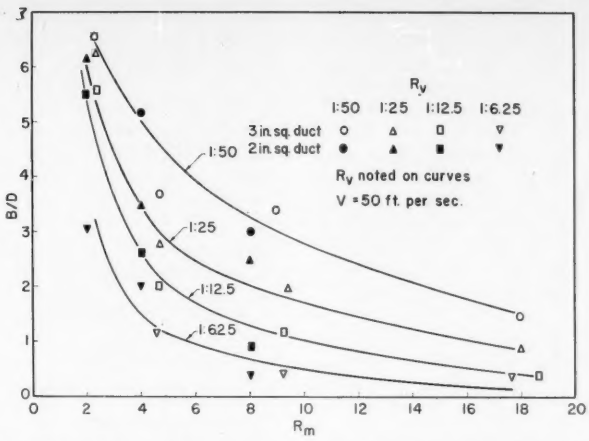

Fig. 6. Bulk mixing distance: duct width as a function of mass velocity and volume flow ratios, 2- and 3-in. square ducts, cylindrical side tube.

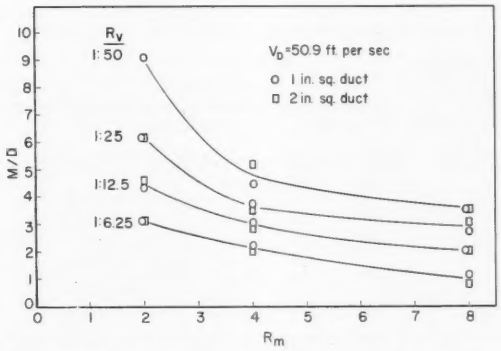

Fig. 7. Macromixing distance: duct width as a function of mass velocity and volume flow ratios, 1- and 2-in. square ducts, cylindrical side tube.

sion, in the jet as well. At higher $R_m (> 8)$ and R_v ($> 1:25$) values, the sidestream jet collides with the opposite wall with great momentum, and mechanical distribution of the type described undoubtedly plays the larger part in macromixing. At smaller R_m and R_v values, turbulent mixing plays the more important role. The predominance of mechanical distribution effects at $R_m > 8$ and turbulent mixing at $R_m < 8$ probably accounts for the reversal of the variation of macromixing distance.

There is hardly any doubt that similar results would have been obtained with the smaller ducts if the experiments had been conducted for $R_m > 8$. See for example the results obtained for the rectangular side tubes, page 400.

The effect of density on M/D was studied in the 1-in.-square duct by inverting the roles of the air and carbon dioxide. The results for a duct velocity of 50.9 ft./sec. indicate that the M/D is independent of density ratio.

It was found that M/D data for the 1- and 2-in.-square ducts could be correlated by

$$M/D = \frac{K_m}{(R_m R_v)^{1/2}} \qquad (7a)$$

the exponent η of the density ratio being zero again, as in the case of penetration distance. Graphical representation of the correlation is shown in Figure 9.

The effect of main duct velocity on M/D is given in Figure 9*a*, where K_m, obtained from the data by means of the least squares method, is given as a function of the duct velocity, the effect of which is seen to be small. The K_m value in the 1-in.-square duct inversion study is slightly larger ($\sim 6\%$) than the value found with air as the main duct gas. However, a K_m value of 1.7 can be used for correlating all the data in both 1- and 2-in.-square ducts within $\pm 20\%$ with the exception of two points of questionable accuracy. For $R_m > 8:1$ the equation does not describe the variation of M/D satisfactorily.

Correlation of the results for the 3-in.-square duct is shown in Figure 10. For this size of duct the equation

$$M/D = \frac{6.0}{R_m^{0.7} R_v^{0.2}} \qquad (7b)$$

correlates the data for all the main duct velocities studied, 25 to 100 ft./sec., within $\pm 25\%$. The equation is valid for $R_m \leq 18.5$ and for $R_v \leq 1:25$. For larger R_v values the correlation applies only to $R_m \leq 8$.

The exponents of R_m and R_v in Equation (7), then, vary for ducts larger than 2 in. square. In the 3-in.-square duct the effect of R_m is greater and the effect of R_v smaller than in the smaller ducts; i.e., the exponent of R_m increases and that of R_v decreases. Larger space, therefore, puts a premium on high momentum.

Quality of Micromixing. The micromixing qualities were estimated for the 1-, 2- and 3-in. square ducts at a nominal main-duct air velocity of 50 ft./sec. For the 1-in.-square duct at $R_v = 1:6.25$, the quality of micromixing is D independent of R_m in the range 2 to 8. As R_v is increased to the range $1:12.5$ to $1:50$, the quality improves to C/D if an $R_m = 8$ is used. The quality of micromixing for the 2-in.-square duct is the same as for the 1-in.-square duct except at $R_v = 1:50$ and $R_m > 2$; for $R_m = 4$ and 8, the quality is C/D and C respectively. A large improvement in micromixing is observed for the 3-in.-square duct. At $R_v = 1:6.25$ the quality of micromixing is D, C/D, and A/B for $R_m = 4$, 8, and 16 respectively. At $R_v = 1:12.5$ the quality is D, C, C, and B at $R_m = 2$, 4, 8, and 16 respectively. At $R_v = 1:25$ and $1:50$, the quality improves to D, C, B, and A corresponding to $R_m = 2$, 4, 8, and 16.

It may be seen that at constant R_v, the quality of micromixing improves with an increase in R_m and/or duct size. For a given R_m and duct size the quality of micromixing improves with a decrease in R_v. It is apparent also that R_m and duct scale have much stronger influences on the quality of micromixing than R_v does.

It was found in a study of the effect of main-duct air velocity on the quality of micromixing in the 3-in.-square duct that only small improvements in micromixing are obtained by an increase in duct velocity. However, an increase in duct velocity for a given R_m and R_v means an increase in the amount of material mixing and a shorter time in which to mix it for any given duct length. A small improvement in micromixing with increased duct velocity therefore takes on more significance. The same comment holds for bulk mixing and macromixing.

A definite improvement in micromixing is observed when the lighter gas forms the sidestream. When the roles of the

carbon dioxide and air are changed in the 1-in.-square duct, i.e. air is the side stream, at R_v from 1 : 12.5 to 1 : 50 the quality of micromixing is D, C, and B for $R_m = 2$, 4, and 8 respectively. At $R_v = 1 : 6.25$ the quality is D, D, and B for the same values of R_m. These qualities may be compared with those given above for carbon dioxide as the sidestream. For micromixing, then, the sidestream jet *velocity* is the important factor, whereas penetration, bulk mixing, and micromixing depend on *momentum*. Qualitatively the effects of R_m and R_v in the inversion tests are similar to those found in the case where air is the mainstream.

Opposed Cylindrical Side Tubes. An obvious method of improving mixing is to introduce the sidestream gas from a number of opposed jets. A brief investigation was made, therefore, of mixing with two opposed sidestream jets. The results are summarized in Tables 1 and 2.

It is evident from the data that mixing takes place more rapidly with opposed jets than with a single sidestream jet. It may be noted that the reversal of the variation of M/D with R_m and R_v at $R_m > 8$, noted for single-jet mixing, is not observed with opposed jets.

If penetration distance is defined as the distance between the upstream boundary of the sidestream-jet shadow image at the side tube port and the plane where the schlieren of the two jets meet, the data in Table 1 indicate that penetration distance is decreased by more than the factor of two that might be expected from the symmetry of the arrangement. It appears that the reduction in tube diameter in the opposed configuration is responsible for reducing penetration distance further. Consequently, the two opposed jets impinge with greater momentum, and the turbulence produced results in mixing in a smaller duct length.

The data for M/D for the 1- and 2-in.-square ducts with opposed jets indicate shorter relative macromixing distances than for the 3-in.-square duct (Table 2). Thus the scale effect found for the single-jet mixing configuration appears to hold also for the opposed-jet configuration.

Rectangular Side Tubes. Although the bulk of the work was done with cylindrical side tubes, some study was made of the effect of jet shape and orientation. The studies were conducted in the 2-in.-square duct at a duct velocity of 50 ft./sec.

Rectangular tubes with length-width ratios of 1.9 were studied with orientations in which the short side of the tube was placed perpendicularly to the air stream and also with orientations in which the long side was placed perpendicularly. Square tubes were also studied.

When the sidestream enters through a tube the diameter of which is small compared with the width of the duct, the bulk of the main gas slips by the sidestream without contact. In order to

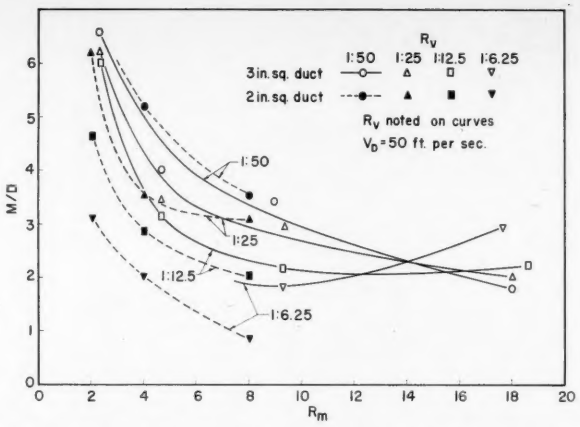

Fig. 8. Macromixing distance: duct width as a function of mass velocity and volume flow ratios, 2- and 3-in. square ducts, cylindrical side tube.

TABLE 1. OPPOSED JET STUDY

Three-in square duct, carbon dioxide entering sidewise

Air velocity, ft./sec.	Volume flow ratio, CO_2:air	Mass velocity ratio, CO_2:air	Penetration distance/duct width		Bulk mixing distance/duct width		Macromixing distance/duct width		Quality of micromixing	
			Opposed Jets	Single Jet	Opposed Jets	Single Jet	Opposed Jets	Single Jet	Opposed Jets	Single Jet
50.1	1:50	7.45:1	0.26	1.7	2.10	3.5	2.30	3.5	*B*	*B*
50.1	1:50.5	3.74:1	1.26	5.2	1.61	4.8	2.30	4.8	*B*	*C*
50.1	1:50	1.93:1	2.13	6.6	2.10	6.6	3.70	6.6	*C*	*D*
50.1	1:50	0.97:1	3.83	6.6	3.83	6.6	4.60	6.6	*C*	*D*
50.1	1:25.7	14.50:1	0	0.1	0.40	1.3	1.24	2.3	*A*	*B*
50.1	1:25.5	7.42:1	0.11	1.1	1.23	2.2	1.24	3.1	*B*	*B*
50.1	1:25.4	3.81:1	0.61	3.8	1.30	3.4	2.30	4.7	*C*	*C*
50.1	1:25	1.92:1	1.43	6.6	1.35	6.6	2.30	6.6	*C*	*D*
50.1	1:13	14.60:1	0	0	0.29	0.6	0.31	2.2	*A*	*B*
50.1	1:12.5	7.75:1	0	0.4	0.88	1.3	1.34	2.4	*A*	*C*
50.1	1:12.7	3.81:1	0.425	2.0	0.70	2.6	2.83	4.4	*C*	*C*
50.1	1:6.25	7.75:1	0	0.3	0.64	0.6	0.88	1.9	*A*	*C/D*
12.7	1:50	7.41:1	0.32		4.60		4.60		*C*	
12.7	1:50	3.77:1	1.00		0.94		2.00		*B*	
12.7	1:25	7.51:1	0.16		1.37		2.30		*B*	
12.7	1:25	3.86:1	0.47		0.55		2.30		*B*	
12.7	1:12.8	14.75:1	0		0.26		0.65		*A*	

TABLE 2. OPPOSED JET STUDIES

Comparison of Data from 3-in.-square Ducts with Data from 1- and 2-in.-square Ducts

Duct velocity	Volume flow ratio	Mass velocity ratio	Macromixing Distance/Duct Width				
			3-in. duct, opposed jets	3-in. duct, single jets	2-in. duct, opposed jets	2-in. duct, single jets	1-in. duct, opposed jets
50	1:12.5	4.0	2.83	3.13			1.3
50	1:25	2.0	2.30	6.00		6.20	1.2
50	1:50	1.0	4.60				3.1
50	1:50	8.25	2.30	3.41	1.7	3.54	
50	1:50	4.2	2.30	4.00	1.3	5.20	
50	1:25	16.0	1.24	2.00	0.75		
50	1:25	8.2	1.24	2.95	1.20	3.04	
50	1:12.5	16.4	0.31	2.22	0.58		
12.7	1:50	7.75	4.60		2.67		
12.7	1:50	3.9	2.00		2.10		
12.7	1:25	7.75	2.30		1.20	3.50	
12.7	1:25	4.0	2.30		2.30	4.1	
12.7	1:12.5	16.0	0.65		0.87		

avoid this, in a small number of tests the sidestream carbon dioxide was introduced through a slit extending over the whole width of the duct.

PENETRATION DISTANCE. In general, the P/D values for the rectangular and square side tubes could be correlated in the same form of equation as for the tube jets, Equation (4*a*). K_p values were obtained from the data by the method of least squares and are compared with the result for a cylindrical side tube:

Configuration	K_p
Air → □	0.9
→ ▭	0.9
→ ○	1.1
→ ▯	1.2

The square tube and the rectangular tube placed with the short side perpendicular to the main gas stream produce the smallest penetration distance, followed by the cylindrical tube and the rectangular tube with the long side perpendicular to the main flow. The results agree qualitatively with the conclusions of references *1*, *3*, and *8*.

A simplified, dynamic analysis of the bending of a rectangular jet predicts that the penetration distance, for jets of the same cross-sectional area, should be shorter for the rectangular jet with the short side perpendicular to the main gas flow than for the jet placed transversely. This is supported by the experimental results. The cylindrical- and square-jet penetration distances should lie somewhere between the two extremes if break-up of the jet boundaries by turbulent diffusion were not important. It is clear from these results and the shadowgraph (Figure 1) that the effect of turbulence on the side jet cannot be neglected.

The results of mixing when the sidestream enters from a slit extending over the whole width of the main duct show that, not unexpectedly, a thin sheet of carbon dioxide is easily bent and the penetration distance is very much larger than, for example, for a cylindrical-tube jet.

BULK MIXING DISTANCE. For values of $R_m < 6$, and for all the R_v values studied, the cylindrical-tube jet produces about 25% longer bulk mixing distances than the rectangular or square ports. For the higher R_m values the distances for the cylindrical-tube jet approach closely those for the rectangular and square ports. Just as for the cylindrical side tubes, the data could not be correlated by Equation (6).

MACROMIXING DISTANCE. In Figure 11 the macromixing-distance results are presented. The reversal of M/D variation with R_m and R_v, described previously in connection with the cylindrical-side-tube data, is particularly evident for the rectangular and square side tubes. The reversal appears to occur at smaller R_m and R_v values for the rectangular side tubes than for the cylindrical side tubes, especially in the case of the rectangular side tube with its long side perpendicular to the main air stream. The reversal already occurs at an R_v of 1 : 25 and R_m of 7.

A qualitative comparison between the different side tubes studied may be made. The cylindrical tube jets consistently produce the shortest macromixing distances, followed by the square tube jets, the rectangular tube with the short side perpendicular to the main stream, and the rectangular tube with the long side perpendicular to the air stream in increasing order of distance required. A slit extending over the width of the duct requires longer macromixing distances than do the other side tubes used.

QUALITY OF MICROMIXING. A comparison between the various kinds of sidestream jets is given in Table 3. The results for the rectangular and square jets indicate that R_m has a more important influence on micromixing than R_v does. At lower R_v ratios of 1 : 50 and 1 : 25 the rectangular-tube transverse to the air stream produces the best micromixing followed closely by the other orientation

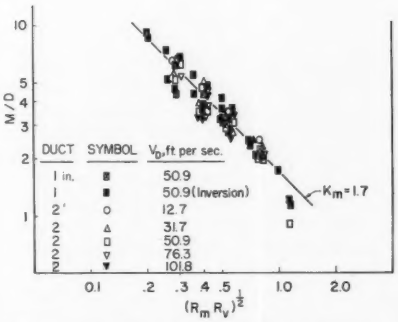

Fig. 9. Correlation of macromixing distance: duct width with mass velocity and volume flow ratios, 1- and 2- in. square ducts, cylindrical side tube.

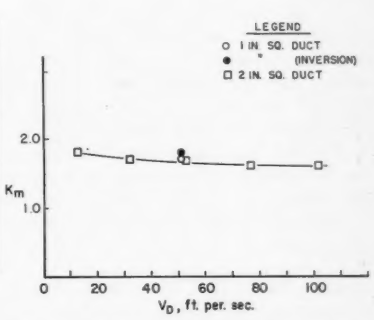

Fig. 9*a*. K_m as a function of duct velocity and duct size.

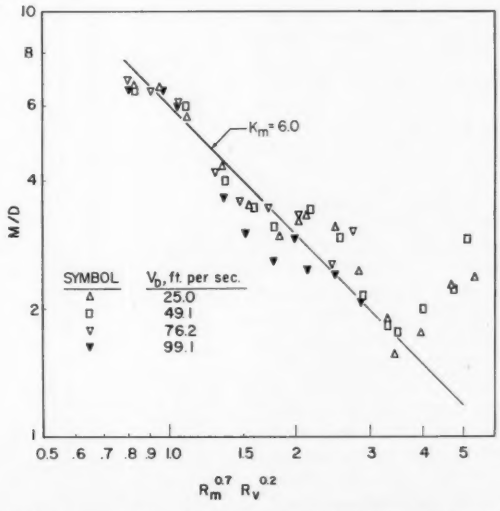

Fig. 10. Correlation of macromixing distance: duct width with mass velocity and volume flow ratios, 3-in. square duct, cylindrical side tube.

and then the square tube in decreasing order of quality. At higher R_v values, $\geq$ 1 : 12.5, the square tube or the rectangular tube with the short side perpendicular to the air stream is best, followed by the rectangular tube with the long side perpendicular to the air stream.

The cylindrical-tube jet mostly produces the poorest micromixing of all the configurations studied, just the opposite of the macromixing situation. The rectangular side tube with the short side perpendicular to the main gas stream consistently gives good mixing; it never is worse than second best of the arrangements studied. If good macromixing is desired, a cylindrical side tube should be used. If good micromixing is required, the rectangular side tube in general is recommended, oriented in a sense dictated by the R_m and R_v conditions if possible or with the short side perpendicular to the mainstream.

It was predicted that if the carbon dioxide stream were made to enter from a slit extending from one side wall to the other, the air would have to break through the carbon dioxide barrier in order to proceed. This should be favorable to mixing. Actually, although such a slit produces better micromixing quality than the tube jet, it does not show any advantage over the rectangular or square side tubes.

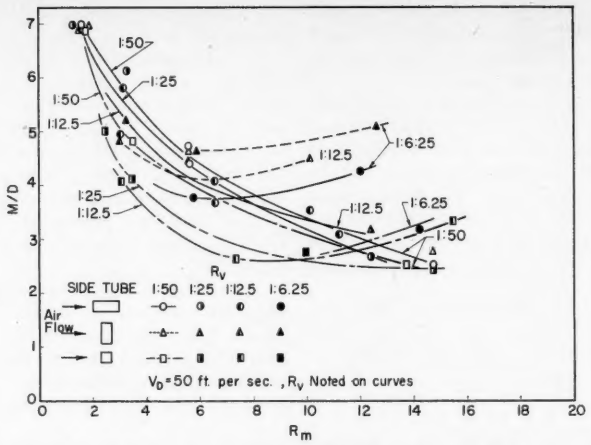

Fig. 11. Macromixing distance: duct width as a function of mass velocity and volume flow ratios, 2-in. square duct, rectangular and square side tubes.

Sampling Studies

In the 3-in.-square duct, at a constant duct velocity of 25 ft./sec. and R_v of 1 : 25, sampling traverses were made at R_m values of 2.2, 9.0, and 17.5.

The duct cross section was divided into nine equal squares and the samples were taken in the center of each:

	Left	Center	Right
Top	1	2	3
Middle	4	5	6
Bottom	7	8	9

Shadowgraphs were taken for comparison in the horizontal and vertical planes at each of the conditions studied by the sampling technique.

The sampling data are presented in Figures 12, 13, and 14 as R_s the ratio of the concentration of carbon dioxide in the sample to the total concentration of carbon dioxide flowing in the duct, vs. the distance down the duct. The designations *left side*, *center*, and *right side* and *top*, *middle*, and *bottom third* in the figures refer to the particular portion of the duct involved, as shown above.

In confirmation of the shadow method, there was no carbon dioxide detected by the sampling technique in the vicinity of the entering jet where no schlieren were observed. Also, when the shadowgraph showed an even distribution or disappearance of schlieren, the sampling technique indicated that the carbon dioxide concentration was approximately uniform across the duct.

From Figures 12, 13, and 14, a three-dimensional picture may be obtained of the mechanism by which the sidestream jet mixes with the main stream. When the high-velocity jet at R_m of 17.5 strikes the opposite wall, it spreads out across the top, depleting the carbon dioxide concentration in the center of the top section. The gas reaching the side walls streams down to the bottom of the duct

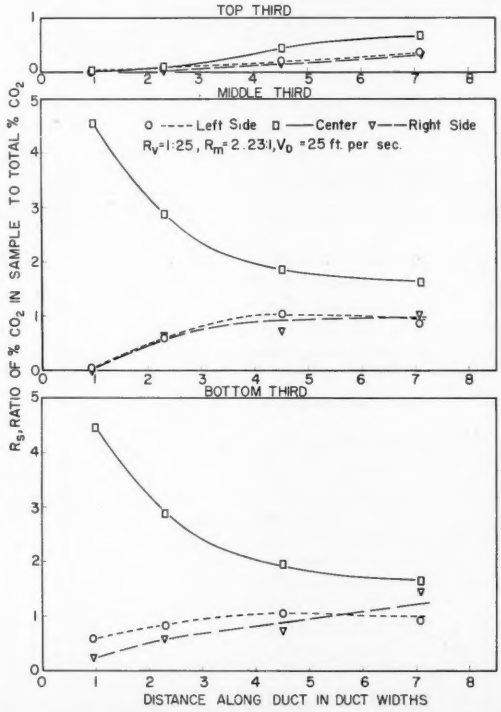
TOP THIRD
MIDDLE THIRD
BOTTOM THIRD
o ---- Left Side □ —— Center ▽ —— Right Side
R_v=1:25, R_m=2.23+l, V_D =25 ft. per sec.
R_s, RATIO OF % CO_2 IN SAMPLE TO TOTAL % CO_2
DISTANCE ALONG DUCT IN DUCT WIDTHS

Fig. 12. Ratio of percentage of carbon dioxide in sample to total percentage of carbon dioxide vs. distance along duct, 3-in. square duct, cylindrical side tube.

and then gradually fills the center of the duct. After this occurs, the slower micromixing takes place. At an R_m of 9.0, the mechanism is much the same except that the distances required to accomplish these phases of mixing are much longer, as is readily seen from Figure 13.

At an R_m of 2.2, when the sidestream jet is at a low velocity, the situation is different. Here there is a problem of carrying the sidestream gas to the upper portions of the duct. Also, rather than a depletion there is an excess in the center sections of the duct. Mixing takes place by virtue of the turbulence present without any assistance from mechanical distribution.

The correlation between the sampling method and the shadowgraphic technique is further illustrated in Table 4. Average R_s values are given here. *Top* means the average R_s over *left top, center top, right top*, etc. It may be seen here that mixing in the horizontal plane is better than mixing in the vertical plane.

Table 3.

Rectangular-slit Mixing Studies,
Quality of Micromixing vs. Slit Configuration

Mixing of Air Flowing in a 2-in. Square Duct with Carbon Dioxide Entering Sidewise from Rectangular Slit; Air Velocity, 50 ft./sec.

		Slit configuration			
R_v	R_m	→ ▭	→ ▯	→ □	→ ○
1:50	16	*B*	*B*	*B*	—
	8	—	—	—	*C*
	6	*B*	*B*	—	—
	4	*C*	*B*	*C*	*C/D*
	2	*D*	*D*	*D*	*D*
1:25	16	*A*	—	—	—
	11	—	*A/B*	—	—
	8	*B*	—	*C*	*C/D*
	4	*C/D*	*C/D*	*C/D*	*D*
	2	*D*	*D*	*C/D*	*D*
1:12.5	16	—	—	*B*	—
	11	*B*	*B*	—	—
	8	—	—	*C*	*C/D*
	6	*C*	*D*	—	
	4	—	—	—	*D*
	3	*C*	*C/D*	*C*	—
	2	—	—	—	*D*
1:6.25	16	—	—	—	—
	12	*C*	*C*	*B/C*	—
	8	—	—	—	*D*
	6	*C/D*	*D*	*C/D*	—
	4	—	—	—	*D*
	2	—	—	—	*D*

SUMMARY

By means of shadowgraph and probe sampling techniques, a description has been given of the manner in which a gas flowing in a square duct mixes with a secondary gas introduced sidewise. Mixing is described in terms of the mixing parameters—penetration distance P, bulk mixing distance B, macromixing distance M, and the quality of micromixing. These parameters may be expressed as functions of duct diameter D, mass velocity ratio R_m, and volume flow ratio R_v (sidestream : mainstream) of the two gases.

Experimental penetration-distance data are correlated by $P/D = K_p/R_m^2 R_v$, independently of gas density ratio. The constant K_p increases with duct size for ducts greater than 2-in. square and decreases slightly with increasing duct velocity. A rectangular side tube with the short side perpendicular to the main gas stream or a square side tube gives the shortest penetration distance, followed by the cylindrical side tube, the rectangular side tube with the long side perpendicular to the main stream, and the slit extending from side wall to side wall of the main duct, in increasing order of penetration distance.

B/D cannot be correlated by any simple mathematical relation, although generally it decreases with an increase in R_m and R_v independently of duct size and duct velocity. For $R_m < 6$, the cylindrical-tube jet produces longer bulk mixing distances than the rectangular- or square-tube jets. Above an R_m of 6 the distances required for all jets are about the same.

Experimental macromixing-distance data for the 1- and 2-in. square ducts for $R_m \leq 8$ over the range of R_v 1 : 50 to 1 : 6.25 can be correlated by $M/D = K_m/(R_m R_v)^{1/2}$ independently of gas-density ratio. A limitation of $R_v \leq 1 : 25$ at $R_m \leq 8$ must be applied for rectangular or square side tubes. K_m is independent of duct velocity and size in this range. For the 3-in. square duct the macromixing data for $R_m \leq 8$ *or* $R_v \leq 1 : 25$ are correlated by $M/D = K_m/R_m^{0.7} R_v^{0.2}$ where K_m is independent of duct velocity. The effect of gas-density ratio was not established at this scale.

Above the limiting values of R_m and R_v mentioned, M/D no longer decreases with an increase in R_m and R_v and the data cannot be correlated by the given equations. At sufficiently high values of R_m and R_v, M/D increases with an increase in R_m and R_v.

The shortest macromixing distances are obtained with two opposed cylindrical

Table 4. Sampling Study, Mixing of Air Flowing in 3-inch Square Duct with Carbon Dioxide Entering Sidewise from a Tube

$R_v = 1:25$
$V_D = 25$ ft./sec.

		Macromixing						Micromixing						
R_m	M/D	Average R_s							Average R_s					
		Top	Middle	Bottom	Left	Center	Right	Quality	Top	Middle	Bottom	Left	Center	Right
2.2	6.7	0.45	1.20	1.30	0.80	1.30	0.90	*D*	0.45	1.20	1.30	0.85	1.30	0.90
9.0	3.1	0.90	1.15	0.59	1.20	0.40	1.10	*C*	0.85	1.00	1.05	1.00	1.00	0.95
17.5	1.8	0.85	0.65	1.05	1.05	0.42	1.10	*C*	0.95	1.30	1.20	1.00	1.00	1.10

side tubes, followed in increasing order of required distance by a single cylindrical side tube, the square side tube, the rectangular side tube with the short side perpendicular to the main stream, and the rectangular side tube with the long side perpendicular to the mainstream. Macromixing with a slit extending from side wall to side wall is poorer than with the other side tubes.

The quality of micromixing improves with an increase in R_m, duct size, and duct velocity and with a decrease in R_v. It is observed that velocity ratio rather than mass-flow ratio is the decisive parameter for micromixing. A rectangular side tube with its short side perpendicular to the mainstream consistently gives good mixing. The cylindrical tube produces the worst quality of micromixing. Mixing with a cylindrical tube may be improved by using opposed sidestream jets. A slit is also superior to a single cylindrical tube.

In general, the sampling studies confirm the picture of mixing obtained with the shadowgraph technique.

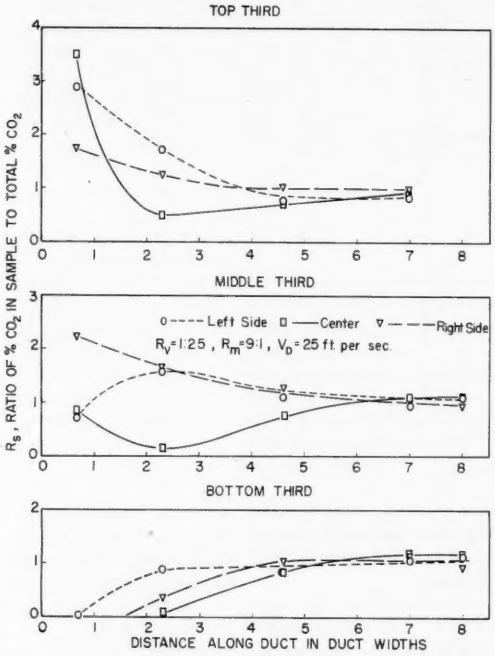
TOP THIRD
MIDDLE THIRD
BOTTOM THIRD
o----- Left Side □—— Center ▽— — — Right Side
R_V=1:25 , R_m=9:1 , V_D=25 ft. per sec.
R_s, RATIO OF % CO_2 IN SAMPLE TO TOTAL % CO_2
DISTANCE ALONG DUCT IN DUCT WIDTHS

Fig. 13. Ratio of percentage of carbon dioxide in sample to total percentage of carbon dioxide vs. distance along duct, 3-in. square duct, cylindrical side tube.

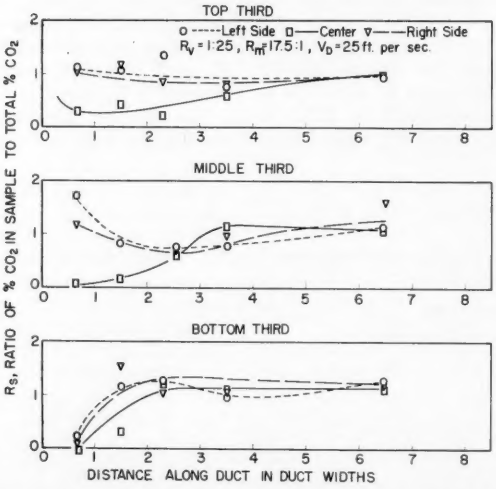
TOP THIRD
o -----Left Side □—— Center ▽——Right Side
R_V=1:25 , R_m=17.5:1 , V_D=25 ft. per sec.
MIDDLE THIRD
BOTTOM THIRD
R_s, RATIO OF % CO_2 IN SAMPLE TO TOTAL % CO_2
DISTANCE ALONG DUCT IN DUCT WIDTHS

Fig. 14. Ratio of percentage of carbon dioxide in sample to total percentage of carbon dioxide vs. distance along duct, 3-in. square duct; cylindrical side tube.

ACKNOWLEDGMENT

The authors wish to express appreciation to the Pratt and Whitney Aircraft Corporation for providing the funds for this research.

NOTATION

B = bulk mixing distance
d = diameter of side duct
D = diameter of main duct
K_b = constant in bulk-mixing-distance correlation
K_m = constant in macromixing-distance correlation
K_p = constant in penetration-distance correlation
M = macromixing distance
P = penetration distance
R_m = mass velocity ratio, sidestream : main stream
R_s = ratio of concentration of CO_2 in sample to total concentration of CO_2 flowing in duct
R_v = volume flow ratio, sidestream : main stream
S = distance downstream of jet entrance
u = sidestream-jet-port velocity
V_D = average main-duct velocity
ρ = density

Subscripts

d = sidestream
D = main stream

LITERATURE CITED

1. Callaghan, E. E., and R. S. Ruggeri, *Natl. Advisory Comm. Aeronaut. Tech. Note* 1615 (June 1948).
2. Callaghan, E. E., and D. T. Bowden, *ibid.*, 1947 (Sept. 1949).
3. Callaghan, E. E., and R. S. Ruggeri, *ibid.*, 2466 (1951).
4. Chilton, T. H., and R. P. Genereaux, *Trans. Am. Inst. Chem. Engrs.*, **25**, 102 (1930).
5. Cleeves, V., and L. M. K. Boelter, *Chem. Eng. Progr.*, **43**, 123 (1947).
6. Ehrich, F. F., *J. Aeronaut. Sci.*, **20**, 99 (1953).
7. Frazer, J. P., *ibid.*, **21**, 59 (1954).
8. Hawthorne, W. R., G. F. C. Rogers, and B. Y. Zaczek, *Roy. Aircr. Est. Tech. Note Eng.* 271 (March 1944).
9. Kalinske, A. A., and C. L. Pien, *Ind. Eng. Chem.*, **36**, 220 (1944).
10. Kuethe, A. M., *J. Applied Mech.*, **2**, A87 (1935).
11. Prandtl, L., *Z. angew. Math. Mech.*, **5** (2) 136 (1925).
12. Reichardt, H., *ibid.*, **21**, 257 (1941).
13. Ruggeri, R. S., E. E. Callaghan, and D. T. Bowden, *Natl. Advisory Comm. Aeronaut. Tech. Note* 2019 (Feb. 1950).
14. Ruggeri, R. S., *ibid.*, 2855 (Dec. 1952).

Thermal and Material Transfer in Turbulent Gas Streams: Local Transport from Spheres

N. T. HSU and B. H. SAGE

California Institute of Technology, Pasadena, California

Local convective thermal transfer is difficult to predict for nonuniform three-dimensional boundary flows. Direct measurements of local transfer from objects of practical interest are therefore useful in the prediction of thermal transfer and in an understanding of multidimensional boundary flows.

Measurements of the gross and local transfer were made upon a silver sphere 0.5 in. in diameter and a ceramic porous sphere of the same size from which *n*-heptane was permitted to evaporate. The air stream had a level of turbulence of approximately 5.4% and only small variation in velocity with position. Temperature distributions in the boundary flows around these spheres were determined, and from these distributions local transfer coefficients were established for the forward hemisphere. The gross transfers were established from the electrical energy added to the silver sphere and from the quantity of *n*-heptane evaporated from the porous sphere.

The local thermal transfers were in reasonable agreement with some of the theoretical analyses based upon a three-dimensional laminar-boundary layer. Satisfactory agreement was obtained between spatial integration of the local transfer and the simultaneously measured over-all values. These, in turn, were in fair agreement with correlated values of the gross thermal and material transfer from spheres.

The gross thermal transfer from spheres to fluids in fully developed turbulent flow has been well summarized by McAdams (*21*). Measurements for nearly potential flow were reported by Johnstone (*13*), and such transfers have also been studied by Tang (*31*). Significant differences in transfer resulting from the level of turbulence encountered in the air stream appear to exist. However, only limited experimental information has been available concerning the local transfer from spheres. Cary (*3*) reported experimental results for a 5-in. iron sphere in an air stream at Reynolds numbers between 4.4×10^4 to 1.5×10^5; no information as to the level of turbulence was available. Lautman and Droege (*16*) determined the local transfer from a 9-in. copper sphere in air at Reynolds numbers between 1.3×10^5 to 1.0×10^6. Xenakis and coworkers (*34*) repeated the work of Lautman and Droege in approximately the same range of Reynolds numbers, with a 9-in. sphere and with other spheres 6 and 12 in. in diameter. In these investigations a localized portion of the sphere was separately heated to the same temperature as the remainder of the sphere, and the energy transport from the localized portion to the air stream was determined as a function of angular position in the stream.

In the present study the rates of thermal transfer for 0.5-in. spheres with and without material transfer were determined at Reynolds numbers in a range of 1,530 to 4,200. The local thermal transport was established from the radial temperature gradients of the air stream

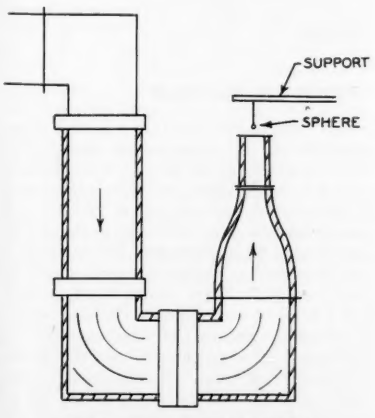

Fig. 1. Arrangement of air jet.

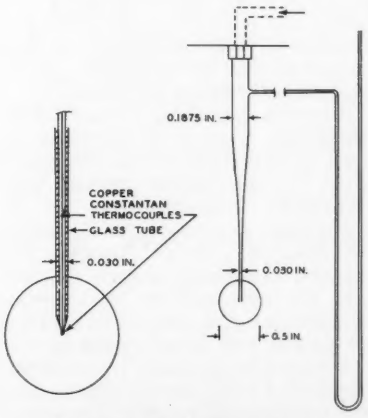

Fig. 2. Details of porous sphere.

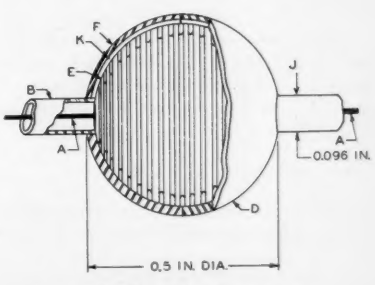

Fig. 3. Details of heated sphere.

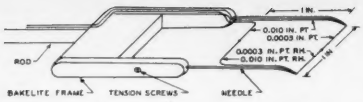

Fig. 4. Traversing thermocouple.

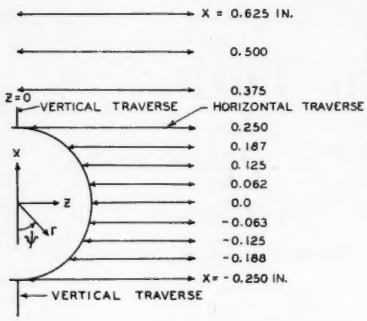

Fig. 5. Location of thermocouple traverses.

immediately adjacent to the sphere. This study constitutes a portion of a more general investigation of the influence of the level and scale of turbulence upon thermal and material transport.

ANALYSIS

The analysis of local thermal transfer for bodies immersed in a flowing stream is based upon a solution of the equation of motion of the boundary flows and the conservation of energy. Such work was carried out by Sibulkin (*29*), who presented an exact solution of thermal transfer at the stagnation point of the sphere for an incompressible fluid of constant intensive properties. The work of Sibulkin is based upon the equation of continuity, as well as upon the conservation of momentum and energy which apply to an incompressible fluid of constant heat capacity:

$$\frac{\partial(\sigma u)}{\partial s} + \frac{\partial(\sigma v)}{\partial n} = 0 \qquad (1)$$

$$u\frac{\partial u}{\partial s} + v\frac{\partial u}{\partial n} = u_1\frac{du_1}{ds} + \nu\frac{\partial^2 u}{\partial n^2} \qquad (2)$$

$$u\frac{\partial t}{\partial s} + v\frac{\partial t}{\partial n} = \mathrm{K}\frac{\partial^2 t}{\partial n_2} \qquad (3)$$

Equation (3) assumes a constant heat capacity for the air stream which permits a simple relationship between enthalpy and temperature. The boundary conditions for this situation are as follows:

$$n = 0 \quad : u = 0\,, \quad v = 0, \quad t = t_i$$

$$n = \infty \; : u = u_1, \quad t = t_\infty$$

The local thermal flux at the surface of the sphere is established from

$$\overset{\circ}{q}_n = -k_i\left(\frac{\partial t}{\partial n}\right)_{n=0} \qquad (4)$$

The velocity distributions in a boundary layer about a sphere were established by Homann (*10*) by assuming a linear velocity profile with respect to distance along the surface of the sphere from stagnation.

Much effort has been directed (*7, 8, 15, 30*) to the application of the Kármán-Pohlhausen integral method (*14*) to include the prediction of the temperature distribution in the boundary layer of a sphere. Under the approximations of this method the following integral equations are obtained for the conservation of momentum and energy:

$$\frac{\partial}{\partial s}\int_0^{\delta M} u^2\,dn - u_1\frac{\partial}{\partial s}\int_0^{\delta M} u\,dn - \frac{1}{z}\frac{\partial z}{\partial s}\left(u_1\int_0^{\delta M} u\,dn - \int_0^{\delta M} u^2\,dn\right) = \delta_M u_1\frac{du_1}{ds} - \nu\left(\frac{\partial u}{\partial n}\right)_{n=0} \qquad (5)$$

$$\frac{\partial}{\partial s}\int_0^{\delta t} u(t - t_\infty)\,dn + \frac{1}{z}\frac{\partial z}{\partial s}\int_0^{\delta t} u(t - t_\infty)\,dn = -\mathrm{K}\left(\frac{\partial t}{\partial n}\right)_{n=0} \qquad (6)$$

In these expressions δ_M is the momentum-boundary-layer thickness and δ_t the thermal-boundary-layer thickness. The approximations of the Kármán-Pohlhausen analysis lead to the relation shown in Equation (7).

$$\frac{u}{u_1} = \phi_1\left(\frac{n}{\delta_M}\right) \qquad (7)$$

From this expression it follows that the temperature of the boundary layer may be related to the temperature of the main stream and of the surface of the sphere in the following way:

$$\frac{t - t_\infty}{t_i - t_\infty} = \Upsilon = \phi_2\left(\frac{n}{\delta_t}\right) \qquad (8)$$

Coefficients of the polynomial functions ϕ_1 and ϕ_2 may be established for the appropriate boundary conditions.

Korobkin (*15*) reported results from his studies in which he computed the local thermal transfer at the stagnation point by the integral method using Tomotika's distribution (*32*) for the temperature and velocity in the boundary layer of a sphere. Korobkin (*15*) included unpublished results of Sibulkin, who also calculated the local thermal transfer associated with the forward half of the sphere by integral methods.

Eckert (*8*) and Drake (*7*) submitted approximate methods for determining the local thermal transfer on a surface of revolution. Eckert's work yielded an exact solution to the energy equation for an incompressible laminar boundary layer over a wedge-shaped body. An approximate expression for the local thermal transport on an axially symmetric body was given by Drake (*7*), who applied the Mangler transformation (*20*) to the solution of this problem.

Table 1. Decay of Longitudinal and Transverse Turbulence Behind Grid Used in Present Study

Distance downstream, in.	Gross velocity, ft./sec. 8 Longitudinal	8 Transverse	16 Longitudinal	16 Transverse
6	0.107*	0.085	0.100	0.082
9	0.075	0.064	0.072	0.062
12	0.059	0.054	0.056	0.050
13†	0.056	0.052	0.052	0.048
15	0.050	0.047	0.047	0.043

*Fluctuation velocity expressed as root-mean-square fraction of gross velocity.
†Downstream distance for present study.

The foregoing analyses are based on the assumption that the radial velocity at the surface of the sphere can be taken as zero. In the case of evaporation from the surface of a sphere there usually exists a small hydrodynamic radial velocity at the surface. The solutions for boundary flows over a flat plate for situations with a velocity normal to the boundary have been obtained by Schlichting and Bussmann (*27*). Mickley and coworkers (*22*) extended these solutions by similarity considerations to the prediction of both thermal and material transfer. Spalding (*30*) established similar relationships for material transfer at the stagnation point of a sphere.

Under the conditions encountered in the present experimental investigations the normal velocity at the surface was not more than 0.005 ft./sec., as compared to a minimum stream velocity of 8 ft./sec. The composition of the gas phase at the surface of the porous sphere was always less than 0.05-mole fraction *n*-heptane. Under these conditions estimates based upon the results of the foregoing simplified analyses were used to establish the effect of material transfer on the temperature gradient.

METHODS AND EQUIPMENT

The present investigation involved measurement of the temperature distribution about a silver sphere and a porous sphere, each 0.5 in. in diameter. The sphere was located in an air stream at 100°F. and measurements were made at gross stream velocities of 8 and 16 ft./sec. The equipment employed to furnish the air supply has been described (*11*). The undisturbed stream had a level of turbulence of 0.013 as established by the methods of Schubauer (*28*). A perforated steel plate was used to create turbulence (*5*) and measurements were made with the sphere at a position 13 in. downstream from the plate. Some of the characteristics of the turbulent flow of the

air stream as taken from the measurements of Davis (*5*) are presented in Table 1. The velocity of the air stream was determined from its temperature and the weight rate of flow, which was established by means of a calibrated Venturi meter and associated equipment.

The porous sphere was prepared from synthetic-ceramic filter material. The general arrangement is shown in Figures 1 and 2. Liquid was introduced to the sphere at a known rate (*24*) through a small glass tube as shown in Figure 2. Copper-constantan thermocouples 0.003 in. in diameter were located at the positions indicated. Figure 3 gives a sectional view of the silver sphere, construction details of which are available (*1*). A small electrical heater was wound within a spiral groove E and was surrounded by the hemispheres F and D. A groove in the shell F, which is shown at K, permitted thermocouples to be mounted on the exterior shell. The thermocouples were brought out through the tubes B and J alongside the supporting wire A. These thermocouples were used for control purposes in the current measurements.

The temperatures in the boundary flows around the sphere were measured with a platinum, platinum-rhodium thermocouple 0.0003 in. in diameter, illustrated in Figure 4. The thermocouple was mounted upon a conventional "bird" with the reference junction in the air stream at a distance about 1 in. from the sphere. Corrections to the indicated temperature were made to account for thermal flux along the thermocouple (*19*). The locations of the traverses made in the boundary flows about the sphere are shown in Figure 5.

MATERIALS

The properties of air and n-heptane employed in this investigation are available (*12*): the properties of air are based in part upon a set of critically chosen values (*23*), and thermal conductivity of n-heptane in the liquid phase was taken from McAdams (*21*). The effect of water and n-heptane upon the thermal conductivity of the air was determined by the methods proposed by Hirschfelder (*9*) and Lindsay and Bromley (*18*), respectively. The enthalpy change upon vaporization and the isobaric heat capacity of liquid n-heptane were taken from the data of Rossini (*25*) and Douglas and coworkers (*6*), respectively. In the calculations associated with this study it was not nesessary to consider the equation of state of the fluids in detail and, aside from minor corrections for the behavior of n-heptane, it was assumed that perfect gas laws applied, that local equilibrium obtained on the surface of the porous sphere, and that mixtures of n-heptane and air followed the laws of ideal solution (*17*).

The n-heptane was obtained as research grade from Phillips Petroleum Company and was subjected to a single fractionation in a column containing sixteen glass plates. The center 90% fraction of the overhead was retained for use.

EXPERIMENTAL RESULTS

The detailed experimental conditions which obtained in the course of the four sets of measurements are recorded in Table 2. Only two bulk velocities, of approximately 8 and 16 ft./sec., were investigated. The longitudinal turbulence level (*5*) was approximately 5.6% at the lower velocity and 5.2% at the higher velocity. The Reynolds number based upon the gross velocity and the kinematic viscosity of the fluid at the interface varied between 1,530 and 4,200.

A sample of the temperature measurements involving two different traverses is shown in Table 3. The radial distance

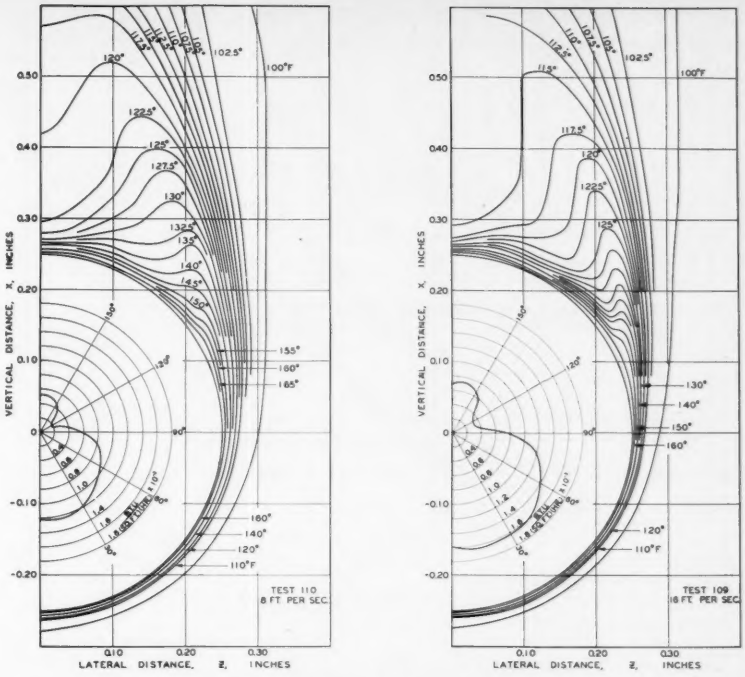

Fig. 6. Temperature distribution and local thermal flux around silver sphere.

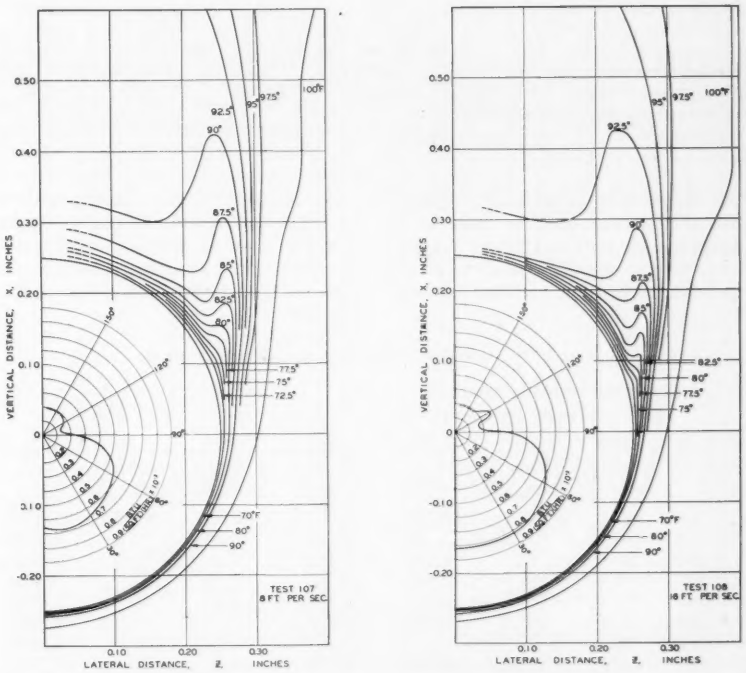

Fig. 7. Temperature distribution and local thermal flux around porous sphere.

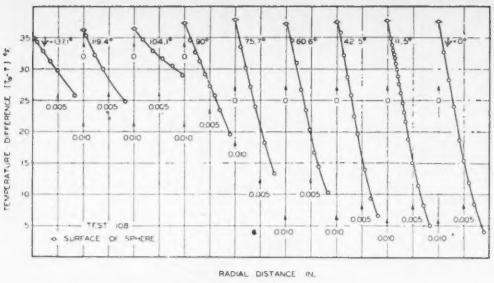

Fig. 8. Radial temperature distribution for test 108.

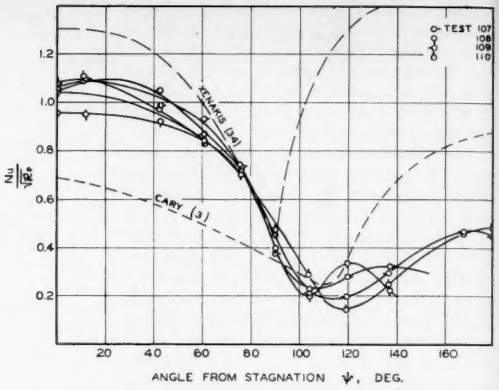

Fig. 9. Local experimental thermal transfer.

TABLE 2. EXPERIMENTAL CONDITIONS

Test number	107	108	109	110
Sphere				
Type	Porous	Porous	Silver	Silver
Diameter, in.	0.500	0.500	0.500	0.500
Total heptane evaporation rate $\times 10^6$, lb./sec.	3.878	5.515		
Total energy input $\times 10^3$, B.t.u./sec.			1.533	1.094
Average surface temperature, °F.	63.2	63.4	169.7	170.2
Temperature of liquid heptane entering sphere, °F.	96.9	97.9		
Air stream				
Bulk velocity, ft./sec.	8.04	16.23	16.13	8.06
Bulk temperature, °F.	100.1	100.1	100.1	100.1
Pressure, lb./sq. ft.	2,066.3	2,060.4	2,069.1	2,055.9
Weight fraction water	0.0065	0.0061	0.0030	0.0042
Turbulence level, %	5.6	5.2	5.2	5.6
Reynolds number, conditions at interface	2,100	4,200	3,060	1,530

from the center of the sphere as calculated from the traverse-position data is included, and the wire and the air temperatures are indicated. The details of all the experimental measurements are available (*12*). Results of the experimental investigations are summarized in Figures 6 and 7, which present the temperature distribution and local thermal flux around the silver and porous spheres for velocities of 8 and 16 ft./sec. The distribution of thermal flux at the surface of the sphere was evaluated by application of Equation (4) and is presented in polar coordinates in parts of Figures 6 and 7. An example of the radial temperature distribution for which the data of test 108 was utilized is shown in Figure 8. The radial temperature distribution shown was determined by appropriate graphical manipulations of the data of Figure 7.

TABLE 3. SAMPLE OF TEMPERATURE MEASUREMENTS

Vertical traverse below sphere at $z = 0$ in. ($\psi = 0$ deg.)				Horizontal traverse at $x = -0.188$ in. ($\psi = 42.5$ deg.)			
Position x, in.	Wire temperature, °F.	Air temperature, °F.	Radius r, in.	Position z, in.	Wire temperature, °F.	Air temperature, °F.	Radius r, in.
−0.274	100.1	100.1	0.274	0.201	100.1	100.1	0.2752
−0.271	99.8	99.8	0.271	0.191	99.2	99.2	0.2680
−0.269	99.5	99.5	0.269	0.186	97.5	97.5	0.2645
−0.267	98.9	98.9	0.267	0.183	95.5	95.3	0.2624
−0.265	98.4	98.4	0.265	0,181	94.0	93.7	0.2610
−0.263	97.8	97.8	0.263	0.179	91.7	91.4	0.2596
−0.261	95.2	95.2	0.261	0.177	88.8	88.4	0.2582
−0.260	94.0	94.0	0.260	0.175	85.6	85.1	0.2568
−0.259	92.3	92.3	0.259	0.173	81.8	81.3	0.2555
−0.258	90.5	90.3	0.258	0.171	77.3	76.6	0.2541
−0.257	88.5	87.8	0.257	0.169	72.6	71.6	0.2528
−0.256	86.2	85.3	0.256	0.168	70.5	69.6	0.2521
−0.255	83.5	82.5	0.255	0.167	68.4	67.5	0.2515
−0.254	80.6	79.6	0.254	0.166	66.9	65.8	0.2508
−0.253	77.6	76.7	0.253	0.165*	63.0	61.5	0.2500
−0.252	74.4	73.3	0.252				
−0.251	70.5	69.1	0.251				
−0.250*	63.6	61.6	0.250				

*Indicates surface point.

The results for the local thermal transport at the surfaces of the spheres are available in tabular form (*12*). These data for local thermal transport at the surface of the spheres, as well as the average values of the data of Cary (*3*) and of Xenakis and coworkers (*34*), are presented in Figure 9. The standard deviation of the experimental points from the smooth curve is 0.0080 when it is assumed that all the error is in the Nusselt number. Cary's data covered the range of Reynolds numbers from 4.4×10^4 to 1.5×10^5, whereas the data of Xenakis were obtained at Reynolds numbers between 8.7×10^4 and 1.8×10^5. It is not clear what states were employed by Cary for evaluation of thermal conductivity and kinematic viscosity of the air stream. Xenakis used the temperature of the free stream for evaluation of these quantities. Korobkin (*15*) pointed out that Cary's data (*3*) may be low because of internal thermal exchange between the calorimeter and the remainder of the sphere. It is possible that the data of Xenakis were influenced by the position of the guy wires used in steadying the sphere in the wind tunnel.

Figure 10 which shows the average of the present experimental results in comparison with several theoretical investigations involving the work of Sibulkin (*29*), Eckert (*8*), Drake (*7*), and Korobkin (*15*), is limited to the forward hemisphere, for which several solutions of the boundary flow have been obtained. The present data are in fair agreement with the work of Eckert (*8*) and of Drake (*7*) and with the exact solution of Sibulkin (*29*) at stagnation. Current data yield

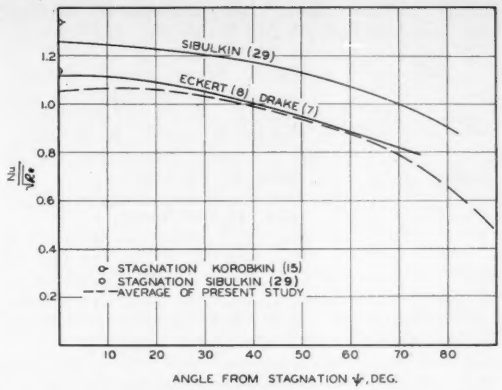

Fig. 10. Comparison of experimental and predicted local thermal transfer.

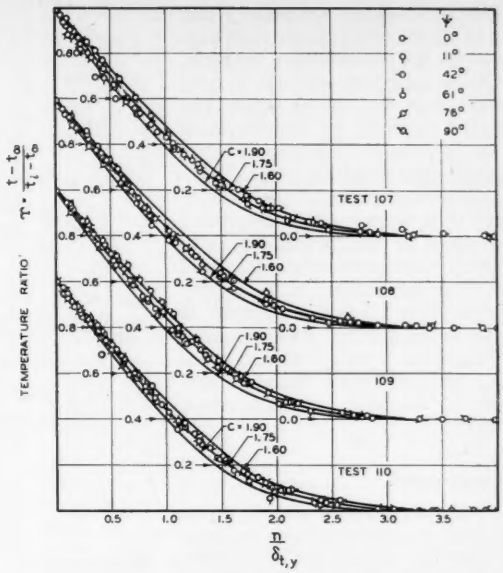

Fig. 11. Temperature distribution in boundary flow.

smaller values of local thermal transfer for conditions in the wake than were obtained from the experimental measurements of Xenakis (*34*) and Cary (*3*). The data of Cary (*3*) are closer to the current measurements than those of Xenakis (*34*). A larger uncertainty exists in the local thermal transfer in the wake as established from the current measurements than in the forward hemisphere.

Temperature distributions in the thermal boundary layer for the four investigations are recorded in Figure 11. The relationships between momentum and thermal boundary layers were established by assuming that the temperature ratio may be evaluated from

$$\Upsilon = 1 - f'\left(\frac{n}{\delta_{t,v}}\right) \qquad (9)$$

The displacement thickness of the thermal boundary layer was established from

$$\delta_{t,v} = \int_0^\infty \Upsilon \, dn \qquad (10)$$

The following empirical expression, which is based on the Blasius (*2*) function for a two-dimensional boundary flow, is included for comparison:

$$\Upsilon = 1 - f'\left(\frac{\eta}{c}\right) \qquad (11)$$

The behavior for varying values of the coefficient C is shown in Figure 11. The function f' was developed by Blasius (*2*), and numerical values are available (*4*). It is apparent that most of the current data satisfy Equation (11) for values of coefficient C varying between 1.60 and 1.90, with a probable value of C of 1.75. The assumptions underlying the derivation of Equation (11) are such as to make the detailed applicability of such a simple treatment uncertain.

Figure 11 illustrates the relatively narrow range of temperature distribution encountered for all positions and conditions of flow and transport. A detailed and exact analysis of the local thermal transfer to spheres awaits a satisfactory analysis of the three-dimensional boundary flow associated with the motion of a gas of varying properties around a spherical surface. No effect of the level of turbulence has been considered in available analyses.

The arrangement of the supports for the silver sphere made undesirable the integration of the local thermal transport for comparison with the gross transport established from the measured electrical power. As yet unpublished experimental data gathered from tests made with a larger silver sphere supported by a single tube in the aft hemisphere led the authors to believe that uncertainties of the order of 1% may be involved. The presence of the tubes at the equator results in an increase in the gross thermal transport (*26*). In the case of the porous sphere, calculations of the total thermal transport appeared worth while. The total interfacial thermal flux determined from the local temperature gradients was established from

$$\mathring{Q} = -\oint_0^A k_i \left(\frac{\partial t}{\partial n}\right)_{n=0} dA \qquad (12)$$

In Equation (12) the scalar total thermal flux is considered positive when energy is transmitted in the direction of increasing coordinate n. The total interfacial thermal flux determined from an over-all energy balance may be established from the following equation:

$$\mathring{Q} = -\mathring{m}[L + C_{P,i}(t_g - t_i)] + (k_h A_h + k_t A_t + k_w A_w) \cdot \left(\frac{\partial t}{\partial x}\right)_{n=0} - \mathring{Q}_r \qquad (13)$$

In Equation (13) the vectorial nature of the transport was taken into account when signs were determined. The radiation correction in Equation (13) is given by

$$\mathring{Q}_r = A\beta(T_i^4 - T_{sr}^4) \frac{1}{\frac{1}{\epsilon_{sr}} + \frac{1}{\epsilon_{sp}} - 1} \qquad (14)$$

It was found, as shown in Table 4, that with an emissivity for wetted silica (*21*) of 0.8, reasonable agreement was obtained between the gross thermal transports from the porous sphere as established from Equations (12) and (13), respectively.

The gross thermal transport associated with the porous and silver spheres is presented in Figure 12 as a function of Reynolds number. The results of McAdams (*21*), based primarily upon data

Table 4. Comparison of Measured and Integrated Total Convective Transfer for Porous Sphere

Test	Enthalpy change	Thermal flux: Corrections, Conduction	Corrections, Radiation	Evaporation*	Temperature† gradient	Difference, %
107	0.544‡	−0.003	−0.033	0.508	0.519	−2.2
108	0.772	−0.003	−0.036	0.733	0.680	6.4

*Established from evaporation rate with Equation (10).
†Established from local temperature gradient at surface with Equation (9).
‡Values expressed in B.t.u./sec. × 10^{-3}; for example, first entry is 0.000544 B.t.u./sec.

of Williams (*33*), yield somewhat higher values of the thermal transfer than were obtained for the porous sphere; however, the data of Johnstone (*13*) are in good agreement with the current study. The information reported for low Reynolds numbers by Tang (*31*) is markedly below the present measurements.

The agreement between the data of other investigators and the present measurements as presented in Figure 12 is deemed satisfactory when the level of turbulence encountered in the present measurements is taken into account. It has been found that the level of turbulence introduces a rather marked influence on the convective transport particularly at Reynolds numbers above 4,000 (*26*).

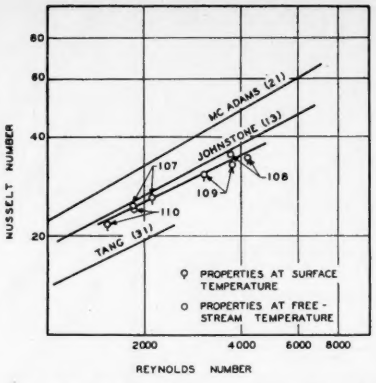

Fig. 12. Comparison of gross thermal transfer to spheres from several investigators.

ACKNOWLEDGMENT

The Fluor Corporation contributed to the support of the experimental program. N. T. Hsu was a Peter E. Fluor Fellow during the period in which these experimental data were obtained Kazuhiko Sato assisted with the experimental measurements, Betty Kendall and Virginia Berry contributed markedly to the reduction of the experimental data, and June Gray prepared the figures. W. N. Lacey reviewed the manuscript.

NOTATION

A = area, sq. ft.
C = constant
C_P = isobaric heat capacity, B.t.u./(lb.)(°F.)
D = diameter, ft.
d = differential operator
f' = Blasius function
h = thermal transfer coefficient, B.t.u./(sq. ft.)(sec.)(°F.)
k = thermal conductivity, B.t.u./(sq. ft.)(sec.)(°F./ft.)
L = latent heat of vaporization, B.t.u./lb.
$\mathring{m}$ = total weight rate of transport from surface, lb./sec.
n = radial or normal distance from surface, in. or ft.
Nu = Nusselt number, hD/k_i
$\mathring{Q}$ = gross rate of convective thermal transfer from surface, B.t.u./sec.
$\mathring{Q}_r$ = gross rate of radiant transfer from surface, B.t.u./sec.
$\mathring{q}_n$ = local thermal flux in direction n, B.t.u./(sq. ft.)(sec.)
r = radial distance from center of sphere, in. or ft.
Re = Reynolds number, DU/ν_i
s = distance parallel to surface in direction of main flow, ft.
T = thermodynamic temperature, °R.
t = temperature, °F.
U = bulk or free stream velocity, ft./sec.
u = local velocity along s, ft./sec.
u_1 = local velocity at the edge of momentum boundary layer, ft./sec.
v = local velocity along n, ft./sec.
x, z = coordinate axes with origin at center of sphere, in. or ft.

Greek Letters

β = Stefan-Boltzmann constant, 0.1713 $\times 10^{-8}$ B.t.u./(sq. ft.)(hr.)(°R.^{4})
δ_M = momentum-boundary-layer thickness, ft.
δ_t = thermal-boundary-layer thickness, ft.
$\delta_{t,v}$ = displacement thickness of thermal boundary layer, ft.
ϵ = emissivity
η = Blasius parameter
K = thermometric conductivity, sq. ft./sec.
ν = kinematic viscosity, sq. ft./sec.
σ = specific weight, lb./cu. ft.
Υ = nondimensional temperature ratio, $(t - t_\infty)/(t_i - t_\infty)$
ϕ = function of
ψ = polar angle measured from the stagnation point, deg.
∂ = partial differential operator

Subscripts

g = gas phase
h = liquid n-heptane
l = liquid phase
i = interface
t = tube
sp = sphere
sr = surroundings
w = thermocouple wire
∞ = free stream condition

LITERATURE CITED

1. Baer, D. H., W. G. Schlinger, V. J. Berry, and B. H. Sage, *J. Appl. Mechanics*. **20**, 407 (1953).
2. Blasius, Heinrich, *Z. angew. Math. u. Phys.*, **56**, 1 (1908).
3. Cary, J. R., *Trans. Am. Soc. Mech. Engrs.*, **75**, 483 (1953).
4. Corcoran, W. H., J. B. Opfell, and B. H. Sage, "Momentum Transfer in Fluids," Academic Press, Inc., New York (1956).
5. Davis, Leo, *Rept.* 3-17, Jet Propulsion Laboratory, Calif. Inst. Technol. (1952).
6. Douglas, T. B., G. T. Furukawa, R. E. McCoskey, and A. F. Ball, *J. Research Nat'l. Bur. Standards*, **53**, 139 (1954).
7. Drake, R. M., Jr., *J. Aeronaut. Sci.*, **20**, 309 (1953).
8. Eckert, Ernst, *Forsch. Gebiete Ingenieurew., Forschungsheft* No. 416, p. 1 (1942).
9. Hirschfelder, J. O., R. B. Bird, and E. L. Spotz, *Trans. Am. Soc. Mech. Engrs.*, **71**, 921 (1949).
10. Homann, Fritz, *Z. angew. Math. u. Mech.*, **16**, 153 (1936).
11. Hsu, N. T., Kazuhiko Sato, and B. H. Sage, *Ind. Eng. Chem.*, **46**, 870 (1954).
12. Hsu, N. T., and B. H. Sage, Document 5311. Am. Doc. Inst., Washington 25, D. C.; $5.00 for photoprints or $2.25 for 35-mm. microfilm.
13. Johnstone, H. F., R. L. Pigford, and J. H. Chapin, *Trans. Am. Inst. Chem. Engrs.*, **37**, 95 (1941).
14. Kármán, Th. von, *Z. angew. Math. u. Mech.*, **1**, 244 (1921).
15. Korobkin, Irving, *Am. Soc. Mech. Engrs.*, Paper 54-F-18, Am. Soc. Mech. Engrs. Milwaukee Meeting (September 1954).
    Milwaukee Meeting, (September 1954).
16. Lautman, L. G., and W. C. Droege, Serial No. AIRL A6118, Air Materiel Command, 50-15-3 (August, 1950).
17. Lewis, G. N., *J. Am. Chem. Soc.*, **30**, 668 (1908).
18. Lindsay, A. L., and L. A. Bromley, *Ind. Eng. Chem.*, **42**, 1508 (1950).
19. Longwell, P. A., W. W. Short, and B. H. Sage, submitted to *J. Appl. Phys.*
20. Mangler, W., *Z. angew. Math. u. Mech.*, **28**, 97 (1948).
21. McAdams, W. H., "Heat Transmission," McGraw-Hill Book Company, Inc., New York (1954).
22. Mickley, H. S., R. C. Ross, A. L. Squyers, and W. E. Stewart, *Natl. Advisory Comm. Aeronaut., Tech. Note* 3208 (July 1954).
23. Page, Franklin, Jr., W. H. Corcoran, W. G. Schlinger, and B. H. Sage, Doc. 3293, Am. Doc. Inst., Washington, D. C. (1951).
24. Reamer, H. H., and B. H. Sage, *Rev. Sci. Instr.*, **24**, 362 (1953).
25. Rossini, F. D., et al., "Selected Values of Physical and Thermodynamic Properties of Hydrocarbons and Related Compounds," Carnegie Press, Pittsburgh (1953).
26. Sato, Kazuhito, and B. H. Sage, *Trans. Am. Soc. Mech. Engrs.* (to be published).
27. Schlichting, Hermann, and K. Bussmann, *Schriften. deut. Akad. Luftfahrtforsch.*, **7B**, Heft 2 (1943).
28. Schubauer, G. B., *Natl. Advisory Comm. Aeronaut. Tech. Rept.* 524 (1935).
29. Sibulkin, Merwin, *J. Aeronaut. Sci.*, **19**, 570 (1952).
30. Spalding, D. B., *Proc. Roy. Soc. (London)*, **A221**, 78 (1954).
31. Tang, Y. S., J. M. Duncan, and H. E. Schweyer, *Natl. Advisory Comm. Aeronaut., Tech. Note* 2867 (March, 1953).
32. Tomotika, S., *Aeronaut. Research Comm. Reports* and *Mem.* 1678 (July 1935) (England).
33. Williams, G. C., Sc.D. thesis, Massachusetts Inst. Technol., Cambridge (1942).
34. Xenakis, G., A. E. Amerman, and R. W. Michelson, *WADC Tech. Rept.* 53-117, Wright Air Development Center, Dayton, Ohio (April, 1953).

Effects of Bubbling and Stirring on Mass Transfer Coefficients in Liquids

D. L. JOHNSON, HIROTARO SAITO, J. D. POLEJES and O. A. HOUGEN

University of Wisconsin, Madison, Wisconsin

In the hydrogenation of α-methylstyrene by means of a suspended palladium-alumina catalyst in a stirred reactor the mass transfer of hydrogen through the liquid is the rate-controlling step and the resistance to chemical reaction at the catalyst surface is negligible except at extremely rapid rates of stirring. This system therefore provides an excellent means of establishing the effects of operating variables and mechanical construction on mass transfer coefficients in liquids in stirred reactors. It is convenient to consider the total resistance to mass transfer as consisting of two separate resistances: in the liquid adjoining the bubbles and in the liquid adjoining the suspended solid particles; thus $R = R_b + R_s$.

A general equation was evaluated from experimental data based upon unit volume of liquid.

This investigation was undertaken to measure and correlate experimental data on mass transfer coefficients from gas bubbles to suspended catalyst solids in a liquid subject to stirring and bubbling. The results are given in dimensionless terms to make them applicable to other systems. In the system chosen, namely the hydrogenation of α-methylstyrene catlyzed by suspended palladium-alumia in powder form, the transfer of hydrogen from the surface of the bubble to the surface of the catalyst was found to be the rate-controlling step. The chemical reaction at the surface of the catalyst imposed little resistance over the range of experimentation, and the uncatalyzed reaction did not occur. Since the gas phase consisted of pure hydrogen the bubble itself offered no resistance to mass transfer. These results are in remarkable contrast to the behavior of the same reaction in a trickling-bed reactor wherein the resistance to mass transfer was found to be negligible and the reaction at the surface of the catalyst was the rate-controlling step, as reported by Babcock, Mejdell, and Hougen (*1*).

PREVIOUS WORK

Milligan and Reid (*10*) investigated the hydrogenation of cottonseed oil in a stirred reactor in contact with bubbles of hydrogen and a suspended nickel catalyst. They found that reaction rates were nearly proportional to the rate of stirring, an indication that mass transfer was rate controlling. No rate equations were given. Maxted (*9*) gave a summary of rates of hydrogenation of organic liquids with similar observations. No other investigations dealing with the specific problem of mass transfer from gas bubbles to suspended solids in stirred vessels were found; however a few related investigations are summarized here.

Hixson and Gaden (*8*) gave the following equations for over-all mass transfer coefficients of oxygen from air bubbles into sulfite solutions. The reaction took place in the liquid phase with no solid catalyst present.

1. Single bubble sparger with no mechanical agitation

$$K_G a V_s^{0.82} \qquad (1)$$

2. Single bubble sparger with mechanical agitation using a vaned-disk impeller rotating at 300 to 430 rev./min.

$$K_G a V_s^{0.68} \qquad (2)$$

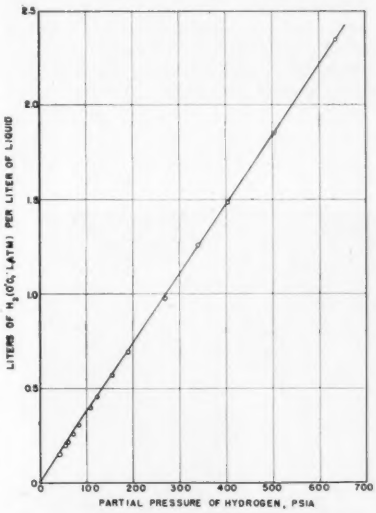

Fig. 1. ↑Solubility of hydrogen in α-methylstyrene at 80°F.

3. Sintered stainless steel sparger with no mechanical agitation with openings of 65μ in the sintered sparger.

$$K_G a V_s^{0.33} \qquad (3)$$

Cooper, Fernstrom, and Miller (*2*), measured rates of oxygen transfer from air into aqueous solutions of sodium sulfite in a reactor stirred with a flat-blade impeller using a single open-end sparger. Their data were correlated with the following equation. No solid catalyst was involved.

$$K_G a V_s^{0.67} \qquad (4)$$

These experiments covered a tenfold variation in linear gas flow rates ranging from 20 to 360 ft./hr.

Hixson and Baum (*5, 6, 7*) reviewed the work of several investigators on reaction rates between solids and liquids in stirred reactors. No gas phase was involved. In general these rates could be expressed in terms of stirring speed N as

$$r \alpha N^{\beta} \qquad (5)$$

In systems where the reaction rate is controlled by mass transfer β is nearly unity; where the surface reaction is rate controlling β is zero.

From dimensional analysis Rushton (*11*) developed the following general mass transfer equation for a liquid in a stirred reactor:

$$\left(\frac{kD}{\mathbf{D}}\right) = a\left(\frac{D^2 N \rho}{\mu}\right)^x \left(\frac{\mu}{\rho \mathbf{D}}\right)^y \qquad (6)$$

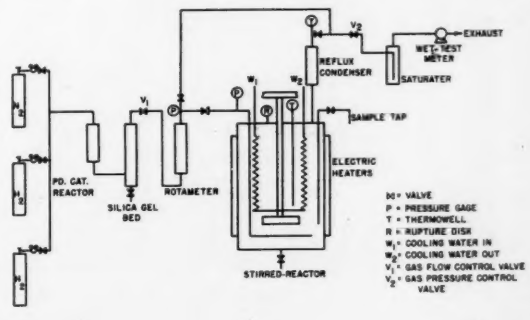

Fig. 2.→Flow diagram.

D. L. Johnson is with Courtaulds (Alabama) Inc., Mobile, Alabama, and H. Saito with Nagoya University, Nagoya, Japan.

No experimental data were supplied to support this equation and no values were given for the constants. This case does not cover reactions with gas bubbles.

THEORY

The theory of reaction rates in gas-liquid reactions catalyzed by suspended solids in stirred reactors is discussed herein with specific reference to the hydrogenation of α-methylstyrene in the presence of a suspended palladium-alumina catalyst with bubbling of the hydrogen through the liquid. Reaction rates and mass transfer rates are based upon unit volume of bubble-free liquid. Tbe volume of bubbles entrained per unit volume of liquid is designated as hydrogen holdup H and is dependent upon the speed of rotation and the rate of hydrogen flow through the liquid.

The rate of reaction is controlled by three resistances in series, namely, the resistances to transfer of hydrogen through the liquid film surrounding the bubble and through the liquid film surrounding the solid particles and the resistance offered to the chemical reaction itself taking place at the surface of the catalyst. In this case the reaction takes place at the surface of a 300-mesh powdered palladium catalyst with no uncatalyzed reaction occurring.

With this particular catalyst the resistance offered by the surface reaction is negligible over the range of experimental conditions used for evaluating mass transfer coefficients.

The rate of mass transfer of dissolved hydrogen through the liquid may be expressed as

$$r = k_0'(c_b' - c_s') \qquad (7)$$

Where mass transfer is controlling and the resistance to the surface reaction is negligible, c_s' is negligible and Equation (7) becomes

$$r = k_0'c_b' \qquad (8)$$

The concentration of hydrogen dissolved in α-methylstyrene was found experimentally to be directly proportional to pressure and over the temperature range of experimentation (77° to 95°F.) inversely proportional to temperature; hence

$$c_b' = \frac{\alpha p}{T} \qquad (9)$$

In this case p is equal to the total pressure since the vapor pressure of the liquid is negligible.

The concentration of hydrogen in the gas phase can be expressed by ideal gas laws at the temperatures and pressures used in this experiment.

$$c_b = \frac{p}{RT} \qquad (10)$$

where p = atmospheres of pressure

R = gas-law constant, 0.08205 (liter)(atm.)(g.-mole)(°K.)

Combining (9) and (10) gives

$$c_b' = \alpha R c_b \qquad (11)$$

Combining (8) and (11) gives

$$r = k_0 c_b \qquad (12)$$

where $k_0 = \alpha R k_0'$

In terms of resistance

$$r = \frac{c_b}{R_o} \qquad (12a)$$

where $R_0 = R_b + R_s$

R_b, R_s, R_0 = resistances of liquid surrounding the bubble and surrounding the catalyst and over-all resistance, all per liter of liquid.

Resistance of Liquid Surrounding the Bubbles

The resistance of the liquid surrounding the bubbles is inversely proportional to the bubble area A_b per unit volume of liquid and to the mass transfer coefficient k_b''; thus

$$R_b = \frac{1}{A_b k_b''} \qquad (13)$$

This resistance may also be expressed in terms of the hydrogen holdup H. For a bubble of diameter D_b

$$\text{Volume} = \pi D_b^3/6 \qquad (14)$$

$$\text{Area} = \pi D_b^2 \qquad (15)$$

Hence, the number of bubbles per liter of liquid is

$$6H/\pi D_b^3 \qquad (16)$$

and the total bubble area per liter of liquid is

$$6H/D_b \qquad (17)$$

Combining Equations (17) and (13) gives

$$R_b = \frac{D_b}{6Hk_b''} \qquad (18)$$

The diameter D_b of a bubble is dependent upon the diameter of hole in the sparger from which the bubble emerges but also upon the rate of stirring, decreasing with increase in stirring rate. These facts were established experimentally by observations in glass vessels.

The holdup H is dependent upon the rates of gas flow and of stirring. The mass transfer coefficient k_b'' is dependent upon the rate of stirring. These combined effects can be expressed by dimensional analysis in terms of the Schmidt number

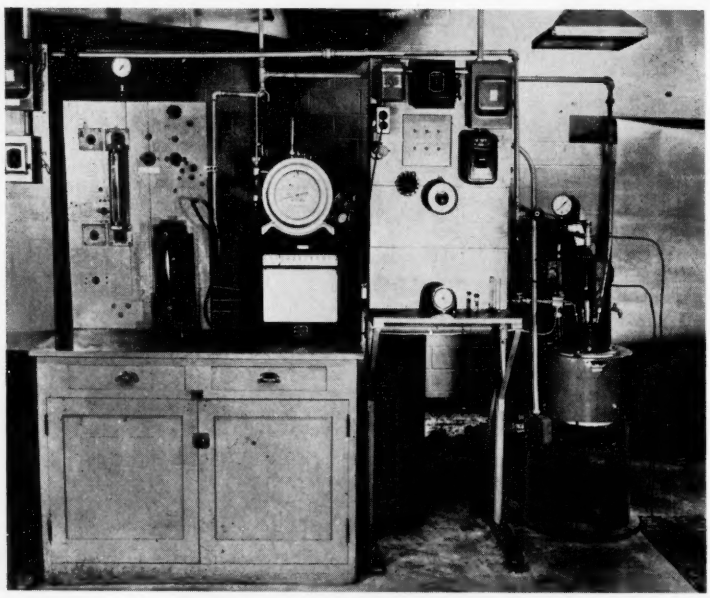

Fig. 3. Experimental assembly.

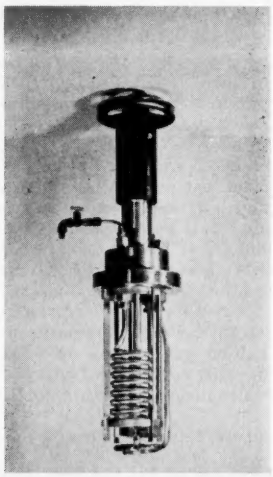

Fig. 4. Stirrer, baffle, and heat exchanger.

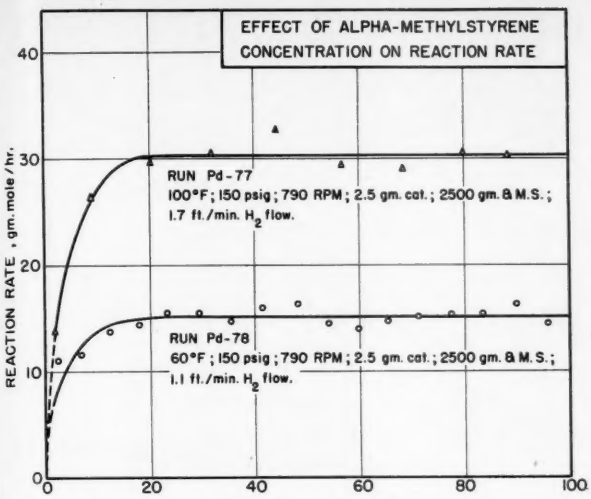
EFFECT OF ALPHA-METHYLSTYRENE CONCENTRATION ON REACTION RATE
REACTION RATE, gm. mole/hr.
RUN Pd-77
100°F; 150 psig; 790 RPM; 2.5 gm. cat.; 2500 gm. B & M.S.; 1.7 ft./min. H2 flow.
RUN Pd-78
60°F; 150 psig; 790 RPM; 2.5 gm. cat.; 2500 gm. B & M.S.; 1.1 ft./min. H2 flow.

Fig. 5. Mole percentage of α-methylstyrene.

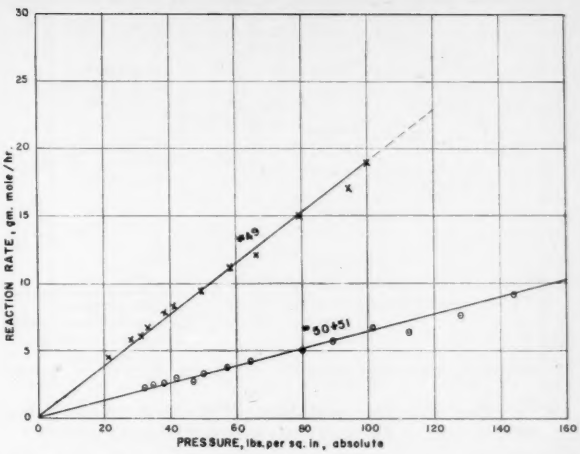

Fig. 6. Effect of hydrogen pressure on reaction rate. Palladium-49: 80°F., 790 rev./min., 14.0 cu. ft./hr., H_2 out, S.C.; palladium-50, 51: 80°F., 203 rev./min., 30.5 cu. ft./hr., H_2 out, S.C.

$\mu/(\rho\mathbf{D})$, a gas flow number $\sigma/(\mu V_g)$, and a Reynolds number $(D^2N\rho)/\mu$, thus

$$R_b = A'\left(\frac{\rho D}{\mu}\right)^{1/3}\left(\frac{\sigma}{\mu V_s}\right)^{\alpha}\left(\frac{D^2N\rho}{\mu}\right)^{\beta} \quad (19)$$

The velocity V_s is calculated by dividing the volume of gas flowing per minute at the temperature and pressure of the system by the total cross-sectional area of the reaction. Values of V_s were taken as the averages of inlet and outlet values. A large excess of hydrogen was used in every case. The physical properties of the liquid solution were evaluated as additive for a given composition.

Resistance of Liquid Surrounding the Solid

The resistance to transfer of hydrogen through the liquid surrounding the solid is inversely proportional to the area A_s of the solid per liter of liquid and upon the mass transfer coefficient k_s''; thus,

$$R_s = \frac{1}{A_s k_s''} \quad (20)$$

The area A_s is proportional to the catalyst loading m and inversely proportional to the density ρ_s and diameter D_s of the catalyst particle.

For a single spherical particle,

$$\text{area} = \pi D_s^2 \quad (21)$$

$$\text{mass} \quad w_p = \pi D_s^3 \rho_s/6 \quad (22)$$

For a catalyst loading of m g./liter of liquid the number of particles n per liter from Equation (22) is

$$n = \frac{m}{w_p} = 6m/\rho_s \pi D_s^3 \quad (23)$$

The area of solid surface A_s per liter of liquid is obtained by combining Equations (21) and (23) to give

$$A_s = \frac{6m}{\rho_s D_s} \quad (24)$$

The total resistance of the liquid surrounding the solid is obtained by combining Equations (20) and (24) to give

$$R_s = \frac{\rho_s D_s}{6mk_s''} \quad (25)$$

For particles other than spherical a constant other than 6 would appear.

The turbulence in the liquid surrounding the solid is dependent upon the velocity of the stirrer and the viscosity and density of the liquid. These combined effects can be expressed by dimensional analysis in terms of a Reynolds number $(D^2N\rho)/\mu$, a catalyst loading term (ρ_s/m) and a Schmidt number $(\mu/\rho\mathbf{D})$ for the liquid; thus

$$R_N = B'\left(\frac{D^2N\rho}{\mu}\right)^{\gamma}\left(\frac{\rho_s}{m}\right)\left(\frac{\rho\mathbf{D}}{\mu}\right)^{1/3} \quad (26)$$

where B' is a constant dependent upon the mechanical dimensions of the stirrer, baffles, and reactor.

The total resistance R_0 offered to the transfer of hydrogen through the liquid from bubble to solid is then the sum of the two resistance, $R_0 = R_b + R_s$.

Combining Equations (19) and (26) gives

$$R_0 = A'\left(\frac{\rho\mathbf{D}}{\mu}\right)^{1/3}\left(\frac{\sigma}{\mu V_s}\right)^{\alpha}\left(\frac{DN\rho}{\mu}\right)^{\beta} + B'\left(\frac{\rho\mathbf{D}}{\mu}\right)^{1/3}\left(\frac{\rho_s}{m}\right)\left(\frac{D^2N\rho}{\mu}\right)^{\gamma} \quad (27)$$

The over-all resistance R_0 is inversely proportional to the over-all mass transfer coefficient k_0. To introduce k_0 into this equation and retain dimensionless form, the dimensionless number $\mathbf{D}/(k_0D^2)$ is used with a corresponding change in constants A' and B' to A and B.

Equation (27) becomes

$$\left(\frac{\mu}{\rho\mathbf{D}}\right)^{1/3}\left(\frac{\mathbf{D}}{k_0D^2}\right) = A\left(\frac{\sigma}{\mu V_s}\right)^{\alpha}\left(\frac{D^2N\rho}{\mu}\right)^{\beta} + B\left(\frac{D^2N\rho}{\mu}\right)^{\gamma}\left(\frac{\rho_s}{m}\right) \quad (28)$$

SELECTION OF SYSTEM

The hydrogenation of α-methylstyrene in a stirred reactor catalyzed by palladium was selected as an appropriate system for study because for this system rate data were already available for the same reaction taking place in a trickling-bed flow reactor. This system is also favorable because the vapor pressures of α-methylstyrene and cumene are low; hydrogenation yields only one product, cumene, and the liquid is easy to analyze accurately by measurements of indexes of refraction. The reaction involved is

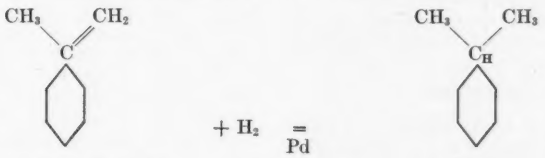

α-methylstyrene — catalyst — cumene

Palladium was selected as the catalyst because it directed the hydrogenation to the side chain without causing polymerization or hydrogenation of the benzene ring and permitted the surface reaction to proceed so rapidly as to confine the resistance to mass transfer. The α-methylstyrene was 98.5% pure with 1.0% of β-methylstyrene and traces of impurities.

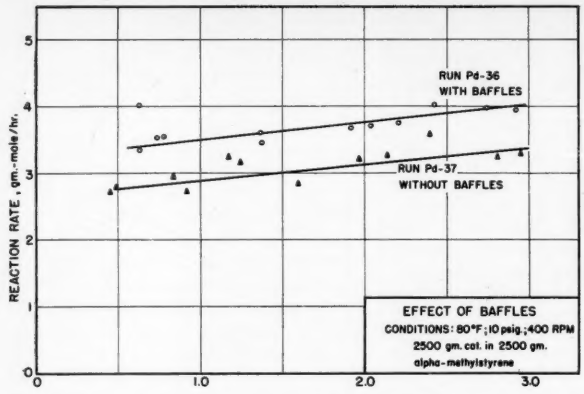

Fig. 7. Effect of baffles; conditions: 80°F., 10 lb./sq. in. gauge, 400 rev./min., 2,500 g. catalyst in 2,500 g. α-methylstyrene.

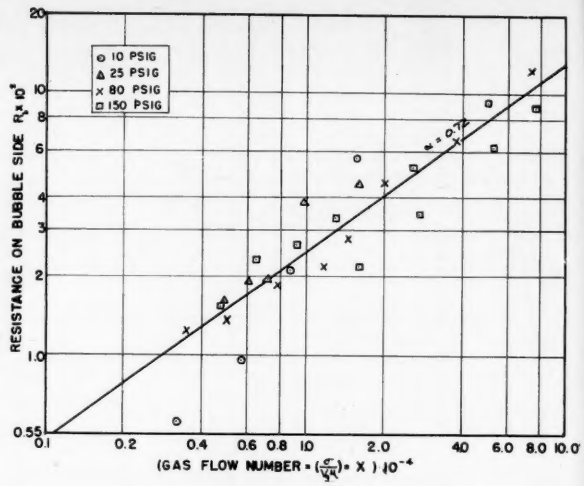

Fig. 8. Evaluation of α at 80°F.

Some physical properties of α-methylstyrene and cumene needed in this investigation are the following:

	α-methylstyrene	cumene
Boiling point at 760 mm. Hg	165.38°C.	152.4°C.
Freezing point, 760 mm. Hg	−23.21°C.	−96°C.
Density at 25°C., g./cc., 20°/4	0.9062	0.862
Index of refraction at 25°C.	1.53586	1.48890
Viscosity at 20°C., centipoise	0.940	0.791
Surface tension at 20°C. dynes/cm.	31.5	28.2

The hydrogen supply was purified to remove traces of oxygen by passing the gas over an auxiliary palladium catalyst. The resultant water vapor was removed by silica gel. The removal of water vapor was important, as its presence caused coagulation of the suspended catalyst.

The catalyst consisted of palladium supported on a 300-mesh alumina powder (2% metal), supplied by Baker and Company with the following properties,

Surface mean diameter = 7.15 μ
Volume mean diameter = 13.46 μ
Density at 20°C. = 4.14 g./cc.
Internal surface area = 75 sq. meters/g.

EXPERIMENTAL EQUIPMENT

A flow chart of the experimental process is shown in Figure 2 and a photograph of the assembly in Figure 3.

The reactor consists of a 316–stainless-steel high-pressure forged vessel of 1-gal. capacity, 5 in. I.D., and 12 in. inside height, designed to operate at a maximum pressure of 1,200 lb./sq. in. gauge and at a maximum temperature of 650°F., as manufactured by Autoclave Engineers. The agitator consisted of impellers with two flat turbine blades.

Diameter of blade rotation, in.	3.50
Length of blades, in.	1.25
Width of blades, in.	0.75

The impellers were driven by a ¾-hp. motor with V-belt speed reducers to permit variations in speed from 130 to 800 rev./min.

To promote agitation and prevent vortex motion four equally spaced baffles ½ in. wide and 11⅛ in. long surrounded the agitator and were held in place 1/16 in. from the cylinder walls. A photograph of the stirrer, sparger, heat exchangers, and baffles is shown in Figure 4. Hydrogen was introduced through a ring sparger placed ½ in. from the bottom of the reactor with holes of 0.0135-in. diam. directed downward.

Diameter of ring, in.	3½
Holes in ring	25
Diameter of holes, in.	0.0135

Temperature was controlled by electrical heaters surrounding the vessel.

A cooling coil of stainless steel with a heat transfer surface of 0.77 sq. ft. was immersed in the charge. Temperatures were measured by an iron-constantan thermocouple mounted in a stainless steel well. Pressure was measured by a Bourdon gauge.

The rate of hydrogen flow to the reactor was controlled by a needle valve in combination with a rotameter. The hydrogen leaving the reactor was passed through a reflux condenser consisting of a ⅜-in. stainless steel coil immersed in ice water. The hydrogen was cooled to 5°C. with return of condensate to the reactor.

A second precision needle valve on the outlet of the condenser permitted control of the reactor pressure by release of hydrogen to the atmosphere. The hydrogen leaving the condenser was saturated with water and its rate of flow measured with a wet-test meter.

The liquid feed and product were analyzed by a dipping refractometer with bath temperature maintained at 25° ± 0.01°C. and with room temperature maintained at 24° to 26°C. This dual control of temperature permitted measurements of index to a precision of ±0.00001, corresponding to ±0.05 mole % α-methylstyrene.

EXPERIMENTAL PROCEDURE AND DATA

Many preliminary runs were made to establish proper techniques, to obtain reproducible operation, and to ensure that cumene was the only product of hydrogenation.

The following variables were studied: rate of stirring, rate of hydrogen flow, temperature, pressure, liquid composition, catalyst loading, number of propeller blades, effect of baffles, and type of sparger. The detailed experimental data are filed.*

With a given reactor fixed in every detail of mechanical design the effects of such operating variables as pressure, temperature, liquid composition, gas velocity, and stirring rate were each studied independently as far as practicable. In each run 2,500 g. of liquid feed were used and 2.5 g. of catalyst powder suspended therein. Later the effect of loading was studied with variation in mass of catalyst per liter of liquid. The percentage conversion of the α-methylstyrene with time was measured from changes of index of refraction. From a plot of such data the reaction rate at any instant of time is obtained from the slope of the conversion-time curve. For concentrations above 20 mole % α-methylstyrene a plot of conversion x vs. time gave straight lines.

Polymerization Negligible

First it was confirmed that the only product in the hydrogenation of α-methylstyrene with a palladium catalyst in a stirred reactor was cumene with no polymerization products and with no hydrogenation in the benzene ring.

Reverse Reaction Negligible

Complete conversion of α-methylstyrene to cumene could be obtained with no reverse reaction over the range of temperatures and pressures used in this investigation.

Uncatalyzed Reaction Negligible

In the absence of the catalyst no appreciable hydrogenation took place over the experimental range of operation.

*Data have been deposited as document 5308 with the American Documentation Institute, Photoduplication Service, Library of Congress, Washington 25, D. C., and may be obtained for $2.50 for photoprints or $1.75 for 35-mm. microfilm.

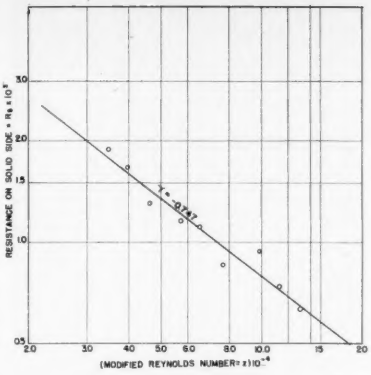

Fig. 9. Evaluation of γ.

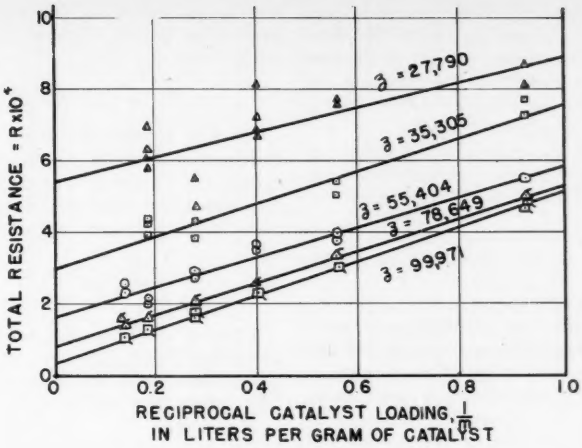

Fig. 10. Evaluation of R_b.

Negligible Effect of Catalyzed Support and Equipment Surface

It was proved experimentally that the catalyst support of alumina powder did not catalyze the hydrogenation reaction nor did the surface of the vessel, stirrers, heat exchanger, or baffles.

Negligible Effect of Liquid Level and Removal of Samples

Removal of samples of liquid during an experimental run resulted in an appreciable lowering of the liquid level. It was found that reduction of the liquid content of the reactor by even one third had no noticeable effect on the reaction rate when such rates were based upon unit volume of liquid. The mass of catalyst per liter of liquid was the same inside the reactor as in the sample withdrawn. The rate of reaction per liter remained independent of liquid level over the experimental range.

Effect of Liquid Composition

The reaction rate was found to be independent of the composition of the liquid solution for concentrations above 20% α-methylstyrene, as shown in Figure 5. This independence is evidence that mass transfer controls the reaction rate except at low concentrations.

The independence of reaction rate on liquid composition in the stirred reactor was established by thirty runs over a temperature range from 60° to 100°F. at a pressure of 150 lb./sq. in. gauge, gas velocity of 1.7 ft./min., and a stirring rate of 790 rev./min. By reducing the rates of bubbling and stirring and by lowering pressure and temperature this independence of reaction rate on concentration could be extended to concentrations of α-methylstyrene below 20%.

Effect of Hydrogen Pressure

Forty runs were made at 80°F. over a pressure range from 20 to 144 lb./sq. in. abs. at stirring rates of 203 and 790 rev./min. and at a hydrogen flow rate of 30.5 ft./hr. and 14.0 ft./hr. respectively. For pressures up to 150 lb./sq. in. gauge the reaction rates were found to increase linearly with pressure, as shown in Figure 6. This straight line relationship supports the theory that mass transfer is the rate-controlling step. At pressures above 150 lb./sq. in. gauge the resistance of the surface reaction became evident as shown by a downward trend.

Effect of Baffles

The presence of baffles increased turbulence and uniformity in mixing and prevented the formation of a vortex in the agitated liquid. The effect of baffles was to increase the reaction rate by 13%, as shown in Figure 7. Baffles were used in all subsequent runs.

Effect of Number of Impeller Blades

Comparisons were made of two- and eight-blade impellers with the same size, shape and dimensions of blades. Five tests were made at 80°F. and 10 lb./sq. in. guage. The eight-blade impeller increased the rate of mass transfer by 65% in the range of low stirring rates from 130 to 300 rev./min. but only 22% in the high range from 600 to 800 rev./min.

Visual Observation of Holdup and Bubble Size

In order to observe and measure the effects of bubbling and stirring rates on hydrogen holdup and bubble size, separate visual experiments were made by bubbling hydrogen through α-methylstyrene with a suspended catalyst in a stirred glass vessel of the same dimensions as the reactor autoclave and using the same stirrer, paddles, heat transfer coils, and baffles. The following observations were made:

1. The diameter of bubbles decreased with the rate of stirring.
2. The diameter of bubbles was not influenced by the rate of gas flow.
3. The gas holdup increased with the 0.5 power of the rate of stirring.
4. The gas holdup increased with the 0.6 power of the rate of gas flow.

These observations are consistent with the theory presented and with the experimental data on mass transfer rates.

Mass Transfer the Rate-controlling Step

That mass transfer imposes the rate-controlling resistance in the hydrogenation of α-methylstyrene in a stirred reactor is based upon the following evidence: In the stirred reactor the mass transfer rate (1). is greatly dependent upon the rate of stirring, (2) is greatly dependent upon the rate of bubbling, (3) varies directly with pressure, (4) is independent of concentration of α-methylstyrene. In contrast to these findings, from independent experiments made on the same reaction in a trickling-bed reactor where mass transfer was negligible and the resistance of the chemical reaction at the surface was rate controlling, opposite effects were found by Babcock, Mejdell, and Hougen (*1*). In the trickling-bed reactor the chemical reaction rate (1) is independent of rate of liquid flow, (2) is independent of rate of gas flow, (3) varies nearly as the square root of pressure, and (4) varies greatly with concentration of α-methylstyrene.

Correlation of Data

Over conditions of operation where resistance offered by the surface reaction is negligible, the total resistance offered to hydrogen transfer is represented by the following equation:

$$R_0 = Ax^{\alpha}z^{\beta} + B\left(\frac{\rho_s}{m}\right)z^{\gamma} \qquad (29)$$

The principal objective of this investigation was to confirm or modify the theory summarized by Equation (29) and, if confirmed, to establish the constants A, B, α, β, and γ.

Effect of Schmidt Number. Several investigators have found that the mass transfer coefficients of dissolved gases through liquids vary with the $\frac{1}{3}$ to $\frac{1}{2}$ power of the Schmidt number. No de-

tailed correlation of this variable was attempted. Calculation of all the data with both exponents by the method of least squares showed the exponent $\frac{1}{3}$ to give better agreement between experimental and calcplated results.

Effect of the Gas Flow Number, x. Under conditions of constant Reynolds number z, Equation (29) may be written as

$$R_0 = A'x^{\alpha} + R_s \qquad (30)$$

Values of R_o at constant temperature and constant rate of stirring N were plotted against values of x and extrapolated to a zero value of x. A value of x equal to 0 corresponds to an infinite rate of gas flow where the resistance of the liquid surrounding the bubble becomes zero ($R_b = 0$) and hence R_0 becomes equal to R_s. Values of R_b were thus obtained at 135 rev./min. at temperatures of 60°, 80° and 100°F.

Values of R_b were plotted against x on logarithmic scales as shown in Figure 8 to give a slope of α equal to 0.72 at 80°F. The same procedure was repeated at 60° and 100°F. to give values of 0.78 and 0.77. an average value of $\alpha = 0.75$ was accepted.

Effect of the Reynolds Number upon the Resistance of the Liquid on the Solid Side. Where the flow number x equals 0, corresponding to an infinite rate of gas flow, the mass transfer resistance exists entirely in the liquid surrounding the solid and is zero surrounding the bubble. Under these conditions

$$R_0 = R_s = B'z^{\gamma} \qquad (31)$$

These values of R_s were obtained by extrapolating values of R_0 at constant values of z to zero values of x. These values of R_s were plotted against the modified Reynolds number on a logarithmic scale to give a slope γ equal to -0.75, as shown in Figure 9.

Effect of the Reynolds Number upon the Resistance of the Liquid Surrounding the Bubbles. From Equation (29) it will be observed that when the catalyst loading m is increased the mass transfer resistance surrounding the solid disappears as $1/m$ approaches zero. This relationship was shown earlier by Davis (*3*). For constant values of gas flow numbers x and for four values of Reynolds numbers z, values of R_0 were plotted against reciprocal values of loading, $1/m$, as shown in Figure 10. The various plots were established by the method of least squares. These values of R_0 extrapolated to values of $1/m$ equal to zero correspond to the resistance R_b on the bubble side; thus

$$\text{at } 1/m = 0, \quad R_0 = R_b = Ax^{\alpha}z^{\beta} \qquad (32)$$

Values of R_b were plotted against the Reynolds number z at constant values of gas flow numbers both on logarithmic scales, Figure 11. The slope of this plot was evaluated by the method of least squares to give a value of β equal to -1.67; thus

$$R_b = Ax^{0.75}z^{-1.67} \qquad (33)$$

Effect of Catalyst Loading. According to Equation (29) the resistance to mass transfer at constant values of gas flow numbers x and rates of stirring z varies with the reciprocal of catalyst loading m.

$$\frac{R_s}{z^{0.75}} = \frac{B\rho_s}{m} \qquad (34)$$

A plot of $R_s/z^{0.75}$ against m on logarithmic scales, Figure 12, gave a slope of -1, in agreement with the original Equation (29), where the exponent of the term ρ_s/m is unity.

The final equation for mass transfer of a gas through a liquid to a solid surface in a stirred recator with bubbling of the gas through the liquid is given by the relation.

$$\left(\frac{\mathbf{D}}{k_0D^2}\right)\left(\frac{\mu}{\rho\mathbf{D}}\right)^{1/3} = A\left(\frac{\sigma}{V_s\mu}\right)^{0.75} \cdot\left(\frac{D^2N\rho}{\mu}\right)^{-1.67} + B\left(\frac{\rho_s}{m}\right)\left(\frac{D^2N\rho}{\mu}\right)^{-0.75} \qquad (35)$$

where the values of the constants A and B are characteristics of the mechanical construction and position of impellers, baffles, sparger, and vessel.

For the given two-blade flat impeller and construction the $A = 29.4$ and $B = 6.55 \times 10^{-4}$. The average deviation of calculated from experimental values is $\pm 14\%$. This deviation is due to the intrinsic difficulties involved in the simultaneous control of pressure, temperature, stirring, and loading.

The relative resistances of the liquid surrounding the bubble and surrounding the solid as a function of gas velocity are shown in Figure 13 at 135 and 790 rev./min. It will be observed that the resistance of the liquid film surrounding the bubbles becomes negligible at high gas velocities and suggests that higher rates of bubbling represent a waste of gas and power without increasing the rate of mass transfer. The same effects are shown in Figure 14, where the relative resistance of the two liquid films is shown as a function of gas velocity at four rates of stirring.

DISCUSSION OF RESULTS

The exponent 0.75 on x for the effect of gas velocity on the bubble resistance surrounding the bubbles is comparable with the value of 0.68 obtained by Hixson and Gaden (*8*) and Cooper et al. (*2*) on the rate of absorption of oxygen in bubbling through sodium sulfite solutions where only one resistance is involved.

The exponent -0.75 on the effect of rate of stirring on the film surrounding the solid is comparable with the value of

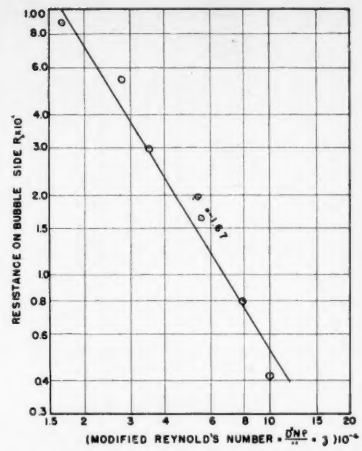

Fig. 11. Effect of Reynolds number z on R_b at constant gas-flow numbers.

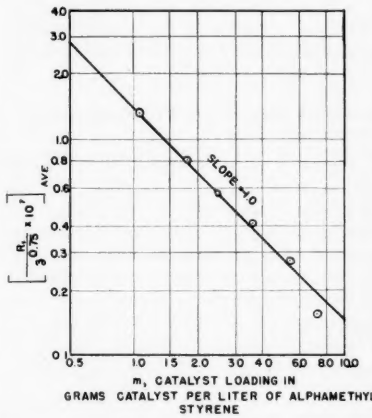

Fig. 12. Effect of catalyst loading on R_s at constant gas-flow and Schmidt numbers.

-0.6 obtained by Hixson and Baum (*5*) on the dissolution of a solid in a solvent where any one resistance was involved.

The exponent -1.67 on z for the effect of stirring rate on the film surrounding the bubble is comparable with the exponent -1.5 obtained by Vermeulen at al. (*12*) on the interfacial area of bubbles in an agitated liquid.

SUMMARY OF RESULTS

1. A theory with experimental confirmation of the effects of bubbling and stirring on mass transfer coefficients from gas bubbles to solid particles in liquids has been presented.
2. The total resistance to mass transfer from bubble to solid per unit volume of liquid is equal to the resistance of liquid surrounding the bubble plus the resistance of the liquid surrounding the solid.
3. The resistance of the liquid surrounding the bubble is given by the relation $R_b = Ax^{0.75}z^{-1.67}$.
4. The resistance of the liquid on the solid side is given by the relation

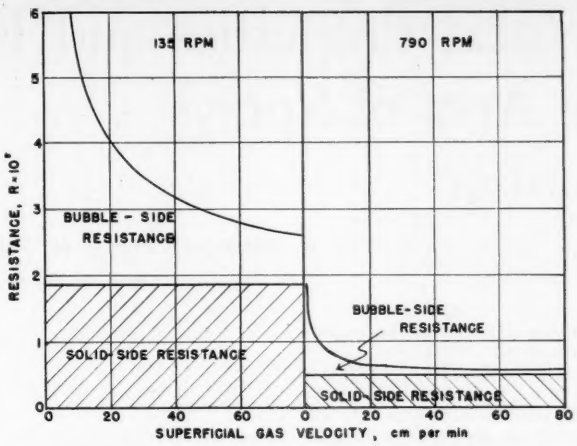

Fig. 13. Change of resistances with gas-flow rate.

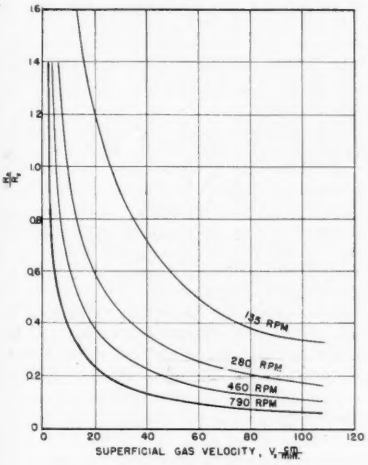

Fig. 14. Ratio of bubble-side to solid-side resistances.

$$R_s = B\,\frac{\rho_s}{m}\,z^{-0.75}$$

5. The constants A and B depend upon the mechanical construction of the vessel, agitator, baffles, and sparger and require separate evaluation in terms of these mechanical factors for scale-up purposes.

6. The effects of bubbling rates, stirring rates, and catalyst loading on holdup, bubble size, and particle motion were observed visually in a glass vessel with the same stirring equipment, heating coils, and baffles as used in the steel reactor. These observations were consistent with the theory proposed for mass transfer.

7. At high gas velocities the resistance surrounding the bubble becomes negligible. High gas velocities result in a waste of gas and power with no corresponding increase in rates of mass transfer.

8. The hydrogenation of α-methylstyrene by use of a suspended palladium catalyst provides a simple and convenient means for evaluating the mass transfer performance of stirring equipment and the effects of changes in mechanical construction and baffling thereon.

ACKNOWLEDGMENT

The Wisconsin Alumni Research Foundation gave financial support through grants-in-aid for personnel, supplies, and equipment, the Dow Chemical Corporation donated α-methylstyrene, and the International Nickel Company through the courtesy of E. M. Wise donated rare metal catalysts. N. Berman, D. Pagel, D. Blumke, and J. Rychlowski helped in the work, B. D. Babcock and Glør T. Mejdell provided scientific collaboration.

NOTATION

A, A' = constants
A_b = area of bubbles, sq. cm./liter of liquid
A_s = area of solid surface; sq. cm./liter of liquid
A_p = surface area per particle, sq. cm.
B = number of blades on impeller
B, B' = constants
c_b', c_s', c' = concentration of hydrogen in liquid phase, g.-moles/liter
c_b, c_s, c = concentration of hydrogen in gas phase, g.-moles/liter
$\mathbf{D}$ = diffusivity of hydrogen through liquid, sq. c./secm.
D = diameter swept by impeller, cm.
D_b = diameter of bubble, cm.
D_s = diameter of solid particle, cm.
H = total holdup, liter/liter of liquid
K_G = over-all mass transfer coefficient
k_b, k_s, k_0 = proportionality constants
k_b', k_s', k_0' = mass transfer coefficients
k_b'' = mass transfer coefficient/unit area of bubble
k_s'' = mass transfer coefficient/unit area of solid surface
m = catalyst loading, g./liter of liquid
N = stirring rate, rev./sec.
n = number of moles
n = catalyst loading, particles/liter
p = partial pressure of hydrogen, atm.
R = gas law constant 0.08206 (liter)(atm.)/(g.-mole)(°K.)
R_b, R_s, R_0 = resistances to mass transfer
r = reaction and transfer rate, g.-moles/(liter)(sec.)
T = absolute temperature, °K.
V = volume, liters
V_s = average superficial gas velocity based on inside diameter of reactor and temperature and pressure of gas, cm./sec.
α = constant
α = exponent of gas flow number
β = constant
β = exponent of Reynolds number (bubble side)
γ = exponent of Reynolds number (solid side)
μ = viscosity of liquid, g./(sec.)(cm.)
σ = surface tension, g./sec.²
π = total pressure, atm.
π = 3.1416
ρ = density of liquid, g./cc.
ρ_s = density of solid, g./liter

Subscripts

b = bubble side
0 = over all
s = solid side

Dimensionless Numbers

$S_s = (\mu/\rho\mathbf{D})$ = Schmidt number
$x = (\sigma/\mu V_s)$ = gas flow number
$z = (D^2N\rho/\mu)$ = modified Reynolds number
$Nu = (k_0D^2/\mathbf{D})$ = modified Nusselt number

LITERATURE CITED

1. Babcock, B. D., G. T. Mejdell, and O. A. Hougen, *A.I.Ch.E. Journal*.
2. Cooper, C. M., G. A. Fernstrom, and S. A. Miller, *Ind. Eng. Chem.*, **36**, 504 (1944).
3. Davis, H. S., C. Thomson, and G. S. Crandall, *Jour. Am. Chem. Soc.*, **54**, 2340 (1932).
4. Dow Chemical Company, "Alpha-methylstyrene Monomer," Bulletin of Coatings Technical Service, Midland, Mich. (1955).
5. Hixson, A. W., and S. J. Baum, *Ind. Eng. Chem.*, **33**, 478 (1941).
6. *Ibid.*, **34**, 194 (1942).
7. *Ibid.*, **36**, 528 (1944).
8. Hixson, A. W., and E. L. Gaden, *Ind. Eng. Chem.*, **42**, 1792 (1950).
9. Maxted, L. B., "Handbuch der Katalyze."
10. Milligan, C. H., and E. E. Reid, *Ind. Eng. Chem.*, **15**, 1048 (1925).
11. Rushton, J. H., *Chem. Eng. Progr.*, **47**, 485 (1951).
12. Vermeulen, Theodore, C. M. Williams, and G. E. Langlois, *Chem. Eng. Progr.*, **51**, 85 (1955).

Effect of Liquid Physical Properties and Flow Rates on the Surface Area of Sprays from a Pressure Atomizer

J. A. CONSIGLIO and C. M. SLIEPCEVICH

University of Michigan, Ann Arbor, Michigan

The effects of the physical properties and volume flow rate of liquids on the surface area of sprays produced by a pressure type of atomizing nozzle were determined experimentally. The specific surface area of the sprays is correlated by an equation of two dimensionless groups in terms of the variables surface tension to the −1.0 power, kinematic viscosity to the −0.4 power, and volume flow rate to the 2.4 power. The volume flow rate is correlated by an equation of two dimensionless groups containing the variables viscosity to the 0.17 power, density to the −0.58 power, and spray pressure to the 0.42 power. The conversion of compression energy to surface-area energy appears to be constant at approximately 0.1%.

The purpose of this investigation was to determine the effect of physical properties and flow rates of liquids on the surface area of sprays produced by a commercial pressure type of atomizer by means of an optical sampling technique developed by Gumprecht and Sliepcevich (*1, 2*). This technique is based on the light-scattering properties of spherical particles. The method consists of measuring continuously the intensity of the transmitted light beam through a dispersion of droplets as they settle differentially under the influence of gravity through a known settling distance. The size distribution of the spray is calculated from the light-intensity measurements by means of a modified form of the Lambert-Beer transmission equation and Stokes's Law. The size of the spray chamber employed and the turbulence generated in the chamber during the spray period restrict the use of the technique to drops 40μ or less in diameter. The changes in the drop-size distribution of the spray caused by the turbulence during the spray period are corrected for by an empirical procedure of extrapolation to zero volume sprayed. The surface area for drops greater than 40μ is estimated by means of an empirical distribution equation.

The specific surface area of the sprays is correlated as a function of the physical properties and volume flow rate of the liquid. The volume flow rate is correlated as a function of the spray pressure and the physical properties of the liquid.

The optical sampling technique was selected in preference to the more common sampling techniques in order to avoid the large sampling errors inherent in mechanical devices such as slides, cups, and probes. These errors are dependent on the size of the drops, the size and shape of the sampling device, and the flow pattern at the sampler (*5*), and the magnitude of the error is difficult to predict primarily because the flow pattern is not always known.

EXPERIMENTAL EQUIPMENT

A block diagram of the experimental equipment is shown in Figure 1. The components of the equipment are a spray chamber, a pump unit to supply liquid to the nozzle, a constant-intensity light source, and an optical and electrical system to measure and record the intensity of the light beam transmitted through the dispersion of drops undergoing settling in the spray chamber.

The spray chamber, constructed of ½-in. plywood, is 3 by 3 by 10 ft., with a volume of 2.55 by 10^6 cc. The floor area of the chamber is covered by a removable drawboard. The settling height from the top of the chamber to the light beam is 279 cm. and the length of the path of the light beam through the dispersion of drops in the chamber is 89.5 cm.

The pump unit, shown in Figure 2, is capable of delivering a maximum volume of 350 cc. at a maximum rate of 32 cc./sec. at pressures up to 3,000 lb./sq. in. The volume of liquid delivered to the nozzle is determined by the position of a calibrated, adjustable screw stop in the positive displacement cylinder. Mercury is used as an intermediate fluid to prevent contamination of the liquid being sprayed by the oil.

The light source consists of a 6-volt automobile-headlight bulb. It is modulated at a frequency of 300 cycles/sec. by means of a rotating perforated disk having ten 5/64-in. holes equally spaced on a 4 in.-diam. circle. An essentially parallel and monochromatic light beam is obtained by means

J. A. Consiglio is at present with General Electric Company, Schenectady, New York, and C. M. Sliepcevich with University of Oklahoma, Norman, Oklahoma.

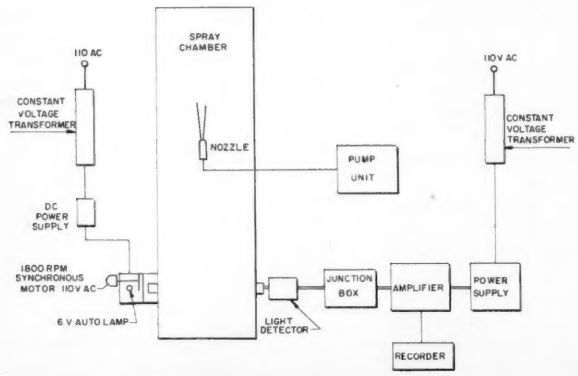

Fig. 1. Block diagram of equipment.

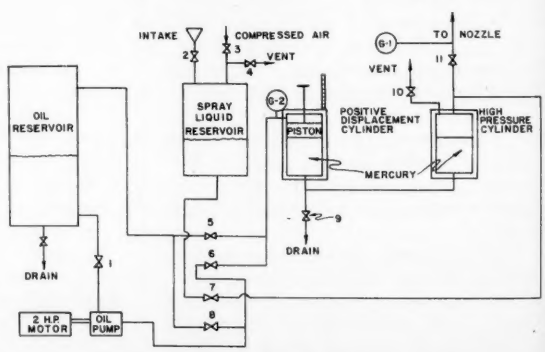

Fig. 2. Pump unit.

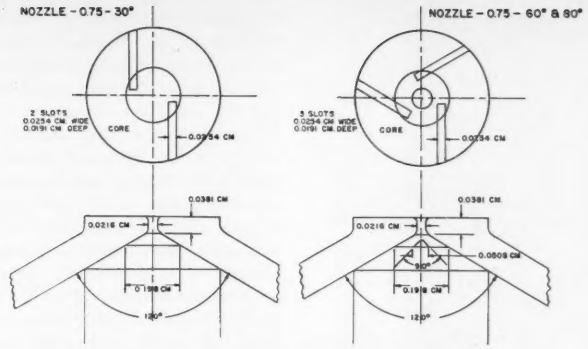

Fig. 3. Dimensional sketch of nozzles.

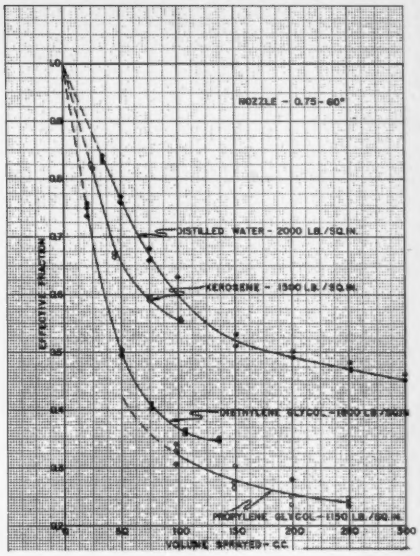
NOZZLE - 0.75 - 60°
DISTILLED WATER - 2000 LB./SQ.IN.
KEROSENE - 1500 LB./SQ.IN.
DIETHYLENE GLYCOL - 1500 LB./SQ.IN.
PROPYLENE GLYCOL - 1150 LB./SQ.IN.
EFFECTIVE FRACTION
VOLUME SPRAYED - CC.

Fig. 4. Effective fraction vs. volume sprayed.

of a collimating lens system and interference type of filter which has a peak transmission at 4,700 Å ± 50Å.

The light detector consists of a lens-pinhole optical system which focuses the light beam on the cathode of a type-929 vacuum phototube. The half angle of the cone which the detector subtends with the drops at any point in the light beam is 0.92°. The a.c. signal developed by the phototube is amplified and then rectified to a d.c. voltage, which is applied to a strip-chart recorder. The deflection of the recorder is a linear function of the intensity of the light beam focused onto the phototube.

EXPERIMENTAL PROCEDURE

Determination of the drop-size distribution of sprays by the light-scattering method requires two types of measurements, the continuous measurement of the intensity of the light beam transmitted through the dispersion of spray drops setting in the chamber and the measurement of the amount of liquid that drops out of the system during the spray period.

Prior to a run the chamber is saturated by spraying liquid into the closed chamber and allowing the drops to settle to the floor of the chamber. A light-transmission run is made by spraying a known volume of liquid into the chamber and continuously recording the intensity of the light beam transmitted through the dispersion as the drops settle differentially after the spray period.

The amount of liquid that drops out of the system during the spray period is determined by collecting and weighing the liquid on a tared piece of absorbent paper placed on the removable drawboard at the bottom of the chamber. For each liquid and flow rate a series of light-transmission and drop-out runs is made by varying the volume of liquid sprayed into the chamber.

Three pressure-type swirl-chamber nozzles manufactured by the Kopp Nozzle Products Company were used. The majority of the runs were made with a nozzle rated by the manufacturer at 0.75 gal. of water/hr. and 60° cone angle when spraying at a pressure of 100 lb./sq. in. One liquid, water, was sprayed with two other nozzles of the same rated capacity but having rated cone angles of 30° and 80° respectively. Sketches of these nozzles and dimensions given by the manufacturer are shown in Figure 3. The measured dimensions for the orifice diameters are given in Table 5.

Six liquids were used in this study, the physical properties and volume flow rates of which are given in Table 1. Atomization was achieved for all liquids and flow rates reported in the study; the minimum spraying pressure used being 500 lb./sq. in.

THEORY

The intensity of a parallel monochromatic light beam I which passes through a dispersion of heterogeneous drop sizes of diameter D is given by the following equation (*2*):

$$\ln I = \ln I_0 - \frac{\pi l}{4} \int_0^\infty RK_t N D^2 \, dD \quad (1)$$

The ratio between the total scattering cross section and the geometric cross section of the drop K_t is known as the *Mie theory total scattering coefficient* (*7*). The total scattering coefficient is a complex function of the drop size, the refractive index of the drop with respect to the surrounding medium, and the wave length of the incident beam as shown in Figure 7 (*3, 7*). The term R, a correction factor to the total scattering coefficient, expresses the fraction of the total amount of light scattered by a drop which is excluded from the view of the light-measuring device (*2*). In general R is a function of the half angle θ, which the device subtends with the drops; the parameter α (circumference of the drop divided by the wave length of the incident light); and the relative refractive index. N is the derivative with respect to D of the cumulative drop-size distribution function per unit volume of dispersion. (The dimensions of N are length^{-4}.)

For a dispersion of drops undergoing differential settling under tranquil conditions, the size range of drops removed from the path of the light beam during an interval of time t can be computed from Stokes's Law:

$$D = kt^{-1/2} \quad (2)$$

Differentiation of Equation (1) with respect to time and substituting for D in terms of time yields

$$RK_t N = \frac{8}{\pi l k^3 I} \left(\frac{dI}{dt}\right) t^{5/2} \quad (3)$$

The quantity $RK_t N$ can be calculated from the light-transmission data of I vs. t at any time t. For a known settling height the diameter D can be calculated from Stokes's Law at any time t. Therefore, the term $RK_t N$ is obtained as a function of the drop diameter D. Finally, since R and K_t are known functions of D, N can be calculated as a function of D to obtain the size-frequency-distribution curve. The surface- and volume-distribution curves are obtained by multiplying the ordinate of the size-frequency curve by the square and cube of the corresponding diameter respectively. Equations (2) and (3) are valid provided that (1) the drops are initially uniformly dispersed throughout the volume of the system, (2) settling is under tranquil conditions, and (3) there is no interception, coalescence, or evaporation of drops during the settling process. For the concentration of drops encountered in this study, the effects of multiple scattering are negligible.

In practice it is difficult to produce a heterogeneous dispersion of drops that is initially uniformly dispersed and to fulfill the condition required by Equation (3) that the drops settle under tranquil conditions. The turbulence generated in the chamber during the spray period by the high-velocity jet emerging from the spray nozzle provides the mixing action necessary to disperse the drops formed by the nozzle throughout the volume of the chamber. Observations of the drops by means of a Tyndall beam indicated that essentially tranquil conditions are obtained in the chamber within 45 to 60 sec. from the end of the spray period.

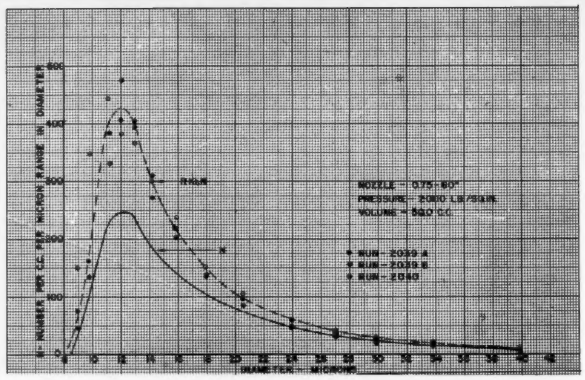

Fig. 5. Size-frequency distribution curve for water.

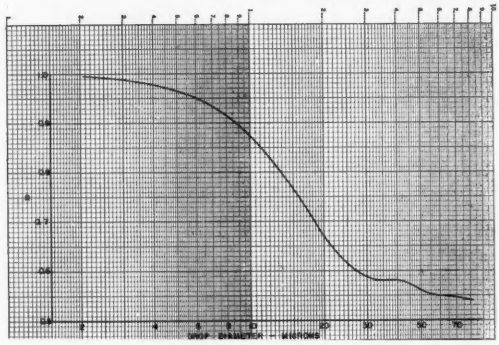

Fig. 6. R vs. D for $\theta = 0.92°$, $\lambda = 0.47\ \mu$.

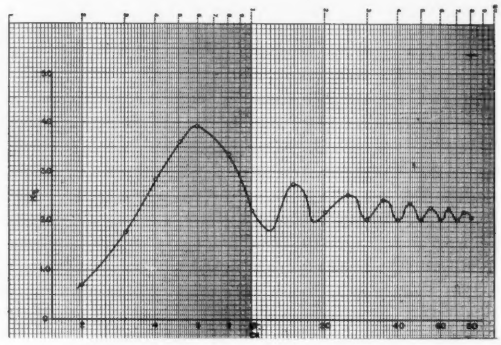

Fig. 7. The scattering coefficient as a function of α for water.

For the purposes of computation, zero settling time was taken as the time at which spraying ceased and Stokes's Law was assumed to be valid for drops up to 40 μ in diameter.

The turbulence during the spray period causes some attenuation of all drop sizes owing to coalescence, impingement on the walls of the chamber, and evaporation. In addition, drops are lost by settling to the bottom of the chamber during the spray period. The extent of these phenomena for a given spray condition is a function of the spraying time or the volume sprayed. Thus, the *observed* drop-size distribution after the completion of the spray period depends on the volume sprayed or time of spraying; however, it is not implied that the drop-size distribution produced by the nozzle depends on the volume sprayed. A dependence of size distribution on volume sprayed exists only during the initial transient period at spray start-up, the time involved here is only a fraction of a second, which is negligible when compared with spraying times varying from 16 to 150 sec. The size, surface, and volume-frequency distribution curves calculated from the light-transmission data for the various volumes sprayed for a given spray condition must therefore be corrected for the changes in drop sizes that occur during, and as a result of, the spray period.

An empirical procedure based on the drop-out measurements previously described was developed to make the required correction. These measurements provide a quantitative measure of the mass of liquid that drops out of the system during the spray period as a function of the volume sprayed. A mass balance for the system during the spray period is written as follows:

(mass sprayed) = (mass in suspension) + (mass impinging on walls) + (mass that drops out) + (mass evaporated)

$$m_s = m_{is} + m_w + m_d + m_e \qquad (4)$$

Equation (4) rearranged with all measurable quantities on one side of the equation becomes

$$\frac{m_s - m_d}{m_s} = \frac{m_{is} + m_w + m_e}{m_s} \qquad (5)$$

The term on the left-hand side of equation is defined as the *effective fraction*. A few typical experimental curves illustrating the relationship between the effective fraction and the volume sprayed are shown in Figure 4. It is noted that the effective fraction approaches unity as the volume sprayed approaches zero and by extrapolation the curves appear to intersect the ordinate at an effective fraction of unity for zero volume sprayed. Experimental measurements of the mass of liquid that drops out of the system during the spray period indicate that the drop out approaches zero as the mass sprayed approaches some small value ϵ. The numerator of the right side of Equation (5) must also approach ϵ as the mass sprayed approaches ϵ. A consideration of the physical significance of the terms in the numerator and the experimental conditions leads to the following conclusions. As the mass sprayed approaches ϵ, there is insufficient turbulence generated in the chamber to deposit liquid on the walls of the chamber, and the term m_w approaches zero.

The mass that evaporates from the drops approaches $\chi\epsilon$ as m_s approaches ϵ, where χ is some small fraction of ϵ. Therefore, the mass remaining in suspension m_{is}, approaches $\epsilon(1 - \chi)$ as m_s approaches ϵ. Experimental evidence, given under Results, indicates that the atmosphere of the chamber is saturated by spraying before a series of runs is made and that the magnitude of the evaporation term is negligibly small.

The changes in drop-size distribution caused by coalescence or interception

during the spray period are a function of (1) the degree of turbulence during the spray period, (2) the product of the concentrations of the drops undergoing coalescence or interception, and (3) the size of these drops. Decreasing the mass sprayed, and therefore the concentration of drops, reduces the changes in drop size caused by coalescence or interception to a negligible factor as the mass sprayed approaches zero. These factors as well as the changes in drop size caused by coalescence or interception during the differential settling period are discussed briefly under Results.

Thus, at an effective fraction of one the changes in drop-size distribution that occur during the spray period as a result of coalescence or interception, impingement on the walls, and drop out are minimized. The effect of evaporation is minimized by saturating the chamber prior to an experiment.

In the present investigation it was desired to characterize the spray in terms of the specific surface area. The specific surface area for drops up to 40 μ in diameter for the various volumes sprayed at a given spray condition is obtained by integrating the surface-frequency distribution curves. The correction to the specific-surface-area values for drops up to 40 μ in diameter is made by plotting those values against their corresponding effective fractions and extrapolating the curve to effective fraction equal to 1. For the liquids and operating conditions studied, the relationship between the specific surface area and the effective fraction is found to be linear.

The specific surface area of drops greater than 40 μ is estimated by the following empirical procedure. The volume-frequency distribution curves for each volume sprayed in a series of runs for the same liquid and spray pressure are integrated to obtain the volume-fraction curves as a function of the drop diameter. The volume fraction is defined as the volume of spray drops up to a given drop diameter per unit of volume sprayed. A cross plot is then made of the values of the volume fraction for various constant drop diameters vs. the effective fraction corresponding to the volume sprayed. The values of the volume fraction at a constant drop diameter are found to be linear functions of the effective fraction and are readily extrapolated to effective fraction equal to 1 to correct for the changes in drop sizes that occur during the spray period. For the liquids investigated, the logarithm of the corrected volume fraction is a linear function of the reciprocal of the diameter in the region between 15 and 40 μ.

It was assumed that the logarithm of the corrected volume fraction for drop diameters greater than 40 μ continued as a linear function of the reciprocal of the diameter. Drop-size data reported by other investigators (*4, 9, 13*) for different nozzles also exhibit a linear relationship between the logarithm of the volume fraction and the reciprocal of the diameter in the region of larger drop diameters.

Table 1

Liquid Physical Properties and Flow Rates

Liquid and nozzle	μ, cp.	ρ, g./cc.	γ, dynes/cm.	Refractive index	Volume rate, cc./sec.	Spray pressure, lb./sq. in.
Distilled water						
Nozzle 0.75–30 deg.	0.91	1.0	70.0	1.33	1.83	2,000
Nozzle 0.75–60 deg.	0.91	1.0	70.0	1.33	2.10	2,000
Nozzle 0.75–80 deg.	0.91	1.0	70.0	1.33	2.04	2,000
Nozzle 0.75–60 deg.						
Kerosene	1.63	0.807	28.0	1.52	1.53	700
	1.68	0.808	28.0	1.52	2.07	1,500
Butyl cellosolve	2.99	0.900	29.9	1.42	2.10	1,400
	2.99	0.900	29.9	1.42	2.49	2,100
Ethylene glycol	17.8	1.112	50.0	1.43	2.52	1,400
	17.8	1.112	50.0	1.43	2.90	2,000
Diethylene glycol	29.1	1.118	47.5	1.43	3.10	1,800
Propylene glycol	45.5	1.034	38.0	1.43	2.96	1,150

The analytical expression for the linear relationship between the logarithm of the volume fraction and the reciprocal of the drop diameter is

$$\frac{V_D}{V} = e^{(a/D+b)} \tag{6}$$

The volume of drops up to any diameter in terms of the volume-frequency distribution curve is

$$V_D = \frac{\pi}{6} \times 10^{-12} V_c \int_0^{\infty} ND^3\, dD \tag{7}$$

Substituting for V_D from Equation (7) in Equation (6), differentiating with respect to D, and dividing by the density of the liquid ρ gives:

$$\frac{\pi \times 10^{-8} V_c N D^2\, dD}{V\rho} = \frac{-6 \times 10^4 a e^b e^{a/D}\, dD}{\rho D^3} \tag{8}$$

Since the integral of the left-hand side of Equation (8) is equal to the specific surface area, the specific surface area of drops greater than 40 μ in diameter is obtained by integrating Equation (8) between the limits of D equal to 40 μ and D_m.

$$S_{>40} = \frac{6 \times 10^4 e^b}{\rho} \cdot \left[e^{a/D} \left(\frac{1}{D} + \frac{1}{a} \right) \right]_{D=40}^{D=D_m} \tag{9}$$

D_m is determined from the value of the abscissa at which the extrapolated straight line intersects the volume frac-

Table 2

Sample Calculation for Distilled Water

Nozzle: 0.75–60 deg. Pressure: 2,000 lb./sq. in. Volume sprayed: 50.0 cc.

Run					2,039*A*				2,039*B*	2,040	
Elapsed time, sec.	Deflection M	t, sec.	t_{avg}, sec.	$\frac{1}{2}$ t_{avg}	5/2 $t_{avg} \times 10^{-4} \Delta M$		M_{avg}	RK_tN	RK_tN	RK_tN	D, μ
23	59.0										
46	66.0	23	34.5	5.9	0.7	4.0	61.0				
69	66.0	23	57.5	7.6	2.5	3.0	64.5	5.15	7.0	10.0	40.1
92	72.0	23	80.5	9.0	5.8	6.0	69.0	22.3	16.0	18.0	33.9
115	76.0	23	103.5	10.2	10.9	4.0	74.0	25.9	22.7	29.0	29.9
138	79.5	23	126.5	11.2	17.8	3.5	77.8	35.2	39.1	42.0	27.1
183	86.0	45	160.5	12.7	32.4	6.5	82.8	57.3	55.0	68.0	24.0
252	94.5	69	217.5	14.8	69.9	8.5	90.3	96.6	85.0	104.0	20.6
321	101.0	69	286.5	16.9	138.5	6.5	97.3	136.0	136.0	149.0	18.0
413	109.0	92	367	19.2	257	8.0	105.0	216	199	234	15.9
504	115.0	91	459	21.4	450	6.0	112.0	268	307	298	14.2
595	121.0	91	550	23.5	710	6.0	118.0	401	391	363	13.0
687	126.3	92	641	25.3	1,040	5.3	123.7	471	401	377	12.0
778	129.3	91	733	27.1	1,450	3.0	127.8	379	325	439	11.2
859	131.2	81	819	28.6	1,910	1.9	130.3	348	348	441	10.6
1,031	132.5	172	945	30.8	2,750	1.3	131.9	160	133	344	9.9
1,260	132.8	229	1,146	33.9	4,450	0.3	132.7	45	73	148	9.0

tion equal to 1. It should be noted that this procedure does not predict the maximum drop size present in the spray but does give an accurate estimate of the surface area of the drops above 40 μ in diameter.

The specific surface area of the spray is the sum of the specific surface for drops up to 40 μ corrected by extrapolating to effective fraction equal to 1 and the specific surface area of drops greater than 40 μ estimated by means of Equation (9).

The corrected volume, surface, and size-frequency curves of the spray are obtained by differentiation of the corrected volume-fraction-vs.-diameter curve.

SIZE- SURFACE- AND VOLUME-DISTRIBUTION CURVES

The data from the series of runs made with water at a spray pressure of 2,000 lb./sq. in. with nozzle 0.75 to 60 deg. are used to illustrate the method of computation and extrapolating procedures. The physical properties of the air for these runs are viscosity, 1.8×10^{-4} poise, and density, 0.0011 g./cc.

The quantities RK_tN as a function of the drop diameter are calculated for a set of duplicate runs by means of Equations (2) and (3). The original light-transmission curves of recorder deflection vs. elapsed time from the end of spray are divided into small time increments so that the original curve may be represented by a series of straight-line segments of slope $\Delta M/\Delta t$. Since the deflection of the recorder is linear with the intensity of the light beam, the recorder deflection may be substituted for the light intensity in Equation (3).

The equations for the water runs are

$$RK_tN = \frac{0.1012}{M_{avg}}\left(\frac{\Delta M}{\Delta t}\right)(t_{avg})^{5/2} \qquad (3a)$$

$$D = 304(t_{avg})^{-1/2} \qquad (2a)$$

The average values indicated in the in the equations for the recorder deflection and the time are the arithmetic average for the particular increment of the curve. The calculations for run 2,039*A*, in which 50 cc. of water was sprayed are summarized in Table 2. The values of RK_tN for the duplicate runs are also listed. The dotted line in Figure 5 indicates the relationship between RK_tN and the diameter. The size-frequency distribution curve, the solid line, is obtained by dividing the ordinate values of the RK_tN curve by the values RK_t for the diameters corresponding to the particular ordinate values. The relationships between R and D and K_t and α are shown in Figures 6 and 7 respectively (*1, 2*).

The surface-area and volume distribution curves are obtained by multiplying the ordinate values of the size-frequency curve by the square and cube respectively of the corresponding diameter. The specific surface area of the spray for drops up to 40 μ in diameter is obtained by integrating the surface-area distribution curve and multiplying the result by the quantity $(V_c \times 10^{-8})/V\rho$. The volume fractions of the spray up to a given drop diameter are obtained by partial integrations of the volume dis-

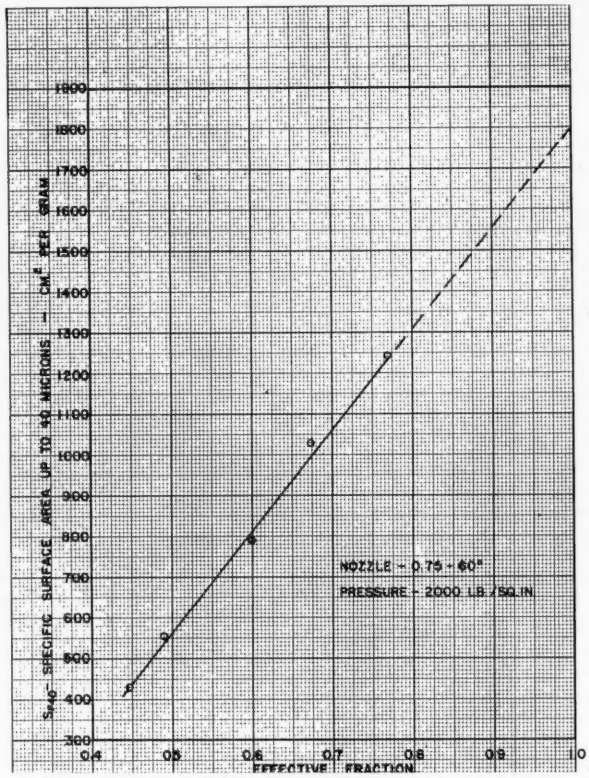

Fig. 8. Specific surface area vs. effective fraction for water spray.

TABLE 3

SUMMARY OF CALCULATION FOR DISTILLED WATER

Nozzle: 0.75–60 deg. Pressure: 2,000 lb./sq. in.

Volume sprayed, cc.	Volume fractions up to diameter D, μ									$S_{<40}$, sq. cm./g.	Effective fraction
	8	10	12	14	16	20	24	32	40		
300	0.00	0.001	0.010	0.019	0.028	0.047	0.067	0.110	0.155	425	0.450
200	0.00	0.001	0.009	0.021	0.035	0.062	0.090	0.148	0.205	551	4.485
100	0.00	0.002	0.011	0.027	0.046	0.087	0.130	0.219	0.300	787	0.600
75	0.00	0.002	0.013	0.036	0.062	0.116	0.173	0.288	0.387	1.025	0.675
50	0.00	0.002	0.016	0.044	0.072	0.134	0.201	0.336	0.462	1,232	0.770
	0.00	0.003	0.024	0.063	0.103	0.196	0.292	0.485	0.665	1,800	1.000
									$S_{>40}$ = 406		
									S = 2,206		

tribution curve. The calculations for the series of water runs at 2,000 lb./sq. in. are summarized in Table 3.

The extrapolation of the specific surface area for drops up to 40 μ to an effective fraction equal to 1 is shown in Figure 8.

A similar plot for the volume fractions taken from Table 3 is shown in Figure 9. The corrected values of the volume fractions up to various diameters, obtained by extrapolation of the curves to an effective fraction equal to 1 in Figure 9, are tabulated in the last line of Table 3. The relationship between the corrected volume fraction and reciprocal of the diameter is shown in Figure 10. The dotted-line extrapolation of the straight-line region intercepts the volume fraction at unity at a value of $1/D$ equal to 0.0165 or a value of the maximum diameter D_m equal to 60.5 μ. The slope of this line a and the constant b are -48.0 and 0.792 respectively. Equation (9) for estimating the specific surface area of drops greater than 40 μ in diameter becomes

$$S_{>40} = 6 \times 10^4 e^{0.792} \cdot \left[e^{-48/D} \left(\frac{1}{D} + \frac{1}{48} \right) \right]_{40.0}^{60.5} \qquad (9a)$$

The value of $S_{>40}$ by this equation is 406 sq. cm./g. The specific surface area of the spray, the sum of the corrected specific surface area for drops up to 40 μ, and $S_{>40}$ is 2,206 sq. cm./g.

The corrected volume-distribution curve, obtained by differentiation of the corrected volume-fraction-vs.-diameter curve of Figure 10 is shown in Figure 11. The corrected surface-area distribution and size-frequency curves, obtained by dividing the ordinate of the curve in Figure 11 by the diameter and the square of the diameter respectively, are shown in Figures 12 and 13. It should be noted that integration of the corrected surface distribution curve in Figure 12 up to 40 μ gives a value of 1,865 sq. cm./g., which compares favorably with the value of 1,800 sq. cm./g. obtained by direct extrapolation of the specific surface area for drops up to 40 μ from Figure 8.

The corrected volume fractions and specific surface areas of the sprays for the liquids investigated are summarized in Table 4.

CORRELATION OF DATA

The specific surface area of the sprays is correlated empirically with the aid of dimensional analysis. For a given nozzle of a specific design it is possible to express the specific surface area as a function of the flow rate, liquid physical properties, and a single parameter for the nozzle. The relationship is of the following form:

$$SD_0\rho = k\left(\frac{q\rho}{D_0\mu}\right)^d \left(\frac{D_0\rho\gamma}{\mu^2}\right)^f \qquad (10)$$

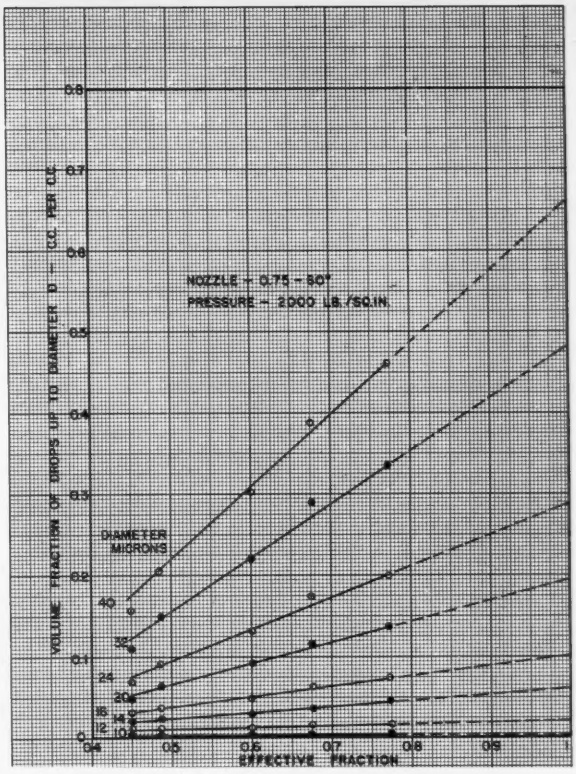
VOLUME FRACTION OF DROPS UP TO DIAMETER D – CC. PER CC.
NOZZLE – 0.75 – 80°
PRESSURE – 2000 LB./SQ.IN.
DIAMETER MICRONS
EFFECTIVE FRACTION

Fig. 9. Volume fraction vs. effective fraction for water spray.

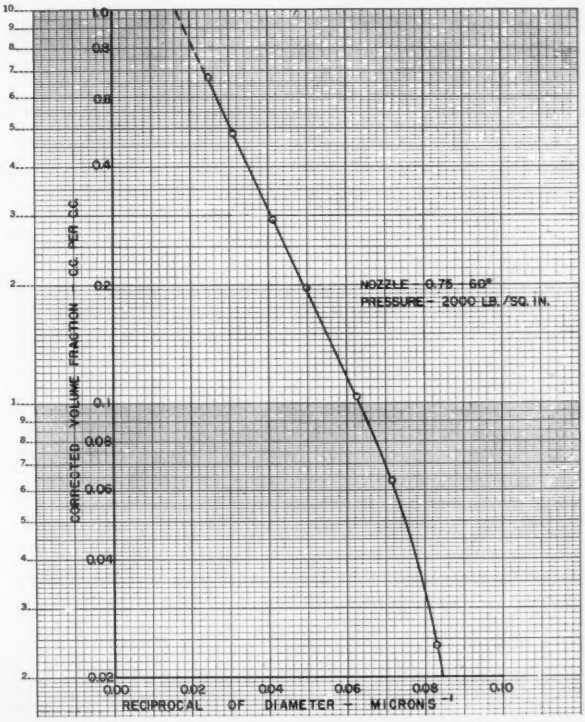

Fig. 10. Corrected volume fraction vs. reciprocal of diameter for water.

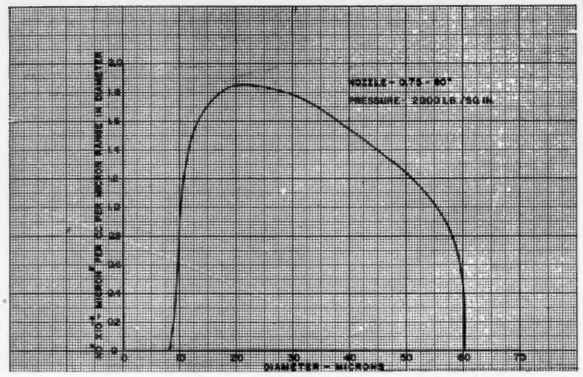

Fig. 11. Corrected volume distribution curve for water.

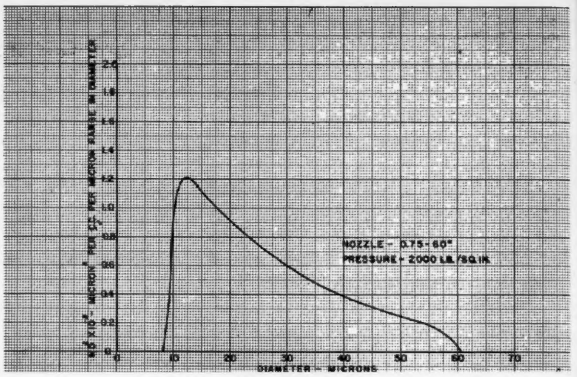

Fig. 12. Corrected surface-area distribution curve for water spray.

TABLE 4

SUMMARY OF CORRECTED VOLUME FRACTIONS AND SPECIFIC SURFACE AREAS OF SPRAYS

Nozzle and liquid	Spray Pressure, lb./sq. in.	Corrected volume fractions up to diameter D, μ												$S_{<40}$, sq. cm./g.	$S_{>40}$, sq. cm./g.
		2	4	5	8	10	12	14	16	20	24	32	40		
Distilled water															
Nozzle–0.75–30 deg.	1,000	—	—	—	—	0.000	0.006	0.033	0.065	0.150	0.200	0.352	0.525	1,360	539
Nozzle–0.75–60 deg.	2,000	—	—	—	0.00	0.003	0.024	0.063	0.103	0.196	0.292	0.485	0.665	1,800	406
Nozzle–0.75–80 deg.	2,000	—	—	—	—	0.000	0.020	0.070	0.225	0.300	0.400	0.717	0.950	2,500	70
Nozzle 0.75–60 deg.															
Kerosene	700	0.00	0.004	0.013	0.035	0.058	0.089	0.120	0.140	0.195	0.245	0.343	0.420	1,975	485
	1,500	0.00	0.020	0.055	0.115	—	0.182	—	0.220	0.264	0.310	0.415	0.540	3,500	575
Butyl cellosolve	1,400	—	—	—	0.00	—	0.021	—	0.092	0.165	0.230	0.405	0.525	1,630	530
	2,200	—	—	—	0.00	0.000	0.013	0.095	0.147	0.245	0.325	0.468	0.610	2,250	450
Ethylene glycol	1,400	—	0.00	0.012	0.035	—	0.100	—	0.149	0.193	0.247	0.345	0.455	1,500	394
	2,000	—	0.00	0.005	0.024	—	0.098	—	0.163	0.255	0.335	0.480	0.623	2,010	380
Diethylene glycol	1,800	—	0.006	0.032	0.050	—	0.120	0.167	—	0.410	0.495	0.60	0.680	2,400	260
Propylene glycol	1,150	—	0.00	—	0.025	—	0.054	—	0.070	0.094	0.110	0.140	0.190	970	600

A general equation to include the effects of internal nozzle design leads to additional dimensionless groups. For swirl-chamber nozzles of the grooved-core type, the number, size, shape, and pitch of the grooves; the size and shape of the swirl-chamber; and the length and diameter of the orifice have to be considered. The feasibility of a general correlation of this type however is doubtful because of the lack of complete geometric similarity for commercial nozzles of the same type but of different rated capacities.

In this investigation, since the range of the density variable is small (0.80 to 1.0 g./cc.), it is assumed that the flow conditions may be characterized by the kinematic viscosity, instead of the density and viscosity as in Equation (10). This assumption leads to the following simplified relationship:

$$\frac{SD_0^2\gamma}{(\mu/\rho)^2} = k''\left(\frac{q}{D_0\mu/\rho}\right)^{d'} \qquad (11)$$

The values of the dimensionless groups for Equation (11) are given in Table 5* and are plotted in Figure 14.

*Tables 5 and 6 are deposited as document 5300 with the American Documentation Institute, Photoduplication Service, Library of Congress, Washington 25, D. C., and may be obtained for $1.25 for photoprints or 35-mm. microfilm.

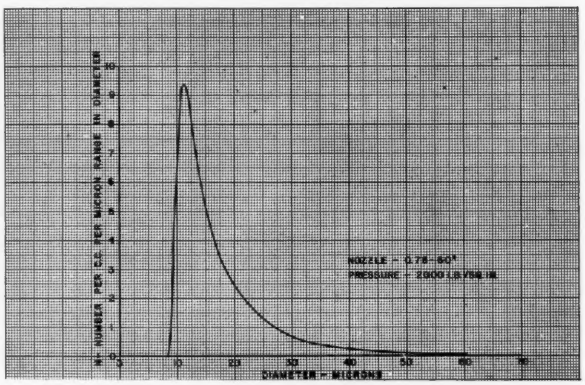

Fig. 13. Corrected size-frequency distribution curve for water.

The volume flow rate is correlated as a function of the pressure drop, viscosity, density, and orifice diameter. The relationship obtained is

$$\frac{D_0^2\Delta P\rho}{\mu^2} = k'''\left(\frac{q\rho}{D_0\mu}\right)^{g} \qquad (12)$$

The values of the dimensionless groups for Equation (12) are given in Table 5 and are plotted in Figure 15. An alternative correlation of the volume flow rate can be made in terms of the coefficient of discharge for the nozzle vs. a Reynolds number based on the diameter of the nozzle orifice. However, it should be noted that ether procedure is empirical.

The equality of the exponents for the Reynolds number for the surface-area and volume-flow-rate correlations (Figures 14 and 15) leads to the following relation between the compression energy in the fluid supplied to the nozzle and the conversion to surface-area energy:

$$S\gamma = 1.04 \times 10^{-3}\,\frac{\Delta P}{\rho} \qquad (13)$$

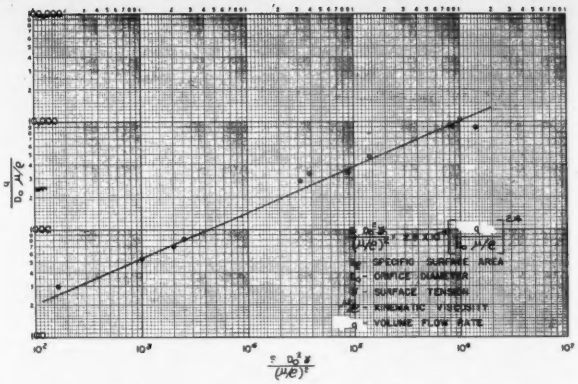

Fig. 14. Correlation of specific surface area and operating variables.

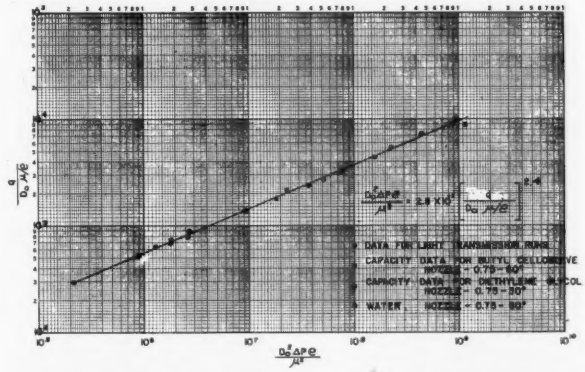
DATA FOR LIGHT TRANSMISSION TUBE
CAPACITY DATA FOR BUTYL CELLOSOLVE NOZZLE = 0.75 - 80°
CAPACITY DATA FOR DIETHYLENE GLYCOL NOZZLE = 0.75 - 30°
WATER NOZZLE = 0.75 - 80°

Fig. 15. Correlation of nozzle flow rate and operating variables.

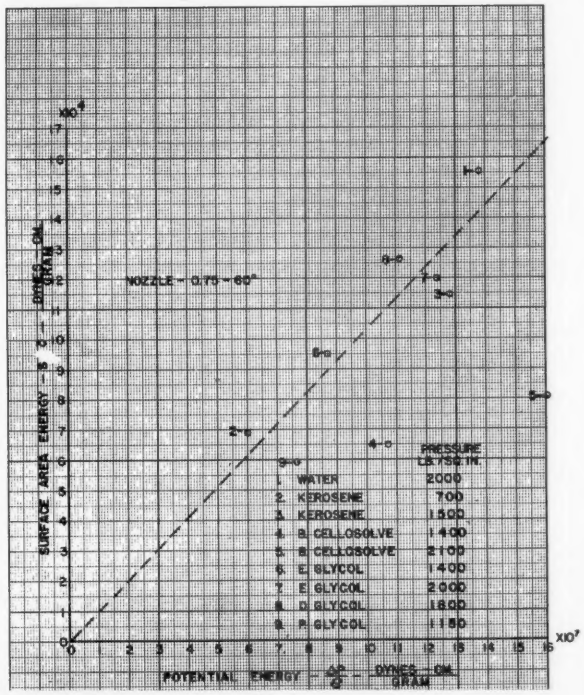
NOZZLE - 0.75 - 60°
SURFACE AREA ENERGY - S - DYNES - CM. / GRAM
POTENTIAL ENERGY - ΔP/ρ - DYNES - CM. / GRAM
PRESSURE LB./SQ. IN.
1. WATER 2000
2. KEROSENE 700
3. KEROSENE 1500
4. B. CELLOSOLVE 1400
5. B. CELLOSOLVE 2100
6. E. GLYCOL 1400
7. E. GLYCOL 2000
8. D. GLYCOL 1800
9. P. GLYCOL 1150

Fig. 16. Conversion of potential energy to surface-area energy.

Equation (13) can be anticipated from the general Bernoulli equation by expressing the kinetic energy and irreversibilities as a fraction of the pressure drop. The data obtained with a nozzle of 0.75 to 60 deg., plotted according to Equation (13), are shown in Figure 16.

RESULTS

The deviation of the data for nozzle 0.75—80 deg. from the correlation lines in Figures 14 and 15—is due to the noncircular shape of the orifice and the difficulty of assigning a correct value for the diameter of the orifice. A high value for the diameter magnifies the error in the surface area and pressure dimensionless groups on Equations 11 and 12. The deviation of the data for the butyl cellosolve sprays from the surface-area–correlation line in Figure 14 is due to low values of the specific surface area. Additional experiments indicate that the butyl cellosolve vapor reacted with the paint on the interior walls of the spray chamber, which caused the smaller drops to evaporate during the settling period.

The low value of the propylene glycol point is probably due to a low value of the specific surface and represents the limit of the experimental technique for the present equipment. This spray contained such a large percentage of drops greater than 40 μ in diameter that the extrapolations to effective fraction equal to 1 could not be done very accurately. The same difficulty was encountered in attempting to take data for the liquids at flow rates lower than those reported.

An attempt to check the surface-area values obtained from the present study by means of a high-speed photographic technique (*13*) was not successful. The available equipment could not resolve the droplets because of the high velocity of discharge from the nozzle orifice. Any other method which depends on collecting a sample of the settling spray would necessarily involve corrections similar to those employed in this study.

The effects of the initial humidity in the spray chamber on the size-frequency distribution curves and the corrected volume fractions of the spray obtained by extrapolation to an effective fraction of 1 are shown in Figures 17 and 18.

The curves in Figure 17 show the relative size-frequency distribution curves obtained for runs in which the same quantity of water was sprayed into the chamber at three different conditions of initial humidity. The upper curve is the result of spraying into the chamber and keeping the door closed between runs, which was the normal experimental procedure; the middle curve of opening the chamber door and turning on a ¼-in. compressed air line at the top of the chamber for approximately 1 min.

between runs; the lower curve of opening the chamber door and directing the air stream of an electric fan into the chamber for approximately 3 min. The curves show that the evaporation of the smaller drops is greater the lower the initial humidity. It is seen from the lower curve that the initial humidity was so low that all drops between 8 and 13 μ evaporated completely. Obviously under these conditions it is impossible to extrapolate to effective fraction equal to 1 in order to obtain the true distribution of drops produced by the nozzle.

Figure 18 shows the results of two series of runs at the same conditions except for the initial humidity of the chamber. The solid lines represent runs made at an initial humidity equivalent to the upper curve of Figure 17 and the dotted line equivalent to the middle curve of Figure 17. The volume fractions extrapolate to within 3% of the same values. These results are believed to be within the range of experimental error. These tests indicate that the closed chamber should be saturated by spraying in order to minimize the loss of drops by evaporation during the spray and settling periods. For small departures from the saturated conditions, the results indicate that the extrapolation of the volume fraction to effective fraction equal to 1 may correct for some of the losses caused by evaporation.

The phenomena of interceptions of small drops by larger drops and the coalescence of smaller drops by diffusion during the differential settling period can give rise to errors in the calculated values of the number of drops from Equation (3). Equation (3) assumes that the removal of the surface area from the light beam at any time is due only to drops leaving the light beam as a result of settling process. If the rate of removal of surface area from the light beam by interception and coalescence is appreciable, it would cause the calculated values of the number of drops to be higher for the larger drop sizes and lower for the smaller drop sizes.

Calculations based on Langmuir's work on interception (*5*) and Smoluchowski's expression for coalescence (*10*) indicate that the orders of magnitude of these phenomena for the most concentrated sprays encountered in this study are not serious. For the most concentrated spray produced in this study in terms of drops per unit of volume of dispersion approximation calculations indicate that the interception process causes a rate of removal of surface area of less than 5% of the rate of removal of surface area by the settling process and for the coalescence phenomena the corresponding value is less than 0.1%.

More important, however, is the fact that the degree of both these phenomena is a function of the product of the concentration of the drops under any interception or coalescence. Thus, decreasing

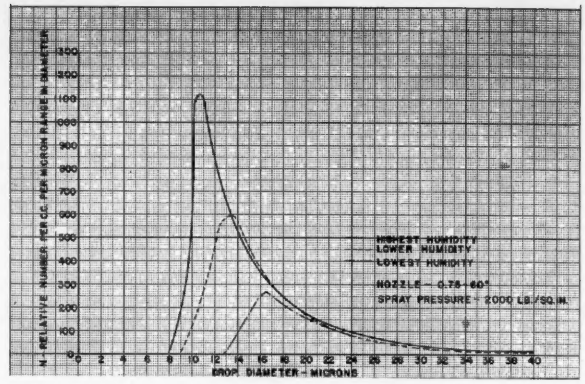
N - RELATIVE NUMBER PER CC. PER MICRON RANGE IN DIAMETER
DROP DIAMETER - MICRONS
HIGHEST HUMIDITY
LOWER HUMIDITY
LOWEST HUMIDITY
NOZZLE - 0.75 - 60°
SPRAY PRESSURE - 2000 LB./SQ.IN.

Fig. 17. Size-frequency curves for water at various degrees of initial humidity.

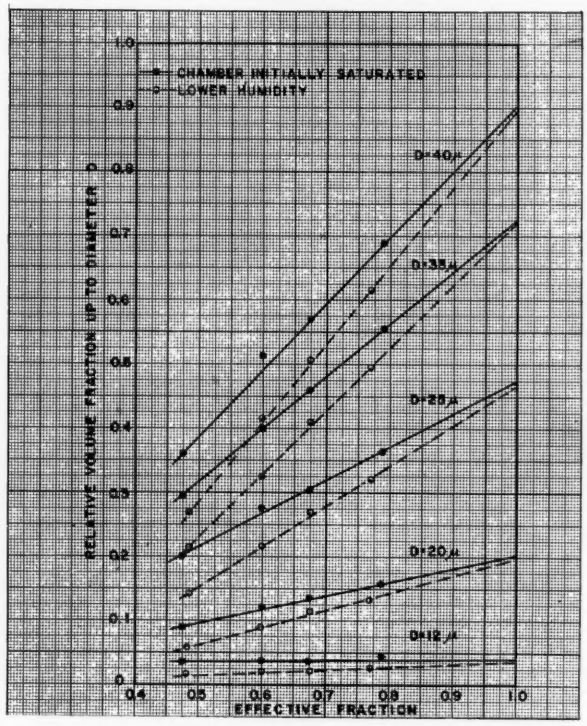

Fig. 18. Comparison of extrapolation for different degrees of initial chamber humidity.

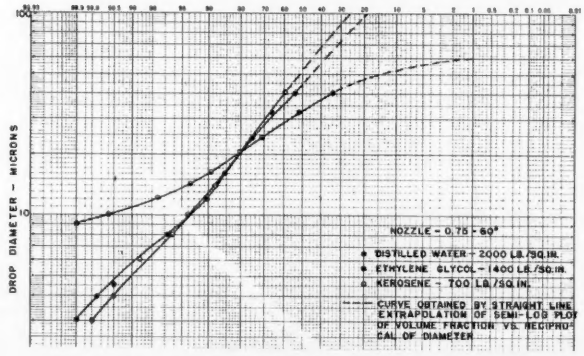
DROP DIAMETER - MICRONS
NOZZLE - 0.75 - 60°
DISTILLED WATER - 2000 LB./SQ.IN.
ETHYLENE GLYCOL - 1400 LB./SQ.IN.
KEROSENE - 700 LB./SQ.IN.
CURVE OBTAINED BY STRAIGHT LINE EXTRAPOLATION OF SEMI-LOG PLOT OF VOLUME FRACTION VS. RECIPROCAL OF DIAMETER

Fig. 19. Logarithmic-probability type of plot of spray data.

the volume of material sprayed into the chamber and then extrapolating the calculated results to an effective fraction equal to 1 minimizes the effects on these phenomena to a negligible value. This reasoning also applies to the changes in the drop-size distributions that occur during the spray period.

The errors introduced by the convection currents in the transition period following the end of the spray period and the assumption that Stokes's Law is valid from the end of the spray period are difficult to assess quantitatively. It is estimated the use of Stokes's Law results in underestimating the diameter by 3% in the region of 10 μ and less than 1% in the region of 5 μ. The use of Stokes's Law instead of the Stokes-Cunningham equation for the smaller drops results in an error of less than -2% in the value of the specific surface area for drops up to 40 μ.

The use of the Rosin-Rammler (*8*) and logarithmic-probability equations to estimate the surface area contributed by drops greater than 40 μ yields values for the specific surface area of the sprays which were within 1% of those obtained by the procedure used in this study. A few typical curves, shown in Figure 19, illustrate the fit of the drop-size distribution data to the log-probability distribution equation.

The quantitative effects of the physical properties of liquids on the specific surface area are in accord with deductions from theoretical considerations (*4*) which indicate that the drop-size of the spray should increase with surface tension and viscosity or kinematic viscosity. Data reported by Turner and Moulton (*12*) for grooved-core nozzles indicate that the logarithmic mean diameter varies directly as the 0.813 power of the surface tension and the 0.159 power of the viscosity. For their data the logarithmic diameter is approximately inversely proportional to the specific surface area. Thus the dependence of the specific surface area for their data on surface tension and viscosity is approximately to the -0.7 and -0.2 power, respectively. For the present study the dependence is to the -1.0 and 0.4 power, respectively. The effect of the volume flow rate on the specific surface area appears to be greater for this nozzle than that reported by previous investigators. Data reported by Rupe (*9*), Lloyd (*6*), Tate and Marshall (*11*), and Houghton (*4*) indicate exponents ranging from 0.3 to 0.80 on the flow rate vs. an exponent of 2.4 for the nozzle used in this study.

ALTERNATIVE FLOW-RATE CORRELATION

The usual method for correlating flow rate with spray pressure is by means of the nozzle discharge coefficient defined as follows:

$$K = \frac{4q}{\pi D_0^2 \left(2g_c \frac{\Delta P}{\rho}\right)^{0.5}} \qquad (14)$$

In terms of the correlation presented above, Equation (12) and Figure 15,

$$K = \frac{4}{\pi[(2.81 \times 10^{-4})(2g_c)]^{1/2}} \cdot \left(\frac{q}{D_0 \mu/\rho}\right)^{-0.2} \qquad (15)$$

Typical values for the discharge coefficient for nozzle 0.75 to 60 deg. are given in Table 6.*

Since the discharge coefficient varies with the flow rate and the physical properties of the fluid, it is evident that viscous forces are not negligible over the range of variables covered by this study (*11*).

NOTATION

a = slope of empirical volume fraction equation $V_D/V = e^{(a/D+b)}$

b = intercept of volume fraction equation at point $V_D/V = 1.0$

D = drop diameter, μ

D_m = maximum drop diameter obtained by extrapolation of the corrected volume fraction

D_0 = orifice diameter of spray nozzle, cm.

d, d', f, g = exponents for dimensionless groups in Equations (11) and (12)

h = settling height from top of spray chamber to center of light beam, cm.

I = intensity of light beam after traversing through a dispersion of drops through a path length of l cm.

I_0 = intensity of light beam without a dispersion of drops in the spray chamber

k = Stokes's Law equation constant equal to $[18h/g_L(\rho_L - \rho_a)]^{1/2}$

k', k'', k''' = constants in dimensionless equations (*11*) and (*12*).

K_t = Mie theory total scattering coefficient

l = length of light beam through a dispersion of drops, cm.

M = recorder deflection, a linear function of the light intensity, I

m_d = mass of liquid that drops out of the spray chamber and onto a removable drawboard at the bottom of the chamber during the spray period

m_e = mass of liquid that evaporates from the spray drops during the spray period

m_{is} = mass of liquid that remains in suspension in the form of drops at the end of the spray period

m_s = mass of liquid sprayed

m_w = mass of liquid that impinges on the walls of the spray chamber during the spray period

N = derivative with respect to D of the cumulative drop-size distribution function per unit of volume of dispersion, cm.$^{-4}$

ΔP = spray pressure, lb./sq. in.

q = volume flow rate through spray nozzle, cc./sec.

R = correction factor to the total light-scattering coefficient

S = specific surface area of the spray equal to the sum of the extrapolated value of $S_{<40}$ and $S_{>40}$, sq. cm./g.

$S_{<40}$ = specific surface area of spray for drops up to 40 μ obtained by integration of surface-area–frequency curve

$S_{>40}$ = specific surface area of spray for drops greater than 40 μ estimated by means of Equation (9)

t = elapsed settling time from the end of the spray period, sec.

V_c = volume of spray chamber, cc.

V_D = volume of spray drops up to a diameter D, cc.

V = volume of liquid sprayed into the spray chamber, cc.

α = light-scattering–coefficient parameter equal to $\pi D/\lambda$

γ = surface tension of liquid, dynes/cm.

λ = wave length of incident light beam, cm.

μ = viscosity, poise

$(\rho_L - \rho_a)$ = density difference between the drops and surrounding medium g./cc.

χ = fraction of liquid evaporated from spray drops during the spray period

LITERATURE CITED

1. Gumprecht, R. O. and C. M. Sliepcevich, *J. Phys. Chem.*, **57**, 90 (1953).
2. *Ibid.*, p. 95.
3. ———, "Tables of Light-Scattering Functions for Spherical Particles," Univ. Mich., Eng. Research Inst., Special Publications, Ann Arbor (1951).
4. Houghton, H. G., in "Chemical Engineers' Handbook," ed. by J. H. Perry, 3 ed., p. 1170–1175, McGraw-Hill Book Company, Inc., New York (1950).
5. Langmuir, Irving, *Gen. Elec. Research Lab. Rep.* RL 140, pp. 51–59, Schenectady, N. Y. (Dec. 31, 1948).
6. Lloyd, P., *Proc. Inst. Mech. Engrs.* (London), **15**, 462 (1945).
7. Mie, Gustave, *Ann. Physik*, **25**, 377 (1908).
8. Rosin, P., and E. Rammler, *J. Inst. Fuels*, **7**, 29 (1933).
9. Rupe, J. H., in "Third Symposium on Combustion and Flame and Explosion Phenomena," The Williams and Wilkins Company, Baltimore (1949).
10. Sinclair, D., "Handbook on Aerosols," chap. 5–8, U. S. Atomic Energy Commission, Washington, D. C. (1950).
11. Tate, R. W., and W. R. Marshall, Jr., *Chem. Eng. Progr.*, **49**, 226 (1953).
12. Turner, G. M., and R. W. Moulton, *ibid.*, **49**, 185 (1953).
13. York, J. L., Ph.D. dissertation, Univ. Mich., Ann Arbor (1949).

*See footnote on page 424.

Critical Constants of the Aromatic Hydrocarbons

GEORGE THODOS

The Technological Institute, Northwestern University, Evanston, Illinois

Following an approach similar to that presented for the aliphatic (*6*, *7*) and naphthenic (*8*) hydrocarbons, methyl-group contributions have been developed that now make possible the calculation of van der Waals' constants for aromatic hydrocarbons of considerable size and complexity. These constants are then utilized to calculate the critical temperatures, pressures, and volumes for these aromatic hydrocarbons.

In addition, simple relationships have been developed that permit the evaluation of both van der Waals' constants for the unsubstituted linearly fused aromatic hydrocarbons.

Comparisons of calculated critical constants with values presented in the literature for over twenty aromatic hydrocarbons produced average absolute deviations of 0.70% for the critical temperature and 2.14% for the critical pressure.

The critical temperatures and pressures available in the literature (*3*) for over twenty aromatic hydrocarbons have been used in this study as the background necessary for the prediction of critical constants for this type of compound. To make this investigation consistent with studies of the aliphatic and naphthenic hydrocarbons (*6*, *7*, *8*), the van der Waals' constants a and b have been considered as the basic building blocks necessary to define the critical temperature and pressure through the relationships

$$T_c = \frac{8a}{27Rb} \tag{1}$$

and

$$p_c = \frac{a}{27b^2} \tag{2}$$

The available critical temperatures and pressures of several aromatic hydrocarbons have permitted the evaluation of van der Waals' constants a and b, for these hydrocarbons from the relationships

$$a = \frac{27R^2T_c^{\,2}}{64p_c} \tag{3}$$

$$b = \frac{RT_c}{8p_c} \tag{4}$$

In order to make the treatment of van der Waals' constants for these aromatic hydrocarbons consistent with that of the constants for the aliphatic and naphthenic hydrocarbons (*6*, *7*, *8*), values of $a^{0.626}$ and $b^{0.76}$ were produced which permitted the replacement of hydrogen atoms by methyl group substitutions in a similar way.

A comparison of $a^{0.626}$ and $b^{0.76}$ values available for benzene and naphthalene produces the following differences for these two compounds:

	$a^{0.626}$	$b^{0.76}$
Naphthalene	58,047	55.256
Benzene	35,385	37.707
	22,662	17.549

These differences have been taken to be the additive contributions for the calculation of both van der Waals' constants of linearly fused aromatic hydrocarbons. Therefore, the following relationships may be used for the calculation of van der Waals' constants for these unsubstituted polycyclic aromatic hydrocarbons:

$$a^{0.626} = 35{,}385 + 22{,}662(r - 1) \tag{5}$$

and

$$b^{0.76} = 37.707 + 17.549(r - 1) \tag{6}$$

where r represents the number of rings present in the unsubstituted aromatic hydrocarbons. With Equations (5) and (6), van der Waals' constants have been produced for the linearly fused aromatic hydrocarbons through hexacene, from which the critical temperatures and pressures have been calculated with Equations (1) and (2). Both van der Waals' constants and the critical values calculated for these compounds are presented in Table 1.

Average group-contribution values $\Delta a^{0.626}$ and $\Delta b^{0.76}$ involving the replacement of hydrogen atoms present in the aromatic ring and alkyl side chains by methyl groups have been calculated and are presented in Table 2. These quantities are the results of values obtained as differences of $a^{0.626}$ and $b^{0.76}$ values for hydrocarbons having similar structures but differing in molecular dimensions by a single methyl group. Thus the values $a^{0.626}$ and $b^{0.76}$ for toluene can be obtained through the addition of a methyl-group contribution on benzene to produce

$$a^{0.626} = 35{,}385 + 6{,}384 = 41{,}769$$

$$b^{0.76} = 37.707 + 6.548 = 44.255$$

Further replacements in the aromatic ring to produce dimethyl and trimethyl benzenes involve methyl-group-contribution values that are specific to the order of substitution and position occupied by these additional methyl groups. The group-contribution values for these types of substitutions are presented in Table 2, along with those associated in the replacement of hydrogen atoms from the alkyl-type carbon atoms present in the side chains.

To produce values of $a^{0.626}$ and $b^{0.76}$ for aromatic hydrocarbons having long alkyl side chains, substitutions should be made on methyl side chains only after all the necessary hydrogen atom replacements in the ring have been completed. Methyl-group contributions for the replacement of hydrogen atoms present in the methyl side chains are also presented in Table 2 and represent substitutions in which alkyl carbon atoms are involved. In this connection the classification proposed by Andersen, Beyer, and Watson (*1*) has been used to differentiate between the different types of carbon atoms present in the alkyl side chains. These investigators directly associate the numbers of carbon-to-carbon bonds to define the following types of alkyl carbon atoms:

Type	1	2	3	4
Structure	$-CH_3$	$-CH_2-$	$-CH<$	$-C-$

In Table 2, the designation $A \leftarrow 1$ indicates the substitution of a methyl group for a hydrogen atom present in a type-1 carbon attached to an aromatic ring. Thus this substitution indicates that the following structural changes must occur:

$$C_6H_5\cdot CH_3 \rightarrow C_6H_5\cdot CH_2CH_3$$

(toluene) (ethylbenzene)

Table 1. Calculated van der Waals' Constants and the Critical Temperatures, Pressures, and Volumes Resulting from Them for Some Linearly Fused Aromatic Hydrocarbons

	Van der Waals' constants		Critical constants			
	a, (cc./g.-mole)²(atm.)	b, cc./g.-mole	β_a	T_c, °K.	p_c, atm.	v_c, cc./g.-mole
Benzene	18.471×10^6	118.64	0.7315	562.2	48.60	260.4
Naphthalene	40.726×10^6	196.16	0.6906	749.7	39.20	406.4
Anthracene	68.950×10^6	281.97	0.6497	883.0	32.12	549.6
Naphthacene	102.39×10^6	374.64	0.6088	986.9	27.02	684.2
Pentacene	140.52×10^6	473.20	0.5679	1072	23.24	806.2
Hexacene	183.00×10^6	576.98	0.5270	1145	20.36	912.2

Similarly, the designation $A \leftarrow 2 \rightarrow 1$ signifies that a type-2 carbon atom is attached to an aromatic ring and a methyl group and that a replacement of the hydrogen present in the type-2 carbon atom must be made by a methyl group as follows:

$$C_6H_5 \cdot CH_2CH_3 \rightarrow C_6H_5 \cdot \underset{\displaystyle CH_3}{\underset{|}{C}}HCH_3$$

(ethylbenzene) (isopropylbenzene)

Further methyl-group substitutions can be made to produce the van der Waals' constants for aromatic hydrocarbons having larger alkyl side chains. For these types of substitutions, the group-contribution values and order of substitution developed for the aliphatic hydrocarbons (*6, 7*) are recommended as long as the carbon atom involved in the substitution is not attached to an aromatic or naphthenic ring. To illustrate the use of the contribution values presented in Table 2, the calculation of the critical temperature and pressure is presented for 1-methyl-2-isopropylbenzene:

1-Methyl-2-isopropylbenzene

	$a^{0.626}$	$b^{0.76}$
A. Base group—benzene	35,385	37.707
B. First methyl substitution	6,384	6.548
C. Second methyl substitution (ortho)	6,975	6.632
D. Alkyl methyl substitutions:		
$A \leftarrow 1$	5,700	5.987
$A \leftarrow 2 \rightarrow 1$	5,432	6.535
	$a^{0.626} = 59{,}876$	$b^{0.76} = 63.409$

$a = 42.795 \times 10^6$ (cc./g.-mole)²(atm.)
$b = 235.11$ cc./g.-mole

From Equations (1) and (2):

$$T_c = \frac{8a}{27Rb}$$

$$= \frac{8(42.795 \times 10^6)}{27(82.055)(235.11)} = 657.3°K$$

$$p_c = \frac{a}{27b^2}$$

$$= \frac{42.795 \times 10^6}{27(235.11)^2} = 28.67 \text{ atm.}$$

Kobe and Lynn (*3*) report critical values of 651.8°K. and 28.6 atm. for 1-methyl-2-isopropylbenzene.

By a similar procedure both van der Waals' constants were calculated for a number of aromatic hydrocarbons for which critical temperatures and pressures are available in the literature. With these constants, critical temperatures and pressures have been calculated with Equations (1) and (2) to produce the critical values presented in Table 3*. Comparisons of these calculated values with those available in the literature have been made to produce average absolute deviations of 0.70% for the critical temperature and 2.14% for the critical pressure. Excessive critical-pressure deviations were found to exist for 1-methyl-2-ethylbenzene, 1,2,4,-trimethylbenzene, and 1,3,5-trimethylbenzene. If the deviations for these aromatic compounds are not included, the average deviation for the critical pressure reduces to 1.46% for the remaining aromatic hydrocarbons. In addition, both van der Waals' constants and the critical temperatures and pressures resulting from them have been calculated for twenty-two aromatic hydrocarbons for which critical values are not available in the literature. These calculated values are presented in Table 4*.

CRITICAL VOLUME

After a careful screening of the critical values available in the literature, Kobe and Lynn (*3*) present reliable critical volumes for only benzene and toluene. Their selected values are for benzene, 260.4 cc./g.-mole and for toluene, 317.7 cc./g.-mole. These critical volumes have been used with the corresponding volume van der Waals' constants b to produce the volume factors β from the relationship

$$v_c = 3\beta b \qquad (7)$$

The calculated volume factors for benzene and toluene were found to be 0.7315 and 0.7231, respectively. Therefore, the difference of these values, $\Delta\beta = 0.7231 - 0.7315 = -0.0084$, represents the only available value involving the replacement of a hydrogen atom attached to an aromatic ring by a methyl group. The value $\Delta\beta = -0.0084$ has been assigned to this type of substitution and is considered reliable because it is of the same order of magnitude as that of a comparable substitution involving naphthenes (*8*), for which the value was found to be $\Delta\beta = -0.00785$. For the further substitution of methyl groups to produce longer alkyl side chains, the values produced for the aliphatic hydrocarbons have been assumed to apply. These values were $\Delta\beta = -0.01337$ for the methyl substitution to produce normal alkyl side chains and $\Delta\beta = -0.0138$ for branched alkyl side chains.

Since no reliable critical volume is available for naphthalene, the extension of volume factors to include the unsubstituted linearly fused aromatic hydrocarbons becomes limited. In order to circumvent this limitation, a critical volume of 408 cc./g.-mole for naphthalene was calculated by the method of Lydersen (*2*). This critical volume along with the corresponding volume van der Waals' constant, $b = 196.15$ cc./g.-mole, produces from Equation (7) the following volume factor for naphthalene:

$$\beta = \frac{408}{3(196.15)} = 0.6933$$

Following an analogous approach, the volume factor for 1,2-diethylbenzene was

Table 2. Group Contributions, $\Delta a^{0.626}$ and $\Delta b^{0.76}$ Associated in the Replacement of Hydrogen Atoms of Aromatic Hydrocarbons

Methyl-group contributions	$\Delta a^{0.626}$	$\Delta b^{0.76}$
First methyl substitution	6,384	6.548
Second methyl substitution		
ortho	6,975	6.632
meta	7,072	7.188
para	7,168	7.749
Third methyl substitution		
unsymmetric (1, 2, 3)	6,023	6.717
unsymmetric (1, 2, 4)	6,120	7.024
symmetric (1, 3, 5)	5,776	7.159
Fourth, fifth, and sixth methyl substitutions	6,945	7.530
Methyl-group substitutions on alkyl carbon atoms*		
$A \leftarrow 1$	5,700	5.987
$2 \leftarrow 1$	6,417	6.686
$A \leftarrow 2 \rightarrow 1$	5,432	6.535
$A \leftarrow 2 \rightarrow 2$	5,050	5.300
$2 \leftarrow 2 \rightarrow 1$	5,261	5.879
$A \leftarrow 3 \rightarrow 1$ (with $\downarrow$ 1)	5,185	5.050
Phenyl-group contributions		
First phenyl substitution	32,899	28.321
$A \leftarrow 1$	32,043	28.189

Note: A represents aromatic ring

*A more extensive list of methyl-group contributions involving the substitution of hydrogen in alkyl carbon atoms can be found elsewhere (*6*).

*Complete table is available from the American Documentation Institute, Photoduplication Service, Library of Congress, Washington 25, D. C., as document 5303 for $1.25 in microfilm or photoprints.

Table 3. Calculated Van der Waals' Constants and Comparisons of Critical Values Produced by the Present and the Methods of Riedel (4, 5) and Lydersen (2) with Values Available in the Literature (3) for Several Aromatic Hydrocarbons

	Calculated van der Waals' constants		Critical temperature, °K.				Critical pressure, atm.				Critical volume, cc./g.-mole	
	$a \times 10^{-6}$, (cc./g.-mole)^2 (atm.)	b, cc./g.-mole	Literature (3)	Riedel (5)	Lydersen (2)	This investigation	Literature (3)	Riedel (4)	Lydersen (2)	This investigation	Lydersen (2)	This investigation
Benzene	18.470	118.64	562.2	559.8	562.0	562.2	48.6	48.28	48.88	48.60	262	260.4
Toluene	24.074	146.47	594.0	593.2	594.5	593.5	41.6	40.84	41.44	41.56	316	317.7
Ethylbenzene	29.533	173.09	619.6	617.4	618.5	616.1	38	35.39	35.96	36.51	371	368.5
o-Xylene	30.810	176.02	631.6	629.8	631.0	632.1	36.9	35.39	35.96	36.83	370	377.4
m-Xylene	30.909	178.55	619.2	621.8	623.0	625.1	36	35.39	35.96	35.91	370	382.8
p-Xylene	31.006	181.12	618.2	620.7	621.8	618.2	35	35.39	35.96	35.01	370	388.3
i-Propylbenzene	35.114	203.30	635.9	629.5	634.1	623.7	32	31.23	32.34	31.47	422	424.2
1-Methyl-2-ethylbenzene	36.764	203.76	653.2	645.5	647.4	651.5	31	31.23	31.77	32.80	425	428.7
1-Methyl-4-ethylbenzene	36.972	209.04	636.2	640.9	642.7	638.7	31	31.23	31.77	31.34	425	439.8
Diphenylmethane	59.781	280.14	770.2	764.4	773.3	770.6	28.20	28.16	28.85	28.22	537	562.8
Average absolute deviation, %				0.70	0.75	0.70		2.64	2.56	2.14		

calculated from the background already presented to be

$$\beta = 0.7315 - 2(0.0084) - 2(0.01337) = 0.6880$$

Although the value 0.6880 has been specifically produced for 1,2-diethylbenzene, it is assumed to be applicable to naphthalene and together with the calculated value 0.6933 resulting from the critical volume calculated by the method of Lydersen (2) produces the average volume factor 0.6906, which is assumed to apply for naphalene. Consequently, the difference of volume factors between naphthalene and benzene represents the contribution necessary for the upgrading of an aromatic nucleus by one more ring. This value becomes $\Delta\beta = 0.6906 - 0.7315 = -0.0409$ and can be assumed to be the contribution for the addition of one more ring to an aromatic nucleus. Thus, for the linearly fused unsubstituted aromatic hydrocarbons, the volume factor β_a can be expressed as

$$\beta_a = 0.7315 - 0.0409(r - 1) \qquad (8)$$

where r represents the number of fused rings present in the unsubstituted aromatic hydrocarbon. With Equation (8), volume factors β_a have been calculated for the linearly fused aromatic hydrocarbons presented in Table 1, and together with their volume van der Waals' constants b the critical volumes have been calculated for these hydrocarbons with Equation (7). When alkyl side chains are attached to the linearly fused aromatic nucleus, the volume factor β_{as} becomes

$$\beta_{as} = 0.7315 - 0.0409(r - 1) - 0.0084(\alpha_n + \alpha_i) - 0.01337(n_{cn}' - \alpha_n) - 0.0138(n_{ci}' - \alpha_i) \qquad (9)$$

where

α_n, α_i = total number of normal and branched side chains attached to the aromatic nucleus, respectively

n_{cn}', n_{ci}' = total number of carbon atoms present in the normal and branched side chains, respectively

For the nonfused polycyclic aromatic hydrocarbons, the difference of values between benzene and *n*-hexane (6) has been taken as the contribution necessary to produce an aromatic ring from a corresponding normal paraffin. In this case

	β
benzene	0.7315
n-hexane	0.7047
	0.0268

the value $\Delta\beta = 0.0268$ represents the effective volume-factor contribution associated in the formation of an aromatic ring from a corresponding normal paraffin. Thus the volume factor of diphenyl can be obtained by the addition of 0.0268 to the value for *n*-hexyl benzene. From Equation (9) the volume factor for *n*-hexyl benzene is calculated to be

$$\beta_{as} = 0.7315 - 0.0084 - 0.01337(5) = 0.6563$$

and consequently that of diphenyl becomes $\beta = 0.6563 + 0.0268 = 0.6831$. By a similar procedure the volume factor of diphenylmethane is produced from the value for *n*-heptyl benzene. Thus, the volume factor for diphenylmethane becomes

$$\beta = 0.7315 - 0.0084 - 0.01337(6) + 0.0268 = 0.6429 + 0.0268 = 0.6697$$

These procedures have enabled the calculation of volume factors for all the aromatic hydrocarbons presented in Table 3*, and by use of the calculated volume van der Waals' constants b the critical volumes presented in this table were produced. Since the literature background for the critical volumes of the aromatic hydrocarbons is limited to benzene and toluene, no direct comparisons of any significance can be made.

COMPARISON OF RESULTS

For the hydrocarbons presented in Table 3*, critical temperatures and pressures have been calculated by the present method and also by the methods of Riedel (4, 5) and Lydersen (2). The methods of Riedel and Lydersen are similar and require the use of temperature group-contribution values and the normal boiling point for the estimation of the critical temperature (5, 2). These methods permit the evaluation of the critical pressure from the molecular weight of the substance and pressure-group contributions (4, 2) but fail to account for isomeric variations of compounds. Consequently, the same critical pressure results for such isomers as *o*-xylene, *m*-xylene, *p*-xylene, and ethylbenzene. These calculated critical temperatures and pressures are presented in Table 3* and have been compared with the values available in the literature to produce the following average absolute percentages of deviation:

	Riedel (4, 5)	Lydersen (2)	This method
Critical temperature	0.70	0.75	0.70
Critical pressure	2.64	2.56	2.14

From these average deviations, it is apparent that all three methods are

*See footnote on page 429.

capable of producing critical temperatures and pressures with essentially the same degree of accuracy. The critical volumes of the aromatic hydrocarbons appearing in Table 3* have been calculated by the method of this investigation and also that of Lydersen (*2*). No absolute comparisons can be made on these calculated values since the literature background for the critical volumes of the aromatic hydrocarbons is limited to those of benzene and toluene. Comparisons of these calculated critical volumes shows a closer agreement for the simpler aromatic hydrocarbons. By the method of this investigation, critical volumes have also been calculated for the twenty-two aromatic hydrocarbons of Table 4* and are presented in this table along with the critical temperatures and pressures calculated for these compounds from their corresponding van der Waals' constants.

NOTATION

a = pressure van der Waals' constant, (cc./g.-mole)^2(atm.)
b = volume van der Waals' constant, cc./g.-mole
n_{ci}' = total number of carbon atoms present in alkyl side chains
n_{cn}' = total number of carbon atoms present in normal alkyl side chains
p_c = critical pressure, atm.
r = number of aromatic rings in nucleus
R = gas constant, 82.055 (cc.) (atm.)/(g.-mole)(°K.)
T_c = critical temperature, °K.
v_c = critical volume, cc./g.-mole
α_i = total number of branched alkyl chains attached to the aromatic nucleus
α_n = total number of normal alkyl chains attached to the aromatic nucleus
β = volume factor
β_a = volume factor for unsubstituted linearly fused aromatic hydrocarbons
β_{ae} = volume factor for alkyl aromatic hydrocarbons
Δ = difference

LITERATURE CITED

1. Andersen, J. W., G. H. Beyer, and K. M. Watson, *Natl. Petroleum News*, Tech. Sec., **36**, R476 (1944).
2. Hougen, O. A., K. M. Watson, and R. A. Ragatz, "Chemical Process Principles," pp. 87–95, John Wiley and Sons, New York (1954).
3. Kobe, K. A., and R. E. Lynn, Jr., *Chem. Rev.*, **52**, 117–236 (1953).
4. Riedel, Leopold, *Z. Elektrochem.*, **53**, 222–28 (1949).
5. ———, *Chem. Ing. Tech.*, **24**, 353–7 (1952).
6. Thodos, George, *A.I.Ch.E. Journal*, **1**, 168–173 (1955).
7. *Ibid.*, 165–168 (1955).
8. *Ibid.*, **2**, 508–513 (1956).

*See footnote on page 429.

ERRATA

Interpretation and Correlation of Ion Exchange Column Performance Under Nonlinear Equilibria

N. K. Hiester, S. B. Radding, R. L. Nelson, Jr., and Theodore Vermeulen

The ordinate of Figure 1 should read: "Ratio of Breakthrough Slope to Column-capacity Parameter, $d(c/C_0)/dt$, at $c/C_0 = 0.5$; also equals $s \cdot V_{stoic}\ d(c/C_0)/dV$." The slopes in Figures 2 and 3 are correctly identified and conform to the slope-term in Equation (15).

This article appeared on page 404 of the September, 1956, issue of the Journal.

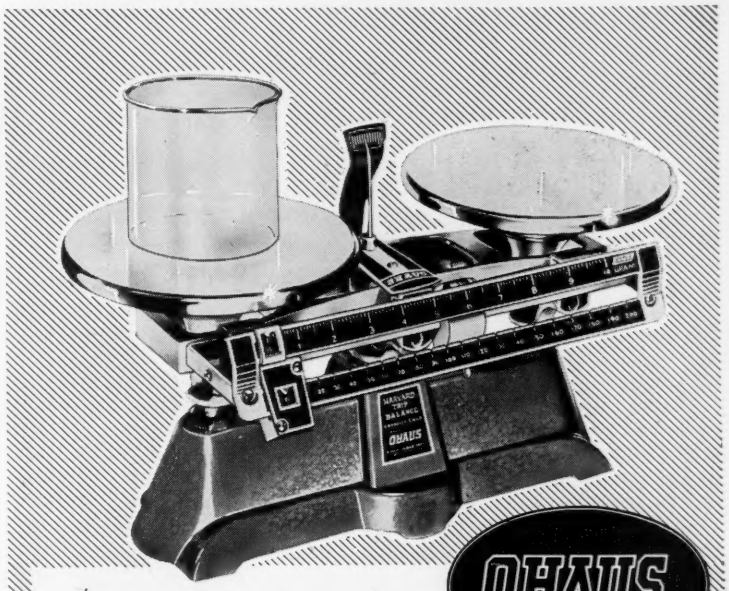

OHAUS

the newest balance from

the new model

HARVARD TRIP BALANCES

represent the greatest advance in trip balance construction in many years. In addition to other fine features is the . . . . . **UNDIVIDED TARE BEAM and POISE** which makes possible *direct reading* of net value thereby greatly increasing the utility of these fine new balances.

TARE CAPACITY: 160 GRAM

OHAUS SCALE CORPORATION
1050 Commerce Ave.
Union, N. J.

Solve Your Drying Problems

in the WYSSMONT DRYING LABORATORY

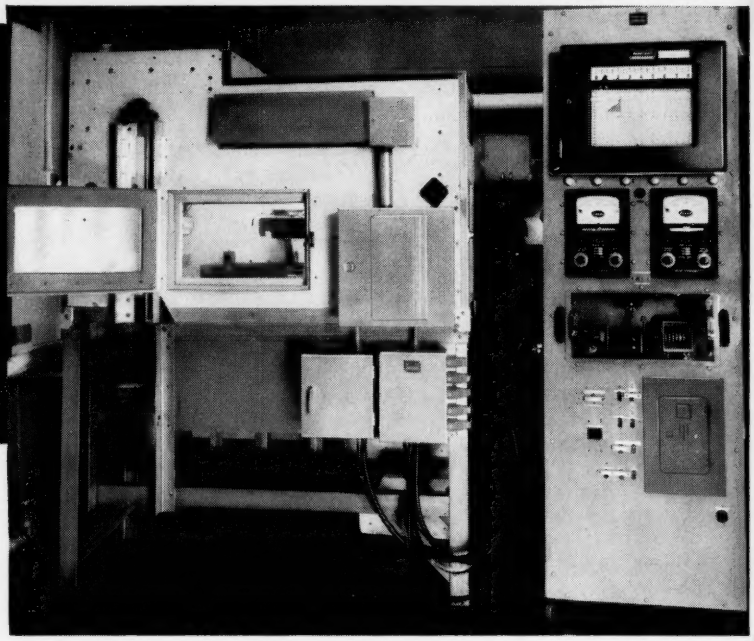

Wyssmont automatic transfer type test dryer with control panel.

As drying engineers we constantly strive to improve not only our design but also our methods of testing to eliminate guessing. After years of development, we have come up with the last word in laboratory test drying facilities. That is why increasing numbers of manufacturers are calling on the facilities and "know-how" of the Wyssmont drying laboratory to help solve drying problems in connection with products that may be fragile, heat sensitive, oxidizable, toxic, hazardous or otherwise difficult to process.

Here in our Wyssmont Test Dryer, simulated actual operating conditions such as material temperature, drying temperature, drying rates, air velocities, turnover cycles are established. These tests are further fortified with complete moisture, chemical and physical determinations. The recording and data are translated into graphs, such as those shown here.

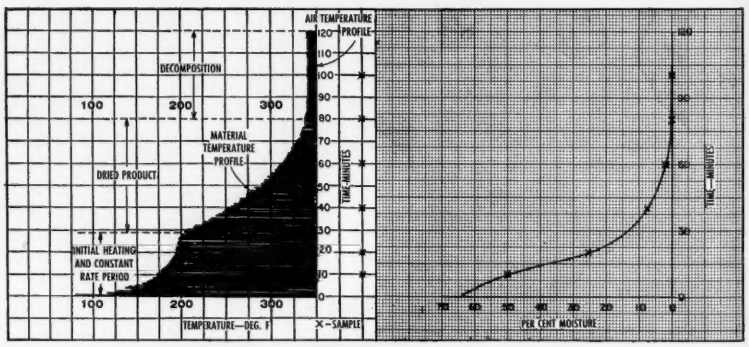

Typical record of drying product which sublimes or decomposes.

Whether the problem involves drying only, solvent removal and recovery, purification by sublimation or gas-solids reactions, the tests are exhaustive, the product analysis complete and accurate, the report and the conclusions objective and unbiased.

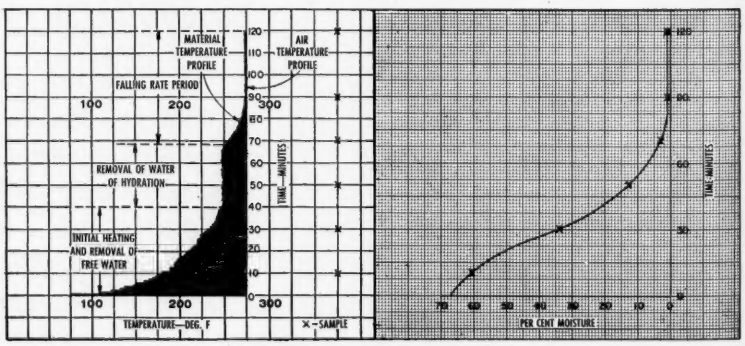

Typical record of drying a hydrate.

WYSSMONT COMPANY, INC.

TURBO DRYER

DRYING ENGINEERS

DRYING • SUBLIMATION • OXIDATION • COOLING

Home Office: 42-07B 27th Street (Bridge Plaza South) Long Island City 1, New York • *Representatives in principal cities*

COMMUNICATIONS TO THE EDITOR

On the Correlation of Data in Nucleate Pool Boiling from a Horizontal Surface

NOVAK ZUBER

University of California, Los Angeles, California

Depending on the characteristic length of the system, there appear to be two scaling methods used in the analysis of boiling heat transfer. Some investigators in their proposed correlation used the diameter of the pipe or the length of the plate as the characteristic length. This method, however, requires knowledge of the bubble population, which is not yet available analytically. Inasmuch as in nucleate boiling bubbles act as strong agitators and the heat flux appears to be independent of the geometry of the surface, it is also possible to scale boiling heat transfer by considering the action of a single bubble. In this case there is, however, a choice of three characteristic lengths: the critical radius R_0, the bubble radius R, and the diameter D of a bubble at the instant of departure from the heating surface. The purpose of this note is to consider the difference between the latter two.

There is by now enough experimental evidence to indicate that the large heat transfer rates associated with nucleate boiling are a consequence of the microconvection in the superheated liquid sublayer. This motion is caused by the dynamics of bubbles which nucleate and grow in the superheated liquid film. In a theoretical analysis of nucleate boiling it is, therefore, necessary to take into account both processes, nucleation and bubble dynamics, if the similarity to the physical system is to be preserved. It appears that nucleate boiling is a balance between these two processes; at low pressures the motion caused by the growing bubble is more important, but at high pressure the nucleation becomes the controlling factor. In a recent paper (*1*) we have pointed out the physical reason for this. The rate of evaporation ($\rho_v R^2 \dot{R}$) for a given amount of superheat is much higher at low pressures than at high pressures, and the rate of nucleation which depends on the surface tension and the slope of the saturation line increases with an increase of pressure.

Consider now the diameter of a bubble at departure given by the Laplace relation:

$$D = C\sqrt{\frac{\sigma}{g(\rho_L - \rho_v)}} \qquad (1)$$

where C is a constant. The physical significance of this length is that it is related to the maximum size of a bubble for which a static equilibrium exists between the buoyant and adhesive forces. We have already pointed out that at low pressure the dynamic forces are predominant. One can, therefore, expect that these forces would be important in determining the size of a bubble departing from the heated surface, as has been shown in experiments reported by Rohsenow and Clark (*2*) and Ellion (*3*). This can be also shown analytically. However, as the pressure is increased and the dynamic forces decrease, one would expect that the static forces (buoyant and adhesive) would gradually determine the diameter. Since in the pressure range of interest ($0.01P_{crit}$ to $0.8P_{crit}$) this diameter, given by Equation 1, decreases by a factor between 2 and 3, it could be expected that the size of departing bubbles at high pressures would appear approximately constant. This

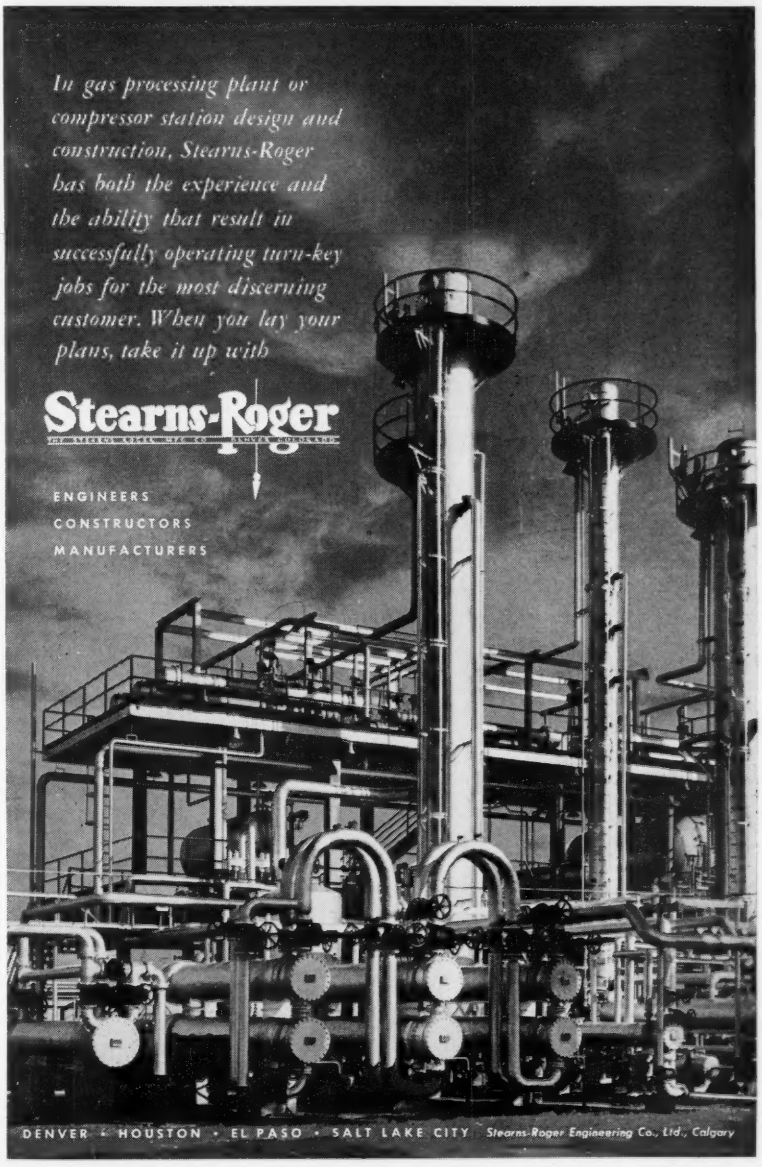
In gas processing plant or compressor station design and construction, Stearns-Roger has both the experience and the ability that result in successfully operating turn-key jobs for the most discerning customer. When you lay your plans, take it up with
Stearns-Roger
ENGINEERS
CONSTRUCTORS
MANUFACTURERS
DENVER • HOUSTON • EL PASO • SALT LAKE CITY
Stearns-Roger Engineering Co., Ltd., Calgary

MIN CHEMISTRY *at work*

case: how M & C materials and methods get the job done by sorption processing

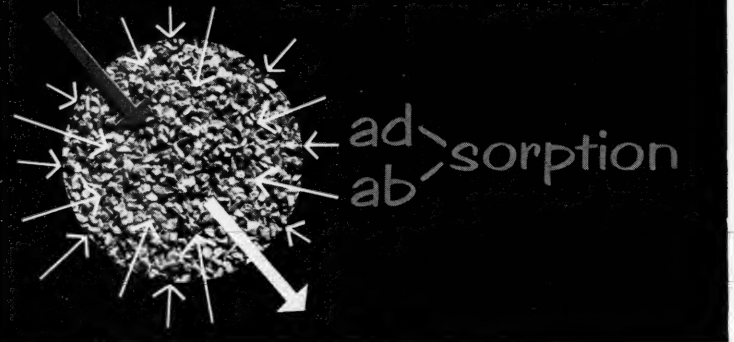

Ad- or *ab-* . . . whichever prefix to sorption you prefer . . . M & C works with you to get the right balance of medium, efficiency, purity, treating conditions and economy.

Sorptive Mineral Report: M & C offers many grades for many jobs.

Molecules Out—you can refine, purify, decolorize; remove odors, colors, taste, moisture, acids, sulfur compounds, fluorides, unsaturates, many others.

Molecules In—other grades serve as carriers in scores of processes.

Anti-Caking—often 1% or less of specific sorptive grades make sticky, waxy, hygroscopic chemicals free flowing.

Drying—M & C desiccants dry air, hydrogen, CO_2, hydrocarbons, other fluids and gases.

Our business is to supply low-cost, nature-given materials that are *process-engineered* to make things go smooth in your plant . . . good in your markets. Use the coupon.

MINERALS & CHEMICALS CORPORATION OF AMERICA
3058 Essex Turnpike, Menlo Park, N. J.

I'm interested in a natural mineral product for_____

_____

Send: ☐ Adsorbent Information ☐ Free samples

name_____title_____

company_____

address_____

city_____zone_____state_____

For more data, see Chemical Materials Catalog Pages 330-334

MINERALS & CHEMICALS
CORPORATION OF AMERICA
3058 Essex Turnpike, Menlo Park, N.J.

Leaders in creative use of non-metallic minerals
ATTAPULGITE (*Attapulgus*)
ACTIVATED BAUXITE (*Porocel*)
KAOLIN (*Edgar • ASPs*)
LIMESTONE (*Chemstone*)
SPEEDI-DRI FLOOR ABSORBENTS

fact was actually observed by Clark (*4*).

An important fact, however, should not be overlooked. While it appears to be true that at high pressure the diameter of the departing bubble is given by Equation (1), such a bubble could not have originated from *one* nucleating center. It is known that the heat transfer rate increases with an increase in pressure up to approximately 0.35 of the critical pressure. Inasmuch as the rate of evaporation constantly decreases while the diameter D remains approximately constant, the only way to account for the increase of the heat flux is by taking into consideration the nucleation. As mentioned previously, a large increase of nucleating centers (for a given degree of superheat) can be expected with an increase in pressure. This fact has been experimentally observed. A bubble of diameter D would then originate by a coalescence of several small bubbles rather than by the growth from a single nucleus. It can be seen, therefore, that if Laplace's relation is used as the characteristic length the dynamic similarity is not preserved as the pressure is increased.

We have shown in our paper mentioned above that it is possible to scale nucleate pool boiling from a horizontal surface by considering the action of a single bubble. Taking the bubble radius R and radial velocity $\dot{R}$ as the characteristic length and velocity of the flow system (superheated film), we expressed the Nusselt modulus in its standard form, that is, as a function of the Reynolds and Prandtl moduli:

$$Nu = 0.0015\, Re^{0.62} Pr^{0.33} \qquad (2)$$

This method made possible not only the formulation of the Reynolds number in terms of the thermodynamic properties of the vapor and liquid

$$Re = \left[\frac{\Delta T C \rho_L \sqrt{\pi a}}{L \rho_v}\right]^2 \frac{\rho_L}{\mu} \qquad (3)$$

but also provided a way to take nucleation into account. We have only to remember that nucleation is a function of the surface energy (σA). The characteristic length in our analysis was the bubble radius R given by

$$R = \frac{\Delta T C \rho_L \sqrt{\pi a}}{L \rho_v} \sqrt{\frac{2\sigma}{\Delta P}} \sqrt[4]{\frac{\rho_L}{\Delta P}} \qquad (4)$$

As

$$R\dot{R} = \left[\frac{\Delta T C \rho_L \sqrt{\pi a}}{L \rho_v}\right]^2 \qquad (5)$$

and

$$R_0 = \frac{2\sigma}{\Delta P} \qquad (6)$$

then Equation (4) can be put in the following form:

$$R = R_0 \sqrt[4]{\frac{\rho_L R^2 \dot{R}^2}{\sigma R_0}} \qquad (7)$$

Multiplying and dividing the expression under the root by a length results in a numerator proportional to the kinetic energy and a denominator proportional to the surface energy; the ratio R/R_0 is thus a function of a modified Weber number. It could have been expected that Weber's modulus would also appear in nucleate boiling inasmuch as it always appears when bubbles are considered. As the dynamic forces are important at low pressure, the ratio R/R_0 is large; at high pressure this ratio decreases to unity, which is again in accordance with the previous considerations.

It can be concluded that if in an analysis of nucleate pool boiling from a horizontal surface the bubble radius R and the radial velocity $\dot{R}$ are taken as the characteristic length and velocity, the two bubble effects, nucleation and liquid agitation, can be taken into account. It is thus possible to preserve the dynamic similarity and correlate the peak nucleate heat transfer rates with a single equation [Equation (2)].

NOTATION

a = thermal diffusivity
c_p = specific heat at constant pressure
D = bubble diameter
g = acceleration due to gravity
k = thermal conductivity
L = latent heat of vaporization
Nu = Nusselt modulus
P = pressure
$\Delta P = P_v - P_\infty$ = pressure difference corresponding to the superheat temperature
Pr = Prandtl modulus
$r = R/R_0$ = dimensionless bubble radius
R = bubble radius
R_0 = radius of critical bubble
$\dot{R}$ = bubble radial velocity
Re = Reynolds modulus
T_0 = initial superheat temperature
T_∞ = saturation temperature corresponding to pressure on system P_∞
$\Delta T = T_0 - T_\infty$ = superheat temperature
μ = viscosity
ρ = mass density
σ = surface tension

Subscripts

L = liquid
v = vapor

LITERATURE CITED

1. Forster, H. K., and Novak Zuber, *A.I.Ch.E. Journal*, **1**, (1955).
2. Rohsenow, W. M., and J. A. Clark, Trans. *Am. Soc. Mech. Engrs.*, **75**, 969 (1952).
3. Ellion, M. E., Ph.D. thesis, Calif. Inst. Technol. (1954).
4. Clark, J. A., Mass. Inst. Technol., personal communication.

Type 70-T
Temperatures to 1950° F.
The new design of these furnaces provides you with a complete and compact self-contained unit. The base contains a tap-changing transformer equipped with two selector switches which offer 36 steps of temperature control. Larger size tube Furnaces are available. Write for Bulletin 552.
HEVI DUTY
Presents...
A NEW SERIES OF
MULTIPLE UNIT
COMBUSTION TUBE FURNACES
• Complete Self-Contained Unit
• Positive Temperature Control
• Hinged Type Construction
Type
123-T
Each Section
Separately
Controlled
This Organic Combustion Tube Furnace, made in three movable sections, is a convenience for the modern organic analysis laboratory. This furnace can act as one or as three separate units. The use of tap-changing transformers allows closer temperature regulation and means savings in power and maintenance. The furnaces are hinged for easier operation. Write for Bulletin 735R.
HEVI DUTY ELECTRIC COMPANY
MILWAUKEE 1, WISCONSIN
Heat Treating Furnaces... Electric Exclusively
Dry Type Transformers
Constant Current Regulators

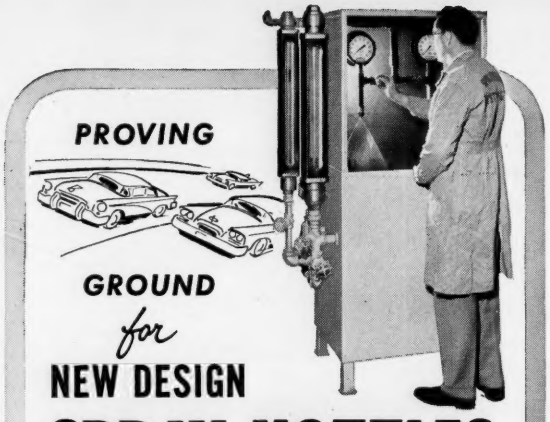

PROVING

GROUND

for

NEW DESIGN

SPRAY NOZZLES

SPRAYING SYSTEMS CO.
3210 RANDOLPH STREET
•
BELLWOOD, ILL.

For new designs or applications, nozzle spray characteristics are exhaustively analyzed in the Spraying Systems laboratory. Spray booths like the one shown here, distribution tables, and stroboscopic cameras are just some of the equipment employed . . . to give you dependable spray nozzles that perform with "precision." For complete information, write for Catalog 24 . . . the most comprehensive catalog of its kind in the field.

ADVANCED SPRAY NOZZLE DESIGN FOR NEW DIMENSIONS IN CONTROL & PERFORMANCE

INDEX OF ADVERTISERS

Beckman Instruments, Inc. . .Inside Back Cover		Ohaus Scale Corporation	7S
Bowen Engineering, Inc.	298	Spraying Systems Company	12S
Curtin Company, W. H.	6S	Stearns Rodger Mfg. Company	9S
Eimco Corporation, The	4S	Titanium Alloy Mfg. Div. National Lead Co.	5S
Hevi Duty Electric Company	11S	Wyssmont Company	8S
Minerals & Chemicals Corp. of America	10S		
Mixing Equipment Co. . . . .Outside Back Cover		York Process Equipment Corp. Inside Front Cover	

Advertising Offices

New York 36—Lansing T. Dupree, Adv. Mgr.; John M. Gaede, Asst. Adv. Mgr.; Paul A. Jolcuvar, Dist. Mgr.; Donald J. Stroop, Dist. Mgr.; Hale H. Carey, Dist. Mgr.; 25 W. 45th St., Columbus 5-7330.

Chicago 11—Richard R. Quinn, Dist. Mgr., 612 North Michigan Ave., Room 507, Superior 7-0385.

Cleveland 15—Eugene B. Pritchard, Dist. Mgr., 1836 Euclid Ave., Superior 1-3315.

Pasadena 1—Richard P. McKey, Dist. Mgr., 465 East Union St., Ryan 1-0685.

Dallas 28—Richard E. Hoierman, Dist. Mgr., 2831 El Capitan Drive, Davis 7-3630.

Birmingham 9, Ala.—Fred W. Smith, Dist. Mgr., 1201 Forest View Lane—Vesthaven, Tremont 1-5762.

BOOKS

Chemical Engineering Kinetics. J. M. Smith. McGraw-Hill Book Company, Inc., New York (1956). 402 pages. $8.00.

Professor Smith has attempted to fill a great need in chemical engineering text books by writing an introductory work on chemical engineering kinetics. The work is eminently suitable for senior-level instruction since no mathematics more advanced than undergraduate calculus need be used in Smith's problems. At times, however, this results in extremely long and tedious calculations. Fundamentally the text is devoted to the problems of designing or sizing equipment, as may be seen by these sample chapter headings: "Introduction to Reactor Design," "Homogeneous Batch Reactors," and "Design of Gas-solid Catalytic Reactors." The material in this work is presented very much in the same form as Smith's earlier well-known book on thermodynamics: generally clear explanatory text followed by worked illustrations of the principles discussed. There are extensive and challenging problems at the end of each chapter which should prove useful to all those who teach kinetics. As in an earlier work on chemical engineering kinetics, Smith, although relying heavily upon his own papers in finding examples, fortunately includes a large body of other works augmented by extensive references.

After a useful review of the thermodynamics of chemical equilibrium the general field of kinetics is introduced in the third chapter. However the summary of the absolute rate theory included in the appendix at best serves as a review for those previously acquainted with statistical mechanics. The practical demands of reactor design are then fairly well presented in the fourth chapter. Homogeneous reactions are the subjects of the fifth and sixth chapters, and semibatch or continuous stirred tank reactors are adequately discussed in the seventh chapter. A discussion of catalysis in the eighth chapter serves as an introduction to heterogeneous reactions, the subject matter for the remainder of the book. The Hougen and Watson approach is used to derive rate equations for heterogeneous reactions in the ninth chapter. The tenth chapter covers heat and mass transfer in packed beds; here one might wish that the author dwelt more on *techniques* rather than *examples*. A brief discussion of the concepts used in setting up partial-differential equations and the solution to finite-difference equations would have been particularly useful to the student. Further, the appendix to this chapter discussing the Argo and Smith paper might well have been eliminated. Given the limitations of the tenth chapter, the final chapter, "Design of Gas-solid Catalytic Reactors," combines the material discussed in the last half of the book quite well.

Chemical Engineering Kinetics is a successful attempt to write an introductory text to engineering kinetics. As the field is growing quite rapidly, most teachers probably will choose to supplement it with material of their own. With the increased popularity of computing machines and more sophisticated mathematical methods the last few chapters of the book may have to be rewritten.

JON OLSON